Universität Rostock

Traditio et Innovatio

Design and Implementation of a Flexible Research Platform for the Study of Deep Brain Stimulation

Der Fakultät für Informatik und Elektrotechnik der Universität Rostock
zur Erlangung des akademischen Grades

Doktor-Ingenieur (Dr.-Ing.)

vorgelegte Dissertation von
Franz Veit Plocksties
geb. am 18.11.1992 in Schwerin
aus Rostock

Rostock, 28.11.2025

https://doi.org/10.18453/rosdok_id00005771

Dissertation
Fakultät für Informatik und Elektrotechnik

Franz Veit Plocksties
Institut für Angewandte Mikroelektronik und Datentechnik

This work is licensed under a Creative Commons ‘Attribution 4.0 International’ license.



Gutachter:

Prof. Dr.-Ing. Dirk Timmermann
Institut für Angewandte Mikroelektronik und Datentechnik
Universität Rostock

Prof. Dr.-Ing. Christian Haubelt
Institut für Angewandte Mikroelektronik und Datentechnik
Universität Rostock

Prof. Dr. Robert Rieger
Institut für Elektrotechnik und Informationstechnik
Christian-Albrechts-Universität zu Kiel

Datum der Einreichung: 28.11.2025
Datum der Verteidigung: 16.03.2026

Danksagung

Ich möchte an dieser Stelle die Gelegenheit nutzen, um all jenen zu danken, die mich während der Entstehung dieser Arbeit begleitet und unterstützt haben.

Meinem Doktorvater, Professor Dirk Timmermann, gilt mein aufrichtiger Dank für die beständige Betreuung dieser Arbeit und seine ermutigenden Worte, die mich insbesondere in herausfordernden Zeiten motiviert haben. Professor Christian Haubelt danke ich für zahlreiche wertvolle Anregungen und seine fortwährende Unterstützung. Auch Professor Robert Rieger möchte ich für die Begutachtung dieser Dissertation danken.

Mein Dank gilt zudem meinen Kolleginnen und Kollegen am Institut für Angewandte Mikroelektronik und Datentechnik, die mit ihrer fachlichen Unterstützung und dem angenehmen Miteinander wesentlich zu einem inspirierenden Arbeitsumfeld beigetragen haben. Ich möchte meinem langjährigen Bürokollegen Felix Uster danken, der maßgeblich zum 3D-Design und 3D-Druck der Implantatgehäuse beigetragen hat. Ich möchte mich bei Dr. Christoph Niemann bedanken, der mich mit seiner fachlichen Expertise und seinem Rückhalt durch viele Herausforderungen begleitet hat. Außerdem danke ich Robert Hauser für seine Unterstützung und den stets ideenreichen fachlichen Austausch.

Ebenso möchte ich mich bei meinen Kolleginnen und Kollegen aus der Medizin bedanken, insbesondere bei Maria Kober, Dr. Kathrin Badstübner, Dr. Mareike Fauser und Dr. Denise Franz, für ihre wertvolle Unterstützung und die immer angenehme Zusammenarbeit.

Ich möchte mich bei Uwe Knüpfer für seine fachkundige Beratung und Unterstützung beim Leiterplattendesign bedanken. Außerdem möchte ich mich bei der Dorazil Mikro-Elektronik GmbH für die zuverlässige Bestückung der Leiterplatten über viele Jahre hinweg bedanken.

Mein tiefster Dank gilt meiner Familie, die mich während der gesamten Arbeit mit Geduld, Vertrauen und Unterstützung begleitet hat. Insbesondere danke ich meinen Eltern für ihren Rückhalt und ihren Glauben an mich. Dir, Franzi, danke ich von Herzen für deine Klarheit, deine Beständigkeit und dafür, dass du die vielen Stunden meiner Abwesenheit mit so viel Liebe und Geduld getragen hast.

Kurzfassung

Die Tiefe Hirnstimulation (THS), bei der elektrische Impulse in spezifische Hirnareale appliziert werden, ist eine etablierte Therapie für Bewegungsstörungen wie die Parkinson-Krankheit. Dennoch sind ihre Wirkmechanismen bis heute nur unvollständig geklärt. Für ein vertieftes Verständnis sind experimentelle Studien an frei beweglichen Nagetieren notwendig, deren Fortschritt jedoch durch das Fehlen funktionsreicher, langzeitfähiger und tierwohlgerechter Neurostimulationsgeräte erheblich eingeschränkt wird. Diese Dissertation präsentiert *STELLA*, eine vollständig implantierbare THS-Plattform, die gezielt entwickelt wurde, um diese Einschränkungen zu überwinden. Vom anfänglichen Konzept bis zum fertigen Implantat wurden sämtliche Entwicklungsschritte realisiert, einschließlich Architekturdefinition, Schaltungsdesign, Firmware-Implementierung, Fertigung, Verkapselung sowie Validierung *in vitro*, *ex vivo* und *in vivo*. STELLA vereint in einzigartiger Weise extrem niedrigen Leistungsverbrauch, zweikanalige Stimulation, integrierte Stimulationsüberwachung, bidirektionale drahtlose Kommunikation und Closed-Loop-Fähigkeiten in einem Formfaktor von weniger als einem Kubikzentimeter—und dies ausschließlich unter Verwendung handelsüblicher Komponenten. Eine speziell entwickelte biokompatible, wasserdichte und kompakte Verkapselung ermöglicht eine dauerhafte subkutane Implantation. Die Plattform hat in *in vivo* Studien einen zuverlässigen Langzeitbetrieb mit stromgesteuerter, ladungsbalancierter Stimulation unter Beweis gestellt und bereits zu einem besseren Verständnis der THS-Mechanismen beigetragen. Indem STELLA natürliches Verhalten der Tiere ermöglicht, verbessert die Plattform entscheidend das Tierwohl in diesen Studien und leistet damit einen wichtigen Beitrag zum Refinement-Aspekt der 3R-Prinzipien. Insgesamt schafft diese Arbeit eine wissenschaftlich robuste und ethisch verantwortungsvolle Grundlage für präklinische THS-Studien an frei beweglichen Nagetieren.

Abstract

Deep brain stimulation (DBS), in which electrical impulses are delivered into specific brain regions, is an established therapy for movement disorders such as Parkinson's disease. Nevertheless, its mechanisms of action remain only partially understood. Advancing this understanding requires experimental studies in freely moving rodents, but progress is hindered by the lack of feature-rich, long-term capable, and animal-welfare-compliant neurostimulation devices. This dissertation presents *STELLA*, a fully implantable DBS platform specifically designed to overcome these limitations. From the initial concept to the final implant, all development stages were realized, including architecture definition, circuit design, firmware implementation, device fabrication, encapsulation, and validation *in vitro*, *ex vivo*, and *in vivo*. STELLA uniquely combines ultra-low power operation, dual-channel stimulation, integrated stimulation monitoring, bidirectional wireless communication, and closed-loop capabilities in a form factor smaller than one cubic centimeter—achieved exclusively with off-the-shelf components. A custom-developed biocompatible, waterproof, and compact encapsulation enables long-term subcutaneous implantation. The platform has demonstrated reliable long-term operation with current-controlled, charge-balanced stimulation in *in vivo* studies and has already contributed to a deeper understanding of DBS mechanisms. By enabling natural animal behavior, STELLA significantly enhances animal welfare in these studies and thus represents an important contribution to the refinement aspect of the 3R principles. Overall, this work establishes a scientifically robust and ethically responsible foundation for preclinical DBS studies in freely moving rodents.

Contents

List of Figures V

List of Tables VII

List of Abbreviations X

1 Introduction 1
1.1 Problem Formulation . . . 1
1.2 Structure and Citation Style . . . 2

2 Fundamentals 4
2.1 Brief Overview of Deep Brain Stimulation (DBS) . . . 4
2.2 Principles of Neurostimulation . . . 6
2.2.1 Conventions and Technical Terms . . . 6
2.2.2 Electrical Properties of the Electrode-Electrolyte System . . . 7
2.2.3 Stimulation Waveforms: Pulse Characteristics . . . 13
2.2.4 Stimulation Waveforms: Principles of Charge Balancing . . . 16
2.2.5 Pulse Generator Architectures . . . 19
2.2.6 Discrete Current Source Design: Practical Considerations . . . 20
2.2.7 Considerations of Blocking Capacitors . . . 22
2.2.8 Electrochemical Safety Limits . . . 24

3 Study of Preclinical Deep Brain Stimulation Systems 26
3.1 Requirements for Preclinical DBS Devices . . . 26
3.2 Why Stimulation Monitoring Matters in DBS Experiments . . . 28
3.3 Critical Review of the State of the Art . . . 32
3.4 Interim Conclusion . . . 42

4 Electrode-Electrolyte Characterization 44
4.1 Stimulation Setup within the Project . . . 44
4.2 Compliance Voltage Characterization . . . 48
4.3 Electrode-Electrolyte Impedance Model . . . 51
4.3.1 Impedance Spectroscopy Setup . . . 52
4.3.2 Impedance Characteristics . . . 52
4.3.3 Equivalent Circuit Modeling and Parameter Extraction . . . 54
4.4 Application of the Model to Passive Charge-Balanced DBS . . . 55
4.4.1 Deriving the DBS Waveforms . . . 56
4.4.2 Bias Voltage without Blocking Capacitors . . . 61

4.4.3 Bias Voltage with Blocking Capacitors . . . 62
4.5 Interim Conclusion . . . 68

5 Design and Implementation of a Flexible DBS Platform: STELLA 70
5.1 Introduction to the STELLA Family . . . 70
5.2 Realizing a Highly Miniaturized DBS Device: STELLA3 . . . 73
5.2.1 System Overview . . . 73
5.2.2 Current-Controlled Pulse Generation . . . 74
5.2.3 Charge Balancing and Safety . . . 78
5.2.4 Built-in Self-test for Stimulation Monitoring (BIST) . . . 79
5.2.5 Timing Control and Energy-Saving Mechanisms . . . 80
5.2.6 Firmware Concept . . . 83
5.2.7 Physical Design and Modularity . . . 83
5.2.8 Encapsulation Method: Epoxy Potting . . . 85
5.3 Results . . . 88
5.3.1 Epoxy-Potted Housing: Physical Properties and *In Vitro* Testing . . . 88
5.3.2 Stimulation Unit: Compliance Voltage . . . 89
5.3.3 Stimulation Unit: *In Vitro* and Brain Tissue Measurements . . . 89
5.3.4 Power Consumption during DBS-only Operation . . . 92
5.3.5 Runtime and Implantability . . . 93
5.3.6 Contributions to Animal Welfare and *In Vivo* Applications . . . 96
5.4 Interim Conclusion of STELLA3 . . . 100
5.5 Extension of STELLA3 with a 2.4 GHz Radio Module: STELLA3.1 . . . 101
5.5.1 PCB and Circuit Design . . . 102
5.5.2 Firmware Architecture . . . 103
5.5.3 Battery Selection for RF Communication . . . 104
5.5.4 Encapsulation Method: Drop-Shaped Air-Filled Housing . . . 106
5.6 Results . . . 108
5.6.1 Air-Filled Housing: Physical Properties and *In Vitro* Testing . . . 108
5.6.2 Power Consumption, Runtime, and Implantability . . . 109
5.7 D-Shaped Air-Filled Housing for STELLA3 . . . 111
5.8 Interim Conclusion of STELLA3.1 . . . 113
5.9 Realizing a Highly Functional DBS Device: STELLA4 . . . 114
5.9.1 System Architecture . . . 115
5.9.2 Physical Design and Battery Integration . . . 118
5.9.3 Evaluation Board . . . 118
5.9.4 Power Management . . . 119
5.9.5 System Communication and Logic-Level Translation . . . 121
5.9.6 Li-ion Battery Charging and Protection . . . 122

5.9.7 Enhancements of the Stimulation Unit 124
5.10 Results 127
5.11 Interim Conclusion of STELLA4 130

6 Summary **132**

7 Outlook **134**
7.1 Future Perspectives with STELLA 134
7.2 Crosstalk Effects in Bilateral DBS 134

References **137**

List of Peer-Reviewed Publications **165**

A State of the Art in Detail (Part I) **I**

B State of the Art in Detail (Part II) **II**

C Overview of STELLA Specifications **III**

D Air-Filled Encapsulation Protocol for STELLA3 **IV**

E Setup for Recording Stimulation Current and Voltage **V**

F DBS Parameters Used in Rodent PD/Dystonia Studies **VI**

List of Figures

1 Areas of application of electrostimulating implants . . . 3
2 Components and X-ray images of a DBS system . . . 6
3 Equivalent circuit of total electrode-electrolyte impedance . . . 9
4 Schematic of the DBS stimulation circuit and equivalent load impedance models, together with corresponding voltage and current waveforms . . . 14
5 Schematic of the DBS current waveform illustrating stimulation and charge balancing phases. . . . 17
6 Common pulse generator circuit topologies . . . 21
7 Schematic and simulation of an npn BJT current source showing operating regions. . . . 23
8 Stimulation waveforms under various failure cases. . . . 31
9 Power consumption vs. compliance voltage for existing rodent DBS systems 37
10 Battery runtime vs. device volume for existing rodent DBS systems . . . 38
11 Comparison of technical features across existing rodent DBS devices . . . 41
12 Electrode setup . . . 47
a Electrode types and their dimensions . . . 47
b Images of electrode types . . . 47
13 Maximum stimulation voltage vs. current amplitude for monopolar and bipolar electrodes . . . 51
14 Impedance measurement in brain tissue . . . 54
15 Model parameter extraction and validation in brain tissue . . . 60
16 Bias voltage measurements with and without compensation . . . 67
17 STELLA evolution . . . 72
18 Circuit schematic of STELLA3 . . . 75
19 Current source architecture and current adjustment simulation . . . 77
20 Schematic of BIST procedure . . . 79
21 Illustration of the adaptive approach utilizing the built-in self-test (BIST) mechanism . . . 81
22 Program flowchart of the STELLA3 firmware . . . 84
23 Manufactured STELLA3 PCB . . . 85
24 Epoxy potting encapsulation process of STELLA3 . . . 87
25 Encapsulated STELLA3 using the epoxy potting method . . . 88
26 Voltage and current recordings of STELLA3 in brain and saline . . . 91
27 Power consumption of STELLA3 under bilateral stimulation . . . 94
28 Postoperative outcomes in rats with implanted STELLA3 vs. backpack devices 98
29 Body weight development of dt^{sz} hamsters with implanted STELLA3 devices 99
30 Manufactured STELLA3 and STELLA3.1 PCBs . . . 103

31 Battery voltage and current behavior during RX events for various coin cells 106
32 Encapsulation process of the air-filled, drop-shaped STELLA3.1 housing . . 108
33 Encapsulated STELLA3.1 implant and base station 109
34 Power consumption and estimated runtime of STELLA3.1 for different communication intervals 111
35 D-shaped housing for STELLA3 113
36 Overview of the STELLA4 system architecture 116
37 Physical design of STELLA4 119
38 Evaluation board for firmware development of STELLA4 119
39 Circuit architecture of STELLA4 120
40 Logic level translation and bus architecture of STELLA4 122
41 Li-ion charging and protection concept of STELLA4 124
42 Increased current amplitude resolution with parallel digital potentiometer configurations 126
43 Manufactured STELLA4 PCBs and encapsulation 128
44 Validation of STELLA4's stimulation unit 129
45 Crosstalk between stimulation channels 136
E.1 Recording setup for DBS voltage and current measurements V
F.1 Overview of applied stimulation parameters in DBS studies using rodent models for movement disorders VI

List of Tables

1 Comparison of essential features in battery-powered, compact rodent DBS devices 40
2 *In vivo* stimulation setups within the ELAINE project 45
3 Fitted impedance parameters for bipolar and monopolar electrodes 55
4 STELLA version history 72
5 Operating modes of the MSP430G2553 and their application in STELLA3. 82
6 Power consumption of STELLA3 across MSP430 operating modes 92
7 Power consumption of STELLA3 at different system voltages 93
8 Battery options and corresponding DBS-only runtime estimates for STELLA3 95
9 Encapsulation dimensions and weights for STELLA3 with different coin cells 96
10 Battery options and DBS-only runtime estimates for STELLA4 130
A.1 Comparison of key features in rodent DBS devices I
B.1 Comparison of technical and physical parameters in rodent DBS devices . . II
C.1 Overview of STELLA3/STELLA3.1/STELLA4 features III

List of Abbreviations

3Rs Replacement, Reduction, Refinement

6-OHDA 6-Hydroxydopamine

dt^{sz} Dystonic Hamster Model

ACLK Auxiliary Clock

aDBS Adaptive Deep Brain Stimulation

ADC Analog-to-Digital Converter

AP Action Potential

ASIC Application-Specific Integrated Circuit

BAC Bacterial Artificial Chromosome

BIST Built-In Self-Test

BJT Bipolar Junction Transistor

CE Counter Electrode

CIC Maximum Reversible Charge Injection Capacity

CPE Constant Phase Element

CRC Collaborative Research Centre

CV Cyclic Voltammetry

DAC Digital-to-Analog Converter

DBS Deep Brain Stimulation

DC Direct Current

DCO Digital Crystal Oscillator

ECF Extracellular Fluid

ELAINE Electrically Active Implants

FDA Food and Drug Administration

GPi Globus Pallidus Internus

I^{2}C Inter-Integrated Circuit

IC Integrated Circuit

IPG Implantable Pulse Generator

IR Infrared

ISM Industrial, Scientific, and Medical Band

LFP Local Field Potential

LPM Low Power Mode

MCU Microcontroller Unit

MOSFET Metal-Oxide-Semiconductor Field-Effect Transistor

OCD Obsessive-Compulsive Disorder

OSI Open Source Instrument

PCB Printed Circuit Board

PD Parkinson's Disease

PEEK Polyether Ether Ketone

PETG Polyethylene Terephthalate Glycol-Modified

PTFE Polytetrafluoroethylene

PWM Pulse-Width Modulation

RF Radio Frequency

SPI Serial Peripheral Interface

STELLA Software-Defined Implantable Platform

STN Subthalamic Nucleus

TVS Transient Voltage Suppressor

VIM Ventral Intermediate Nucleus

VLC Visible Light Communication

WE Working Electrode

WOR Wake-on-Radio

WPT Wireless Power Transfer

1 Introduction

1.1 Problem Formulation

Across the world, societies are becoming older [234, 86]. With rising life expectancy comes an increasing number of people affected by age-related neurological conditions, such as Parkinson's disease (PD), essential tremor, and Alzheimer's disease [243, 10]. These conditions are not only devastating for patients but also create major challenges for healthcare systems [180, 89]. Therapies that can help maintain mobility, independence, and quality of life are therefore of growing importance.

One essential therapy approach is the delivery of controlled electrical stimulation to defined tissue targets within the human body. Such stimulation can modulate neural activity [124], regulate organ function [254, 222], restore lost functions [110], or promote tissue regeneration [69]. Long-term therapies require fully implantable, battery-powered systems that provide continuous and reliable stimulation. Their medical use began in the 1950s with the introduction of the first fully implantable cardiac pacemakers [6] and has since expanded to various therapeutic applications throughout the human body (see Fig. 1).

A prominent example is deep brain stimulation (DBS), a well-established therapy for movement disorders such as Parkinson's disease, with ongoing studies investigating its potential for psychiatric and cognitive disorders as well [144, 90]. However, despite its clinical success, the exact mechanisms by which DBS works are still not fully understood [9]. Gaining insight into these mechanisms is essential if DBS is to be further optimized, tailored to individual patients, or expanded to treat additional neurological and psychiatric disorders.

Progress in this direction is driven mainly by preclinical DBS research [144, 39]. Rodent models play a crucial role in this context, enabling the study of electrophysiological, neurochemical, and behavioral effects of neural modulation [205]. To advance these investigations, continuous stimulation over extended periods, spanning weeks and even months, is required. At the same time, the focus of current research is shifting toward more sophisticated stimulation concepts, including closed-loop approaches that rely on feedback signals. Supporting such modern studies requires highly specialized neurostimulators that combine advanced functional capabilities with a compact form factor to allow for natural, unimpaired behavior in freely moving animals.

However, progress in preclinical rodent DBS research is hindered by functionally limited, bulky, and power-demanding neurostimulators. Consequently, this results in several methodological limitations, including:

- **Inability to study long-term effects**, due to insufficient energy efficiency to sustain

stimulation over extended periods.

- **Increased experimental burden on animals**, as device size and mounting methods lead to stress, restricted behavior, and higher dropout rates, which in turn constrain the validity of behavioral studies.
- **Limited safety and accuracy**, posing risks to animal welfare and compromising the quality of experimental findings.
- **Insufficient monitoring of delivered stimulation**, limiting the reproducibility and interpretability of physiological and behavioral outcomes.
- **Restricted experimental flexibility**, as evolving stimulation protocols cannot be adequately supported.
- **Lack of integrated sensing and on-device processing**, preventing the detection of relevant biomarkers and the implementation of feedback-driven stimulation strategies.

The objective of this dissertation is to bridge these methodological gaps by conceiving and developing a novel research platform that enables reliable and reproducible long-term DBS experiments, maintains natural animal behavior, and provides the flexibility required for future research. The term *research platform* emphasizes the transition from a single-purpose stimulation device to a comprehensive framework that integrates stimulation, sensing, data processing, and adaptable experimental protocols.

Advancing such a research platform requires an interdisciplinary setting that brings together expertise from multiple disciplines. This environment is provided by the collaborative research centre **Electrically Active Implants (ELAINE)** (CRC 1270) at the University of Rostock, within the framework of which the work presented in this dissertation was conducted. The research was funded by the Deutsche Forschungsgemeinschaft (DFG, German Research Foundation) – SFB 1270/1,2 - 299150580.

1.2 Structure and Citation Style

The present dissertation is organized into seven chapters. Chapter 1 introduces the motivation and defines the problem statement. Chapter 2 presents the theoretical and technical fundamentals of deep brain stimulation. Chapter 3 defines design requirements for a DBS system and reviews existing preclinical DBS platforms. Chapter 4 focuses on the characterization and modeling of the electrode-electrolyte impedance. Chapter 5 describes the design and implementation of the DBS platforms STELLA3, STELLA3.1, and STELLA4. Finally, Chapter 6 summarizes the key findings, while Chapter 7 provides an outlook on future research directions.

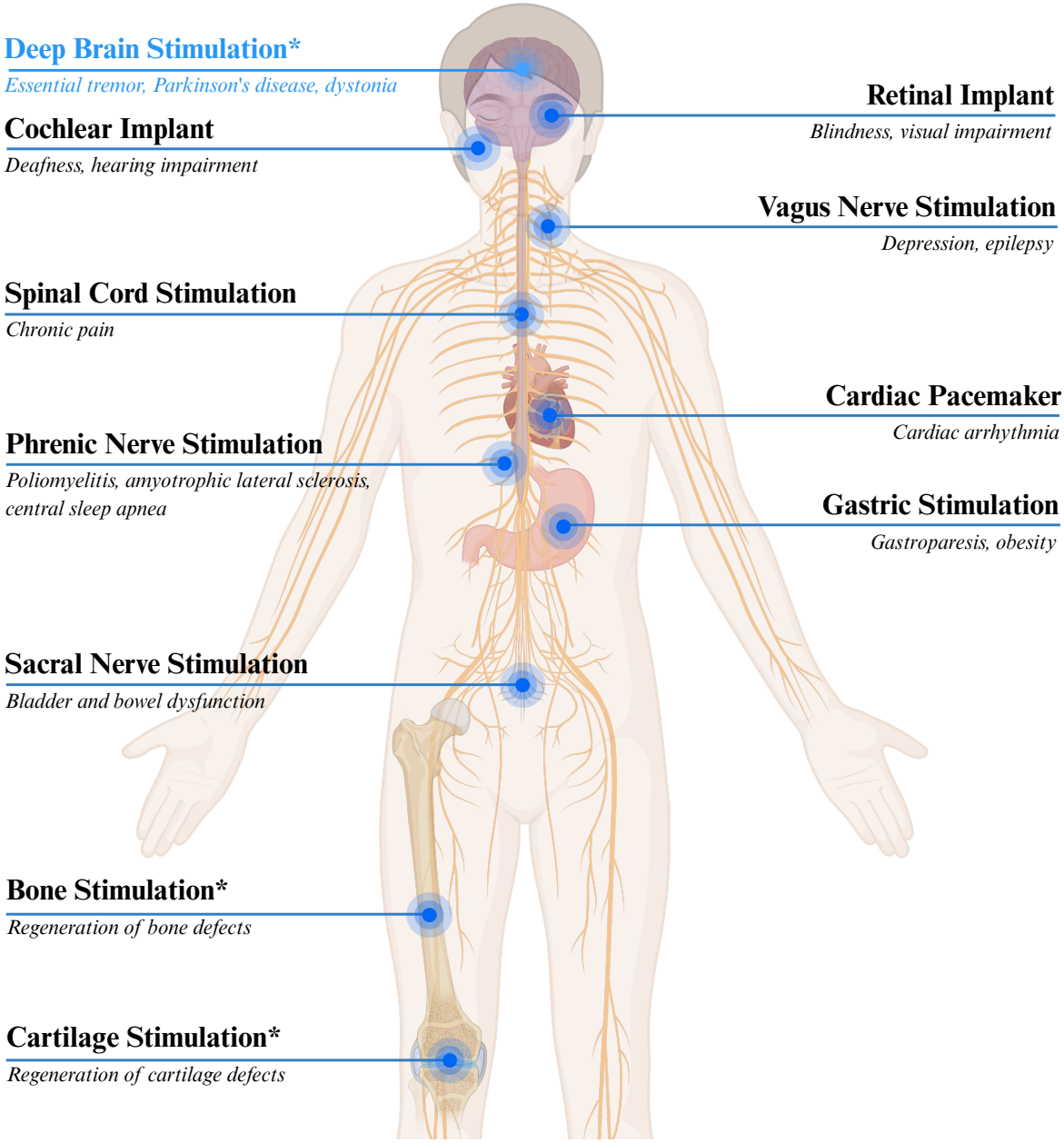

Figure 1: Areas of application of electrostimulating implants from head to knee. Areas marked with an asterisk (*) represent the research focuses within the ELAINE project. Deep brain stimulation is shown in blue text to highlight the topic addressed in this dissertation. Created with BioRender.com.

A uniform citation scheme is applied throughout this work. References without prefixes denote external literature sources, as listed in *References*. Publications authored or co-authored by the author are marked with a prefix 'A' and represent peer-reviewed scientific contributions published in journals or in the proceedings of international conferences, as listed in *List of Peer-Reviewed Publications*.

2 Fundamentals

2.1 Brief Overview of Deep Brain Stimulation (DBS)

Deep Brain Stimulation (DBS) is a neurosurgical therapy in which electrodes are implanted into specific brain targets and connected to an implantable pulse generator (IPG). The IPG delivers controlled electrical pulses that modulate neural activity [78, 144, 122, 196]. Since its clinical introduction in the late 1980s, DBS has become an essential therapy with CE mark and Food and Drug Administration (FDA) approval for Parkinson's disease, essential tremor, and epilepsy, and a humanitarian device exemption for dystonia and obsessive-compulsive disorder (OCD) [78]. Beyond these disorders, DBS is increasingly being investigated for a broad range of neurological and psychiatric conditions, such as depression, Tourette syndrome, chronic pain, and Alzheimer's disease [90].

A DBS system consists of three main components: the IPG, the extension wire, and the DBS electrode (also referred to as DBS lead), the latter being the part that is inserted into the brain. The IPG, implanted subcutaneously in the chest region, is a compact, battery-powered device capable of generating programmable electrical pulses [78]. Stimulation parameters, including amplitude, pulse duration, and frequency, can be wirelessly adjusted by clinicians to meet patient-specific therapeutic needs. Typical stimulation settings range from 1–4 V (or mA) in amplitude, 30–120 µs in pulse duration, and 60–185 Hz in frequency, depending on the brain target [51].

Modern IPGs can operate in either voltage-controlled mode, where the delivered stimulation current varies with the load impedance, or current-controlled mode, which maintains a constant current amplitude independent of impedance changes [78, 122, 132]. The latter is increasingly favored, as it enables more consistent patient-to-patient comparisons [161, 26] (see Section 2.2.3 for details). Battery life depends on device type and stimulation settings. For example, the non-rechargeable Medtronic Activa PC typically lasts 2.6–4.5 years before replacement, whereas the rechargeable Activa RC model can last up to 15 years, but requires regular charging (e.g., 30 minutes daily or 4 hours every 10–14 days [155]) [185]. The Activa RC measures 54 mm × 54 mm × 9 mm, with a volume of 22 cm^3 and a weight of 40 g [154]. Typically, a hermetically sealed titanium housing ensures biocompatibility and long-term waterproof protection for the battery and electronics, while a biocompatible polymer protrusion allows connection of the electrode cables [196].

The extension wire runs under the skin from the chest to the head, connecting the IPG with the DBS electrode. The DBS electrode is stereotactically implanted so that its electrode contacts align with specific brain targets, such as the subthalamic nucleus (STN), the globus pallidus internus (GPi), or the ventral intermediate nucleus (VIM) of the thalamus [106]. DBS

electrodes are thin insulated wires (1.27–1.36 mm in diameter [78]), introduced into the brain via a small opening in the skull [245]. They consist typically of four to eight cylindrical metal contacts (electrode contacts) separated by insulations (1.5 mm contact length with 0.5 mm or 1.5 mm spacing [78]). Depending on the clinical indication, stimulation can be applied unilaterally (in one hemisphere) or bilaterally (in both hemispheres). Furthermore, electrode configurations can be unipolar (also referred to as monopolar), where current flows between one electrode contact and the IPG case, or bipolar, where current flows between electrode contacts. Newer electrode designs employ segmented contacts, enabling current steering for more precise shaping of the electric field, thereby achieving improved selectivity to brain regions. A detailed overview of these stimulation approaches and electrode configurations is provided by [78].

Initial DBS devices operated solely in an open-loop manner, where stimulation parameters remained fixed after adjustment, regardless of neural activity or patient state. Current research and clinical applications are moving toward closed-loop DBS, commonly referred to as adaptive DBS (aDBS), in which stimulation is dynamically adjusted in real time based on detected biomarkers [49, 186]. Common biomarkers include local field potential (LFP) signatures such as beta oscillations, beta bursts, and gamma oscillations [24]. In 2025, Medtronic introduced the world's first aDBS system for Parkinson's disease based on LFP reading, which has a CE mark and is FDA-approved [156]. Beyond neural signals, researchers are also investigating peripheral biomarkers as potential control inputs for adaptive DBS. One promising example is accelerometry, which provides a direct measure of motor symptoms, such as tremor detection [24, 157, 33].

Although DBS is a well-established treatment for movement disorders, its precise mechanisms of action are still not fully understood [196, 102]. Early theories suggested that DBS worked by inhibiting brain activity similar to a lesion, whereas more recent perspectives propose that it instead disrupts neuronal communication, which may lead to both excitation and inhibition near the electrode [22, 213]. Preclinical research has become essential for investigating the underlying mechanisms of DBS, with rodent models playing a central role [39, 144]. To explore these mechanisms and allow translation into clinical applications, preclinical studies require specialized DBS systems that enable long-term (chronic) stimulation in freely moving rodents. It is important to note that clinical DBS systems cannot be repurposed for use in rodent experiments. Their physical dimensions and weight make any form of use in small animals infeasible, and they also lack the experimental flexibility and data access required in preclinical research. Consequently, rodent studies rely on miniature and highly flexible DBS systems specifically designed for laboratory use.

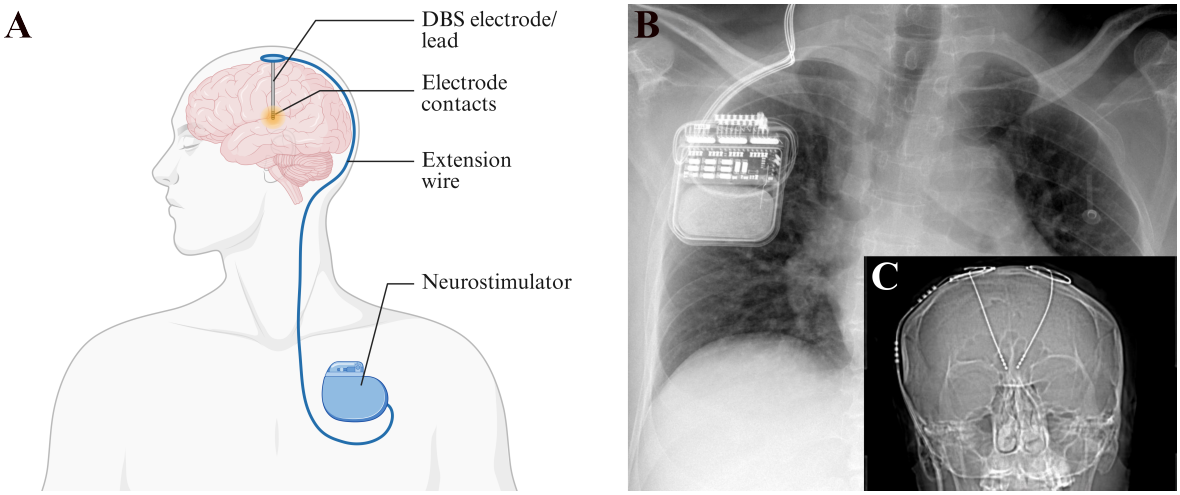

Figure 2: (A) Overview of components in a DBS system, adapted from [169]. (B) X-ray image showing the implantable pulse generator (IPG) and extension cables, adapted from [58]. (C) X-ray image of bilaterally implanted DBS electrodes, adapted from [58].

2.2 Principles of Neurostimulation

2.2.1 Conventions and Technical Terms

Neurostimulation combines concepts from diverse disciplines, including neuroscience, electrochemistry, and electrical engineering. To ensure a uniform understanding, the following section aims to clarify the terminology and definitions used in this work.

Electrical stimulation involves applying a potential difference between two electrodes within the tissue. In neural engineering, the terminology of these two electrodes reflects the spatial placement, in which the *working electrode (WE)* is positioned closest to the target stimulation region, while the *counter electrode (CE)* is placed at a relatively greater distance to complete the circuit [121]. If the stimulation is configured such that the counter electrode is assigned to an externally located and significantly larger electrode (e.g., metal housing of the stimulator in clinical applications), this is referred to as a *monopolar configuration*. In contrast, when the counter electrode is assigned to a contact on the same DBS electrode, typically on an adjacent contact, the setup is referred to as a *bipolar configuration* [122, 78]. Both configurations have an impact on the spatial distribution of the electric field [230, 122]. Additionally, *unilateral stimulation* refers to the implantation of a DBS electrode in a single brain hemisphere, while *bilateral stimulation* involves implantation in both hemispheres.

The electrode terminal into which the conventional current (flow of positive charge) enters is defined as the *anode*, while the electrode terminal from which current leaves is defined as the *cathode* [53]. In DBS and other neurostimulation applications, therapeutic outcomes vary depending on whether conventional current enters (*anodic stimulation*) or leaves (*ca-*

thodic stimulation) the working electrode [216, 21]. Typically, during anodic stimulation, a higher injected charge is required to achieve neural activation compared to cathodic stimulation, which is why cathodic stimulation is more commonly used in practice, though anodic stimulation has also demonstrated clinical benefits [111, 216, 94, 23, 21].

By convention, in the graphical representation of stimulation waveforms, an anodic stimulation pulse is plotted as positive while a cathodic stimulation pulse is plotted as negative along the ordinate. This convention originates from electrophysiology, where the physical flow of electrons is considered rather than the conventional direction of current. During a cathodic stimulation pulse, electrons flow to the working electrode, making it negative relative to the medium (i.e., conventional current leaves, making the electrode cathodic), thus representing the pulse as negative. In contrast, when the working electrode is driven anodically (i.e., conventional current enters, making the electrode anodic), the pulse is plotted positively. This approach has the advantage that the polarity of the working electrode, whether anodic or cathodic, can be simply identified from the graph. However, as a consequence, even when the direction of the current from the stimulation device remains unchanged, the sign of the recorded waveform must be manually inverted if the electrode terminals are swapped. This can create ambiguity when comparing stimulation waveforms with circuit schematics.

As this work focuses on the technical concepts of neurostimulation, a uniform sign convention is used throughout, with the active stimulation phase always displayed as positive, followed by a negative charge balancing phase. This convention is independent of whether cathodic or anodic stimulation is physically applied through the working electrode, and therefore does not imply the actual electrode polarity. By arranging the measurement setup according to the direction of conventional current flow, a consistent relationship between the displayed waveforms and the corresponding circuit schematics is ensured. This convention also offers the advantage that, for stimulator designs implementing a passive charge balancing mechanism as used in this work, the stimulation pulse is displayed in an upright orientation for improved readability. All experimental setups in this work employed a cathodic stimulation, in which the working electrode is connected to ground (conventional current leaves) and the counter electrode connected to the stimulator's output (conventional current enters).

2.2.2 Electrical Properties of the Electrode-Electrolyte System

In neurostimulation, metals serve as the interface to transmit electrical stimulation signals to the brain tissue [160, 20]. Electric current is defined as the movement of electric charge carriers (dQ/dt) set in motion by the applied electric field [188]. In metals, the electric field causes the transport of free electrons. In contrast, in brain tissue, the electric field moves ions, such as Na^+, Cl^-, H^+, K^+, which are present in the extracellular fluid (ECF) [20]. The relationship between electric field strength $\overrightarrow{E}$ and current density $\overrightarrow{J}$ is described by Ohm's law:

$$\vec{J} = \sigma \vec{E}, \tag{1}$$

where σ denotes the conductivity of the material [189]. It should be noted that the conductivity of brain tissue is not a scalar quantity but direction-dependent, resulting in variations in the spatial distribution of the electric field [78].

Charge transfer mechanisms At the electrode-electrolyte boundary, charge transfer occurs through two mechanisms: faradaic and non-faradaic [81].

The non-faradaic mechanism involves the formation of an electrochemical double-layer that exhibits capacitor-like properties. This process is reversible, as no electrochemical reactions occur [20, 28]. The double-layer capacitance (C_{dl}) reflects the charge storage capability of the interface and is directly proportional to the electrode surface area [25, 20]. For metals, C_{dl} typically ranges from 10–20 $\mu\mathrm{F/cm^2}$ [160].

In contrast, the faradaic mechanism involves electron exchange between the metal and the tissue, resulting in a reduction-oxidation (Redox) reaction [150, 28]. The faradaic process can be modeled in its simplest form as a resistor, the so-called charge transfer resistor (R_{ct}) [59]. If the formed products remain bound to the electrode surface, the mechanism is reversible. Otherwise, it is irreversible, leading to electrode corrosion and cell damage [118, 28, 20]. It is essential to note that the charge transfer resistor is known to be the main source of non-linearity (dV/dI) in the electrode-tissue interface [153]. From an electrical engineering point of view, the charge transfer resistor can be represented analogously by a diode in series with a resistor at both electrode-electrolyte interfaces, with one interface accounting for oxidation and the other for reduction processes [181]. This analogy serves to illustrate the exponential course of the current-voltage relationship between the electrochemical reaction described by the Butler-Volmer equation and a diode [125].

In a conventional two-electrode setup, the total impedance $\underline{Z}_{\mathrm{tot}}$ is composed of the impedances of the two interfaces and the electrolyte medium between them:

$$\underline{Z}_{\mathrm{tot}}(\omega) = \underline{Z}_{\mathrm{WE}}(\omega) + \underline{Z}_{\mathrm{Med}}(\omega) + \underline{Z}_{\mathrm{CE}}(\omega), \tag{2}$$

where $\underline{Z}_{\mathrm{WE}}$ and $\underline{Z}_{\mathrm{CE}}$ denote the impedances of the working and counter electrodes, and $\underline{Z}_{\mathrm{Med}}$ represents the electrolyte medium. A schematic representation of the general equivalent circuit is shown in Fig. 3. Both electrode-electrolyte interfaces are modeled by a charge transfer resistance ($R_{\mathrm{ct,WE}}$ and $R_{\mathrm{ct,CE}}$) in parallel with a double-layer capacitance ($C_{\mathrm{dl,WE}}$ and $C_{\mathrm{dl,CE}}$), while the electrolyte medium is represented by a solution resistance (R_{sol}) and capacitance (C_{sol}) in parallel.

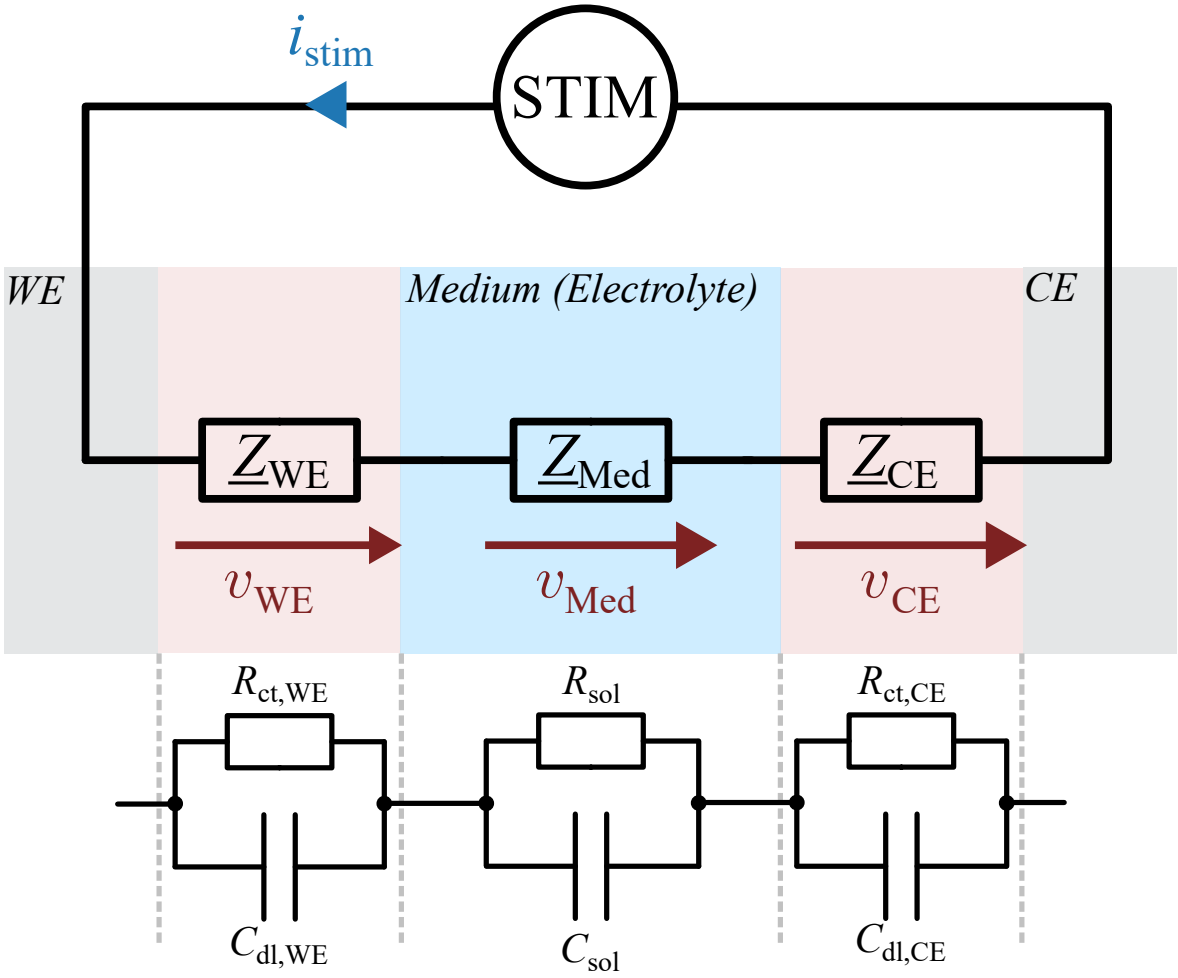

Figure 3: Equivalent circuit representing the total impedance of an electrode-electrolyte system ($\underline{Z}_{tot}$) in an electrical stimulation setup, composed of the working and counter electrode-electrolyte impedances ($\underline{Z}_{WE}$ and $\underline{Z}_{CE}$) and the impedance of the medium ($\underline{Z}_{Med}$).

Non-ideal interface behavior Real-world impedance measurements demonstrate that the double-layer capacitance deviates from ideal capacitive behavior [151]. To account for this, the ideal capacitor is replaced by a fractional-order element, which in general is often a beneficial approach to describe natural effects [62]. In electrochemistry, this fractional model is called *constant phase element (CPE)*, which describes the non-ideal behavior of the double-layer [221]. The reason for the CPE-like behavior of electrodes is still being investigated [127].

The complex impedance of the CPE is mathematically described by:

$$Z_{CPE} = \frac{1}{(j\omega)^{\alpha} Q}, \tag{3}$$

where ω is the angular frequency, α is a dimensionless CPE exponent ($0 < \alpha < 1$), and Q is

the double-layer capacitance parameter in $\mathrm{F\,cm^{-2}}$ [127]. This equation leads to the following special cases: for $\alpha = 0$, the impedance becomes an ideal resistance, for $\alpha = 1$, it becomes an ideal capacitance, and for $\alpha = 0.5$, it represents the Warburg impedance [128]. As implied by its name, the CPE exhibits a constant phase, with the phase angle given by $\Phi = -\frac{\pi}{2}\alpha$ [47].

Under constant current, the voltage across the CPE is given by

$$V_{\mathrm{CPE}} = \frac{I}{Q\Gamma(1+\alpha)} t^{\alpha}, \tag{4}$$

where Γ denotes the Gamma function [140]. In the special case of $\alpha = 1$, this expression simplifies to the linear charging of an ideal capacitor ($V = It/C$).

At the circuit level, the CPE can be approximated by a network of parallel RC branches, allowing practical implementation in simulation environments [248, 56, 235, 236].

Electrolyte impedance The electrolyte provides the path for current flow between electrodes and exhibits both resistive and capacitive properties. In a first-order approximation, its impedance can therefore be represented by a parallel circuit consisting of a solution resistance R_{sol} and a solution capacitance C_{sol} [203, 82, 11, 64, 207, 84].

The solution resistance is related to the specific resistance ρ and the cell constant K [179]:

$$R_{\mathrm{sol}} = K\rho = \frac{K}{\sigma}, \tag{5}$$

where $\sigma = 1/\rho$ is the specific conductivity of the electrolyte. The cell constant K is defined as the ratio of the electrode distance and the electrode area, resulting in a unit of $\mathrm{m^{-1}}$. Hence, R_{sol} depends on the conductivity of the medium and on electrode geometry. By knowing the cell constant and determining the solution resistance, the conductivity of a medium can be determined [34].

For an electrode with a hemispherical geometry of a radius a (counter electrode radius approaches infinity), the solution resistance is given by [170, 207]:

$$R_{\mathrm{sol}} = \frac{1}{2\pi\sigma a}. \tag{6}$$

The associated solution capacitance is given by:

$$C_{\mathrm{sol}} = 2\pi\varepsilon_0\varepsilon_r a, \tag{7}$$

where ε_0 is the vacuum permittivity and ε_r is the relative permittivity of the medium. This situation reflects the case of monopolar stimulation with a distant counter electrode [173].

It should be noted that although a simple RC circuit is generally sufficient to describe the frequency-dependent behavior of basic electrolytes such as saline solutions, neural tissue exhibits more complex electrical properties [82]. It is characterized by resistive pathways inside the cells and in the ECF, as well as by capacitive properties of cell membranes [19, 249]. The Lapicque (1907) [29], Fricke-Morse (1925) [79], and Cole-Cole (1941) [45] models account for these properties by combining resistances and capacitances in series and parallel [151, 19, 249]. In particular, the Cole-Cole model has been successfully applied to various biological materials, including brain tissue [80].

More recent models also account for the encapsulation layer that forms around implanted electrodes as a biological response to insertion [105, 184, 247, 133, 209, 30, 177] . The choice of an appropriate tissue model depends on the biological detail required and the frequency range of interest.

Equivalent circuit models for neurostimulation For neurostimulation applications, the general model illustrated in Fig. 3 is adapted to the specific conditions of the electrode geometry and the surrounding biological medium, while being simplified to capture only the dominant electrical effects within the frequency range relevant to stimulation pulses.

In monopolar stimulation, the counter electrode has a significantly larger area compared to the working electrode. As a result, its impedance is negligible ($X_{\mathrm{dl,CE}} \ll X_{\mathrm{dl,WE}}$) and the total impedance is dominated by the working electrode and medium [128]. Under these assumptions, the total impedance can be approximated by:

$$\underline{Z}_{\mathrm{tot}} = \frac{R_{\mathrm{ct}}}{1 + (j\omega)^{\alpha} Q R_{\mathrm{ct}}} + \frac{R_{\mathrm{sol}}}{1 + j\omega R_{\mathrm{sol}} C_{\mathrm{sol}}}, \tag{8}$$

where the first term represents the electrode component and the second term the electrolyte component.

If, within the frequency range of the stimulation pulses, the impedance of the medium is predominantly resistive ($\omega R_{\mathrm{sol}} C_{\mathrm{sol}} \ll 1$), the capacitive contribution of the medium can be neglected, and the equivalent circuit reduces to the –[CPE$\|R_{\mathrm{ct}}$]-$\mathrm{R_{sol}}$– model. This configuration corresponds to the well-established CPE-based Randles circuit [209]. As a further approximation, it is often assumed that the charge-transfer resistance is much larger than the capacitive reactance ($R_{\mathrm{ct}} \gg X_{\mathrm{dl}}$), indicating that faradaic processes have only minor influence within the operating range of stimulation pulses [134, 200, 214]. Under these assumptions, the total impedance simplifies to

$$\underline{Z}_{\text{tot}} = \frac{1}{(j\omega)^{\alpha} Q} + R_{\text{sol}}, \tag{9}$$

representing a CPE element in series with the solution resistance (–CPE-R_{sol}– model).

Although the CPE does not represent a true capacitance, its behavior in the presence of a solution resistance can be related to an average double-layer capacitance, providing a more intuitive link to an ideal capacitor. This capacitance can be approximated by [127]:

$$\overline{C}_{\text{dl}} = Q^{1/\alpha} \left(\frac{1}{R_{\text{sol}}} \right)^{1-1/\alpha}. \tag{10}$$

Moreover, it should be noted that in a bipolar electrode configuration, both electrode interfaces must be considered because the working and counter electrodes are of comparable size. However, when using a two-electrode impedance spectroscopy setup, the individual contributions of each interface cannot be separated, and the measured impedance reflects their combined behavior [239]. While a three-electrode configuration with a dedicated reference electrode would be required to distinguish the individual interface impedances, this approach is generally impractical in neurostimulation, as the two stimulation electrodes are already implanted [11, 134, 177]. Therefore, the model in Eqs. 8/9 is typically applied, with the resulting electrode-electrolyte impedance representing the combined effect of both interfaces.

Furthermore, it is crucial to consider the impact of parasitic capacitances from the inherent properties of the DBS electrode inserted into tissue. These capacitances can lead to misinterpretation of tissue properties, which dominate in the high-frequency regime. The parasitic capacitances arise from the insulated electrode shaft, which guides the electrode wires and separates the electrode contacts, and also from closely spaced cables inside the shaft in the case of multipolar electrodes [11, 134]. The combined parasitic capacitance C_{x} (typically in the pF range [11, 134, 184]) forms a low-pass filter that shorts high-frequency components to ground [11]. To accurately investigate tissue properties, it is essential to account for this parasitic contribution in impedance analysis.

Fig. 3A summarizes the adapted equivalent circuit used for neurostimulation applications. The model simplifies the general representation to a single electrode interface, replaces the ideal double-layer capacitance with a CPE, accounts for parasitic effects, and adjusts the impedance of the surrounding medium according to the biological detail. The surrounding medium is represented by three models: (a) a simple RC circuit describing basic electrolytes, (b_1) the Cole-Cole model capturing the dielectric dispersion of brain tissue, and (b_2) an encapsulation model accounting for resistive and capacitive effects of the layer formed around

chronically implanted electrodes. Furthermore, the CPE is approximated by a network of parallel RC branches, while the charge transfer resistance is depicted by antiparallel resistor-diode branches that illustrate its voltage-dependent nature. The entire load impedance model is embedded in a DBS circuit employing passive charge balancing, while the resulting DBS voltage and current waveforms are shown in Fig. 4B.

2.2.3 Stimulation Waveforms: Pulse Characteristics

Neurostimulators, including deep brain stimulation (DBS) devices, typically utilize a periodic pulse (rectangular) waveform that can be varied in intensity, duration, and repetition rate to adjust the therapy. DBS devices offer two modes of operation: voltage-controlled and current-controlled [230, 122, 186]. In voltage-controlled mode, pulses maintain a constant voltage, while in current-controlled mode, they maintain a constant current throughout the pulse duration. As the load impedance can be modeled as a capacitor in series with a resistor in its simplest form, a constant voltage causes the current to decrease exponentially when viewed on a microscopic level. From a macroscopic perspective, since biological processes are triggered when the DBS electrode is inserted into the brain [64], the change in load impedance causes the averaged current amplitude to vary over time. In contrast, if current-controlled pulses are applied, the current is constant throughout the pulse duration and also remains constant regardless of load impedance changes over time. While clinical studies have shown that both modes can be effective in alleviating symptoms [197, 253], the current-controlled mode has become the preferred mode in clinical settings [108, 101]. The reason for this is that current-controlled stimulation allows for more precise comparison at different times for the same patient and between different patients by eliminating potential distortions caused by impedance changes [161, 26, 132]. This concept is particularly important in preclinical studies, such as cell cultures and animal models, where high biological variability demands reliable and reproducible results. Therefore, the focus of this dissertation will be exclusively on current-controlled pulses.

In [131], the DBS signal generated by the widely used Activa® PC neurostimulator (Medtronic, Inc., Minneapolis, MN) for clinical applications is presented. Their measurement shows that an interphase delay (see Section 2.2.4 for details) of 80 µs follows the stimulation pulse, succeeded by a passive charge balancing mechanism. In general, passive charge balancing is the standard approach in DBS devices, in which the electrodes are shorted to remove any residual charge [186, 131]. A detailed discussion of why charge balancing is a critical safety aspect is presented in Section 2.2.4. Fig. 4B presents the typical DBS voltage (v_{DBS}) and current (i_{DBS}) waveform over one period T, the course of which is explained below for the specific time intervals.

Stimulation Phase t_{stim} ($t_1 < t < t_2$): At t_1, switch S_1 closes and S_2 opens, initiating the stimulation pulse for a duration of t_{stim}.

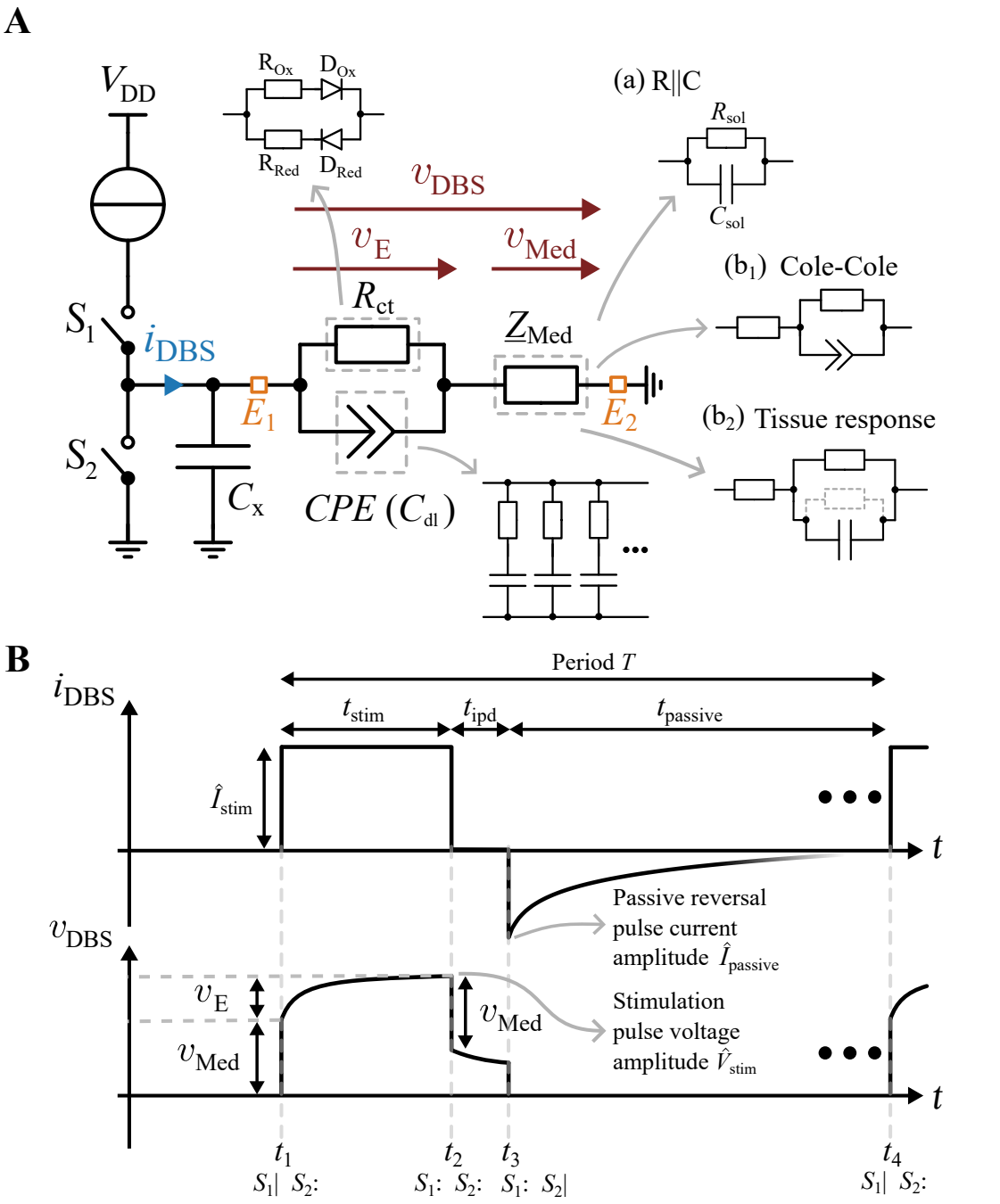

Figure 4: (A) Schematic representation of a DBS circuit (biphasic stimulation with passive charge balancing) connected to a load impedance tailored for DBS setups. The load impedance is depicted by an equivalent circuit model, comprising the electrode-medium interface and the surrounding medium. The electrode-medium interface is shown by a parallel circuit of R_{ct} and $\underline{Z}_{CPE}$ based on electrochemical models, with arrows indicating their realization with electronic components. The models of two different media are shown for $\underline{Z}_{Med}$: (a) the simple RC model for electrolyte solutions, and (b) two common models for brain tissue: the Cole-Cole model (b_1) and a model accounting for tissue response due to electrode insertion (b_2). The DBS electrode's inherent parasitic capacitance is denoted by C_x. (B) Resulting DBS voltage v_{DBS} and current i_{DBS} waveform according to the DBS circuit in (A).

- **Current:** When switch S_1 closes, the current rises rapidly from zero to the preset value $\hat{I}_{\text{stim}}$ and remains constant throughout the pulse duration t_{stim}.
- **Voltage:** The rapid change in current introduces high-frequency components, causing the double-layer capacitance of the electrode-medium to act as a short circuit. If the resistive component of the medium dominates over the capacitive component, the initial voltage drop across the medium v_{Med} is almost vertical ($v_{\text{Med}} = \hat{I}_{\text{stim}} R_{\text{sol}}$). As the pulse continues, the voltage drop across the electrode-electrolyte interface becomes dominant (v_{E}): the double-layer capacitance modeled as CPE accumulates charge while faradaic reactions occur through the charge-transfer resistance. This causes the voltage to gradually increase until, at the end of the pulse, the maximum voltage is reached ($\hat{V}_{\text{stim}}$).

Interphase Delay t_{ipd} ($t_2 < t < t_3$): At t_2, switch S_1 opens and S_2 remains open, initiating the interphase delay for a duration of t_{ipd}.

- **Current:** When S_1 opens, the current drops immediately to zero and remains at zero throughout t_{ipd}.
- **Voltage:** The abrupt cessation of current again produces high-frequency components, resulting in a voltage drop of the same magnitude but opposite sign across the medium v_{Med} as in the case of the pulse onset. Following this, the voltage decays gradually due to the discharge of the double-layer capacitance through the charge-transfer resistance and solution resistance.

Passive Charge Balancing Phase t_{passive} ($t_3 < t < t_4$): At t_3, switch S_1 remains open and S_2 closes, initiating the passive charge balancing phase for a duration of t_{passive}.

- **Current:** When S_2 closes, the electrode contacts are shorted (E_1 and E_2 connected to GND), causing the charged double-layer capacitance to discharge. This initially results in a current spike ($\hat{I}_{\text{passive}}$), followed by an approximately exponential decay towards zero.
- **Voltage:** The DBS voltage drops instantly to 0 V.

This procedure is repeated at t_4.

When evaluating electrochemical safety limits regarding the stimulation pulse, the voltage drop across the electrode-electrolyte interface has to be isolated by subtracting the voltage drop across the medium from the total voltage drop [238]. Additionally, the maximum stimulation voltage ($\hat{V}_{\text{stim}}$) is a crucial parameter for the neurostimulator's circuit design, as the current source's compliance voltage must be greater than this value to ensure a constant current until the end of the pulse (see Section 2.2.6).

2.2.4 Stimulation Waveforms: Principles of Charge Balancing

At first glance, a neurostimulation circuit could be designed simply by a current source and a transistor as a switch (see Fig. 6a). However, this so-called monophasic stimulation does not account for the double-layer capacitance, which is charged by each stimulation pulse. Since the self-discharge of this capacitance is insufficient for typical stimulation periods in the ms-range, subsequent pulses lead to charge accumulation. This results in a continuous rise of the DC bias until equilibrium is reached. Because a certain DC bias can result in prolonged irreversible faradaic reactions (see Section 2.2.8), charge balancing mechanisms are essential in neurostimulators [160].

The charge balancing condition can be mathematically expressed as

$$Q_{\text{net}} = \int_{t=0}^{T} i_{\text{DBS}}(t)dt = 0, \tag{11}$$

where Q_{net} denotes the net charge, T the period and i_{DBS} the DBS current waveform.

Various charge balancing mechanisms have been developed to address this condition (Fig. 5). Each approach relies on using a subsequent reversal pulse to remove the stored charge from the double-layer capacitance. The methods can be broadly classified into *passive* and *active* charge balancing [186]. In *passive charge balancing*, the charge is removed by shorting the electrode to ground, while in *active charge balancing*, an active constant current pulse is generated by a current source in the direction opposite to the stimulation pulse.[1] Hybrid approaches combining both methods also exist [218]. If the active reversal pulse has the same amplitude and duration as the stimulation pulse, it is termed *symmetrical*, and otherwise *asymmetrical*. Additionally, if a delay is introduced between the stimulation pulse and the reversal pulse, this is referred to as the interphase delay t_{ipd} [186].

However, even if Eq. 11 is satisfied by the charge balancing method used, the reversal waveform still critically affects the efficacy and safety of neurostimulation. This is because the chosen charge balancing method must reverse the faradaic reactions induced by the stimulation pulse as fast as possible and also must avoid counteracting its therapeutic effect. Research has shown that different charge balancing methods can produce distinct effects on

[1]Note: The charge balancing terminology used in DBS literature differs from that in other neurostimulation applications, such as functional electrical stimulation (FES) or retinal stimulation. In these systems, charge balancing typically implies the use of an actively generated reversal pulse following the stimulation pulse. Therefore, passive charge balancing refers to the discharge phase following the active pulse, whereas active charge balancing includes additional compensation techniques applied after the active pulse. In contrast, in DBS literature, passive charge balancing denotes a passive discharge immediately following the stimulation pulse, while active charge balancing refers to an actively generated reversal pulse. In this work, the convention used in DBS is applied.

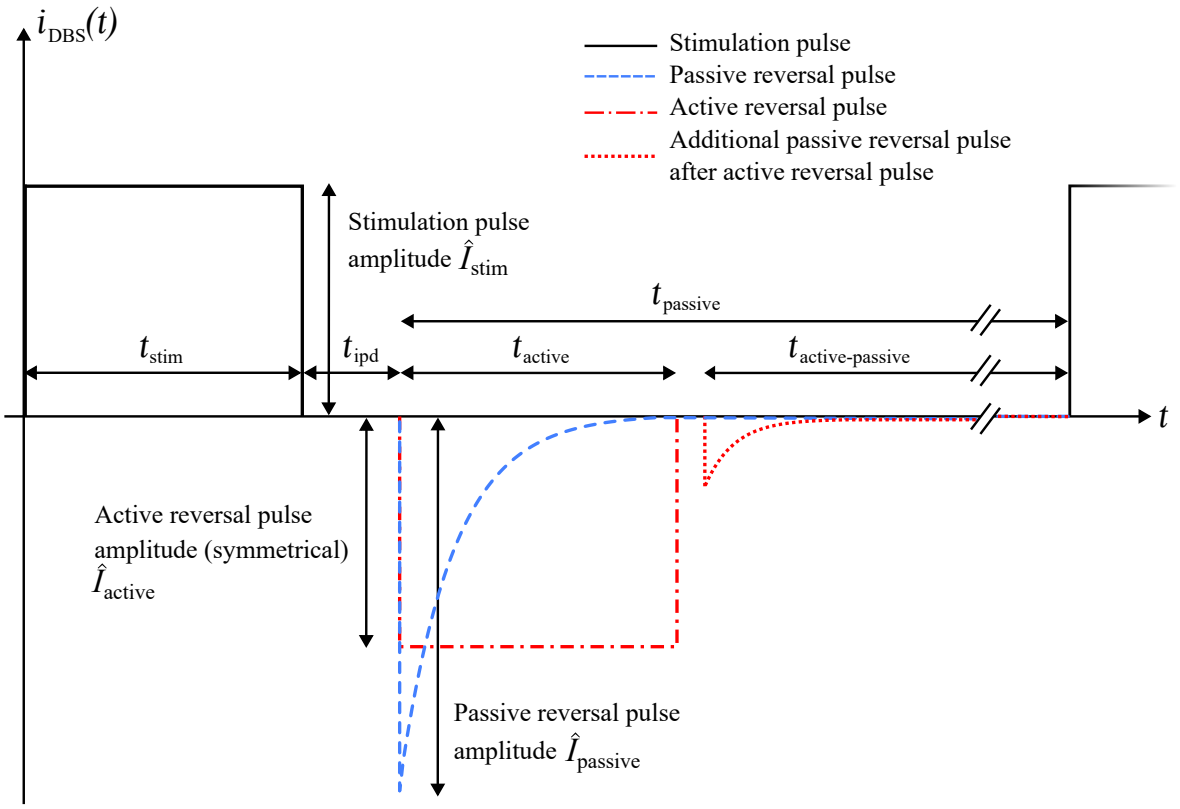

Figure 5: Schematic representation of the DBS current waveform $i_{DBS}(t)$ under current-controlled stimulation. The waveform includes a stimulation pulse of amplitude $\hat{I}_{stim}$ and duration t_{stim}, followed by an interphase delay t_{ipd}. Charge balancing is achieved either by a passive reversal pulse, characterized by an exponential decay with amplitude $\hat{I}_{passive}$ and duration $t_{passive}$, or by an active reversal pulse of amplitude $\hat{I}_{active}$ and duration t_{active}. An additional passive reversal pulse may occur after the active reversal pulse, with duration $t_{active-passive}$, to ensure complete charge removal. In clinical DBS systems, passive discharge is the typically employed charge balancing method.

the action potential (AP) activation threshold, electrode corrosion, and tissue damage [160], though to what extent is unclear [44]. Generally, a reversal pulse increases the AP activation threshold by mitigating the physiological effect of the stimulation pulse. It is assumed that the higher the reversal pulse level, the greater the mitigating effect. Typically, an interphase delay is introduced to compensate for this. On the other hand, the longer it takes to reverse the reaction products, such as in the case of an asymmetrical reversal pulse or interphase delays, the higher the probability of tissue damage. Passive charge balancing is typically considered the most effective method in minimizing tissue damage, albeit at the cost of a higher AP activation threshold [160]. However, it should be kept in mind that, since the double-layer capacitance discharges through the solution resistance, the voltage across the electrode-electrolyte interface may require some time to fall into an electrochemically safe range.

Despite the influence of the reversal waveform, it remains most important that Eq. 11 is satisfied, since otherwise prolonged faradaic reactions may occur due to a sustained DC bias. Since a passive discharge in general cannot reliably ensure complete charge removal, typical circuit designs instead generate an active reversal pulse that injects an equal and opposite charge to the stimulation pulse. This requires satisfying the following condition [214]:

$$\hat{I}_{\text{stim}} \cdot t_{\text{stim}} = \hat{I}_{\text{active}} \cdot t_{\text{active}} \tag{12}$$

Achieving this condition, however, is challenging in practice due to timing differences (see Fig. 6c,e,f) and a current amplitude mismatch between two current sources (see Fig. 6e,f). To compensate for these non-idealities, additional techniques have been proposed, such as including a passive discharge phase following the active reversal pulse (see Fig. 6d,g), whose success in compensating residual charge, however, remains uncontrollable. Alternatively, charge metering may be used, in which any non-zero net charge is compensated with additional current determined using a sensing capacitance [214].

Nevertheless, even if the injected charge of the stimulation pulse equals the injected charge of the active reversal pulse (i.e., Eq. 12 is satisfied), Eq. 11 may still be violated due to the effect of the charge transfer resistance R_{ct}. Specifically, an asymmetrical reversal pulse can induce a charge mismatch due to the voltage-dependent nature of R_{ct}, while an interphase delay t_{ipd} can cause a charge mismatch due to the self-discharge through R_{ct} during this delay. As a result, a residual DC bias may accumulate over successive stimulation pulses until equilibrium is reached [214].

Therefore, since a charge mismatch can be avoided with basic charge balancing techniques only under specific stimulation parameters and load impedance conditions, modern designs rely on continuous bias voltage monitoring with feedback mechanisms. In this approach, the bias voltage is continuously measured, and compensation currents are applied whenever predefined thresholds are exceeded (see Fig. 6h), ensuring that the bias voltage remains within the electrochemically safe window as given by

$$V_{\text{th}-} \leq V_{\text{bias}} \leq V_{\text{th}+}, \tag{13}$$

where $V_{\text{th}-}$ and $V_{\text{th}+}$ denote the negative and positive threshold voltages, respectively. A window of $\pm 100\,\text{mV}$ is typically considered safe (see Section 2.2.8 for details). Comparators are generally used to monitor the bias voltage against such predefined thresholds. If a threshold is exceeded, compensation currents are applied, either through charge packet insertion [182, 200] to immediately neutralize the residual charge within the same stimulation cycle, or through offset compensation [224, 172] to iteratively adjust the reversal pulse cur-

rent in subsequent cycles, ensuring long-term charge balance [214, 139, 135, 217]. Recent work has introduced impedance-aware charge balancing schemes, where the load impedance parameters are estimated from the sampled electrode voltage to dynamically adjust charge compensation [63, 214].

Interestingly, unlike other neurostimulation applications, such as retinal stimulation, where considerable design effort is devoted to actively limiting the bias voltage, clinical DBS devices rely exclusively on purely passive charge balancing. The author assumes that this design choice in DBS systems is justified because the time constant of the electrode-electrolyte system is significantly shorter than the duration of the discharging phase, which ensures that Eq. 11 is consistently satisfied. As demonstrated later in this work, this assumption remains valid for the investigated preclinical DBS setup (see Section 4.4.2).

2.2.5 Pulse Generator Architectures

Several pulse generator architectures have been developed for neurostimulation applications [52, 117, 214, 218, 182], as illustrated in Fig. 6. The architecture for *monophasic stimulation* (a) represents the most area- and energy-efficient design but lacks a charge balancing mechanism, making it unsuitable for safe operation. In contrast, the other architectures are designed to enable *biphasic stimulation*, which incorporates charge balancing mechanisms to reverse electrochemical reactions and prevent net charge accumulation. Biphasic architectures can be broadly categorized into two groups: single-current-source designs (b–d) and dual-current-source designs (e–h).

Single-current-source designs (b–d): These architectures require only one current source and thus a single supply voltage. Architecture (b) uses passive charge balancing by shorting the electrode contact to ground, offering the lowest circuit complexity and power consumption, as no additional current source activation for the reversal phase is needed. Architectures (c) and (d) utilize symmetrical active charge balancing through an H-bridge, enabling bidirectional current flow through the load. Architecture (d) further incorporates a passive discharge by shorting both electrode contacts subsequent to the active reversal pulse, thereby enhancing charge balancing efficacy.

Dual-current-source designs (e–h): These designs allow flexible control of the direction, amplitude, and pulse duration of the reversal pulse. To enable a bidirectional current flow, both current sources must operate from separate supply rails, where one acts as a source and the other as a sink. In (e), the circuit operates between V_{DD} and GND, with one electrode referenced to V_{Ref}, which is typically $V_{\mathrm{DD}}/2$. The disadvantage of this circuit is that the compliance voltage is reduced by $V_{\mathrm{DD}}/2 - V_{\mathrm{o,min}}$, requiring higher supply voltages to maintain a constant current through the load, which affects the energy efficiency. In contrast, archi-

tectures (f-h) use bipolar rails (for example, ±5 V) with one electrode referenced to GND. However, generating bipolar rails from a single battery supply via a virtual ground, capacitive, or inductive method [36], consumes significant power and area, making such designs impractical for lower-power implants. Architecture (g) adds passive discharge following the active reversal pulse, while (h) employs feedback to keep the residual bias voltage within predefined thresholds, at the cost of higher power and area.

In summary, each pulse generator architecture involves trade-offs in terms of circuit complexity, power consumption, and charge balancing performance. Single-current-source designs are generally more area and energy-efficient, while dual-current-source designs allow more precise control of charge balancing at the expense of higher power consumption and circuit area. Selecting an appropriate pulse generator architecture requires careful consideration of the electrode geometry, target tissue properties, stimulation parameters, energy constraints, and safety requirements.

2.2.6 Discrete Current Source Design: Practical Considerations

A current source is a circuit designed to maintain a stable current through a load, regardless of changes in the load. To achieve this, the circuit must dynamically adjust the voltage across it in order to regulate the current. Various circuit architectures can be employed for this purpose, each with distinct performance characteristics such as the minimum voltage drop across the current source, temperature stability, and supply voltage stability [228, 142].

A simple discrete current source can be implemented using a single bipolar junction transistor (BJT) of type npn or pnp. In this example, an npn BJT configuration is considered, as illustrated in Fig. 7A. The principle involves biasing the BJT T_1 with a reference voltage V_{Ref} at its base and connecting a resistor R_{E} between its emitter and ground. Since the base-emitter voltage (V_{BE}) is approximately constant (0.6–0.7 V), a constant voltage drop across the emitter resistor results, leading to a constant emitter current I_{E}. As the collector current I_{C} is approximately equal to the emitter current ($I_{\mathrm{E}} \approx I_{\mathrm{C}}$), a defined current I_{o} flows through the load [228]:

$$I_{\mathrm{o}} = \frac{V_{\mathrm{Ref}} - V_{\mathrm{BE}}}{R_{\mathrm{E}}} \tag{14}$$

The defined current remains independent of the load only when the transistor operates within its active region, where $V_{\mathrm{CE}} > V_{\mathrm{CE,sat}}$. For the circuit shown in Fig. 7A, the minimum tolerable voltage drop across the current source is [228]:

$$V_{\mathrm{o,min}} = V_{\mathrm{E}} + V_{\mathrm{CE,sat}} = V_{\mathrm{Ref}} - V_{\mathrm{BE}} + V_{\mathrm{CE,sat}}. \tag{15}$$

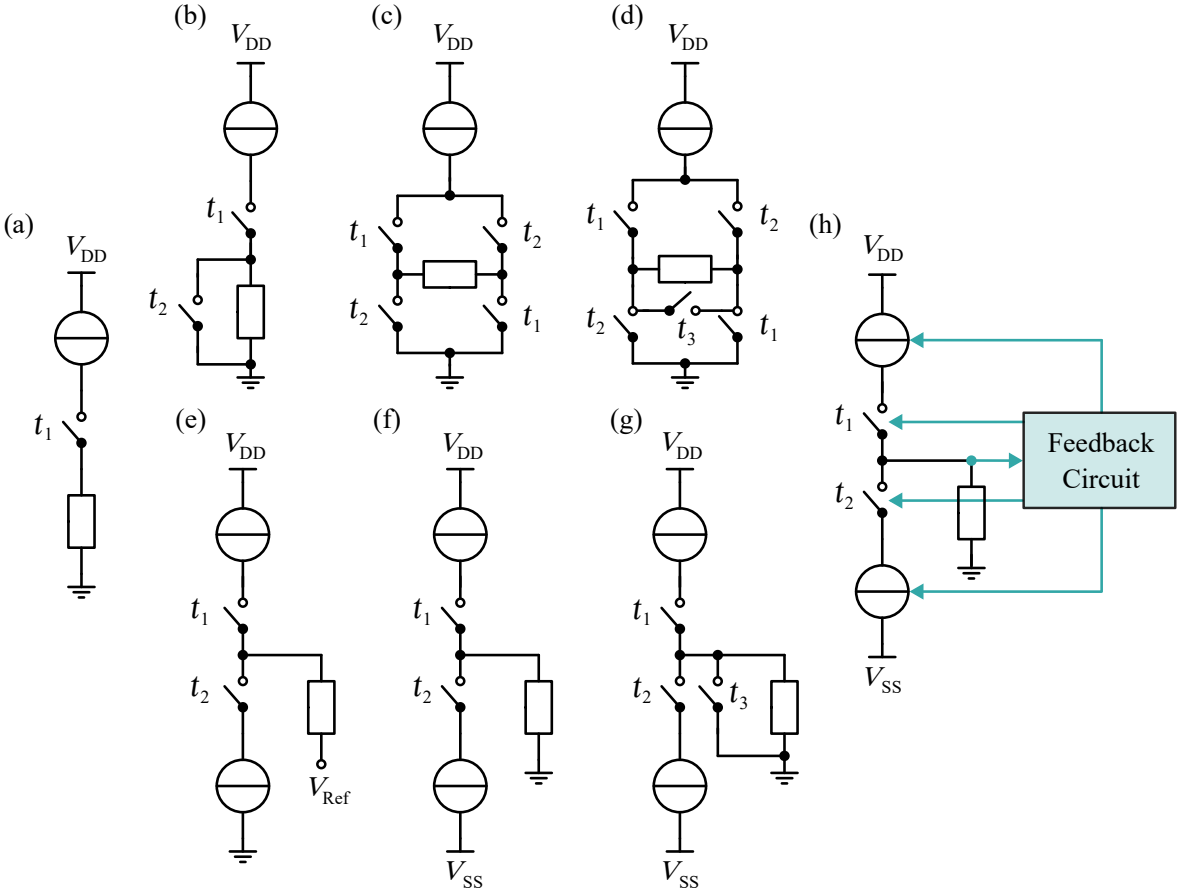

Figure 6: Common pulse generator circuit topologies. (a) Monophasic stimulation. (b–d) Single current source implementations: (b) biphasic passive, (c) biphasic active, and (d) biphasic active with an additional passive phase. (e–h) Dual current source designs: (e) biphasic active using a reference voltage V_{Ref} (typically $V_{DD}/2$), (f) biphasic active using a bipolar voltage supply, (g) biphasic active with an additional passive phase using a bipolar voltage supply, and (h) biphasic active using a bipolar voltage supply with an additional feedback circuit to maintain the bias voltage V_{bias} within safety limits.

Typically, with $V_{BE} \approx 0.7$ and $V_{CE,sat} \approx 0.2$, this yields $V_{o,min} = V_{Ref} - 0.5\,V$. For comparison, current mirrors using BJTs require a minimum voltage drop of about $V_{o,min} \approx 0.2\,V$, whereas current mirrors using n-channel metal-oxide-semiconductor field-effect transistors (MOSFETs) in integrated circuits usually require around $V_{o,min} \approx 1\,V$ [228].

Therefore, circuit designers must be aware that the current source's ability to maintain a constant current is limited by the supply voltage minus $V_{o,min}$. This useful limit is known as the *compliance voltage* of the current source:

$$V_{Compl} = V_{DD} - V_{o,min}. \tag{16}$$

In Fig. 7B, simulation results obtained in *LTspice*[2] illustrate the behavior of the npn BJT current source within and beyond its specification. A constant current of 100 µA is maintained up to a load resistance of 21 kΩ, beyond which the voltage across the load begins to drop, indicating the compliance voltage. At this point, the simulation shows that the transistor operates with $V_{BE} \approx 0.6\,V$ and $V_{CE,sat} \approx 0.1\,V$, leading to $V_{o,min} \approx 0.9\,V$ and thus the observed compliance voltage of about 2.1 V, which is in line with Eqs. 15 and 16.

It should be noted that the circuit shown in Fig. 7A illustrates only the basic concept of a BJT current source. In practical BJT current source implementations, the reference voltage is typically derived from the supply voltage using components such as an LED, a Zener diode, or two diodes in series. Each option provides a different reference voltage, thereby influencing $V_{o,min}$ (see Eq. 15) and the dependence of the output current on supply voltage variations and temperature [142]. As the base-emitter voltage varies by $-2\,mV/°C$, a rise in temperature causes V_{BE} to decrease, and the output current increases accordingly (see Eq. 14). Techniques such as diode compensation or a shunt regulator can be used to stabilize the output current.

In conclusion, designing a current source involves trade-offs between the minimum voltage drop $V_{o,min}$, temperature stability, and voltage stability. For a comprehensive analysis of standard BJT current source circuits, supported by LTspice simulations, refer to [142]. For neurostimulators that deliver constant current pulses to neural tissue, the compliance voltage must be chosen according to the specific stimulation conditions, determined by the target tissue, biological changes around the electrode, electrode geometry and configuration, and the applied stimulation parameters. If the compliance voltage is too low, the current source can no longer sustain its adjusted current. If it is too high, efficiency is reduced. Therefore, the compliance voltage rather than the supply voltage should always be clearly specified in publications and datasheets, as it defines the true capability of the stimulator to deliver a constant current into the electrode-tissue impedance.

2.2.7 Considerations of Blocking Capacitors

Blocking capacitors are essential safety features, preventing a high DC voltage from reaching the electrode in the case of a malfunction [131, 218, 52]. Since high supply voltages are often required to deliver the desired stimulation current into the tissue, a failing hardware component or software issue, such as delivering DC instead of pulsed stimulation, could result in a dangerous voltage across the electrodes. To be effective, a blocking capacitor must be connected in series with the electrode, without any other active electrical elements connected in parallel to it. However, two major concerns arise when using blocking capacitors in neurostimulators.

[2]Circuit simulations were performed throughout this work using *LTspice24*, a free SPICE simulator developed by Analog Devices. The generated netlists and simulation results were accessed from Python via the open-source *spicelib* library [27], an excellent tool for interacting with multiple SPICE simulators.

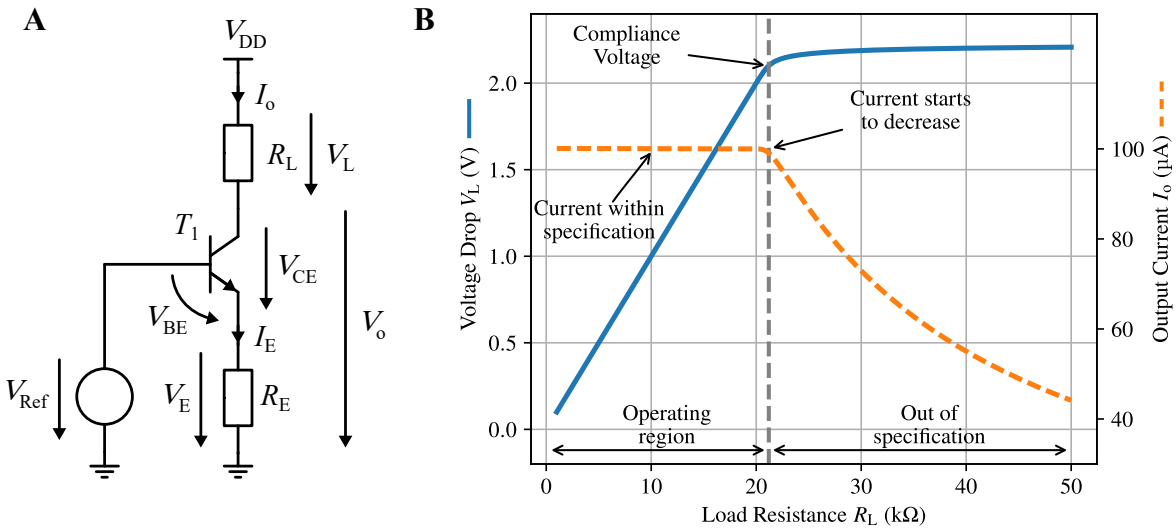

Figure 7: (A) Schematic of a basic npn BJT current source. (B) LTspice simulation results illustrating the operating regions of the npn current source. A constant current is maintained (100 µA) until the compliance voltage is reached, beyond which the circuit no longer behaves as a current source. Simulation parameters: DC operating point analysis with R_L swept from 1–50 kΩ in 100 Ω steps; T_1: 2N2222; $R_E = 8\,\text{k}\Omega$ ($\rightarrow I_o \approx 100\,\mu\text{A}$); $V_{Ref} = 1.4\,\text{V}$; $V_{DD} = 3\,\text{V}$.

The first concern is the additional voltage drop across the blocking capacitor, which increases the current source's output voltage. A capacitor's voltage drop is determined by integrating the current over time, as shown in the equation:

$$v_C(t) = \frac{1}{C}\int_0^T i_C(t)\,dt \tag{17}$$

To prevent the blocking capacitance from causing the current source to exceed its output voltage limit (compliance voltage), the capacitance must typically be in the µF range and rated for a high DC voltage. These requirements make blocking capacitors impossible to integrate into ICs. For example, in retina implants with up to 232 channels (e.g., for epiretinal stimulation [183]), each channel would require its own blocking capacitor, leading to severe space constraints [182]. Since DBS requires only two channels and the voltage drop across the blocking capacitor is small under typical stimulation parameters, the issue can be disregarded for this neurostimulation application.

The second concern is that blocking capacitors, once believed to support the charge balancing process [218, 138], can in fact introduce a DC bias across the electrodes [57]. This occurs due to an additional current path through the charge-transfer resistance, causing a charge mismatch between the blocking capacitor and the double-layer capacitance, which accumulates over successive stimulation pulses until equilibrium is reached. The resulting bias voltage can reach unsafe levels where irreversible faradaic reactions may occur. Since

existing techniques are based on bypassing the blocking capacitor, the capacitor's protective function is compromised [57]. Therefore, when blocking capacitors are intended to be used, the resulting DC bias voltage must be characterized for the specific stimulation setup.

2.2.8 Electrochemical Safety Limits

Electrochemical safety limits define the voltage range in which no irreversible faradaic reactions occur at the electrode-electrolyte interface. When this range is exceeded, oxidation or reduction of the surrounding medium begins to take place. This voltage range is commonly referred to as *electrochemical window*. Since biological tissue is primarily composed of water, the electrolysis of water represents an irreversible faradaic reaction common to all electrodes [20]. Water electrolysis may lead to electrode damage and potentially harm surrounding tissue as a result of local pH changes and gas formation (hydrogen and oxygen) [100, 60, 160, 43, 20]. For this reason, the term *water window* is commonly used to define the voltage range in which electrical stimulation can be applied safely in biological tissue [20].

The theoretical minimum potential difference for water splitting is 1.23 V under standard conditions [107, 242, 229, 250, 126]. However, in practice, an additional voltage, known as the overpotential, is required to overcome the kinetic barrier [242]. The overpotential depends on several factors, with the electrode material being the dominant contributor [96].

The water window is typically characterized using cyclic voltammetry (CV) [42, 20]. In a three-electrode configuration, the current response is measured while the voltage applied to the working electrode is linearly increased and decreased relative to a reference electrode [61]. This approach enables the identification of oxidation and reduction processes occurring at the working electrode. For example, for a Pt/Ir electrode, the water window is typically reported between −0.6 V and 0.8 V versus Ag|AgCl [42], where 'Ag|AgCl' denotes the silver/silver chloride reference electrode. However, these water windows are derived from a three-electrode setup, in which only the electrochemical behavior of the working electrode is characterized by measuring its potential independently of current flow and referenced to a stable electrode. In contrast, in the practical case of a two-electrode stimulation system, the total voltage drop is distributed across both the working and counter electrode-electrolyte interfaces as well as the electrolyte, and therefore cannot be directly compared to the results from the three-electrode CV measurements [238]. Examples in the literature, such as [238, 239], have derived electrochemical safety limits using the same two-electrode configuration as in the intended application, and reported significant differences between the water window obtained from two-electrode and three-electrode configurations, as well as between *in vitro* and *in vivo* conditions.

While the water window defines the upper boundaries, safety limits reported in the literature

are typically set well below the threshold for water electrolysis [204, 12]. These limits originate from research in the field of charge balancing mechanisms, where the objective is twofold: to reverse the electrochemical reactions induced by the stimulation pulse and to maintain the electrode bias voltage within a safe range. The latter consideration led to the definition of specific voltage thresholds, with [172, 198, 32, 218] reporting a safety range of ±100 mV, [183, 148] specifying a limit of ±50 mV, and [139] even proposing a narrower limit of ±25 mV. These voltage ranges correspond to the typical excitation amplitudes used in electrochemical impedance spectroscopy (EIS) to ensure operation within the linear, non-faradaic regime [20, 84, 8].

Although beyond the scope of this work, it is noted that safe stimulation is also limited by the so-called maximum reversible charge injection capacity (CIC), which defines the maximum amount of charge that can be delivered without driving the electrode outside the water window [20, 195]. Typical values for Pt and Pt/Ir electrodes range from 50–150 $\mu C/cm^2$ [42]. However, the values relevant for the intended application must be determined in tissue using the same two-electrode setup used for stimulation [238, 239].

3 Study of Preclinical Deep Brain Stimulation Systems

DBS research in rodent models requires neurostimulation devices that are tailored to the specific demands of these small animals. This chapter defines the key requirements for preclinical DBS systems for rodents and discusses the importance of stimulation monitoring for ensuring reproducible experimental outcomes. It then provides a critical review of existing DBS devices developed from off-the-shelf components, highlighting unresolved technical and ethical shortcomings.

Parts of this section were published in [A10], [A11], and [A13].[3]

3.1 Requirements for Preclinical DBS Devices

Designing DBS systems for preclinical research in rodents presents significant challenges. They must protect animal welfare through a miniaturized, lightweight, and biocompatible design, while also being energy-efficient and robust for long-term use in freely moving rodents. At the same time, they need to deliver precise and safe stimulation, support flexible stimulation protocols, and incorporate modern features such as closed-loop control. The following section summarizes the key design goals for rodent DBS devices.

1st Requirement: Protection of Animal welfare

Animal experiments remain indispensable in DBS research, as neither *in vitro* nor *in silico* approaches can fully replace *in vivo* studies at this stage. Therefore, minimizing animal use and maximizing animal welfare are central goals. These principles are grounded in the ethical framework of the 3Rs: Refinement, Reduction, and Replacement, which are outlined in Directive 2010/63/EU [55].

Device requirements:

- Verification of safety and function through extensive *in vitro* testing prior to animal studies
- Fully subcutaneous implantation of the DBS device and cables, offering the following advantages compared to head- or back-mounted systems:
  - Reduced infection risk
  - Free movement and natural behavior
  - Group housing to reduce stress and anxiety

[3] The review study was conceived, conducted, and analyzed by the author. The requirements for preclinical DBS devices were defined by the author. The concept for verifying stimulation integrity was jointly developed by the author and Christoph Niemann. The *in vitro* experiments were conducted and analyzed by the author.

  - Protection against manipulation by the animal itself or cage mates

- Miniaturized and lightweight design to ensure implantability across species while reducing animal burden
- Biocompatible materials to prevent adverse tissue reactions
- Gentle stimulation parameters to minimize adverse effects

2nd Requirement: Safe, Precise and Flexible Stimulation

To obtain reliable experimental outcomes, stimulation must be delivered within safe limits and with high precision. Simultaneously, the device should provide the flexibility to support diverse stimulation protocols.

Device requirements:

- High accuracy of all stimulation parameters (current amplitude, pulse duration, frequency)
- Charge-balanced stimulation within established safety limits to prevent tissue damage
- Software-based configuration of all stimulation parameters for experimental flexibility
- Two independent stimulation channels to support bilateral DBS

3rd Requirement: Ensuring Reproducibility

The scientific value of experimental results depends on their reproducibility. Devices must therefore not only be able to execute the same protocol multiple times, but also verify correct operation through system monitoring, since otherwise failures may go unnoticed.

Device requirements:

- Current-controlled stimulation to ensure a constant stimulation effect independent of load impedance variations
- On-board system monitoring, including:
  - Detection of stimulation path failures, including open circuits, short circuits, and compliance voltage violations
  - Device status monitoring (e.g., battery voltage, active stimulation parameters)
  - Radio frequency (RF) or optical reporting of monitoring data

4th Requirement: Energy-Efficient Power Management

Modern DBS rodent experiments require continuous operation over several weeks and even months, while device size and weight must remain minimal to protect animal welfare. To meet these demands, devices require an energy-efficient power management strategy that enables long-term operation from a small coin cell.

Device requirements:

- Ultra-low power consumption of $< 100\,\mu W$ during DBS-only operation
- Programmable power modes to selectively activate individual functions (e.g., stimulation, biosensing, telemetry)
- Compliance voltage matched to both electrode geometry and stimulation parameters to minimize power overhead

5th Requirement: Closed-loop Capability

Modern DBS research increasingly uses adaptive stimulation paradigms in which the device adjusts stimulation parameters based on feedback from biosignals. Incorporating closed-loop capability into preclinical DBS systems can be used to explore adaptive stimulation approaches that are relevant to clinical translation and basic science.

Device requirements:

- Acquisition of relevant biomarkers, e.g., accelerometry and local field potentials (LFP)
- Adaptive stimulation control (e.g., on–off control, proportional modulation of current amplitude)
- On-board computing resources capable of executing closed-loop algorithms in real time
- Bidirectional RF interface supporting:
  - Wireless streaming of raw or processed data for offline evaluation
  - Remote stimulation parameter adjustment

3.2 Why Stimulation Monitoring Matters in DBS Experiments

Delivering stimulation within defined specifications is a prerequisite for valid outcomes in DBS experiments with rodents. Nonetheless, such experiments are highly susceptible to technical failures that, if undetected, pose a serious risk to reproducibility and interpretability of scientific results. The most common failures in these experiments include:

- **Cable failures:** Often caused by animal movement or biological degradation of the insulation when subcutaneously implanted.
- **Electrode defects:** The high degree of miniaturization makes electrodes fragile and susceptible to damage during manufacturing, device assembly, or implantation. Typical faults include exposed metal surfaces, as well as soiled or mechanically damaged electrode tips.
- **Compliance voltage violation:** Even with intact connections between the stimulator and the electrode-tissue interface, the DBS voltage demand may exceed the available current source's compliance voltage during a stimulation pulse. This occurs when electrode geometry, stimulation parameters, and the stimulator's compliance voltage are not properly matched. Post-implantation variations in load impedance due to biological processes must also be considered [87].

While broken cables and soiled/damaged electrode tips result in open circuits with no current flow, exposed metal surfaces may cause short circuits. Compliance voltage violations, on the other hand, cause a collapsing stimulation current, producing a mismatch between the intended and delivered stimulation amplitude. Therefore, a built-in self-test within the DBS device is essential to verify that the stimulation signal remains within specifications throughout the entire experimental period. The characteristic effects of the three failure cases (open-circuit, short-circuit, and compliance voltage violation) on DBS current and voltage under current-controlled stimulation are presented in Fig. 8.

Despite its importance, *compliance monitoring* (the term most frequently used in the literature) is rarely implemented in neurostimulation devices, whether in application-specific integrated circuit (ASIC) designs or in systems built entirely from off-the-shelf components. Some ASICs for multi-channel applications [172, 41, 38], such as retina stimulators, and the commercial Intan RHS2116 chip [202], include compliance monitors. However, as this work focuses on solutions that can be realized entirely with off-the-shelf components to ensure reproducibility, the non-commercial ASIC designs fall outside the scope of this work. The commercially available Intan RHS2116 chip, on the other hand, has a power consumption far exceeding what is acceptable for chronically implantable DBS systems. Consequently, these integrated solutions cannot serve as practical options for the type of DBS device targeted in this work.

When considering designs implemented exclusively with off-the-shelf components, on-board compliance monitoring is largely absent. From the 23 reviewed DBS devices for rodents (see Section 3.3), only five report compliance monitoring [223, 75, 74, 85, 137], though none provides an evaluation of how effective their monitoring is in detecting failures. Of these, only [223] describes the stimulation monitoring method, which uses ADC sampling of the stimulation current via a shunt resistor. Nevertheless, the publication does not include any

documentation of the sampled current pulse. In [85, 74, 75], which appear to rely on the same circuit design, it can only be speculated from the microcontroller datasheet and the circuit schematic that the DBS voltage signal might be sampled using the microcontroller's integrated ADC. However, the limited sampling rate of standard microcontrollers makes ADC sampling unsuitable for reliably capturing the rectangular shape of the stimulation current or the maximum stimulation voltage at the end of the pulse (waveforms shown in Fig. 4), which typically require digital signal processors (DSP). Thus, a collapsing current due to compliance voltage violation may go undetected with microcontroller-based ADC monitoring. In [137], the device provides load impedance values that could, in principle, be used to identify failures in the stimulation path. However, the publication does not specify the frequency at which the impedance was measured or the method used, nor does it provide a circuit description.

In summary, the reported discrete approaches lack methodological detail and provide no evaluation of monitoring performance. Consequently, it remains unclear how effectively these designs can detect all three failure cases, with compliance voltage violations in particular likely to go unnoticed. This situation highlights the urgent need for a well-documented monitoring approach capable of reliably detecting all three failure cases in a discrete, energy- and area-efficient microcontroller-based design. This need motivates the new approach described in Section 5.2.4.

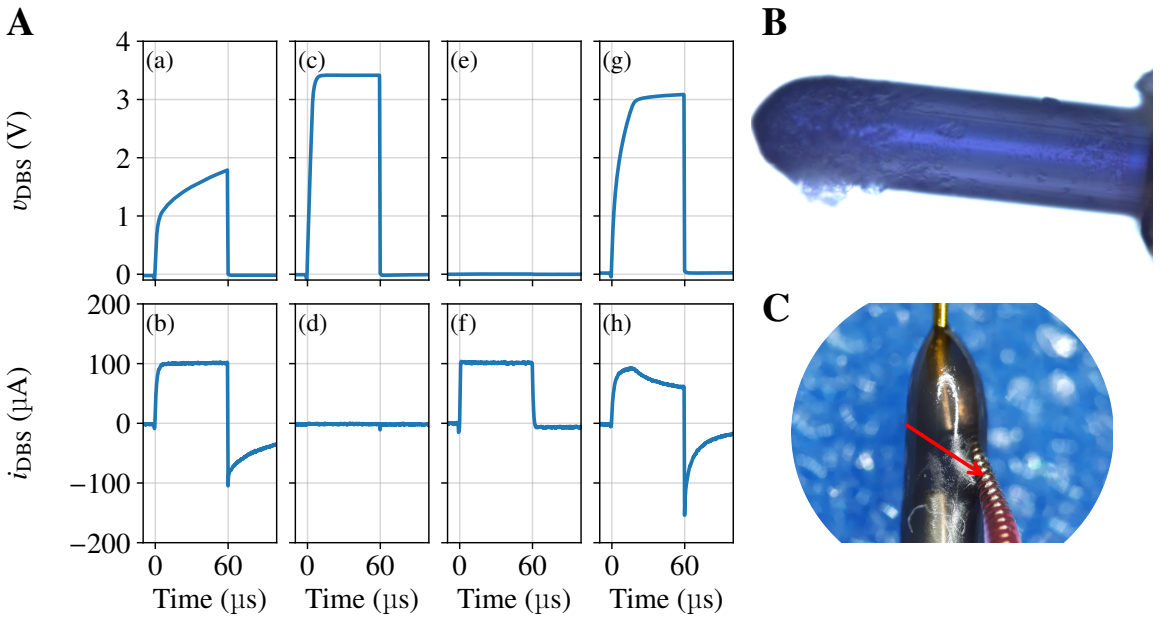

Figure 8: (A) Measured voltage and current waveforms under current-controlled stimulation showing regular operation (a,b); failures in the stimulation path, including the open-circuit (c,d) and short-circuit cases (e,f); and compliance voltage violations (g,h). The failure cases were intentionally induced. The signals were recorded using STELLA3 with various microelectrodes immersed in a 0.1 S m^{-1} NaCl solution under 100 µA, 60 µs, and 130 Hz current-controlled stimulation. (B) and (C) show electrode faults from inspected electrodes prior to the *in vivo* study, with (B)[§] showing a soiled electrode tip and (C)[§] bare metal exposed outside the insulation. Adapted from [A11].

[§] Photographs: (B) by Denise Franz, (C) by Maria Kober.

3.3 Critical Review of the State of the Art

This section evaluates current preclinical DBS devices with respect to the requirements outlined in the previous section. The aim is to identify limitations and unresolved challenges in the field in order to motivate the development of a new solution.

A systematic review of 23 portable DBS devices for rodents designed with off-the-shelf components was conducted. ASIC-based solutions were excluded (e.g., [7]), as their long development time and limited flexibility make them poorly suited to the dynamic demands of preclinical research. Similarly, non-portable devices that only allow tethered stimulation were not considered, as wired connections severely restrict experimental flexibility. They limit stimulation to short periods (hours) and preclude the use of many standard behavioral paradigms. Such constraints are incompatible with modern long-term DBS research in freely moving rodents.

The results are summarized in two complementary tables. Table A.1 provides an overview of implemented features, while Table B.1 reports compliance voltages, charge balancing modes, battery runtime, and physical properties. Devices are organized by publication year and grouped into two main categories: battery-powered and battery-free. To facilitate comparison, the number of implemented features is also summarized in bar charts (Fig. 11). The following paragraphs present a critical analysis of the findings.

Battery-free vs. battery-powered Three of the 23 devices rely on battery-free operation via wireless power transfer (WPT). However, WPT presents two main challenges: First, specialized cages are required [162, 31, 64] that can lead to unreliable operation if coils are misaligned due to animal movement, and prevent essential behavioral experiments like the Morris water maze. Second, when the WPT system is directly attached to the animal, it requires full implantation of the WPT receiver and stimulator, along with a transmitter unit on the skin, adding discomfort while still relying on a battery that requires replacement [99]. In contrast, battery-powered systems provide uninterrupted stimulation, making them the only viable option for reliable, consistent DBS experiments independent of specialized cage setups. Nevertheless, the additional battery volume increases device size and weight, while the limited runtime restricts use to short-term experiments or requires battery replacement under anesthesia, unless power consumption can be reduced sufficiently.

Device control Radio frequency communication is considered the most effective control method as it allows for modifying a wide range of device parameters without disturbing the animal. However, the requirement for considerable printed circuit board (PCB) area, the need for higher power consumption, and the complexity of RF design have limited its widespread use (7/23, including WPT devices). Magnetic sensors are the most common

(9/23), typically enabling simple function triggers such as integrated self-tests. Mechanical controls (switches and potentiometers) are less attractive, as they require a large size to remain manually operable (6/23). Another control mechanism involves transmitting light pulses to a photodiode. However, this approach is unreliable due to the movement of the animals and has so far been implemented in only one stimulator [99] (1/23). Five of the 23 devices provide no control capabilities at all.

Data output technology RF communication enables high data rates, which are required for the wireless transmission of physiological data, such as local field potentials and accelerometer data. However, due to the aforementioned obstacles associated with RF modules, optical transmission of status information is most commonly used in DBS devices (16/23), whereas only 5 of the 23 devices rely on RF communication. Optical transmission is implemented using LEDs operating in either the visible or infrared (IR) range, with simple blinking patterns indicating device information, e.g., low battery voltage alerts. Three of the 23 devices provide no data output technology.

Provided device/physiological data Most systems provide only basic device-specific data, such as low battery voltage alerts (7/23) and/or the stimulation status (on/off) (12/23). In contrast, monitoring whether the stimulation is actually delivered as intended is rarely addressed (5/23), despite its critical role for reproducibility and reliability of experiments. In these five cases, however, the monitoring approaches are insufficiently documented and their effectiveness in reliably detecting failures, particularly compliance voltage violations, remains unverified (see discussion in Section 3.2).

In addition, only two DBS devices support the transmission of the applied stimulation protocol (2/23), which is important for verifying that the stimulation parameters are set correctly, especially when they have been changed. Furthermore, only one device is able to transmit physiological data wirelessly, specifically local field potentials (LFPs) [192] (1/23). Another system enables the measurement of LFPs but processes all data entirely on-board [187] (1/23). Finally, four of the 23 devices report no device-related or physiological data at all.

Stimulation properties Most DBS devices are primarily designed with current-controlled stimulation (18/23). Three additional devices employ current source designs with limitations, as explained in the following. It is not recommended to achieve a current-controlled stimulation by varying the resistor in series with a voltage source, as is the case in [88], or by adjusting the output voltage of a voltage source, as is the case in [137]. First, these approaches require frequent active readjustment due to the dynamic load, which might be energy-intensive. Second, the resulting current amplitudes can only be considered constant on a macroscopic time scale. At a microscopic level, the system still behaves like a voltage

source, which cannot maintain a constant current during the pulse duration due to the capacitive component of the impedance load (see [88]), resulting in only semi-current-controlled stimulation. Furthermore, the boost converter approach in [98] also results in a time-varying rather than a constant current during the pulse duration.

Exclusive voltage-controlled stimulation is rarely implemented (2/23) and is generally no longer recommended for DBS (see Section 2.2.3).

Charge balancing is realized passively (8/23), actively (11/23), in a hybrid manner (1/23), or not at all (3/23). In one device lacking an explicit charge balancing circuit [137], stimulation is delivered in pulse trains interrupted by rest periods, during which the double-layer capacitance can self-discharge. This approach, however, cannot be considered as true charge balancing, since the DC bias generated during stimulation may repeatedly exceed safe limits, and the subsequent rest periods may not provide sufficient compensation to prevent harmful effects.

Most DBS devices are limited to single-channel stimulation (17/23), which limits DBS to one hemisphere. Dual-channel designs are less common (5/23), although a second channel is essential for studying bilateral DBS. One additional device [117] presents an inadequate dual-channel implementation, which is explained in the following. The assumption that a single current source's output will simply split the current into equal halves is invalid, since each channel is subject to different load impedances. The differences in load impedance are due to several factors, including the different conductivity values of white and grey matter [80, 15, 116, 3], the highly dynamic biological encapsulation processes that surround the electrodes after insertion [64, 134], and inherent manufacturing variations in the electrodes themselves [190]. Therefore, multi-channel designs must provide a dedicated current source for each channel. However, even with such designs, crosstalk effects can lead to cross-currents between multipolar DBS electrodes, meaning that the intended constant current from each channel may not follow the desired stimulation pathway (see Section 7.2 for more details).

Software-based adjustment of stimulation parameters is supported in many DBS devices (12/23), in which all three parameters (current amplitude, frequency and pulse duration) can be modified via software. This is an essential condition for closed-loop stimulation. In the remaining 11 of the 23 devices, not all parameters can be adjusted via software. For example, current amplitude is often set using an analog potentiometer or by physically replacing a resistor. Furthermore, nearly every publication reports the stimulation parameter range that a DBS device could provide. However, such reporting is of limited value. Whether the constant current can be delivered throughout the pulse duration depends on the available compliance voltage (see Section 2.2.6). The stimulation voltage must remain consistently below the compliance voltage, which is determined by the chosen stimulation parameters and the electrode-tissue setup. For this reason, it is more meaningful to report the resolution of each stimulation parameter and to specify parameter ranges in combination with the particular

electrode-tissue setup under which the stimulation signal could be reliably delivered.

Finally, closed-loop stimulation capabilities have been implemented in only two DBS devices.

Compliance voltage Most DBS devices for rodents are designed for current-controlled stimulation, which requires a sufficient compliance voltage to maintain constant current. Importantly, the required compliance voltage depends on electrode geometry, stimulation parameters, and electrode-tissue interactions. Smaller electrodes and higher injected charge increase the required maximum stimulation voltage. If the available compliance voltage is insufficient, the current source enters saturation and the current amplitude collapses (see Section 2.2.6). In contrast, oversizing the compliance voltage necessitates higher supply voltages, which increases the system's overall power consumption. Therefore, the compliance voltage must be tailored to the specific electrode and stimulation requirements.

However, in nearly half of the reviewed publications (11/23) this essential parameter is not reported. Instead, the battery voltage or the boost converter output voltage at which the current source operates is given. In reality, the internal resistance of the current source introduces a voltage drop, ranging from hundreds of millivolts to several volts depending on the current source design (for BJT current source designs, see [142]). Compliance voltages, when not reported, could be reconstructed from circuit details for some cases, as shown in the following. In [74, 85, 75], the C8051F330 microcontroller is used with an integrated current output DAC (although circuitry is not always explicitly provided, descriptions match across these publications). The datasheet specifies an output compliance range of $V_{\mathrm{DD}} - 1.2V$, yielding a compliance voltage of 1.9 V for the reported 3.1 V supply. In [119] and [67], a pnp BJT current source IC (PSSI2021SAY) is employed ($V_{\mathrm{o,min}} = 0.9$), resulting in a compliance voltage of 2.1 V for the reported 3 V battery supply and 19.1 V for the reported 20 V DC/DC supply. In [187] the used LM334 requires a minimum output voltage of 0.8 V, giving a compliance voltage of 2.2 V for the reported 3 V supply. In [93] and [76] no appropriate circuit details were given. [137], [98], and [88] do not provide an appropriate current source design (see discussion above). Across all reviewed DBS devices, compliance voltages range from 1.9–34 V (see Table B.1), with reconstructed values reported as $V_{\mathrm{DD}}^{\mathrm{type}} / V_{\mathrm{Compl}}^{\mathrm{corr.}}$, e.g. $3^{\mathrm{batt.}}/2.1^{\mathrm{corr.}}$.

It is important to note that none of the 23 reviewed publications provide current and voltage measurements of the DBS signal in either appropriate *in vitro* solutions or in brain tissue. Instead, most studies evaluate their specific electrode setup only in a 0.9 % saline solution, whose conductivity at room temperature (1.2 S m^{-1} at 20 °C [210]) differs substantially from that of brain tissue ($\approx$ 0.1 S m^{-1} [80]). This validation step is especially important for the devices with compliance voltages around 2 V [74, 85, 75, 119, 187], as their limited compliance voltage makes a careful selection of stimulation parameters and electrode geometries essential.

Power consumption in DBS-only operation Most DBS devices report only runtimes with a specific battery configuration. However, runtime is not a meaningful benchmark, as it depends on the available battery energy, which differs substantially across devices. Power consumption, in contrast, provides a battery-independent measure and thus enables fair comparison across designs. Since continuous stimulation is the primary use case in DBS research, this analysis focuses on power consumption in DBS-only operation.

About half of the reviewed publications (10/23) report power or current consumption in DBS-only operation. For the remaining devices, average power consumption was estimated by dividing the reported battery capacity by runtime. This estimation was restricted to devices that operated continuously throughout the reported runtime and did not include prolonged, power-demanding tasks such as RF communication, or sensor data acquisition. It was further assumed that variations in stimulation parameters had minimal influence on runtime, given the low duty cycles and current amplitudes involved (consistent with the findings in [93]). The works of [223, 4, 137, 98, 187, 16] did not meet the conditions required for estimating power consumption, while [88] was excluded solely due to the lack of a valid current source design. Although compliance voltage values could not be reconstructed from circuit details in [93, 76], the reported current source's supply voltage was used as a proxy in this figure.

Fig. 9 compares reported and reconstructed values of both power consumption in DBS-only operation and compliance voltage for existing DBS devices. Reported DBS devices show a wide spread in both power consumption (tens of microwatts to tens of milliwatts) and compliance voltage (1.9–20 V). The figure shows that DBS devices operating at higher compliance voltages generally come at the cost of increased power consumption, while systems designed to operate at lower compliance voltages, achieve power consumption below the milliwatt range, in some cases even below 100 µW. This relationship is expected, as the generation of higher supply voltages for the current sources requires energy-intensive step-up DC/DC conversion. Nevertheless, the circuit design presented in [93] can partially mitigate this increased power demand by duty-cycling the DC/DC converter, although its ≈ 0.28 mW consumption remains comparatively high, allowing only about 11 days of operation with a CR1216 coin cell. Importantly, neither compliance voltage nor power consumption can be meaningfully compared across devices without reference to the specific stimulation setup they are designed to support. Future stimulator publications should therefore report electrode dimensions, stimulation parameters, and measured voltage and current waveforms under realistic tissue conditions.

Physical properties and mounting Device dimensions and weight are critical parameters, as they dictate the overall impact on the animal. The total weight ranges for battery-powered devices from 1.4–13.8 g, while the lightest battery-free design weighs only 46 mg. Assembled PCB volumes (excluding battery) range for battery-powered devices from 0.1–15 cm^3, and

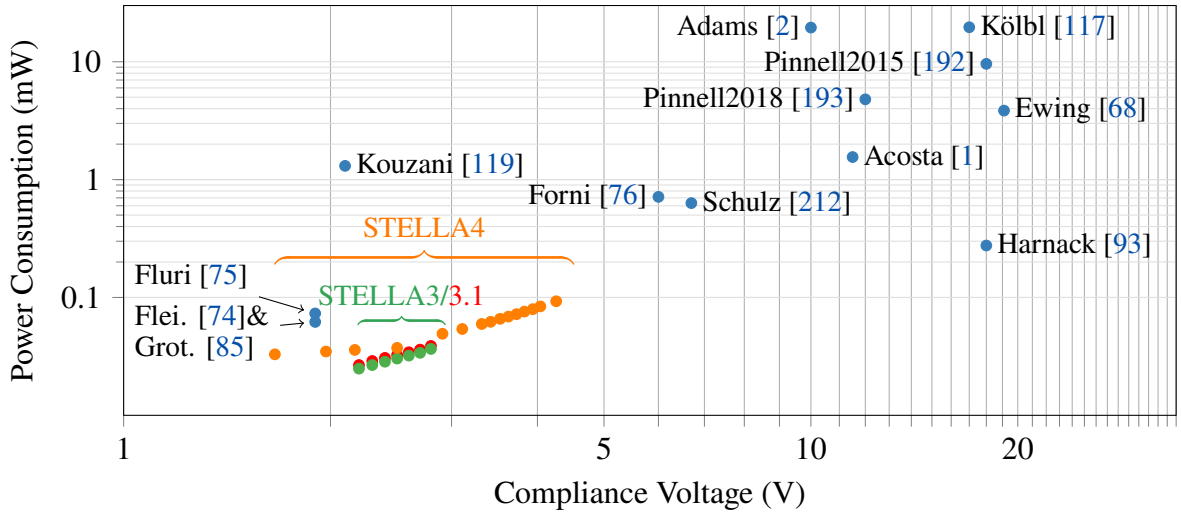

Figure 9: Comparison of power consumption in DBS-only operation and compliance voltage for existing battery-powered DBS devices designed for preclinical research in rodents using off-the-shelf components.

together with the battery configuration, determine the feasible mounting option. Typical size and volume constraints of implantable devices for small rodents are discussed in Section 5.3.5.

To ensure comparability, assembled PCB volumes were extracted from the publications, and the volume of the respective battery configuration was added to the assembled PCB volume (see Table B.1). This approach provides the only fair basis for comparing device sizes, since additional device housings differ considerably between designs. Devices were categorized into five PCB size classes (Very Low to Very High, see Table A.1), with the following distribution: 5 VL, 8 L, 5 M, 3 H, and 1 VH. Mounting approaches included head-mounted (8/23), backpack-mounted (7/23), fully implanted subcutaneously (7/23), and partially implanted (1/23). Fully subcutaneous implants best preserve natural behavior and promote animal welfare (see Section 5.3.6), but are also the most technically challenging to realize due to requirements for high levels of miniaturization and reliable waterproof encapsulation.

Fig. 10 compares reported battery runtimes in DBS-only mode and the assembled PCB volume (with and without the battery volume). Only DBS devices with reported battery runtimes were considered, where continuous DBS operation without prolonged, power-demanding tasks was applied. Each device is represented by a vertical line spanning from the bare PCB volume (blue dot) to the PCB + battery volume (orange dot). Runtimes range from less than a day to nearly two months, while total volumes span from below 0.5 cm^3 to more than 5 cm^3. The figure shows that most designs achieve runtimes of several weeks only with large batteries, which reflects high power consumption and results in bulky devices. The PCB volume without battery is typically less than 1 cm^3 (VL/L PCB size class), but the

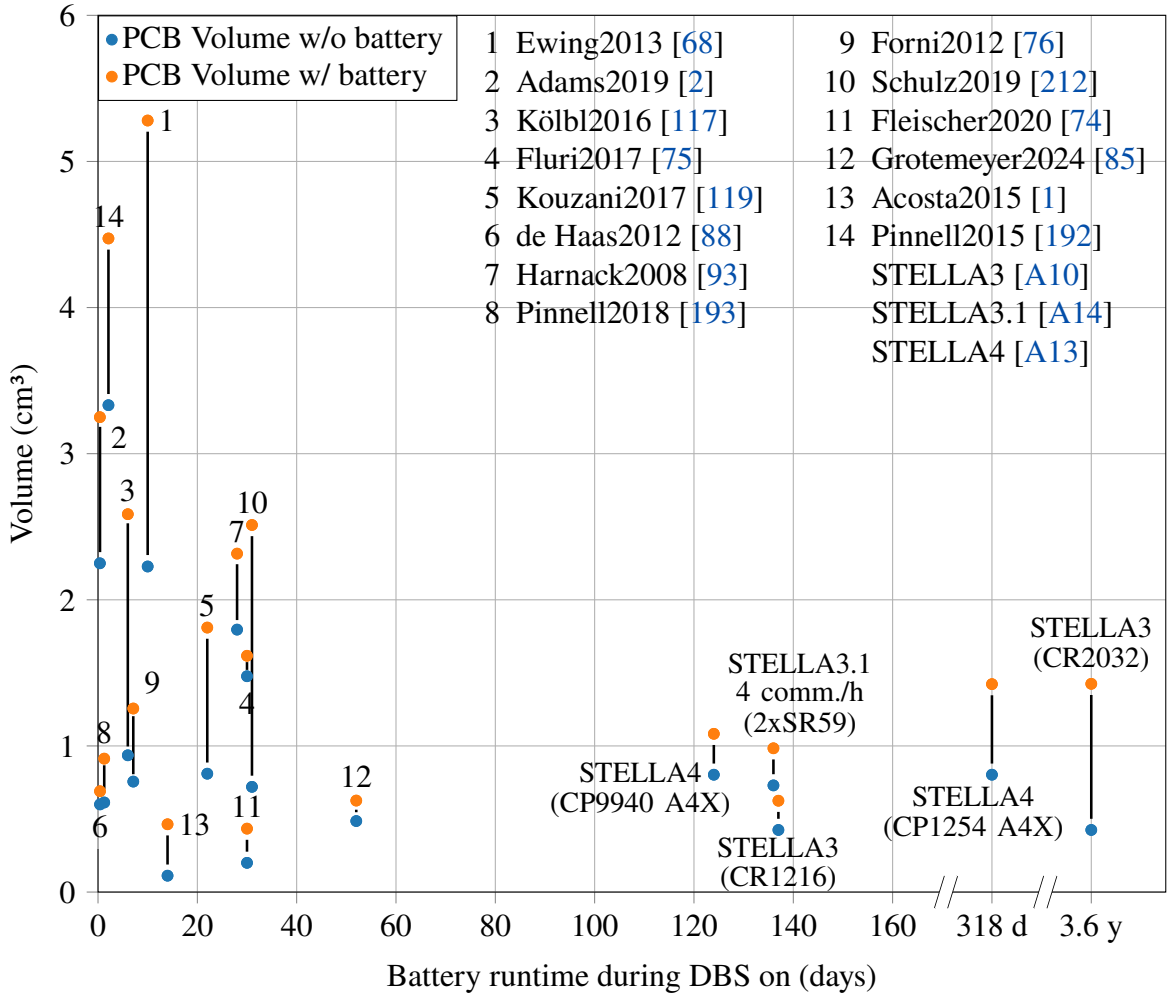

Figure 10: Battery runtime in DBS-only mode versus total device volume (PCB with and without battery) for existing battery-powered DBS devices designed for preclinical research in rodents using off-the-shelf components. Adapted from [A10].

use of batteries often increases the overall size by several cubic centimeters. Only a few devices achieve both a PCB + battery volume below 1 cm^3 and runtimes of several weeks, highlighting the challenge of achieving both a compact form factor and long battery runtime.

Compact comparison of DBS devices To complement the detailed analysis, Table 1 provides a condensed comparison of all battery-powered DBS devices with a total PCB volume below 5 cm^3, which covers the size range in which the majority of existing designs fall and which is therefore used in this work as a practical threshold for portable rodent DBS devices. The table summarizes the presence and absence of the most essential features identified in this review, including bidirectional RF communication, stimulation monitoring (BIST), charge-balanced current-controlled stimulation, dual-channel capability, software-adjustable parameters, ultra-low power consumption, closed-loop functionality, and validated subcuta-

neous implantability. PCB volumes are visualized using color-coded bars to facilitate fast comparison across devices. This simplified overview highlights which requirements current systems meet and which remain unmet, thereby revealing the remaining gaps that motivate the development of STELLA. Please note that, for reasons of brevity and compactness, Fig. 9, Fig. 10, and Table 1 already include results for the STELLA devices, although these are introduced only in a later chapter of this thesis.

Table 1: Comparison of essential features required in battery-powered, compact DBS devices (< 5 cm^3) to enable advanced DBS rodent research. PCB volumes are shown as scaled color bars.

DBS Device	Bidirectional RF	Stim. Monitoring (BIST)	Current-Controlled	Charge-balanced	Dual-Channel	SW-adj. Stim.-params[♯]	Ultra-Low Power Stim.[§]	Closed-loop	Subcutaneous implan. validated in	PCB vol. (cm^3) max. 5 cm^3
Acosta2015 [1]	✗	✗	✓	✓	✗	✓	✗	✗	✗	
Fleischer2020 [74]	✗	(✓)	✓	✓	✗	✓	✓	✗	M	
Parastarfeizabadi2016 [187]	✗	✗	✓	✓	✗	✗	n/a	✓	✗	
→ STELLA3 [A10]	✗	✓	✓	✓	✓	✓	✓	✗	R/H	
Grotemeyer2024 [85]	✗	(✓)	✓	✓	✗	✗	✓	✗	M	
de Haas2012 [88]	✗	✗	(✓)	✓	✗	✗	✗	✗	M	
Pinnell2018 [193]	✗	✗	✓	✓	✓	✗	✗	✗	✗	
Hentall2013 [98]	✗	✗	(✓)	✓	✗	✓	n/a	✗	✗	
Schulz2019 [212]	✗	✗	✓	✓	✓	✗	✗	✗	✗	
→ STELLA3.1 [A14]	✓	✓	✓	✓	✓	✓	✓	✗	R	
Forni2012 [76]	✗	✗	✓	✗	✗	✗	✗	✗	✗	
→ STELLA4 [A13]	✓	✓	✓	✓	✓	✓	✓	✓	R	
Kouzani2017 [119]	✗	✗	✓	✓	✗	✗	✗	✗	✗	
Kölbl2016 [117]	✗	✗	✓	✓	(✓)	✓	✗	✗	✗	
Liu2017 [137]	✓	(✓)	(✓)	✗	✗	✓	✗	✗	✗	
Fluri2017 [75]	✗	(✓)	✓	✓	✗	✓	✓	✗	✗	
Harnack2008 [93]	✗	✗	✓	✓	✗	✗	✗	✗	R	
Ewing2013 [67]	✗	✗	✓	✓	✓	✓	✗	✗	R	
Adams2019 [2]	✗	✗	✓	✓	✗	✓	✗	✗	✗	
Pinnell2015 [192]	✓	✗	✓	✗	✓	✓	✗	✓	✗	
Alpaugh2019 [4]	✗	✗	✓	✓	✗	✗	n/a	✗	M	n/a

✓= full support; (✓) = limited; ✗= not supported;
R = rat, M = mouse, H = hamster. Multiple letters indicate validation in more than one species;
[♯] = all stimulation parameters (current amplitude, pulse duration, frequency) adjustable in SW;
[§] = defined as power consumption < 100 µW in DBS-only operation (excl. power-intensive tasks);

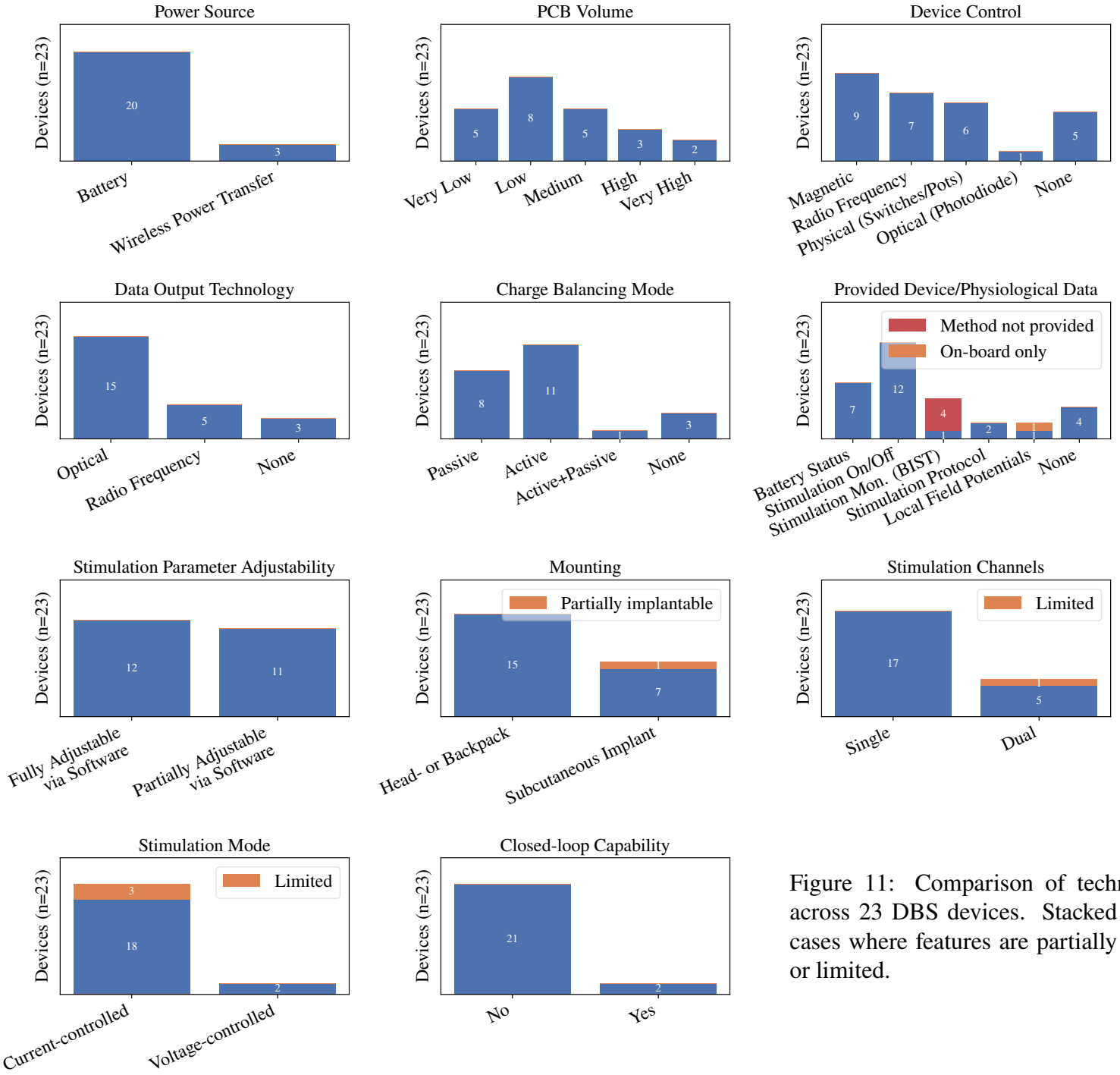

Figure 11: Comparison of technical features across 23 DBS devices. Stacked bars indicate cases where features are partially implemented or limited.

3.4 Interim Conclusion

In this section, the author defined a sharp requirement profile for preclinical DBS systems necessary to enable valid, welfare-compliant, and modern translational research. These requirements are: protection of animal welfare, safe and precise stimulation, experimental reproducibility, energy-efficient power management, and closed-loop capability. Particular attention was given to the risk that the experimental reproducibility can be compromised by technical issues such as broken leads, damaged or misconstructed electrodes, or compliance voltage violations, which may easily go unnoticed during long-term experiments. For this reason, reliable stimulation monitoring was identified as a central requirement for successful DBS studies.

Based on these requirements, a critical analysis of 23 existing preclinical DBS devices for rodents developed from off-the-shelf components was conducted. Most devices are either head- or back-mounted, which are known to restrict the animals' natural movement and thereby limit the validity of behavioral studies while potentially compromising animal welfare [66]. Fully implantable designs remain rare due to challenges in achieving miniaturization, waterproof encapsulation, and sufficiently low power consumption, which otherwise necessitates large batteries. Devices powered exclusively through wireless power transfer introduce further concerns, as they depend on specialized cages and are sensitive to coil misalignment caused by animal movement.

Technical shortcomings were also identified across several devices, including inadequate current source implementations, unsafe charge-balancing methods, and invalid dual-channel designs. Furthermore, no study presented a validated built-in monitoring mechanism for detecting all three major failure conditions (open-circuit, short-circuit, and compliance voltage violations), representing a major obstacle to ensuring experimental reproducibility.

Although compliance voltage is a critical parameter for current-controlled stimulation, many publications report only supply voltages, and none provide sufficient characterization of stimulation under realistic electrode-tissue conditions. Without this information, it remains unclear whether the designs operate with excessive voltage headroom, resulting in unnecessary power consumption, or with insufficient compliance voltage, causing the current source to enter saturation and fail to deliver current-controlled stimulation.

Control and communication interfaces are typically rudimentary. Most devices rely on magnetic or mechanical controls, while only a small fraction provide fully bidirectional RF communication. Consequently, data output is largely limited to basic device status information. Dual-channel and closed-loop functionality remain rare exceptions.

The analysis of power consumption, compliance voltage, and physical properties highlights the trade-offs that currently constrain the design of preclinical DBS devices. Systems offering

higher compliance voltages generally exhibit increased power consumption, which in turn requires larger batteries and results in greater device weight and volume. In contrast, designs optimized for low power operation achieve extended runtimes but at the cost of limited compliance voltage and flexibility.

In conclusion, while many partial solutions exist, no current device simultaneously satisfies all requirements for long-term, reproducible, and welfare-compliant preclinical DBS studies. To bridge these methodological gaps, future systems must combine:

(i) charge-balanced, precise, and bilateral stimulation;
(ii) reliable stimulation monitoring capabilities covering all relevant failure cases (open-circuit, short-circuit, and compliance voltage violations);
(iii) a streaming-capable, bidirectional RF interface that remains functional when subcutaneously implanted;
(iv) battery-powered, ultra-low power operation ($< 100\,\mu W$) in DBS-only operation;
(v) a PCB volume below $1\,cm^3$;
(vi) fully subcutaneous implantation enabled by a compact, biocompatible, and waterproof encapsulation; and
(vii) closed-loop capability with biosignal acquisition and on-board computing capabilities.

However, before such a system can be realized, a precise understanding of the specific stimulation setup under realistic conditions is required. Chapter 4 therefore presents the experimental analysis of the stimulation load, which forms the basis for the device design of STELLA presented in Chapter 5.

4 Electrode-Electrolyte Characterization

Understanding how DBS electrodes interact electrically with the surrounding electrolyte is fundamental for the design of an energy-efficient and reliable stimulation system. However, the electrode-electrolyte interface represents a complex electrochemical system that cannot be described as a linear time-invariant (LTI) system. Even under controlled experimental conditions, such as constant electrolyte volume and temperature, impedance changes were observed over time, reflecting electrochemical processes at the interface. In this work, the same two-electrode configuration used in the *in vivo* setup was applied for characterization to ensure realistic conditions. Since both electrode contacts contribute to the total impedance, the time-dependent impedance variations observed become even more pronounced than in conventional three-electrode configurations. Consequently, the obtained data provide representative ranges rather than reproducible values.

In the following, the electrical properties of the two microelectrodes used within the project are analyzed under *in vitro* and *ex vivo* conditions. By combining experimental measurements and equivalent circuit modeling, the interaction between DBS waveforms and electrode impedance is analyzed to extract parameters relevant for the design of the preclinical DBS device.

The results presented in this section have not yet been published.[4]

4.1 Stimulation Setup within the Project

The *in vivo* DBS setup within the ELAINE project was designed to investigate movement disorders, specifically Parkinson's disease and dystonia.[5] Two rodent models were employed for Parkinson's disease, the widely used 6-hydroxydopamine (6-OHDA) rat model, representing dopaminergic neuron degeneration [233], and the bacterial artificial chromosome (BAC) transgenic rat model, which exhibits genetic characteristics associated with PD [175]. For dystonia, experiments were performed on the dt^{sz} hamster model, a well-established phenotype of paroxysmal dystonia [141].

Stimulation parameters Stimulation was applied unilaterally in the 6-OHDA model (i.e., one hemisphere) and bilaterally in the BAC-transgenic and dt^{sz} models (i.e., both hemispheres). Across all models, rectangular cathodic pulses of 60 µs duration at a frequency of

[4]The author conceptualized the study, conducted the *in vitro* and *ex vivo* experiments, and analyzed the data. Christian Haubelt, Dirk Timmermann, Mareike Fauser, Denise Franz, Rüdiger Köhling and Alexander Storch provided the resources.

[5]The author did not conduct any *in vivo* experiments presented in this dissertation. All *in vivo* studies referenced throughout the entire work were performed by collaborators in the medical research departments within the ELAINE project, in accordance with approved ethical permissions and protocols.

130 Hz were applied, with current amplitudes of either 50 µA or 100 µA, depending on the respective animal model. Table 2 summarizes the stimulation setups for each model.

Table 2: *In vivo* stimulation setup for different rodent models used within the ELAINE project.

Setting	6-OHDA Rat [233]	BAC-transgenic Rat [175]	*dt^{sz}* Hamster [141]
Movement Disorder	PD	PD	Dystonia
Pulse shape	Rectangular	Rectangular	Rectangular
Pulse duration (µs)	60	60	60
Frequency (Hz)	130	130	130
Amplitude (µA)	100	2x100	2x50
Channel	Unilateral	Bilateral	Bilateral
Stimulation time	6 weeks	6 weeks	15 days
Stimulation type	Cathodic	Cathodic	Cathodic
Electrode Type	Custom Hemisph.	PI-SNEX-100	PI-SNEX-100
Electrode Config.	Monopolar	Bipolar	Bipolar

Electrode configurations Two electrode types were employed in the project: the custom-made monopolar electrode, and the commercially available bipolar PI-SNEX-100 (both from Microprobes for Life Science, USA). A gold wire served as the counter electrode for the monopolar electrode, whereas the PI-SNEX-100 integrates a stainless steel counter electrode. By design, the custom-made hemispherical electrode is intended for monopolar stimulation, whereas the PI-SNEX-100 is designed for bipolar stimulation. Therefore, they are also referred to in this work simply as the *monopolar* and *bipolar* electrodes, respectively.

The monopolar electrode, used in the 6-OHDA rat model, features a hemispherical platinum core. According to the manufacturer, its core diameter is specified as 225 µm. However, microscopy performed by ELAINE contributors determined a radius of (155 ± 10) µm [190]. The bipolar electrode, used in both BAC-transgenic and *dt^{sz}* models, features a cylindrical platinum/iridium core with a diameter of 100 µm and a length of 0.25 mm, as specified by the manufacturer. These geometries were not further verified experimentally.

The core electrode acts as the working electrode that is positioned directly within the brain target region intended for stimulation. Throughout this work and in the *in vivo* experiments, a cathodic stimulation configuration is applied. This is ensured by connecting the electrodes such that the conventional current flows into the counter electrode and exits the working electrodes (see Section 2.2.1 for more details).

Fig. 12a summarizes their geometric and material properties, and Fig. 12b shows both electrodes under the microscope.

Literature context The stimulation parameters and electrode designs used within ELAINE align with the state of the art in preclinical DBS research. According to the systematic review by [114], which reviewed 34 rodent DBS studies on Parkinson's disease and dystonia, and summarized the results in a comparative table, typical stimulation parameters fall within current amplitudes of 30–200 µA, with 60 µs and 130 Hz being the most commonly used pulse duration and frequency, respectively. Building on that work, the author extracted additional stimulation parameters from more recent literature for PD and dystonia models and visualized the results in a summary figure shown in Fig. F.1. A broader review by [255], encompassing 407 rodent DBS studies across neurological and psychiatric models, reported the modal parameters of 100 µA, 60 µs, and 130 Hz.

Similarly, the electrode dimensions and material properties used in ELAINE are well aligned with common rodent DBS electrode configurations, with core electrodes typically covering a range of 125–300 µm for rats and 50–125 µm for mice [255]. The hemispherical (310 µm) and PI-SNEX-100 (100 µm) electrodes therefore fall well within these ranges.

Overall, the stimulation parameters and electrode geometries employed in this project represent standard preclinical DBS conditions, making the following analyses and conclusions directly comparable to those reported in the literature.

Electrode Type	Custom Hemispherical	PI-SNEX-100
Manufacturer	Microprobes for Life Science	
Core Material	Platinum	Platinum/Iridium
Core Diameter	310 µm (hemisphere)	100 µm (≈ cylinder)
Core Length	-	0.25 mm
Core Surface Area	0.151 mm^2	0.0784 mm^2
Reference Material	Gold	Stainless steel
Reference Diameter	250 µm	330 µm
Reference Length	2 cm	0.25 mm
Reference Surface Area	15.71 mm^2	0.34 mm^2

(a) Electrode types and their dimensions.

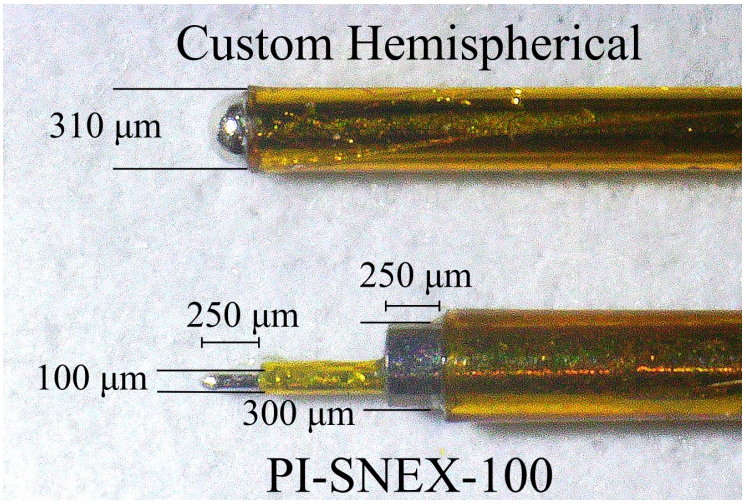

(b) Microscopic images of the custom-made hemispherical monopolar electrode and the bipolar (PI-SNEX-100) electrode with annotated dimensions.

Figure 12: Electrode setup.

4.2 Compliance Voltage Characterization

As highlighted in the critical analysis of existing DBS devices (see Section 3.3), reported compliance voltage values vary widely, ranging from only a few volts up to tens of volts. However, none of these studies provides an analysis for determining the compliance voltage appropriate for the stimulation setup. Such an analysis is crucial because if the compliance voltage is insufficient, the stimulation current will collapse, while if the voltage is excessive, unnecessary power will be wasted.

To address this gap, compliance voltage requirements were characterized for the DBS electrodes used in this study, the custom monopolar electrode and the bipolar PI-SNEX-100 (see Table 2 and Fig. 12a).

Experimental setup A total of 23 DBS electrodes were characterized, comprising 12 bipolar PI-SNEX-100 electrodes and 11 customized monopolar electrodes. Measurements were performed in a 20 mL NaCl standard solution with a conductivity of 0.1 $\mathrm{S\,m^{-1}}$ (Hach, Germany). The 0.1 $\mathrm{S\,m^{-1}}$ conductivity was chosen to closely mimic the electrical conductivity of brain tissue. The electrodes were fully immersed in this solution, and in the monopolar configuration, a gold wire counter electrode was positioned approximately 1 cm from the core electrode. This conductivity was chosen because it lies within reported conductivity values for white and gray matter [80, 15, 3], considering the relevant low- to mid-frequency spectrum excited by the applied DBS pulse signal [11, 82].

Because conductivity is temperature-dependent, all measurements were carried out in a controlled temperature chamber at 25 °C (UN30, Memmert, Germany), corresponding to the temperature at which the manufacturer specifies the conductivity. In contrast, the 0.9 % NaCl solution commonly used for testing the stimulation setup has a conductivity of 1.2 $\mathrm{S\,m^{-1}}$ at 20 °C [210], nearly an order of magnitude larger than that of brain tissue. Therefore, using such a conductive solution to test whether the current source's compliance voltage is sufficient would underestimate the real load impedance.

For the *in vitro* and *ex vivo* stimulation experiments presented in this chapter, a custom-built two-channel laboratory stimulator was used. This device delivers passively charge-balanced constant current pulses without an interphase delay. Each channel provides independent amplitude control via a dedicated analog potentiometer, while pulse duration is jointly adjustable for both channels in 30 µs steps via a push-button. With a compliance voltage of 9 V, it provides sufficient headroom for most experimental stimulation setups. Furthermore, no blocking capacitor is included in the stimulation path, thereby preventing the development of a bias voltage during this investigation [57].

Stimulation setup Measurements were performed at a frequency of 130 Hz and a pulse duration of 60 µs, with stimulation currents ranging from 50–200 µA in 25 µA increments. These settings were chosen because they reflect the typical range for DBS research in movement disorder rodent models (see Fig. F.1). Stimulation current and voltage waveforms were recorded with the setup shown in Appendix E. The maximum stimulation voltage was extracted for each current step. Results are presented in Fig. 13, with panel (A) showing PI-SNEX-100 results, panel (B) showing monopolar electrode results, (C) showing the group mean, and (D) showing both electrode setups.

Validation of the *in vitro* model To confirm that the 0.1 S m^{-1} NaCl solution accurately represents brain tissue electrical conditions, DBS waveform data were obtained from the same PI-SNEX-100 electrode (#5) in rat brain tissue (setup shown in Fig. 13D) and compared to the *in vitro* measurement (Fig. 13A). It is shown that the maximum stimulation voltage values are nearly identical to the results from the *in vitro* measurement (purple solid vs. red dashed), confirming that the chosen *in vitro* model (0.1 S m^{-1} NaCl at 25 °C) accurately reproduces the electrical conditions of brain tissue.

Evaluation In the linear approximation, the maximum stimulation voltage follows

$$\hat{V}_{\mathrm{stim}} = \hat{I}_{\mathrm{stim}} \left[R_{\mathrm{sol}} + R_{\mathrm{ct}} \left(1 - \exp\left(-\frac{t_{\mathrm{stim}}}{R_{\mathrm{ct}} C_{\mathrm{dl}}} \right) \right) \right] \overset{t_{\mathrm{stim}} \ll R_{\mathrm{ct}} C_{\mathrm{dl}}}{\approx} \hat{I}_{\mathrm{stim}} \left[R_{\mathrm{sol}} + \frac{t_{\mathrm{stim}}}{C_{\mathrm{dl}}} \right]. \tag{18}$$

However, experimental data for both electrode types reveal a nonlinear behavior of the maximum stimulation voltage, which bends downward with increasing current amplitude. This deviation from the linear model arises from the voltage-dependent charge-transfer resistance, which according to the Butler-Volmer equation decreases with increasing overpotential [153]. This effect is quite advantageous for the parameterization of the current source's compliance voltage, as with higher injected charge the maximum stimulation voltage decreases, and thus less voltage headroom must be provided, thereby enhancing energy efficiency.

From the measurements, bipolar electrodes required voltages between 1.0–6.7 V across the entire current amplitude range. At 50 µA, values typically were between 1.0–2.0 V, increasing to 3.2–4.0 V at 100 µA, and rising above 6 V at 200 µA. Monopolar electrodes, on the other hand, required significantly lower voltages between 0.67–2.65 V. At 50 µA, values typically were between 0.7–0.9 V, increasing to 1.3–1.5 V at 100 µA, and remaining below 2.7 V at 200 µA.

In addition, the bipolar electrodes show a much wider spread between individual samples. Some electrodes, for example, reached significantly higher voltages than others, which can be attributed to differences in geometry. For example, at a stimulation setting of 100 µA / 60 µs,

the maximum stimulation voltage varied between 2–4 V. In comparison, the monopolar electrodes showed a more uniform behavior, which points to less variance in manufacturing tolerances. This variability is reflected in the grouped mean with shaded regions representing the standard deviation, as shown in Fig. 13C.

Finally, while both electrode types showed a linear voltage increase with current, the slope is clearly steeper for the bipolar electrodes, as shown in Fig. 13C. This indicates a higher load impedance magnitude for the PI-SNEX-100, which explains the higher maximum stimulation voltage.

Implications for device design Manufacturing tolerances in electrode geometry lead to variations in the load impedance, particularly for the PI-SNEX-100 type. It is therefore recommended to design the stimulator on the upper range (90th percentile) of the typical operating values, with an additional margin to account for biological processes such as tissue encapsulation, which can increase the load impedance magnitude over time. Electrodes that exceed this range represent outliers that can be identified and excluded during quality control.

For the specific stimulation setups considered here, 100 µA / 60 µs for monopolar electrodes in the 6-OHDA rat model, and 50 µA / 60 µs for bipolar electrodes required for the dt^{sz} hamster model, the measured data indicate an upper range (90th percentile) of the maximum stimulation voltages of approximately 1.5 V and 2.1 V, respectively. While higher stimulation voltages were observed at larger current amplitudes, these conditions lie outside the range of the defined stimulation setup and are therefore not relevant for device dimensioning.

These results guided the design of the STELLA DBS device family presented in the following Chapter 5. Accordingly, the version STELLA3 was designed for a compliance voltage of 2.8 V, which provides adequate headroom for both electrode types, their variability within the characterized samples and assumed biological processes during *in vivo* studies. Later in the project, the BAC-transgenic rat was introduced, employing a stimulation setup of 100 µA / 60 µs using bipolar electrodes. This configuration required higher stimulation voltages, with a measured upper range of approximately 3.8 V. To meet these extended requirements, STELLA4 was developed, among other reasons, with an increased compliance voltage of 4.3 V. Furthermore, the variability observed between and within DBS electrode types further highlights the importance of an adjustable compliance voltage, which ensures optimal energy efficiency for the specific experimental setup.

Among the 23 preclinical DBS devices reviewed, this study represents the first systematic investigation of maximum stimulation voltage requirements for DBS microelectrodes under realistic conditions.

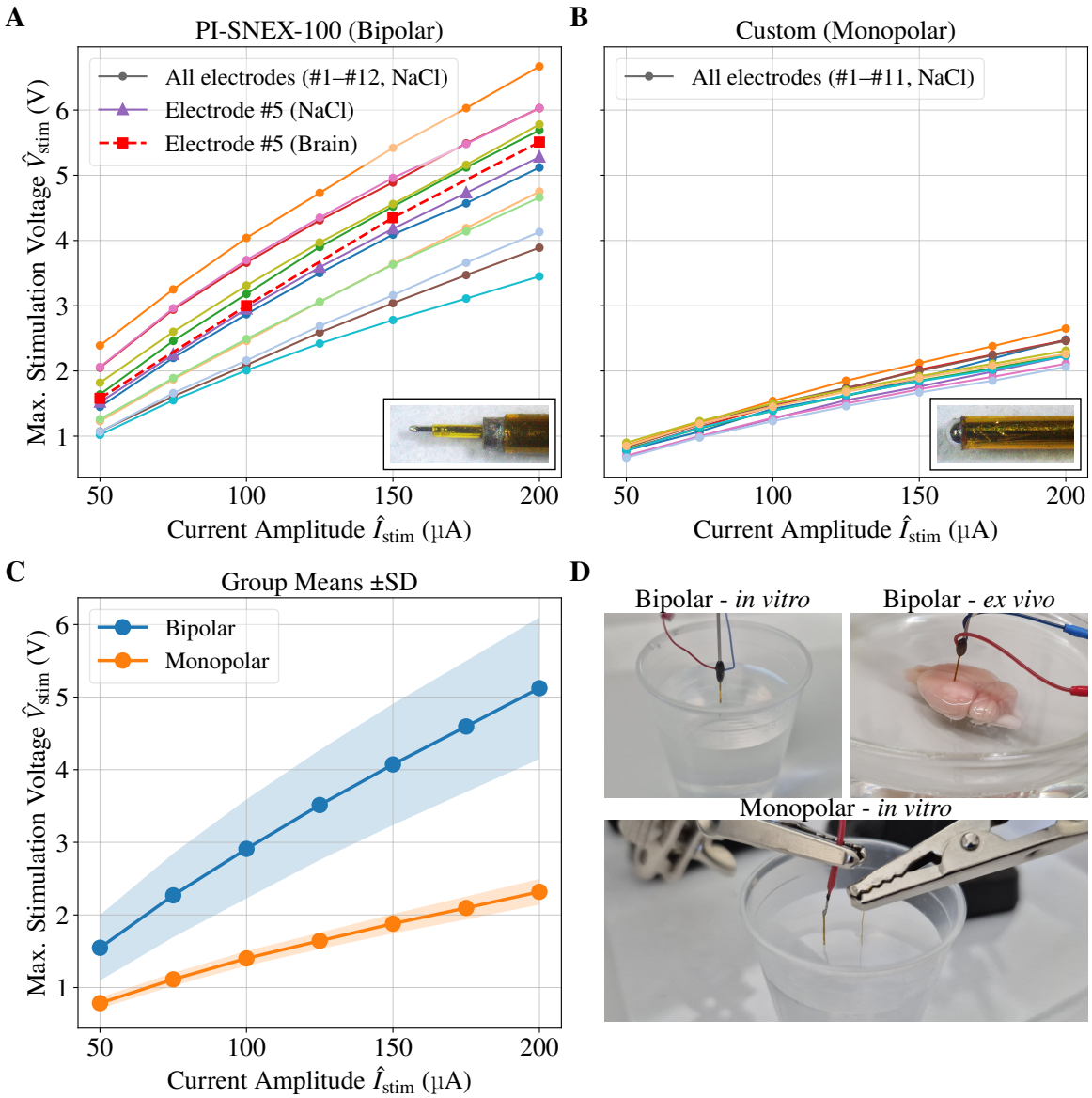

Figure 13: Maximum stimulation voltage as a function of stimulation current at 130 Hz / 60 µs. (A) PI-SNEX-100 bipolar electrodes and (B) custom monopolar electrodes, measured in 0.1 S m^{-1} NaCl solution. Electrode #5 was validated against brain tissue (red dashed line with squares vs. violet solid line with triangles). (C) Group means across electrodes with shaded regions indicating standard deviations at each current amplitude level. (D) Experimental setups for bipolar (*in vitro* and *ex vivo*) and monopolar (*in vitro*) electrode configurations.

4.3 Electrode-Electrolyte Impedance Model

An electrode-electrolyte impedance model is particularly useful during the initial circuit design phase, providing a realistic load for testing the stimulation circuit on a breadboard or within simulation environments such as LTspice. Such models are widely used in the literature to study charge balancing techniques and to evaluate their performance in keeping the

electrode bias voltage within the safe electrochemical window [217, 218, 200, 198, 199, 214, 252]. Many of these models used in these studies, however, provide only a rough approximation of the impedance and are not entirely derived from experimental characterization. Recent work provides detailed methodologies for characterizing the electrode-electrolyte load and deriving models from these data [258, 239, 177].

To accurately model the DBS microelectrodes used in this project under realistic conditions, the complete process is presented in this section, including impedance spectroscopy, parameter fitting, and validation against experimental measurements. The extracted model parameters are subsequently applied to an analytical description of passive charge-balanced DBS. Finally, the performance of passive charge balancing is evaluated both with and without the inclusion of a blocking capacitor.

4.3.1 Impedance Spectroscopy Setup

Impedance spectroscopy was performed in rat brain tissue using a PI-SNEX-100 microelectrode (see Fig. 13D for the bipolar *ex vivo* setup). The brain was maintained at physiological temperature (37 °C) in a temperature-controlled chamber to ensure a stable brain tissue conductivity.

Impedance spectroscopy was performed using sinusoidal excitation amplitudes of 20 mV, 50 mV, 100 mV, 500 mV, 1 V and 2 V. Measurements were conducted with an E4980AL LCR meter (Keysight, USA) across a logarithmically stepped frequency range from 1 MHz down to 100 Hz. Short- and open-circuit compensations were performed prior to the measurement. It should be noted that impedance spectroscopy devices, including the one used in this study, typically specify the excitation signal in terms of their root mean square (RMS) values. Therefore, the RMS voltage was selected to correspond to the intended sinusoidal excitation amplitude (e.g., approximately 71 mV RMS for a 100 mV sine amplitude).

4.3.2 Impedance Characteristics

The results are shown in the Bode plot in Fig. 14, while the measurement obtained with an excitation amplitude of 100 mV is additionally presented as a Nyquist plot in Fig. 15A.

Overall impedance behavior The overall impedance measurement reflects the characteristic frequency-dependent spectrum of immersed electrodes in an electrolytic medium, in which electrode-electrolyte interactions dominate at low frequencies, while tissue-specific properties become evident at higher frequencies [207, 82, 11, 134, 244, 184, 177].

At low frequencies (< 1 kHz), the impedance magnitude is high and the phase angle strongly negative, indicating a dominantly capacitive response. This regime reflects the electrode-electrolyte interface, which is often modeled as charge-transfer resistance in parallel to the

double-layer capacitance, with the latter commonly modeled as a constant-phase element (CPE). In the Nyquist representation, this electrode contribution appears as a straight line (see Fig. 15A).

With increasing frequency (1–10 kHz), the impedance magnitude decreases and the phase angle becomes less negative. In this region, the capacitive contribution of the electrode-tissue interface increasingly diminishes with frequency, and the properties of the brain tissue begin to dominate. Above the corner frequency, at which the impedance magnitude of the electrode-tissue interface and tissue impedance magnitude are equal ($f_1 \approx 1/(2\pi R_{\mathrm{sol}} C_{\mathrm{dl}})$ [207]), the tissue contribution becomes predominant, and $|\underline{Z}|$ approaches the solution resistance, R_{sol}. In the Nyquist plot, the extrapolated intersection of the straight line with the real axis also corresponds to R_{sol} [11].

At higher frequencies (> 10 kHz) the impedance is governed primarily by the resistive and capacitive properties of the brain tissue itself. In the Nyquist representation, this appears as a depressed semicircle, deviating from the ideal $-R_{\mathrm{sol}}||C_{\mathrm{sol}}-$ semicircle. Such deformation is attributed to the dispersive nature of the tissue, whose behavior can be well described by the Cole-Cole model [11, 151, 134]. The point above the semicircle center corresponds to the dielectric cutoff frequency, also called Maxwell-Wagner frequency ($f_2 = \sigma/(2\pi\epsilon_r\epsilon_0)$ [207, 82, 11]), determined near 1 MHz in this measurement. Beyond this frequency, displacement current dominates, while ion migration and diffusion processes become negligible [207]. It is important to note that at such high frequencies, parasitic capacitances begin to contribute to the measured impedance spectrum and must be compensated to accurately extract the tissue properties [11, 134, 184].

Voltage-dependent impedance behavior Impedance spectroscopy was intentionally performed at several excitation amplitudes, including values higher than the commonly recommended limit ($\leq$ 100 mV), to investigate the voltage-dependent behavior of the load impedance.

Fig. 14 shows that at high frequencies ($\geq$ 10 kHz), the spectra for magnitude and phase are nearly identical across all excitation amplitudes. This similarity occurs because the voltage-dependent electrode-electrolyte interface is almost bridged, rendering the voltage dependence negligible in this regime. At lower frequencies (< 10 kHz for phase and < 1 kHz for magnitude), however, deviations become apparent. In this region, the influence of the electrode-electrolyte impedance becomes significant, thereby revealing its voltage-dependent nature. As the interface impedance decreases with increasing voltage, the magnitude of the impedance drops, and the phase shifts toward less negative values, indicating a transition toward more resistive behavior.

Nevertheless, for excitation amplitudes of 20 mV, 50 mV and 100 mV, the spectra almost

overlap even at low frequencies, suggesting that nonlinear faradaic reactions are negligible in this range. The overall observation is consistent with previous findings [82].

These results confirm that maintaining excitation amplitudes below ±100 mV effectively minimizes the probability of faradaic processes. This quasi-DC threshold therefore represents a well-defined electrochemical safety window for the DC bias voltage, corresponding to the limits targeted in charge balancing techniques [172, 198, 32, 218].

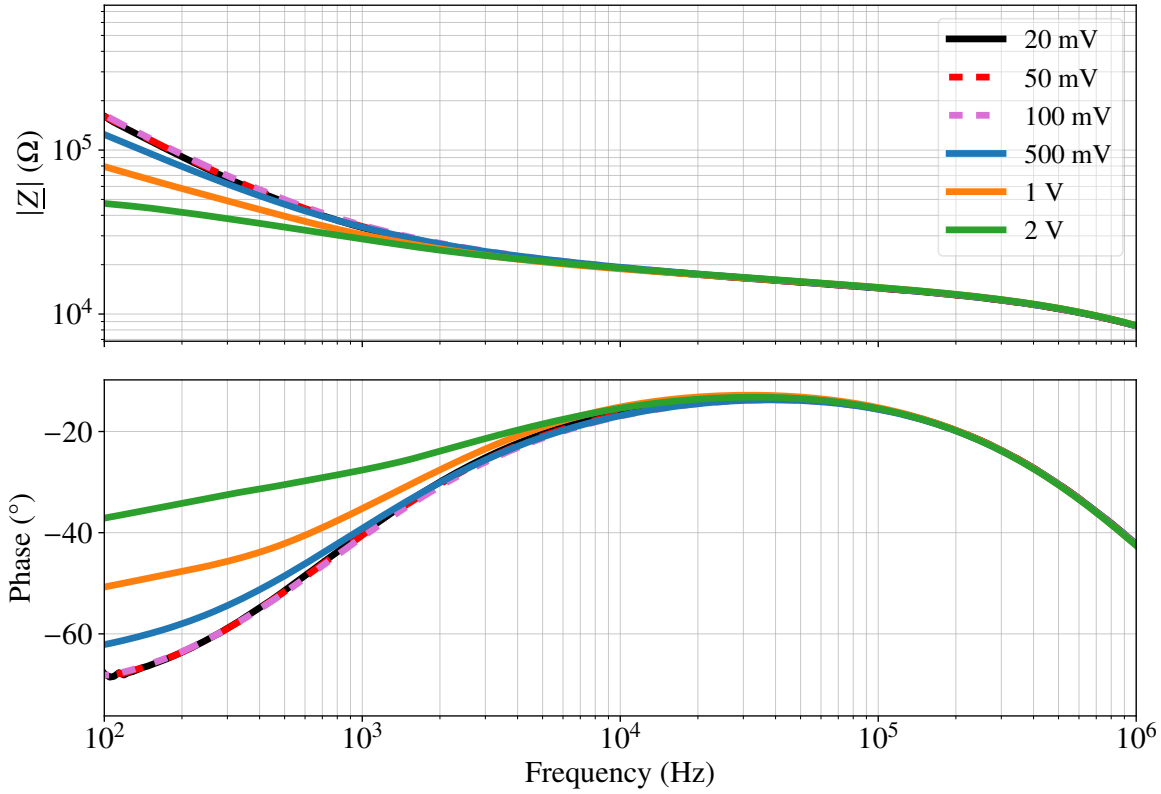

Figure 14: Impedance measurement in rat brain tissue using a PI-SNEX-100 microelectrode over the frequency range 100 Hz to 1 MHz, at excitation amplitudes of 20 mV, 50 mV, 100 mV, 500 mV, 1 V, and 2 V. The results illustrate nonlinear characteristics in the low-frequency range due to increasing faradaic reactions.

4.3.3 Equivalent Circuit Modeling and Parameter Extraction

A simple –CPE-R_{sol}– model was selected to describe the DBS voltage and current response because it offers a good trade-off between analytical simplicity and accuracy for this specific case.

The suitability of this model can be understood from the frequency spectrum of the stimulation signal. The frequency spectrum of a typical DBS pulse with a duration of 60 µs concentrates most of its spectral energy in the low- to mid-frequency range (following a $\mathrm{sinc}(f)$ envelope),

where the total impedance is dominated by the CPE element. Therefore, contributions from solution and parasitic capacitances can be considered negligible. Accordingly, model fitting was restricted to the frequency range where the Nyquist plot shows a linear characteristic corresponding to the CPE behavior (see Fig. 15). It should be noted that this approach is well-suited to the electrode types investigated here. However, for larger electrodes, where the cutoff frequency is considerably lower ($< 100\,\mathrm{Hz}$ [134]), the electrolyte component becomes a dominant part for DBS waveforms and may therefore not be neglected in the impedance model [258].

Parameter extraction was performed using the open-source Python package provided by [167], though alternative open-source impedance fitting tools are also available [18, 257]. The impedance of the PI-SNEX-100 in rat brain tissue was fitted using data from the 100 mV measurement to ensure that the impedance remained within the linear range (see Fig. 14). An additional impedance measurement at 100 mV was performed using the custom monopolar electrode in $0.1\,\mathrm{S\,m^{-1}}$ NaCl solution, following the same procedure. The fitted parameters for both configurations are summarized in Table 3. To facilitate electrotechnical comparability, the table lists the converted CPE parameters into an average double-layer capacitance, $\overline{C}_{\mathrm{dl}}$, according to Eq. 10.

The obtained CPE slope exponents agree well with previously reported values for platinum or platinum/iridium electrode contacts [11, 134, 77]. Likewise, the determined solution resistances show good agreement with earlier findings for electrodes of similar geometry immersed in electrolytes of comparable conductivity [11, 190]. Moreover, applying the theoretical expression from Eq. 6 to a monopolar hemispherical electrode with an assumed diameter of $310\,\mu\mathrm{m}$ in a $0.1\,\mathrm{S\,m^{-1}}$ electrolyte yields a solution resistance of $\approx 10.3\,\mathrm{k\Omega}$. This value is in reasonable agreement with the determined value of $\approx 7.8\,\mathrm{k\Omega}$, especially considering that the actual diameter of the electrode used in this experiment is not known.

Table 3: Fitted parameters from impedance measurements for a single bipolar PI-SNEX-100 in rat brain tissue and a single monopolar hemispherical electrode in $0.1\,\mathrm{S\,m^{-1}}$ NaCl solution.

Electrode Type	R_{sol} (kΩ)	Q ($\Omega^{-1}\mathrm{s}^{\alpha}$)	α	$\overline{C}_{\mathrm{dl}}$ (nF)
Bipolar (in brain tissue)	20.7	2.84×10^{-8}	0.84	6.9
Monopolar (in $0.1\,\mathrm{S\,m^{-1}}$ NaCl)	7.8	2.04×10^{-8}	0.89	6.8

4.4 Application of the Model to Passive Charge-Balanced DBS

This section applies the previously derived equivalent circuit model for the specific preclinical electrode-electrolyte setup to predict the voltage and current responses during passive charge-balanced DBS. Analytical expressions for both waveforms are developed based on the load

impedance model, parameterized using the fitted model parameters and stimulation settings, and subsequently validated against experimental DBS measurements. Additionally, the same model parameters are used to investigate the performance of the passive charge balancing mechanism, both with and without the inclusion of a blocking capacitor. Typically, passive charge balancing represents the standard charge balancing method in clinical DBS systems [186, 131] and is therefore implemented in the preclinical DBS platform *STELLA* proposed in this work (see Section 5). Accordingly, this investigation is essential to determine whether the bias voltage remains within the electrochemical safety limits for the targeted preclinical stimulation setup.

4.4.1 Deriving the DBS Waveforms

Analytical model Based on the equivalent –CPE-R_{sol}– circuit, the electrical behavior of both the DBS voltage and current waveforms can be analytically described.

For the current waveform, the CPE was reduced to an average double-layer capacitance, $\overline{C}_{\mathrm{dl}}$, leading to a simplified –$C_{\mathrm{dl}}R_{\mathrm{sol}}$– model, which captures the average charge storage. For the voltage waveform, however, the full CPE description was retained to reproduce the non-ideal charging behavior of the electrode-electrolyte interface.

The stimulation current, i_{DBS}, is modeled as an ideal constant current source with amplitude $\hat{I}_{\mathrm{stim}}$, applied for the duration of the stimulation pulse t_{stim}, and assumed to have an infinitely fast rise time. Passive charge balancing following the stimulation pulse is represented by an exponential decay of the reversal current, characterized by the time constant $\tau = R_{\mathrm{sol}}C_{\mathrm{dl}}$. Accordingly, the complete model for the stimulation current is given by:

$$i_{\mathrm{DBS}}(t) = \begin{cases} 0, & t < 0 \\ \hat{I}_{\mathrm{stim}}, & 0 \le t \le t_{\mathrm{stim}} \\ -\dfrac{\hat{I}_{\mathrm{stim}}\, t_{\mathrm{stim}}}{R_{\mathrm{sol}}C_{\mathrm{dl}}} \exp\left(-\dfrac{t - t_{\mathrm{stim}}}{R_{\mathrm{sol}}C_{\mathrm{dl}}}\right), & t > t_{\mathrm{stim}}\,. \end{cases} \tag{19}$$

The voltage across the load impedance is modeled as the sum of two components: (i) an ohmic drop across the solution resistance, and (ii) a fractional-order term represented by the CPE [127, 248]. Passive charge balancing is represented by an instantaneous return of the electrode voltage to zero following the stimulation pulse. The resulting model for the voltage waveform is therefore:

$$v_{\mathrm{DBS}}(t) = \begin{cases} 0, & t < 0 \\ R_{\mathrm{sol}}\, i_{\mathrm{DBS}}(t) \;+\; \dfrac{i_{\mathrm{DBS}}(t)\, t^{\alpha}}{Q\,\Gamma(\alpha+1)}, & 0 \le t \le t_{\mathrm{stim}} \\ 0, & t > t_{\mathrm{stim}}\,. \end{cases} \tag{20}$$

where Γ denotes the Gamma function.

Besides the analytical description, it should be noted that the –CPE-R_{sol}– model can also be implemented in SPICE circuit simulation tools. To achieve this, the CPE must be represented as an equivalent network of parallel RC branches, as demonstrated by the authors of [248], who provide a C program that converts the CPE parameters into the corresponding RC network SPICE code [70].

Stimulation setup Following the impedance spectroscopy, the same PI-SNEX-100 in rat brain setup was used to apply current-controlled pulses with a frequency of 130 Hz and a pulse duration of 60 µs with current amplitudes ranging from 50–200 µA in 50 µA steps. The same custom-built two-channel laboratory stimulator as introduced in Section 4.2 was connected.

Model vs. measurement The analytical model was parameterized using the load model parameters of the PI-SNEX-100 microelectrode and the same stimulation parameters as in the experimental setup. Fig. 15A,B compares the measured DBS waveforms (solid lines) in brain tissue obtained with the PI-SNEX-100 microelectrode (Electrode #5) and the predictions of the analytical model (dashed lines).

From the measurements, the stimulation current remains constant as expected from a constant current source, while the voltage initially shows a steep rise, followed by a charging phase of the electrode-electrolyte interface. At the end of each pulse, passive charge balancing (without interphase delay) shorts the electrode contacts to ground, producing a sharp reversal pulse that decays exponentially. Although the parameterized analytical model reproduces these main features with good accuracy, three main deviations can be observed:

(i) **Nonlinearity at higher current amplitudes.** As the current amplitude increases, the model increasingly overestimates the measured DBS voltage and shows rising deviation from the observed discharge behavior. This discrepancy arises because the electrode-electrolyte interface behaves nonlinearly at higher voltages. The main source of nonlinearity is the charge transfer resistance, R_{ct}, which decreases at higher voltages, thereby reducing the total impedance [152, 153]. Additionally, the discharge curve is

altered because less charge is stored on the double-layer capacitor, which results in a lower actual voltage across it prior to discharge.

(ii) **Bent voltage response.** Ideally, the voltage response should initially start with a vertical rise ($\hat{I}_{\mathrm{stim}} R_{\mathrm{sol}}$), and then increase almost linearly up the maximum stimulation voltage. However, the measured voltage shows only a relatively small initial onset, followed by a continuously bending increase throughout the pulse duration. For example, with $R_{\mathrm{sol}} \approx 20.7\,\mathrm{k\Omega}$, a $100\,\mu\mathrm{A}$ current would predict $\approx 2.1\,\mathrm{V}$, while the measured onset before bending starts is closer to $\sim 1\,\mathrm{V}$. This behavior is attributed to capacitive effects arising from the solution capacitance C_{sol} and parasitic capacitance C_{x} (see Fig. 4), which causes the initial voltage rise to bend away from the ideal vertical line. These effects were also confirmed by LTspice simulations, including such capacitances in the tens to hundreds of picofarads range. Nevertheless, the maximum stimulation voltage $\hat{V}_{\mathrm{stim}}$ is only marginally influenced by these capacitive contributions.

(iii) **Underestimation of reversal current amplitude.** The model underestimates the amplitude of the measured reversal pulse $\hat{I}_{\mathrm{passive}}$. This occurs because the model restricts the discharge current flow through the solution resistance only. In reality, the solution and parasitic capacitances also release their stored charge during passive charge balancing, which can briefly drive larger currents because no significant resistive limitation exists in the discharge path. Moreover, the measured reversal peak may still underestimate the true current due to bandwidth limits of the measurement device. Therefore, to mitigate excessive current spikes, it is advisable to include a relatively low-ohmic resistance in the discharge path when applying passive charge balancing.

Overall, for the $50\,\mu\mathrm{A}$ and $100\,\mu\mathrm{A}$ pulse targeted within the project (see Table 2), the –CPE-R_{sol}– model demonstrates excellent agreement with experimental measurements in predicting the quantities most relevant to stimulation circuit design, the maximum stimulation voltage and the discharge behavior.

It should be noted that the impedance was measured at an excitation amplitude of 100 mV to remain within the linear regime, since Fig. 14 shows that higher excitation amplitudes introduce nonlinear distortion, particularly below 1 kHz for the impedance magnitude. Nevertheless, the results indicate that the DBS voltage remains predominantly within the linear regime up to approximately 3 V. This can be explained by the spectrum of the DBS pulse, which spans a broad frequency range exceeding 1 kHz. These high-frequency components reduce the voltage-dependent contribution of the electrode-electrolyte interface, thereby shifting the beginning of nonlinear effects to significantly higher voltages than 100 mV. This behavior is advantageous for the model predictions, since it extends the DBS pulse voltage range where the linear impedance model remains accurate.

The bipolar PI-SNEX-100 microelectrode used here (Electrode #5) corresponds closely to

the mean of the maximum stimulation voltages obtained from 12 PI-SNEX-100 electrodes (see Fig. 13). Thus, the fitted model parameters can be regarded as representative for this electrode type for stimulation currents up to 100 µA at 60 µs. According to the monopolar electrode configuration, only very small deviations among the 11 tested electrodes were observed, suggesting that the fitted model parameters from a single microelectrode also reliably characterize this electrode type. These parameters, therefore, provide a solid basis for analyzing further stimulation aspects, such as the bias voltage development in passive charge balancing, as discussed in the following section.

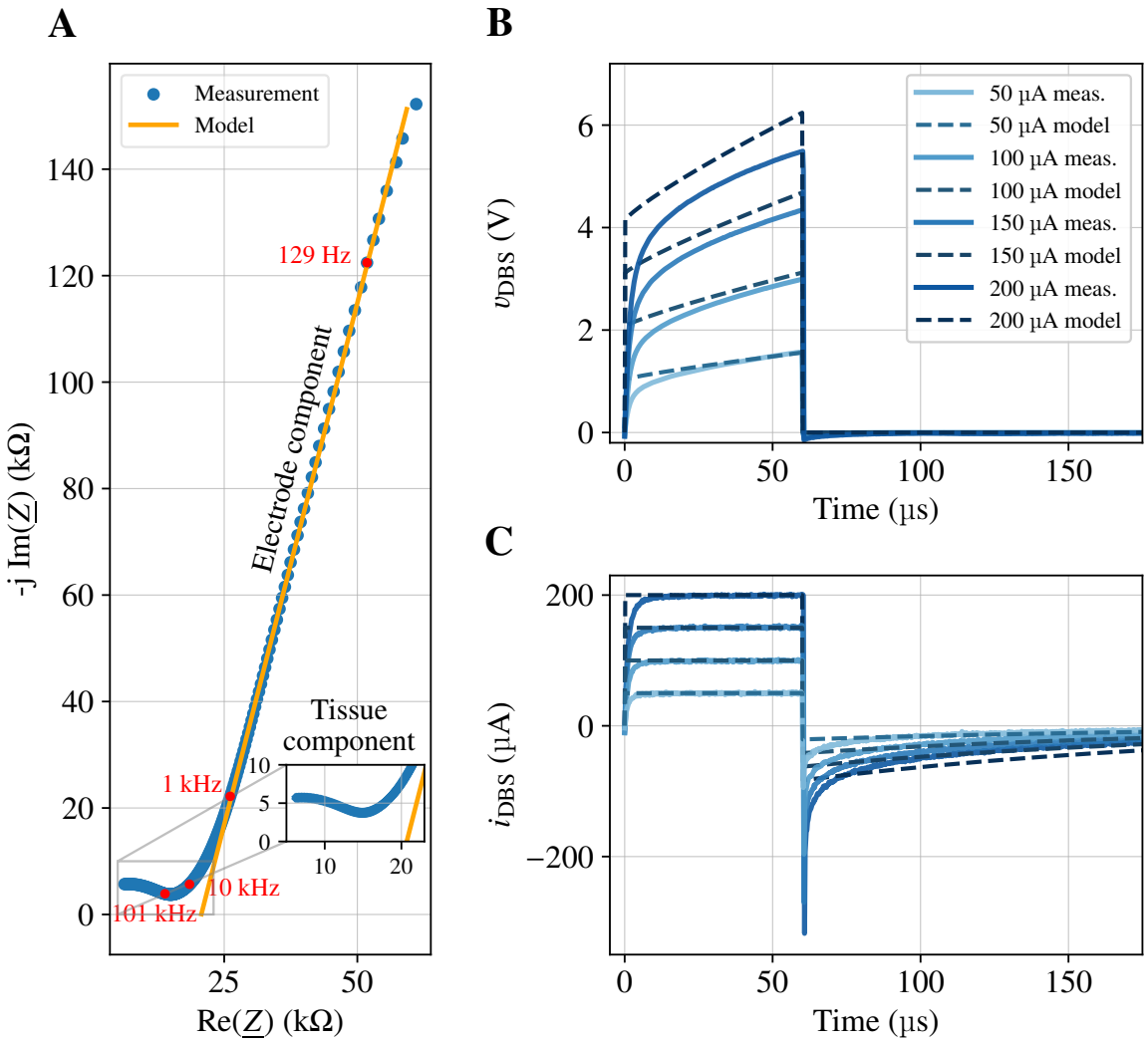

Figure 15: Extraction and validation of model parameters from impedance measurement performed in rat brain tissue using a PI-SNEX-100 electrode. (A) Nyquist plot of measured (blue dots) and modeled (orange line) impedance fitted with the –CPE-R_{sol}– model. (B) Voltage and (C) current waveforms during DBS for different current amplitudes (50 µA, 100 µA, 150 µA and 200 µA), where measured data (solid lines) are overlaid with model predictions (dashed lines). The model shows good agreement with the measured waveforms up to 100 µA, while deviations at higher amplitudes arise from voltage-dependent effects at the electrode-electrolyte interface.

4.4.2 Bias Voltage without Blocking Capacitors

When passive charge balancing is applied, it is essential to ensure that the double-layer capacitance is fully discharged between pulses to avoid accumulating a harmful residual (bias) voltage at the electrode-electrolyte interface. Ensuring that this bias voltage remains within the safe limits (±100 mV) is a critical criterion for device design. In this method, both electrodes are shorted immediately after the stimulation pulse, or following an interphase delay, and held in this state until the next pulse. Consequently, any bias voltage that may develop cannot be directly measured during this interval.

When no circuit approach is implemented to temporarily place an electrode contact in high-Z state prior to the next pulse, the load model $-C_{\mathrm{dl}}R_{\mathrm{sol}}-$ provides a suitable approach to predict the expected bias voltage.

Derivation of bias voltage expression The total charge delivered during stimulation is given by

$$Q_{\mathrm{stim}} = \hat{I}_{\mathrm{stim}} \cdot t_{\mathrm{stim}}. \tag{21}$$

During the passive discharge period, the charge removed is

$$Q_{\mathrm{passive}} = V_{\mathrm{Cdl}}(t_{\mathrm{stim}}) \cdot C_{\mathrm{dl}} \cdot \left(1 - \exp\left(-\frac{t_{\mathrm{passive}}}{R_{\mathrm{sol}}C_{\mathrm{dl}}}\right)\right), \tag{22}$$

where $V_{\mathrm{Cdl}}(t_{\mathrm{stim}})$ is the voltage across the double-layer capacitor at the end of the stimulation phase.

At steady-state, the bias voltage reaches equilibrium when the charge delivered during the stimulation pulse equals the charge removed during the discharge phase ($Q_{\mathrm{stim}} = Q_{\mathrm{passive}}$). Solving for the equilibrium bias voltage yields

$$V_{\mathrm{Cdl,bias}} = \frac{\hat{I}_{\mathrm{stim}} \cdot t_{\mathrm{stim}}}{C_{\mathrm{dl}}} \cdot \frac{1}{\exp\left(t_{\mathrm{passive}}/\left(R_{\mathrm{sol}}C_{\mathrm{dl}}\right)\right) - 1}. \tag{23}$$

This formulation is consistent with previous formulations [204].

The first term is the voltage drop across the double-layer capacitance from a single stimulation pulse, and the second term is the fraction of that voltage which maintains the steady-state bias because of incomplete discharge. In the case where the discharge phase is much greater than the RC time constant ($t_{\mathrm{passive}} \gg R_{\mathrm{sol}}C_{\mathrm{dl}}$), the exponential term dominates and the equilibrium bias voltage approaches zero.

When the derived load parameters for both electrode types (see Table 3) are applied under preclinically relevant stimulation settings of 100 µA, 60 µs and 130 Hz, the passive discharge interval exceeds the electrode-electrolyte time constant by more than an order of magnitude for either electrode type. As a result, the denominator in Eq. 23 becomes very large, such that the predicted steady-state bias voltage is effectively driven to zero, far below any electrochemically relevant threshold. This refers to a perfectly charge-balanced condition.

The safety limit of 100 mV would only be approached at very high frequencies above $\approx$ 2.5 kHz. Although kilohertz-range stimulation has been explored clinically, current evidence indicates poor efficacy [48].

Implications for device design The results gained for the bias voltage reveal that passive charge balancing is a valid tool for the safety of the specific stimulation setup used. Even when including a resistance of 1 kΩ at a typical stimulation frequency in the discharge path to limit the reversal peak current, the predicted bias voltage remains very low. However, it should be noted that, although the bias voltage remains low, adding a discharge resistance increases the time required to discharge the double-layer capacitance. This extended period increases the window during which unwanted electrochemical reactions could occur. Therefore, the need to reduce the current spikes must be weighed against the potential risk of maintaining higher voltages across the electrode-electrolyte interface over longer periods of time.

4.4.3 Bias Voltage with Blocking Capacitors

Blocking capacitors serve as the final protection barrier against a high DC voltage reaching the brain tissue. However, it has been analytically and experimentally shown by van Dongen et al. [57] that even under perfectly charge-balanced conditions, as is the case with the stimulation setup used here, a blocking capacitor can still cause a bias voltage.

Ideally, the blocking capacitor C_B and the double-layer capacitance C_{dl} would hold equal charge at the end of each constant current stimulation pulse. As a result, during the subsequent passive charge balancing phase, the time constant is given by

$$\tau = (C_B \parallel C_{dl}) R_{sol} \overset{C_B \gg C_{dl}}{\approx} C_{dl} R_{sol}. \tag{24}$$

As shown in Section 4.4.2, for typical stimulation setups, this time constant is considerably shorter than the duration of a typical passive discharge phase ($t_{passive}$), ensuring that both capacitors are fully discharged prior to the next stimulation pulse.

In practice, however, the finite charge-transfer resistance (R_{ct}) introduces a leakage path, resulting in a difference between the currents flowing through the two capacitors. Consequently, only a pseudo-steady state is reached, where $V_{Cdl} = -V_{CB} \neq 0$ [57]. The only

discharge path for the double-layer capacitor is through R_{ct} and since the associated time constant $\tau = C_{\mathrm{dl}} R_{\mathrm{ct}}$ is typically much longer than t_{passive}, a residual charge imbalance persists until the next stimulation pulse, which accumulates over many stimulation cycles until equilibrium is reached.

Van Dongen et al. derived an analytical expression for this steady-state bias voltage. Note that the published version contains an algebraic inconsistency in the final formula. The corrected expression is:

$$V_{\mathrm{Cdl,bias}}^{C_{\mathrm{B}}} = \frac{\frac{\hat{I}_{\mathrm{stim}} t_{\mathrm{stim}}^2}{C_{dl}} \left(\frac{1}{2}\zeta\eta^2 - \eta - \frac{1}{2} \right) - (1 - \zeta\eta)\hat{I}_{\mathrm{stim}} t_{\mathrm{stim}} R_{\mathrm{sol}}}{t_{\mathrm{stim}}(1+\eta) + t_{\mathrm{passive}}}. \tag{25}$$

The formula describes active charge balancing with an additional passive discharge phase. The parameters η and ζ describe the ratio of duration and amplitude between the stimulation and reversal pulse phases, respectively.

In the special case of pure passive charge balancing (i.e., no active reversal pulse, so $\eta = \zeta = 0$), the expression simplifies to:

$$V_{\mathrm{Cdl,bias}}^{C_{\mathrm{B}}} = \frac{\hat{I}_{\mathrm{stim}} \left(-\frac{t_{\mathrm{stim}}^2}{2C_{dl}} - R_{\mathrm{sol}} t_{\mathrm{stim}} \right)}{t_{\mathrm{stim}} + t_{\mathrm{passive}}}. \tag{26}$$

Note that the defined positive stimulation phase and corresponding negative charge balancing phase lead to a sign reversal compared to [57] (see Section 2.2.1 for details). When connecting the counter electrode to the blocking capacitor and the working electrode to ground (cathodic stimulation), the developed bias voltage drives the working electrode anodically.

When the derived load parameters for both electrode types (see Table 3) are applied under preclinically relevant stimulation settings of 100 µA, 60 µs and 130 Hz, the predicted steady-state bias voltages are approximately −20 mV for the bipolar electrode and −10 mV for the monopolar electrode. These values could be confirmed via LTspice simulations.

According to these results, the use of a blocking capacitor would appear safe, since the values remain well within the ±100 mV safety range. However, van Dongen et al. also noted that the linear model tends to underestimate the measured bias voltage when nonlinearities become significant. Therefore, final verification should always be performed experimentally for the actual stimulation setup. Accordingly, the following paragraphs evaluate the actual bias voltage for the targeted stimulation setup.

Experimental setup To assess the actual bias voltage, the stimulation device described in Section 4.2 was used again, but this time a 4.7 µF blocking capacitor was integrated between the stimulation output and counter electrode (cathodic stimulation). Passive charge balancing was performed at the stimulation output node, such that the blocking capacitor represented the final element before the electrode.

Stimulation parameters were set to 130 Hz, 60 µs pulse duration and current amplitudes between 50–200 µA in 50 µA. All experiments were carried out in a temperature-controlled 0.1 S m^{-1} NaCl solution at 25 °C. Measurements were recorded after the bias voltage reached its steady state, which typically required approximately one hour.

It is important to note that the bias voltage was measured via a high-impedance unity-gain buffer to avoid loading effects (see Appendix E). Furthermore, since direct measurement of the double-layer voltage is not possible, $V_{\text{bias,tot}}$ serves as a representative indicator.

Bias voltage results Fig. 16A shows a representative waveform for the monopolar configuration, showing a significant negative bias voltage indicated by a downward shift of the signal to nearly a half volt. Fig. 16B quantifies the measured bias voltages for both electrode configurations across the current amplitude range in bar charts. It shows that for a monopolar configuration, the bias voltage was −235 mV for the lowest amplitude of 50 µA, and became more negative with increasing current amplitudes, reaching −433 mV at 200 µA. The bipolar configuration exhibited a comparable behavior, with the bias voltage decreasing from −220 mV to −440 mV over the same current range.

Overall, the measurements reveal a bias voltage an order of magnitude higher than predicted by the linear analytical model. This confirms that the theoretical assumption is not valid under realistic stimulation conditions. The ±100 mV safety range was exceeded even for the lowest current amplitude of 50 µA. Paradoxically, the blocking capacitor, which is intended to enhance safety, now introduces a potential safety risk.

To exclude the possibility that the observed effect resulted from a galvanic effect due to the use of different metals in the specific electrode configuration (platinum vs. gold in the monopolar configuration, Pt/Ir vs. stainless steel in the bipolar configuration), measurements were repeated using two monopolar electrodes, each consisting of a platinum core. One electrode served as the working electrode and the other as the counter electrode. The observations confirmed that, even under these conditions, a bias voltage still developed.

Therefore, when no other safety mechanisms can be integrated to protect the brain from hardware/software failures, additional measures must be implemented to ensure that the bias voltage caused by the blocking capacitor remains within a safe range. Both active compensation techniques and passive discharge paths implemented through switches could, in principle, mitigate this effect. However, all such approaches require bypassing the blocking

capacitor, thereby reintroducing an unprotected fault path and thus negating the safety purpose of the blocking capacitor itself [57]. Consequently, an alternative solution was sought.

A simple but effective approach During measurement, an interesting observation led to a new approach. When the bias voltage was measured against the 1 MΩ input impedance of the oscilloscope only, instead of the high-impedance buffer stage, the observed bias voltage began to decrease.

Motivated by this finding, a simple modification was introduced by connecting a 10 MΩ resistor in parallel with the electrode contacts. The previous measurements were then repeated using the same electrodes and procedures, this time again using the buffer stage to record the true bias voltage. The resistance value of 10 MΩ was chosen so that it represents only a negligible external leakage path for the stimulation current. Even at the highest stimulation voltages observed, around 4 V for bipolar electrodes during a 100 µA / 60 µs pulse (see Fig. 13), the resulting leakage current would amount to only 0.4 % of the nominal current amplitude.

The effect of this modification is also illustrated in Fig. 16A,B. Panel A illustrates that, with the added resistor, the previously observed negative bias voltage in the monopolar configuration almost completely disappears. Panel B quantifies it for both electrode configurations across all current amplitudes, demonstrating that the inclusion of the discharge resistor considerably reduced the bias voltage. For instance, at 100 µA, the monopolar bias voltage was reduced from about −310 mV to nearly −10 mV, and the bipolar bias voltage from −261 mV to −64 mV.

This behavior is assumed to be introduced by the new discharge time constant

$$\tau \approx C_{\mathrm{dl}}(R_{\mathrm{ct}} || R_{\mathrm{ext}}), \tag{27}$$

where R_{ext} represents the high-ohmic external discharge resistor. The equivalent circuit is shown in Fig. 16A. The observations led to the assumption that 10 MΩ $< R_{\mathrm{ct}}$, such that the total resistance decreases, allowing faster discharge of C_{dl} after reaching the pseudo-steady state and therefore stabilization at a lower bias voltage.

For this maximum current amplitude used within the project scope (see Table 2), the measured bias voltages remained within the ±100 mV safety window. However, these results were obtained from a limited *in vitro* setup using only two electrodes of each type and therefore cannot be considered conclusive. These findings nevertheless indicate that introducing a high-ohmic 10 MΩ discharge resistor can substantially reduce the bias voltage and may represent a promising direction for further investigation under more representative experimental conditions.

Results The results demonstrate that the analytical model significantly underestimates bias voltages due to the nonlinear electrode-electrolyte interface. However, introducing a high-ohmic discharge resistance of 10 MΩ in parallel with the electrode contacts provides a simple yet effective way to mitigate this issue. Although further long-term validation is needed *in vivo*, the findings clearly indicate that such a discharge path can maintain a safe electrochemical window.

Blocking capacitors are widely used as a protective measure against fault conditions in neurostimulation systems [52]. Their use ranges from research devices for rodents [67, 117, 119, 162, 187] to clinical systems such as the Medtronic Activa® PC neurostimulator [131]. Despite their use, the electrochemical consequences of the bias voltage that can arise remain insufficiently characterized. Specifically, the studies on rodent DBS devices do not report investigations aimed at identifying such bias voltage, and the devices themselves do not incorporate mechanisms to suppress it. In light of the present findings, these gaps may pose potential electrochemical safety concerns.

The findings further highlight that accurate characterization requires high-impedance instrumentation ($> 1\,\mathrm{G\Omega}$). Otherwise, the measurement setup itself provides a discharge path that suppresses the observed bias voltage. This likely explains why bias voltages have remained unreported in other studies of neurostimulation devices.

To the best of current knowledge, this work presents the first systematic investigation of blocking-capacitor-induced bias voltage using microelectrodes. Previous work addressing this effect has focused only on large clinical electrodes ($14\,\mathrm{mm^2}$) examined by van Dongen. The electrodes investigated here have active areas two orders of magnitude smaller ($0.151\,\mathrm{mm^2}$ and $0.0784\,\mathrm{mm^2}$).

Implications for device design Blocking capacitors provide DC isolation but can lead to the development of a bias voltage over time, potentially introducing electrochemical effects. Early STELLA generations relied solely on blocking capacitors and did not include a dedicated discharge path, reflecting common practice in neural stimulator design. As this finding was obtained only at a later stage of development, an additional 10 MΩ discharge resistor was first incorporated in the latest revision of STELLA3 presented in this work. The same feature is also integrated into the STELLA4 device.

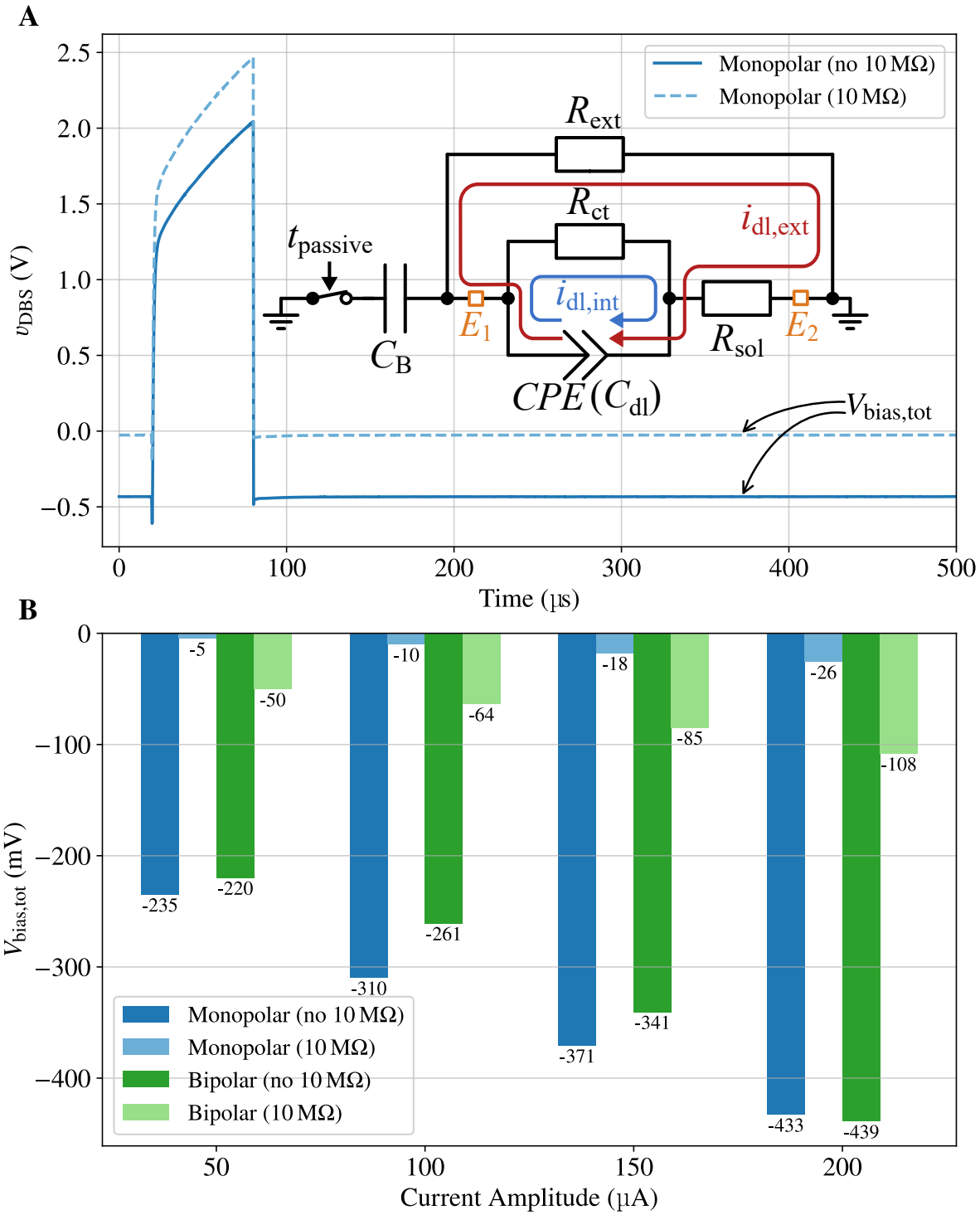

Figure 16: Bias voltage measurements with and without compensation using an external 10 MΩ resistor. (A) Representative waveform of the monopolar electrode at a stimulation setting of 200 µA, 60 µs, and 130 Hz, illustrating the total bias voltage induced by the blocking capacitor as a downward shift of the signal. The inset shows the corresponding equivalent circuit, highlighting the discharge of the double-layer capacitance through both the intrinsic R_{ct} and the externally added resistor R_{ext} after the pseudo-steady state is reached. (B) Steady-state bias voltages for monopolar and bipolar electrodes at different current amplitudes, measured with and without compensation using the external 10 MΩ resistor.

4.5 Interim Conclusion

This section provided a detailed investigation of the electrode types used in the project under preclinical DBS conditions. By combining impedance spectroscopy, analytical modeling, and both *in vitro* and *ex vivo* measurements, the electrical characteristics of the hemispherical monopolar and the bipolar PI-SNEX-100 electrodes were thoroughly analyzed.

The maximum stimulation voltage measurements demonstrated clear differences between the two electrode types. The bipolar electrodes required higher voltages and exhibited greater variability, while the monopolar electrodes showed lower spread and more consistent behavior. Overall, the maximum stimulation voltage increased with the stimulation amplitude but followed a nonlinear trend, reflecting the voltage-dependent charge-transfer resistance. Based on these findings, appropriate compliance voltage values were defined to ensure a stable constant current delivery without unnecessary power overhead. Furthermore, the data indicate that a $0.1\,\mathrm{S\,m^{-1}}$ NaCl solution provides a reasonable *in vitro* model for emulating *in vivo* conditions.

Impedance spectroscopy confirmed the expected frequency- and voltage-dependent behavior of the electrode-electrolyte interface, in which electrode-electrolyte interactions dominate at low frequencies, while electrolyte-specific properties become significant at higher frequencies. Nonlinear effects were observed only above excitation amplitudes of about 100 mV, supporting this value as a practical electrochemical safety limit for the bias voltage. Based on the analysis of impedance measurements, an equivalent circuit in the form of –CPE-R_{sol}– was derived, tailored to capture the essential electrical characteristics of the load impedance. The fitted parameters showed good agreement with literature values.

From this equivalent circuit, an analytical description of passive charge balanced DBS was developed and validated against measurements obtained with the bipolar PI-SNEX-100 electrode. The parameterized PI-SNEX-100-model accurately predicted the voltage and current waveforms up to 100 µA, capturing both the maximum stimulation voltage and the exponential discharge behavior. However, for higher injected charges, nonlinear effects become significant, causing the linear model to overestimate the maximum stimulation voltage and distort the discharge characteristics. In addition, the model showed deviations in the voltage rise and underestimated the reversal current peaks, both of which can be attributed to additional capacitances that were neglected in the model description.

Further analyses using the model parameters were performed to evaluate passive charge balancing regarding a potential bias voltage development for the intended stimulation setup. The results showed that, for both electrode types and the most common stimulation parameters, passive charge balancing without blocking capacitors effectively removed residual charge between pulses, resulting in no measurable bias voltage. However, when a blocking capacitor

was introduced, significant negative bias voltages developed, driving the working electrode anodically by several hundreds millivolts, thereby exceeding the ±100 mV safety range for both electrode types. While this phenomenon had previously been investigated only for larger, clinical electrodes [57], the present findings confirm for the first time that similar effects also occur under preclinical settings. Conventional compensation techniques require bypassing the blocking capacitor, thereby negating its safety function. In contrast, the approach presented here introduces a simple yet novel solution by adding a high-ohmic resistor (10 MΩ) in parallel with the electrode contacts. This modification allows an additional discharge path for the blocking capacitor-induced charge mismatch, reducing the bias voltage to within electrochemical limits without impairing stimulation performance or the blocking capacitor's intended role.

In summary, this study forms the basis for designing the stimulation unit presented in the next section, which is tailored to the project's specific preclinical DBS setup (see Table 2). A systematic analysis combining experimental measurements and modeling approaches enabled the identification of important parameters that ensure electrochemical safety and determine the required compliance voltage without unnecessary power overhead. These results address a critical gap in the state of the art, where existing DBS devices lack a validated characterization of the load impedance under realistic conditions.

5 Design and Implementation of a Flexible DBS Platform: STELLA

5.1 Introduction to the STELLA Family

The review in Chapter 3 revealed that current DBS devices for rodents restrict important methodological approaches, meaning that several relevant research questions cannot be addressed with the available technology. To bridge these methodological gaps, a novel DBS research platform was developed, called **STELLA** – an acronym for *Software-Defined Implantable Platform*.

The STELLA family comprises a series of implantable DBS devices specifically designed for reliable and flexible DBS research in rodents while minimizing the physical burden on the animals through compact and lightweight implantable designs. Each iteration introduces significant enhancements over its predecessor. A key design choice across all STELLA versions is the exclusive use of commercially available discrete components, because it offers maximum flexibility for modifications and extensions while maintaining reproducibility.

The design process began with the analysis of existing preclinical DBS devices, from which circuit concepts such as those presented in [67] served as the starting point for the STELLA platform. All STELLA versions were initially developed on breadboards to enable rapid iteration and testing. In cases where no commercial development boards were available for the required IC, these parts were manually soldered onto adapters for breadboard compatibility. Considerable time was spent identifying suitable ICs, as they had to provide the required functionality, a small footprint, and an ultra-low power consumption. Only very few components, and in some cases just a single part, fulfilled all of these criteria. Once the hardware prototype was finalized, it was transferred to a printed circuit board (PCB) design using EAGLE software (Autodesk, USA), with a particular focus on minimizing the PCB footprint.[6]

The evolution of STELLA is shown in Fig. 17. The first version, STELLA1.0, served as proof of concept, enabling single-channel DBS with basic functions. STELLA2.0 marks a major advancement as the first fully implantable version, successfully demonstrated in [176]. STELLA3.0 represents a milestone in the roadmap, being the first version to combine dual-channel functionality, a built-in self-test mechanism, and a significantly reduced power consumption. When combined with an RF extension module, it becomes STELLA3.1,

[6]From STELLA version 2.1 onwards, the PCB layouts were created by the author in collaboration with Uwe Knüpfer (Uwe Knüpfer Data Transfer, Germany, Königs Wusterhausen). Prior to version 2.1, the PCB layouts were implemented solely by the author. Dirk Timmermann provided general guidance on the overall concept and form factor of the PCBs. PCB assembly was carried out by Dorazil Mikro-Elektronik GmbH (Berlin, Germany), which supported the production process across all STELLA versions.

enabling energy-efficient wireless communication with external devices. STELLA4.0 (also known as STELLA+) is the latest version and stands as the family's highlight, offering a unique and advanced feature set, such as closed-loop capabilities, in comparison to all other modern preclinical DBS devices for rodents. Table 4 summarizes the key features, release dates, and publication years for each version.

STELLA versions 3.0, 3.1, and 4.0 have been extensively evaluated *in vitro*, *ex vivo* and *in vivo* and represent the family's most suitable platforms for preclinical DBS research in rodents. Accordingly, these versions are the primary focus of this section. For simplicity, they are referred to herein as STELLA3, STELLA3.1, and STELLA4. For an overview, the detailed device specifications are provided in Appendix C.

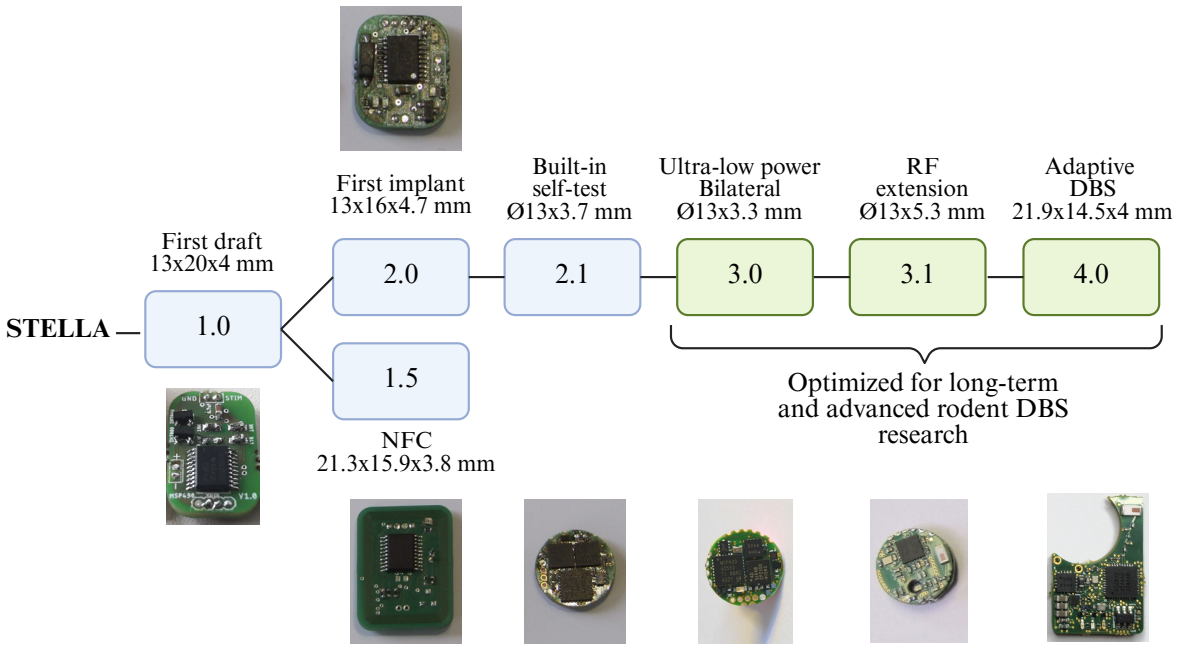

Figure 17: Evolution of the STELLA family across multiple design generations for DBS research in rodents, progressing from the first basic prototype to the advanced STELLA4.0 system. Each version builds on the strengths of its predecessor.

Table 4: STELLA version history summarizing major design features, release years, and related publications.

Version	**Key Features**	**Release Date**	**Published Design**
1.0	Initial prototype, single-channel	2018	-
1.5	Exploratory NFC extension (not continued)	2019	-
2.0	Reduced area (rectangular shape), for the first time fully implanted *in vivo*	2020	-
2.1	Further area reduction (circular shape), built-in self-test	2020	-
3.0	Significantly reduced power consumption, dual-channel	2021	[A10]
3.1	2.4 GHz RF extension module for 3.0	2021	[A14]
4.0	On-implant biosignal acquisition and processing, improved RF communication via Bluetooth Low Energy, adaptive DBS, rechargeability via electrode leads	2024	[A13]

5.2 Realizing a Highly Miniaturized DBS Device: STELLA3



Photograph by the IT and Media Centre of the University of Rostock.

STELLA3 represents the third version of the STELLA family and was developed to enable chronic, bilateral DBS research in small, freely moving rodents. This version marks a milestone in the STELLA family roadmap, as it was the first with dual-channel functionality and a significantly reduced power consumption. The design, implementation, and evaluation of STELLA3 are presented in detail in this chapter and have been partly published in [A11] and [A10].[7]

5.2.1 System Overview

STELLA3's architecture is organized into four units: power, control, stimulation, and monitoring. The overall circuit schematic is shown in Fig. 18.

The power unit comprises a boost converter (MAX17220) to step up the battery voltage (V_{Bat}) to the system supply voltage (V_{DD}). Additionally, the microcontroller's internal analog-to-digital converters (ADCs) digitize both the battery and system voltages, and n-channel MOSFETs (T_1,T_2) prevent continuous current draw through the voltage divider circuits. The control unit, built around an MSP430G2553 [166], coordinates the interaction of all modules. It configures stimulation and monitoring functions via six 100 kΩ digital potentiometers (AD5142/AD5144) using the Serial Peripheral Interface (SPI) bus. The stimulation unit provides two independent current-controlled channels that enable bilateral DBS. Stimulation pulses are generated by toggling pnp BJT current sources via a pulse-width modulation (PWM) signal from the MSP430, which delivers constant current pulses to the

[7]The author defined the system architecture, designed the circuit schematic, built and tested the hardware prototypes, and implemented the firmware of STELLA3. Dirk Timmermann and Christoph Niemann provided technical input to support design decisions. The built-in self-test (BIST) for stimulation monitoring was jointly developed by the author and Christoph Niemann. The *in vitro* experiments and other technical characterizations of STELLA3 were conceptualized, carried out, and analyzed by the author. The *in vivo* data presented in this work, conducted with STELLA3, were obtained by Maria Kober and Anika Lüttig. Dirk Timmermann, Mareike Fauser, Denise Franz, Rüdiger Köhling, Angelika Richter, and Alexander Storch provided the resources for this research.

load impedances ($\underline{Z}_1$, $\underline{Z}_2$). Each channel includes passive charge balancing via open-drain inverters (SN74AUP1G06) to avoid harmful charge accumulation and blocking capacitors to prevent a prolonged, high voltage bias across the electrode terminals. The monitoring unit integrates a Hall sensor (DRV5032AJ), two operational amplifiers (TLV9002S), and a variable reference voltage (V_{Ref}) via a digital potentiometer to detect short circuits, open circuits, and compliance voltage violations (BIST, Built-in Self-Test). Results of the BIST are reported through LED blink codes. In addition, a discharge resistor incorporated in parallel with the electrode contacts for each channel mitigates the bias voltage induced by the blocking capacitors.

All design files, including hardware, software, and documentation are available open-source in the repository [194], and represent the latest version of STELLA3 corresponding to the circuit schematic shown in Fig. 18.

5.2.2 Current-Controlled Pulse Generation

This section details how current-controlled stimulation pulses are generated.

Current source architecture STELLA3 supports bilateral stimulation via two current-controlled output channels, each equipped with an adjustable current source. To maintain a constant current during the entire pulse duration, a compact commercial IC (PSSI2021SAY, Nexperia) was selected. This IC integrates a pnp bipolar junction transistor (T_1) with two diodes (D_1 and D_2) connected to its base. This configuration creates a classic BJT current source, where the reference voltage is formed by two diodes (compare with Fig. 7A). A resistor (R_{B}) connects the transistor's base to a dedicated IC pin, enabling external control of the current source. When this pin is pulled to V_{DD}, the current source is deactivated, resulting in a high-impedance collector output. In contrast, pulling the pin to GND activates the current source, allowing a defined constant current to flow through the load. By applying a PWM signal to this control pin, the output current is switched on and off according to the PWM timing. The internal architecture and external circuitry are illustrated in Fig. 19A. Both current sources are driven by a PWM signal generated by the MSP430 microcontroller. The PWM signal defines the frequency and pulse duration of the stimulation pulses with high timing accuracy (see Section 5.2.5). Since both current sources are controlled by the same PWM signal, the stimulation for both channels is synchronized. For unilateral application, one output can simply remain unconnected.

Software-adjustable current amplitude The stimulation current amplitude is determined by the voltage across the emitter resistor ($V_{\mathrm{E}} \approx 0.7\,\mathrm{V}$) and its resistance value (compare to Eq. 14). The IC includes an internal resistor $R_{\mathrm{Int}} \approx 52.8\,\mathrm{k\Omega}$ in the emitter path. To allow current adjustment, an external resistor can be connected in parallel using a dedicated pin.

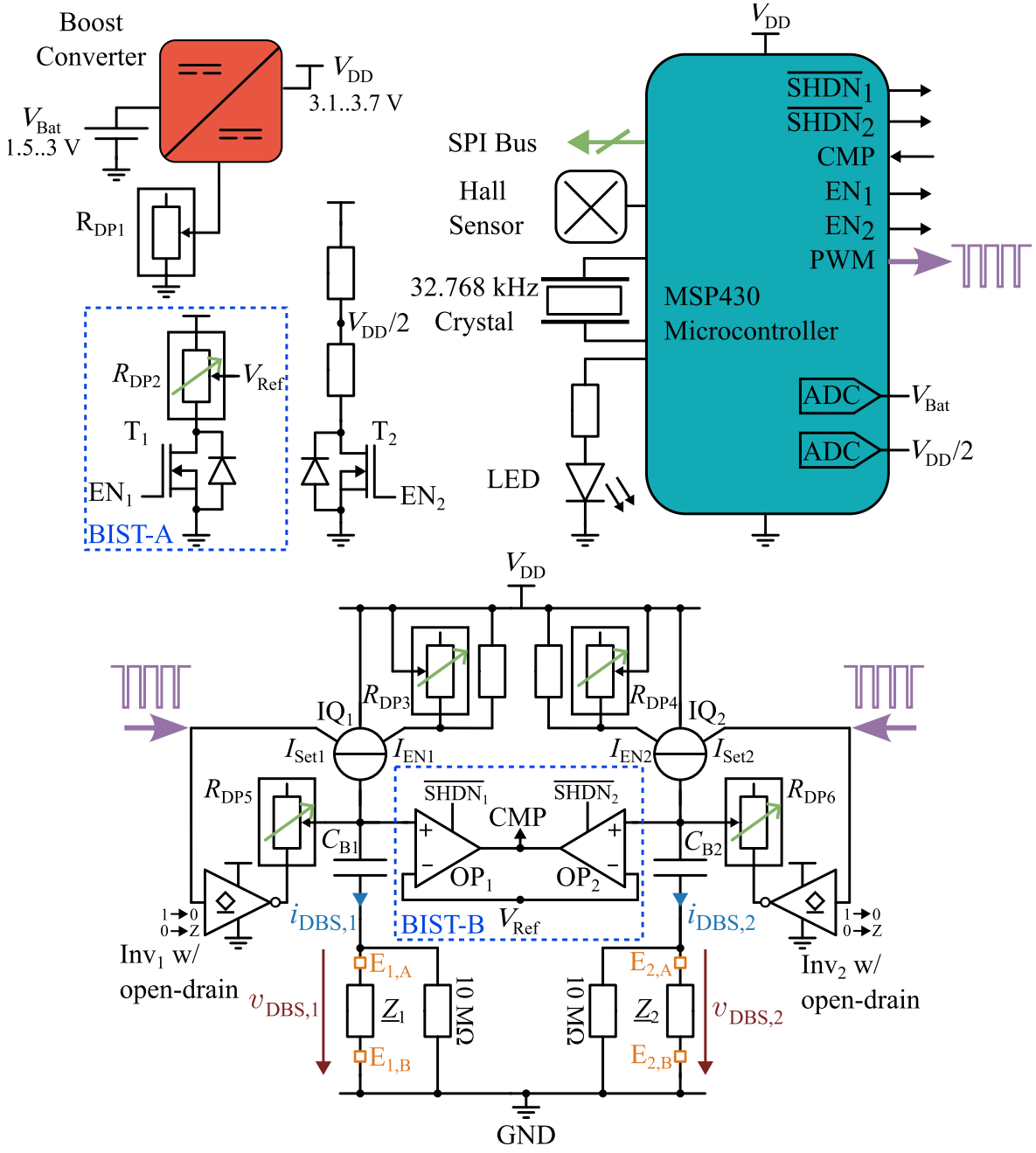

Figure 18: Circuit schematic of STELLA3. The device features two current-controlled stimulation channels with passive charge balancing. A boost converter raises the battery voltage to a stabilized system voltage. An MSP430G2553 microcontroller coordinates parameter settings and monitoring functions. Adapted from [A10].

In STELLA3, an 8-bit digital potentiometer (AD5142), configured in rheostat mode, is used for this purpose. Its resistance is given by

$$R_{DP} = \frac{D}{2^n} \cdot R_{AB} + R_W, \tag{28}$$

where D is the decimal equivalent to the binary code, R_{AB} is the end-to-end resistance of the digital potentiometer and R_W is the wiper resistance (typically 130 Ω). The total emitter resistance R_E is thus defined by the parallel combination of R_{DP} and R_{Int}, allowing software-controlled adjustment of the stimulation current amplitude.

Achievable current range and resolution LTspice DC operating point simulations using the PSSI2021SAY's SPICE model (provided by Nexperia) were used to evaluate the relationship between the digital potentiometer code and output current amplitude. Fig. 19B shows that the output current follows a hyperbolic curve, resulting from the inverse dependency on the emitter resistance (see Eq. 14). As a result, resolution is high at lower currents and becomes coarse at higher levels.

Using a digital potentiometer with $R_{AB} = 100\,\text{k}\Omega$, this configuration achieves a minimum output current amplitude of 21 µA, with precise settings at 50.38 µA and 101.64 µA. These values closely match the ELAINE project's stimulation targets of 50 µA (for the dt^{sz} hamster model) and 100 µA (for the 6-OHDA rat model) (see Table 2). In practice, however, component tolerances prevent such exact values from being reliably achieved. Therefore, fine resolution around the target values is necessary to allow for precise device calibration, ensuring consistent stimulation current across devices.

Fig. 19C shows the resulting current amplitude resolution, where each colored vertical line represents a specific resolution interval. With $R_{AB} = 100\,\text{k}\Omega$, sub-µA resolution is obtained around 50 µA, while the resolution interval around 100 µA is $[3, 5)$ µA. Since resolution around 50 µA was already sufficient, the focus was on increasing the resolution around 100 µA. To achieve this, a 30 kΩ resistor was added in parallel (R_P) with the digital potentiometer ($R_{DP,100k\Omega} \parallel 30k\Omega$). This modification increases the minimum output current to 42 µA but improves resolution around 100 µA, achieving a finer resolution interval of $[3, 5)$ µA compared to the previous $[2, 3)$ µA (see Fig. 19C).

Beyond the requirements within the project scope, other experimental protocols may demand different current amplitude ranges. The typical current amplitude range for movement disorder models according to Fig. F.1 is 30–200 µA. However, the results in Fig. 19B,C show that achieving high resolution across this entire range with a single digital potentiometer and a parallel connected resistor is not feasible. For example, using 14 kΩ or 9 kΩ resistors allows for finer resolution at higher currents, but shifts the minimum achievable current upwards. Thus, selecting the parallel resistor involves a trade-off between minimum achievable current amplitude and resolution at higher levels, and must be adapted to the specific experimental needs. Further flexibility can be achieved by selecting digital potentiometers with lower end-to-end resistance values.

In a nutshell, the selected configuration ($R_{DP,100k\Omega} \parallel 30k\Omega$) provides high resolution near the

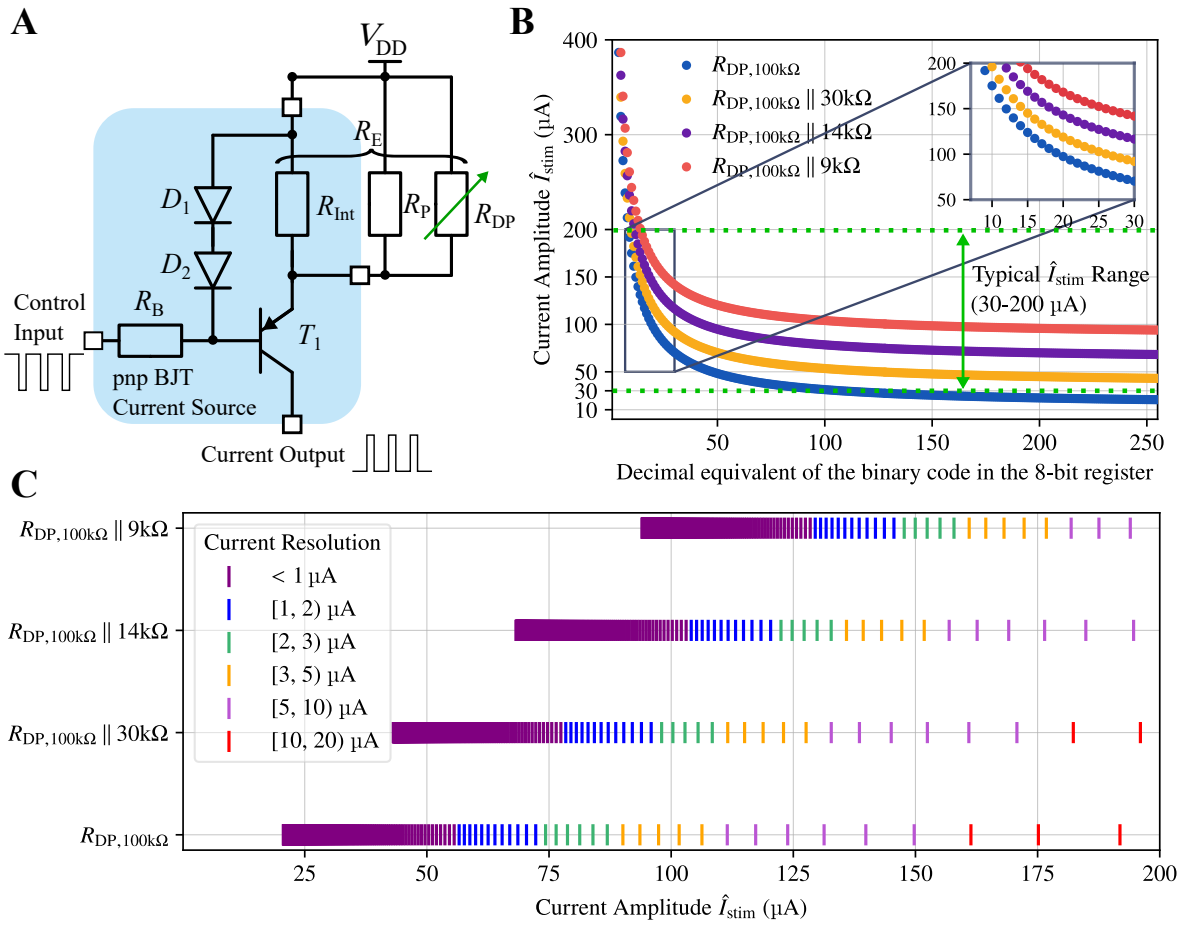

Figure 19: (A) Architecture of the current source IC (PSSI2021SAY) with external circuitry. (B) LTspice DC operating point analysis using the SPICE model of the PSSI2021SAY at V_{DD} = 3 V. The output current is simulated as a function of the digital potentiometer resistance by sweeping a resistor in 100 kΩ / 256 increments. The x-axis shows the corresponding digital code mapped from the swept resistance value. Curves for different parallel resistor values (30 kΩ, 14 kΩ, 9 kΩ) illustrate their effect on the output current. (C) Corresponding current resolution for each configuration, illustrating trade-offs between minimum current and current resolution.

target currents of 50 µA and 100 µA, thereby fulfilling the requirements within the project (see Table 2). Therefore, this configuration was chosen for both stimulation channels in STELLA3. For other currents or current ranges, both the parallel resistor and the digital potentiometer must be chosen accordingly before PCB fabrication. This limitation was addressed in STELLA4 by implementing a more flexible approach (see Section 5.9.7).

5.2.3 Charge Balancing and Safety

Passive charge balancing has been verified as safe for the stimulation setup used within the project (see Section 4.4.2), provides the most area- and energy-efficient charge balancing approach (see Section 2.2.5), and is also implemented in clinical DBS devices [186, 131]. Therefore, it was adopted across the STELLA family, including STELLA3.

To achieve this, the PWM signal that is used to activate and deactivate the current sources is simultaneously utilized to control the input of an inverter with an open-drain output. When the current source is activated, the output of the inverter transitions to a high-impedance (high-Z) state, whereas the inverter output shorts both electrode contacts (E_1 and E_2 connected to GND) when the current source is deactivated. Furthermore, this design also takes advantage of the use of a single PWM signal, which is particularly advantageous for microcontrollers with a small footprint, resulting in limited I/O ports. However, this design inherently precludes the implementation of an interphase delay. Consequently, in STELLA3, v_{DBS} is directly pulled to ground at the end of each pulse, differing from the waveform produced by the Activa® PC neurostimulator (see Fig. 4). Based on [160], the absence of an interphase delay may require a higher injected charge due to the higher reversal current spike, while potentially reducing tissue damage and electrode corrosion through faster charge reversal (see Section 2.2.4 for more details). To provide control over the current spike, adjustable resistances (R_{DP5} and R_{DP6}) implemented via digital potentiometers in rheostat mode are integrated into the discharge path of each channel in STELLA3. While this approach effectively reduces the current spike, it also extends the discharge time of the double-layer capacitance. Therefore, the resistance value must be carefully selected. Increasing the discharge resistance slows the reversal of electrochemical products and may risk incomplete discharge of the double-layer capacitance before the next stimulation pulse. Since this trade-off has not yet been investigated in this work, the digital potentiometers were set to their minimum resistance, which corresponds to approximately 130 Ω.

Finally, a blocking capacitor was incorporated for each channel to prevent dangerous DC voltages across the electrodes arising from hardware or software failures. Please note that the initial revisions, including the version published in [A10], did not include a compensation mechanism to mitigate the blocking-capacitor-induced bias voltage, reflecting common practice in neurostimulator designs. After additional insights were gained (see Section 4.4.3),

the discharge resistor was introduced first in the latest revision of STELLA3 as an additional safety measure.

5.2.4 Built-in Self-test for Stimulation Monitoring (BIST)

The method presented in this section provides a discrete, energy- and area-efficient solution suitable for microcontroller-based systems.

Approach The approach takes advantage of current-controlled stimulation, in which the voltage across the electrodes reveals the fault conditions. If $\hat{V}_{\text{stim}}$ approaches the compliance voltage V_{Compl}, a constant current cannot be maintained, signaling an excessive load impedance. In contrast, an unusually low $\hat{V}_{\text{stim}}$ suggests a short circuit. To detect these faults, an operational amplifier is configured as a comparator, comparing the stimulation voltage v_{DBS} to a programmable reference voltage V_{Ref}. With v_{DBS} applied to the non-inverting input and V_{Ref} to the inverting input, the comparator output V_{CMP} transitions high when v_{DBS} exceeds V_{Ref}. By stepwise lowering V_{Ref} in each pulse period, the transition point reveals the maximum stimulation voltage $\hat{V}_{\text{stim}}$ (see Fig. 20).

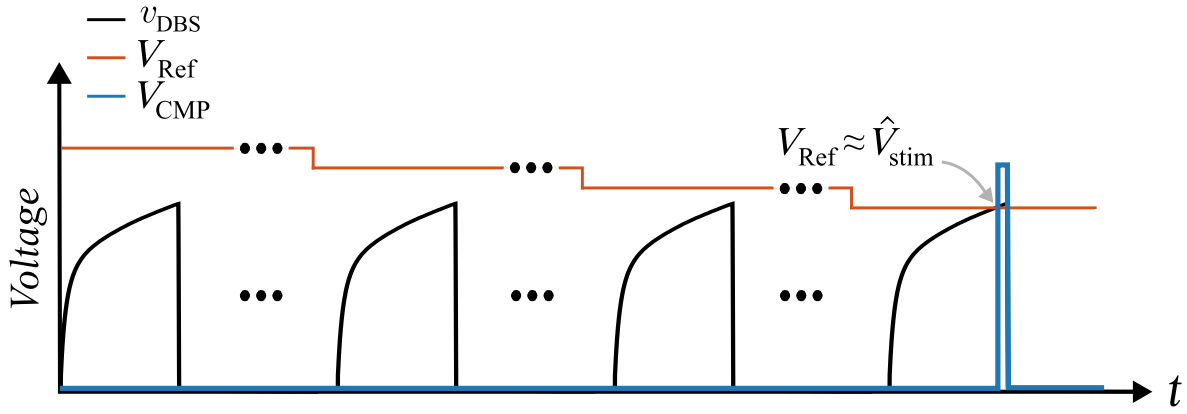

Figure 20: Schematic representation of the built-in self-test (BIST) procedure. The reference voltage (V_{Ref}) is decreased stepwise in each stimulation period to determine the maximum voltage ($\hat{V}_{\text{stim}}$) of the DBS voltage signal v_{DBS}. The comparator output (V_{CMP}) goes high when $v_{\text{DBS}} > V_{\text{Ref}}$, thereby indicating that the reference voltage approximates the maximum stimulation voltage.

Implementation In STELLA3, this approach, referred to as built-in self-test (BIST), is implemented to monitor such faults. Accordingly, two comparators within a single package are used, each monitoring an individual channel. Both comparators share a common reference voltage generated by a single digital potentiometer (R_{DP2}). To conserve energy, an n-channel MOSFET (T_1) disconnects the potentiometer when the BIST is inactive. Furthermore, each comparator features an $\overline{\text{SHDN}}$ pin, allowing it to enter a high-impedance state. This results in a total standby current of approximately 1 µA. The outputs from both comparators are

combined and routed to a single MSP430 pin (CMP), with channel selection controlled by grounding the $\overline{\text{SHDN}}$ pin of the inactive comparator. Consequently, only one channel is monitored at a time. When V_{Ref} drops below the maximum voltage of the pulse, the comparator triggers an interrupt on the MSP430, which compares the programmed reference voltage with predefined thresholds. This method enables accurate detection of the maximum pulse voltage while maintaining excellent area and energy efficiency. Since BIST is activated only a few times per day, the overall energy consumption remains very low.

While the efficiency of this algorithm could be significantly improved by using a binary search instead of decreasing V_{Ref} linearly, this was not necessary given the infrequent activation by the medical personnel. However, RF-linked implants enable frequent monitoring by transmitting data to an external device, making a more efficient algorithm essential.

5.2.5 Timing Control and Energy-Saving Mechanisms

An essential measure for implantable stimulation devices is an optimal ratio between stimulation time and battery volume. Therefore, achieving long-term stimulation experiments despite a small battery is only feasible with a highly energy-efficient stimulator. STELLA3 is designed for minimal power consumption, specifically during the generation of DBS pulses, as this is the application for open-loop rodent DBS research. The following energy-saving mechanisms are implemented in STELLA3:

Adjusting the supply voltage BIST not only detects common faults in rodent DBS research, but also provides $\hat{V}_{\text{stim}}$ if the stimulation is valid, which allows deriving the supply voltage needed to maintain a constant current pulse. Since coin cells cannot deliver the required high voltages and battery stacks would lead to an excessive implant height, a boost converter is typically used in neurostimulators to raise the supply voltage for the current sources. However, the boost converter's output voltage increases the overall power consumption due to conversion losses and the higher power drawn by the connected circuitry. Therefore, adapting the supply voltage in response to the stimulation parameters and the time-varying load impedance can significantly reduce the power consumption. This adaptive approach has been demonstrated in an ASIC for epiretinal stimulation [172]. As the ASIC's operation, however, relies on wireless power transfer and the adaptive approach to regulating this power transfer, the presented solution is not compatible with battery-powered DBS devices. In STELLA3, a straightforward discrete solution is implemented, in which a boost converter IC has been chosen that allows setting its output voltage by an adjustable resistance, which is implemented with a digital potentiometer in rheostat mode (R_{DP1}). This allows for fine adjustments in 100 mV increments from 3.1 V to 3.7 V, resulting in a compliance voltage range of 2.2 V to 2.8 V. Especially in STELLA3, where the stimulation and control unit

share the same supply voltage (single-V_{DD} design), this adaptive approach enables significant power savings. The concept of this method is illustrated in Fig. 21.

Since load impedance varies after implantation, the supply voltage should be adjusted more frequently (about once per hour) using a timer-triggered routine to prevent compliance voltage violations between BIST executions. Furthermore, the implemented current source, in which the reference voltage is generated by two diodes, is not perfectly stable (see [142]). As a result, the output current depends slightly on V_{DD}. Therefore, the current source's output current must be readjusted after each change in the supply voltage to ensure an accurate and consistent stimulation current during the experiment.

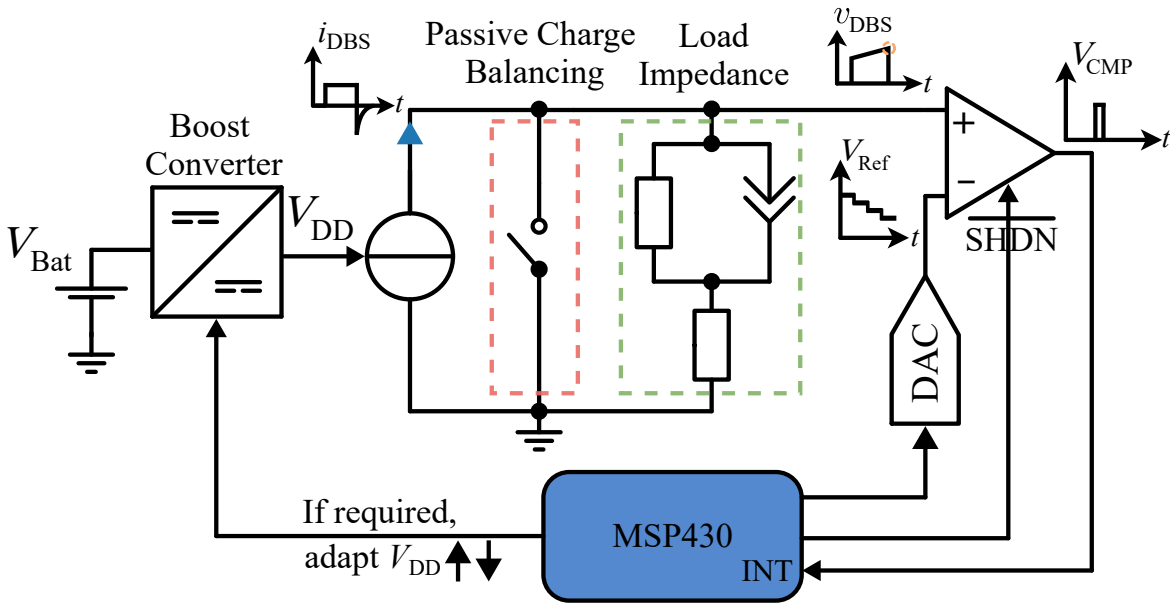

Figure 21: Illustration of the adaptive approach utilizing the built-in self-test (BIST) mechanism. Following a timer or Hall-sensor interrupt, the MSP430 microcontroller activates the operational amplifier to compare the DBS voltage (v_{DBS}) with a stepwise decreasing reference voltage (V_{Ref}), which signals back when the reference voltage corresponds to the maximum stimulation voltage ($\hat{V}_{stim}$). The microcontroller then compares the detected voltage with the current supply voltage and adjusts the boost converter's output (V_{DD}) only as high as necessary (including a safety margin) to ensure a constant current amplitude, thereby maximizing energy efficiency in battery-powered DBS systems.

Passive charge balancing From Section 2.2.5, it is obvious that passive charge balancing is the most power-efficient method to remove the residual charge, as only a switch is required that shorts both electrode contacts, in contrast to active charge balancing where a further current source activation is required. In STELLA3, this is managed by an inverter IC with

Table 5: Operating modes of the MSP430G2553 and their application in STELLA3.

Mode	Clock Source(s)	Active Components	MSP430's I_Q at 3 V (µA)	STELLA3 Application
Active	DCO (1 MHz)	CPU, DCO, peripherals	330	Built-in self-test
LPM0	DCO (1 MHz)	DCO, peripherals (CPU off)	74	High-res stim.
LPM3	ACLK (32.768 kHz)	Specific peripherals (DCO, CPU off)	0.9	Low-power stim.
LPM4	All clocks off	None (full standby)	0.3	Storage

open drain output (see Section 5.2.3), which, according to the datasheet, requires a maximum current consumption of only 0.5 µA.

Component selection All components were selected for ultra-low operating quiescent currents in the sub-microampere range during DBS pulse generation. As the current sources are controlled by a PWM signal, their energy-efficient generation is essential. This requires an microcontroller unit (MCU) with low-power modes that keep only necessary peripherals active. After a thorough analysis of various 16-bit and 32-bit microcontroller families, the 16-bit MSP430G2553 was selected for its exceptionally low current consumption during PWM operation in its designated low power mode (LPM).

A critical design choice was to clock the MSP430's timer with the auxiliary clock (ACLK), sourced from an external 32.768 kHz crystal. This enables PWM generation in the MSP430's LPM3, where both the CPU and the internal digital crystal oscillator (DCO) are disabled, resulting in a drastically reduced current consumption of 0.9 µA. The trade-off in this mode is a pulse duration resolution of 30.5 µs, which is suitable for most DBS applications and is the default mode in STELLA3 (the most common DBS pulse duration is 60 µs, roughly the second step). For applications requiring a higher pulse duration resolution, a dual-timer approach was implemented. Here, two timers alternate between LPM0 (for high-resolution pulse duration at 1 MHz) and LPM3 (for ultra-low power during inter-pulse intervals at 32.768 kHz). This approach allows for a pulse duration granularity of 1 µs, while maintaining a low average current. During the built-in self-test, the MSP430 is placed into the active mode with the CPU clocked at 1 MHz by the DCO. For storage, the MSP430 enters LPM4, where all clocks are disabled and thus the lowest possible current draw is achieved.

Table 5 summarizes the measured current consumption by the MSP430G2553 operating at 3 V in these modes, together with their specific applications in STELLA3.

5.2.6 Firmware Concept

The firmware for the MSP430 microcontroller was developed in C and comprises approximately 5.6 kB of compiled code, utilizing bare-metal implementation. Programming is performed via Spy-Bi-Wire using the MSP-EXP430G2 development board. Configuration and stimulation parameters are easily modifiable through macros, allowing for straightforward adaptation. With 16 kB of flash memory available on the MSP430G2553, sufficient capacity remains for future extensions, such as the RF module (see Section 5.5).

The primary objective of the firmware was to ensure a robust and user-friendly operation, which is particularly crucial in laboratory environments. To achieve this, the firmware was intensively tested and iteratively refined in close collaboration with medical personnel to guarantee the implant's convenient use.

The program flow chart is shown in Fig. 22. On power-up, the microcontroller loads all preconfigured parameters, disables all modules (incl. stimulation) and enters LPM4, reducing the current consumption to a minimum. In this state, the MSP430 remains in deep sleep (LPM4) until a magnetic field activates the Hall sensor, which then triggers the MSP430. Once triggered, the MSP430 is placed in its active mode, where the stimulation is initiated, followed by execution of the main routine, beginning with the built-in self-test (BIST). During this test, the system checks the battery voltage and $\hat{V}_{\text{stim}}$. If necessary, the supply voltage is adjusted to the minimum level that ensures a constant current pulse, with an additional margin included to maintain tolerance until the next BIST execution. Finally, the MSP430 is placed in LPM3 or LPM3/0 for minimum power usage (see Table 5). After this test, feedback is provided to the user through distinct LED blinking patterns, indicating normal operation, low battery voltage, or excessively high or low load impedance. If the Hall sensor is triggered again, the LED lights up for 3 s. A further trigger within this time window deactivates the stimulation (LPM4). If no further trigger occurs, the BIST is repeated.

5.2.7 Physical Design and Modularity

STELLA3 is designed as a circular, four-layer PCB with a diameter of 13 mm and a height of 3.3 mm, making it smaller than a 1 euro cent coin (16.25 mm diameter) (see Fig. 23A,B). The total volume is 425 mm^3 and the assembled PCB weighs only 0.65 g. For rapid, solderless programming, vias enable the attachment of an adapter (located on the left, see Fig. 23A). Additionally, castellated holes run along the PCB edge, providing power and ground connections on the left, two stimulation channels on the top, and SPI bus access on the right (as oriented in Fig. 23A).

Furthermore, STELLA3's design incorporates two modular functions that improve its adaptability for various experimental setups:

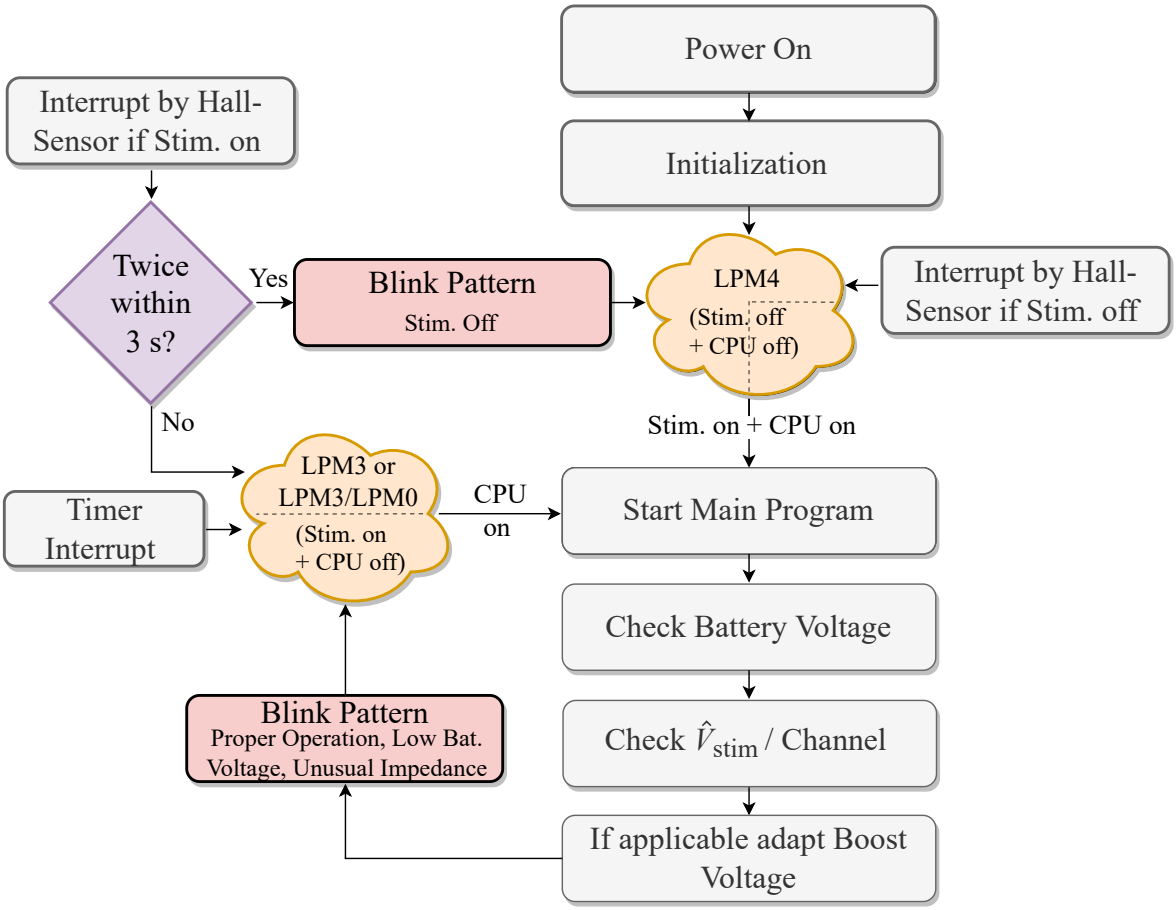

Figure 22: Program flowchart of the STELLA3 firmware. Adapted from [A10].

1. Battery Modularity: The integrated boost converter enables flexible use of different coin cell types such as CR (3 V) and SR (1.55 V) by providing a stable system voltage. Placing the coin cell below the stimulator saves critical space for a single housing. Due to STELLA3's low power consumption, the coin cell's weight and size can be selected depending on the rodent type and stimulation setting to minimize the impact on the animals' comfort and mobility. This allows for a suitable trade-off between size and stimulation time for the specific experiments in rodent DBS research.

2. System Modularity: The SPI bus enables internal control of device functions, such as adjusting current amplitude via digital potentiometers. Externally, the SPI bus is connected to the PCB edge and facilitates communication with additional modules, such as an RF module (see Section 5.5) or sensor units. This modular interface allows for a stackable system with a minimal form factor, as illustrated in Fig. 23C.

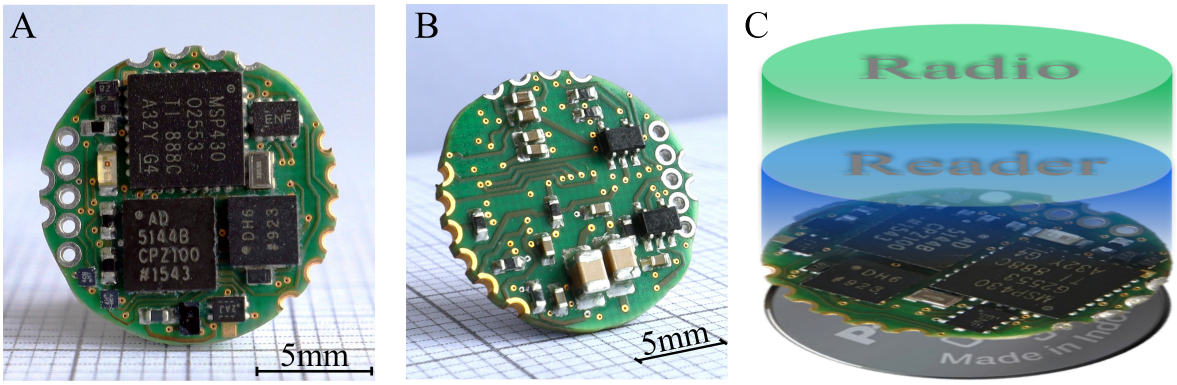

Figure 23: Top (A)[§] and bottom (B)[§] views of STELLA3 (photographed on millimeter paper), highlighting its small footprint. (C) Example of a stackable system configuration demonstrating the modular design. From [A10].

[§] Photographs by Felix Uster.

5.2.8 Encapsulation Method: Epoxy Potting

A fully subcutaneous implantable device demands a reliable encapsulation to protect both the biological tissue and electronics. The implant must meet the following critical requirements:

- **Biocompatibility** to prevent reactions with the tissue.
- **Waterproofing** to avoid fluid ingress.
- **Compactness** to maintain animal mobility and minimize skin tension.

Waterproofing is particularly challenging for long-term implanted systems, as even the smallest gap can allow body fluids to infiltrate the housing over time. This is especially problematic in designs where epoxy potting is avoided, such as systems incorporating an RF interface, where potting influences the RF performance (see Section 5.5.4), or those using Li-ion batteries, which require expansion space in the event of thermal runaway and must therefore remain unpotted (see Section 5.10). In the case of STELLA3, where no RF interface is integrated, a robust encapsulation using epoxy potting was chosen.

The initial encapsulation method for STELLA3 was developed by the Institute of Chemistry at the University of Rostock. It employed an epoxy resin (Polytec EP 655 T, Karlsbad, Germany) that was cast into a custom polytetrafluoroethylene (PTFE) mold containing the fully assembled device (see [A10] for details). This process created a fully enclosed epoxy case, resulting in a robust and biocompatible implant with excellent waterproofing. The effectiveness of this method is presented in [A10], where five fully implanted STELLA3 devices with this encapsulation demonstrated error-free operation throughout the entire stimulation period of 42 days in rats. Despite these advantages, the method was labor-intensive, time-consuming, and resulted in a relatively large implant with dimensions of Ø17.0 mm × 9 mm, a volume of

$\approx 2\,\mathrm{cm}^3$, and a total weight of $\approx 4\,\mathrm{g}$, including the battery, electrode leads, electrodes, and encapsulation. While suitable for implantation in rats, the implant's size precludes its use in smaller rodents, such as hamsters, which serve as an important model for DBS dystonia research in the ELAINE project.

Therefore, a more compact and efficient epoxy potting encapsulation method for STELLA3 was developed, offering faster assembly while maintaining biocompatibility and waterproofing.[8] Unlike the previous approach, which used a mold to form a solid epoxy case around the device, the new method uses a 3D-printed polyether ether ketone (PEEK) housing as a permanent implant enclosure into which the epoxy is potted. The PEEK case (Luvocom 3F PEEK 9581), a material known for its high mechanical strength and biocompatibility, particularly in dental implants [17], was designed as a smooth, cup-shaped enclosure. It includes an eyelet for the implant's subcutaneous fixation and holes for feeding the electrode cables through (see Fig. 24A). Optimal 3D printing settings were determined through iterative testing on a CreatBot F430-420 °C printer, resulting in a lightweight (0.6 g) and robust case (see Fig. 24B).

The assembly process involved the following steps (see Fig. 24C–G):

1. Supply lines were glued to the CR battery (CR1216) using high-conductive silver paint (RS Pro Silver Conductive Paint) to avoid thermal stress and the associated risks with soldering on batteries.

2. Electrode leads were guided through the case and soldered to the stimulator's castellated holes, while the supply lines were soldered to the stimulator's vias.

3. The battery was placed at the bottom of the case, followed by an electrically insulating film and the stimulator.

4. The remaining space was filled with biocompatible (USP Class VI), transparent epoxy resin (Polytec EP 601, Karlsbad, Germany) until a slight dome was formed, ensuring a smooth transition to the surrounding tissue.

5. The epoxy resin was cured at 60 °C for 5 h to accelerate the curing process, although it can alternatively be cured at room temperature over 24–48 h. Attention should be paid to the battery's maximum temperature rating.

[8]The epoxy potting method was developed by the author and applied by him in the assembly of multiple implants. The PEEK 3D housing was conceptualized by the author in collaboration with Felix Uster and the medical team. Felix Uster handled the CAD modeling and 3D printing. Dirk Timmermann provided general guidance on the 3D design and encapsulation method.

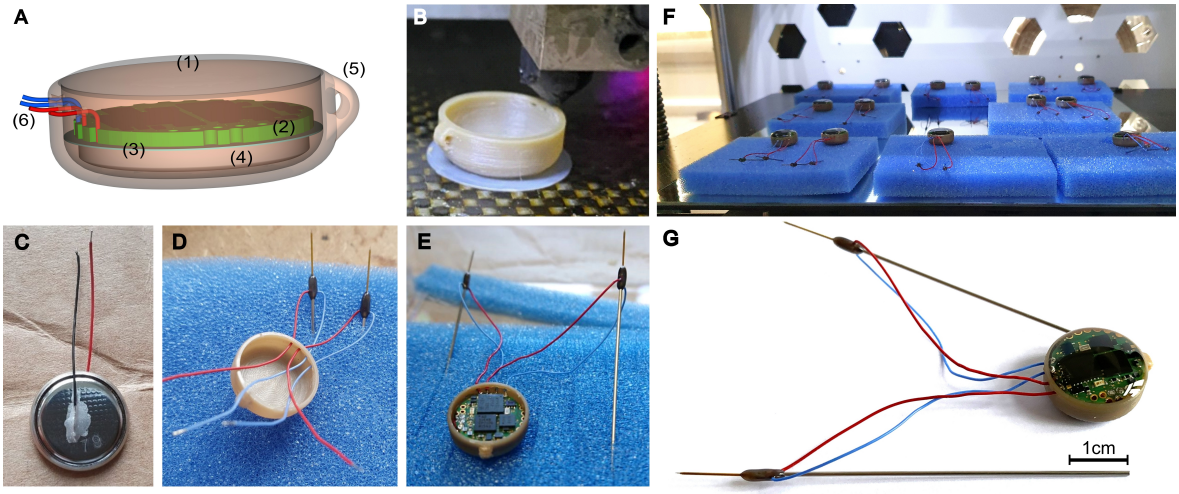

Figure 24: (A) 3D design[§] of the DBS implant, including (1) PEEK case filled with epoxy resin, (2) stimulator, (3) electrically insulating film, (4) coin cell, (5) eyelet, (6) electrode leads. (B) 3D printer during case production. (C) Coin cell with conductive glue, (D) and (E) assembly of parts. (F) Multiple STELLA3 implants during the epoxy curing process inside the 3D printer's build chamber. (G) Fully encapsulated and ready-to-implant STELLA3 device for bilateral operation in rodents. Adapted from [A11].

[§] 3D design created by Felix Uster.

5.3 Results

5.3.1 Epoxy-Potted Housing: Physical Properties and *In Vitro* Testing

Physical properties The encapsulated device is shown in Fig. 25. The DBS implant has a weight of 2.58 g, a diameter of 15 mm and a height of 7.5 mm, corresponding to a volume of approximately 1.3 cm^3. It is designed for bilateral operation and powered by a CR1216 coin cell. For scale, the device is compared with a 1 euro cent coin (16.25 mm, 2.3 g). The implant is slightly smaller in diameter and marginally heavier than the coin.

***In vitro* test** In order to evaluate the reliability of this encapsulation method, a long-term test was performed in which the encapsulated DBS implant, including electrode cables and electrodes (see Fig. 24 F), was exposed to a 0.9 % phosphate-buffered saline at 37 °C. The implant was checked daily by triggering the integrated monitoring system. The transparent epoxy resin facilitates optimal LED transillumination in order to clearly recognize the results of the built-in self-test (BIST). After 21 weeks, no abnormalities were noted in the encapsulated stimulation device, and it was still functioning correctly. The encapsulation method described offers a biocompatible and compact design that is particularly well-suited for long-term implantation due to its waterproof epoxy potting. A major advantage of this encapsulation approach is the flexibility of the 3D customizable PEEK housing, which allows the implant size and battery capacity to be tailored to different animal models and experimental durations.

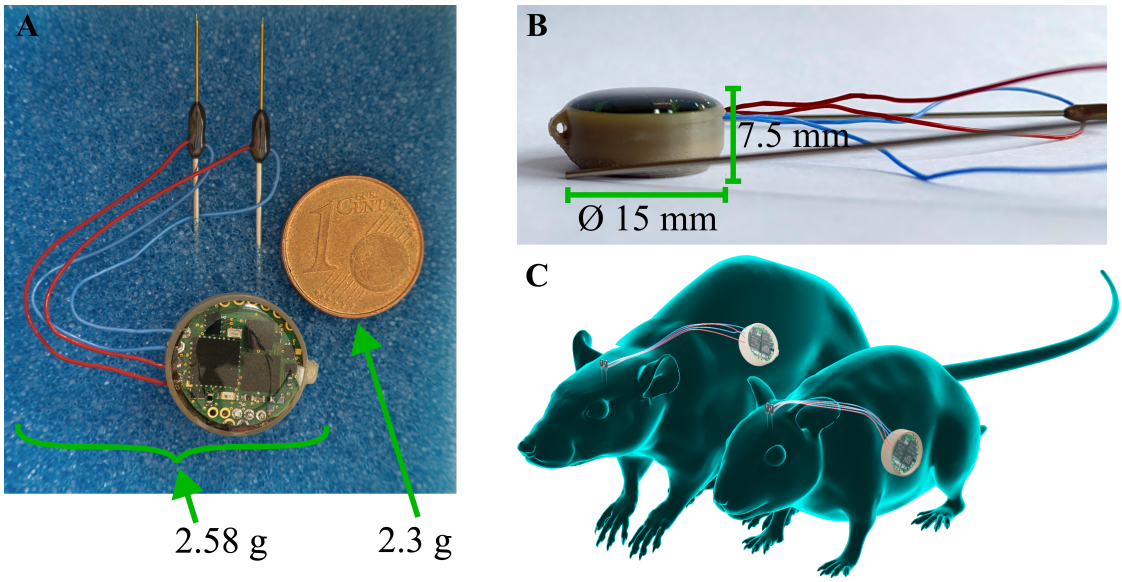

Figure 25: Encapsulated STELLA3 using the epoxy potting method. (A)* Top view next to a 1 euro cent coin for scale. (B) Side view. (C)§ 3D schematic representation showing the subcutaneously implanted STELLA3 in a rat and in a hamster (adapted from [A10]).

§ 3D design by Patrick Timmermann.
* Photograph by Arne Wall.

5.3.2 Stimulation Unit: Compliance Voltage

The compliance voltage of the stimulation unit was determined by delivering current-controlled pulses (100 µA, 60 µs, and 130 Hz) into an analog potentiometer configured as a rheostat. By increasing the resistance, the point at which the current began to drop was identified. This drop typically occurred at a voltage approximately 0.9 V below the current source's supply voltage, which aligns well with the theoretical expectations from Section 2.2.6. Considering the system voltage range of 3.1–3.7 V, this results in a compliance voltage range of 2.2–2.8 V.

In *in vivo* experiments with 6-OHDA rats using a monopolar electrode, the data show that the maximum stimulation voltages typically ranged between 1.0–1.8 V at day 7/8 (n=22) and between 1.2–2.0 V in another group of five rats at day 42 (refer to [A10]). Similarly, in *in vivo* experiments with dt^{sz} hamsters using bipolar electrodes, the maximum stimulation voltages typically ranged between 1.1–2.0 V (only one channel evaluated) after 3 h of continuous stimulation across six animals. Even in several other long-term DBS studies lasting up to 12 days with the dt^{sz} hamster model, as well as in several other DBS studies with the 6-OHDA rat model lasting up to 6 weeks, an appropriate compliance voltage was also confirmed via the blinking patterns resulting from the BIST.

Overall, these results validate that STELLA3's compliance voltage determined from the *in vitro* and *ex vivo* studies in Chapter 4 is optimally tailored for 6-OHDA and dt^{sz} models under their respective stimulation setups.

5.3.3 Stimulation Unit: *In Vitro* and Brain Tissue Measurements

Ensuring that the stimulation pulses are accurately delivered is essential for each stimulation device. To verify that STELLA3 outputs stimulation signals according to the specified parameters, both *in vitro* and brain tissue experiments were conducted. At this stage of the project, the BAC-transgenic rat model has not yet been introduced. Therefore, STELLA3 was tested and validated for the stimulation setup used in the 6-OHDA rat and dt^{sz} hamster models (refer to Table 2).

Brain tissue measurement setup The measurements were performed using extracted rat brain tissue to assess the waveform characteristics under realistic biological conditions. An early revision of STELLA3 was used, which relied solely on blocking capacitors and did not include a discharge resistor. Voltage and current recordings were acquired using a standard oscilloscope. First, the stimulation voltage across the load was recorded. Subsequently, a shunt resistor (329 Ω) was placed in the ground return path that enabled current measurement by recording the voltage drop across it. The stimulation current was then calculated using Ohm's Law. It should be noted that no unity-gain buffer was employed for the voltage

recordings in this setup. As a result, the discharge path was altered, preventing a valid measurement of a developed bias voltage.

***In vitro* measurement setup** The *in vitro* measurements were conducted following the setup described in Appendix E. The microelectrodes were immersed in a temperature-controlled saline solution with a conductivity of $0.1\,\mathrm{S\,m^{-1}}$ at $25\,^{\circ}\mathrm{C}$ (see Section 4.2 and Fig. 13 for details). The latest revision of STELLA3, which incorporates a $10\,\mathrm{M\Omega}$ discharge resistor, was used together with high-impedance voltage recording.

Fig. 26 illustrates the stimulation voltage (v_{DBS}) and current (i_{DBS}) under both bipolar (PI-SNEX-100) and monopolar configurations, in saline and brain tissue.

Current signal In all configurations, the current amplitude remained constant during the stimulation phase, meeting the specified amplitude, pulse duration, and frequency requirements. The current waveform exhibits a steep rise time in the microsecond range and a sharp transition between the pulse and passive charge balancing phases. In the brain tissue setup, a slightly longer rise time was observed compared to the *in vitro* setup. This difference is attributed to the larger shunt resistance used for current measurement ($329\,\Omega$ vs. $50\,\Omega$ in the CX3324A device). Following each stimulation pulse, the passive charge balancing mechanism completely discharged the charged double-layer capacitance within the first few hundred microseconds.

Voltage signal The voltage waveforms show an initial step at pulse onset, followed by a subsequent charging of the electrode-electrolyte interface. The maximum stimulation voltage values remained within the compliance voltage limits of the stimulation unit, confirming that STELLA3 can deliver the programmed current even under realistic tissue loads. Interestingly, the charging of the electrode-electrolyte interface in the saline solution looks similar to that in brain tissue, confirming again that the $0.1\,\mathrm{S\,m^{-1}}$ NaCl solution is a valid *in vitro* model to mimic *in vivo* conditions.

Safety considerations All presented current waveforms show that discharge is completed within a few hundred microseconds, which agrees with previous findings and model predictions (see Section 4.4.2). Therefore, the time to complete discharge remains far below the pulse period of $\approx 7.7\,\mathrm{ms}$. This confirms that passive charge balancing is effective with these stimulation setups, preventing any accumulation of bias voltage.

In the brain tissue measurements, no bias voltage was observed, even though blocking capacitors without a dedicated discharge mechanism have been demonstrated to develop a significant bias voltage (see Section 4.4.3) over time. This absence can be explained by the

measurement setup. Since no unity-gain buffer was used, the low input impedance of the oscilloscope provided an unintended discharge path, preventing a correct measurement.

In contrast, the *in vitro* measurements revealed small bias voltages (approximately −50 mV bipolar and −10 mV monopolar), well below the −100 mV safety threshold. The low bias voltage can be attributed to the additional discharge path introduced by the resistor.

These findings confirm that bias voltages remain undetected if the measurement setup introduces loading effects. Brain tissue measurements should, therefore, be repeated with high-impedance instrumentation and the stimulator revision that includes the discharge resistor. The *in vitro* results further demonstrate the importance of the discharge resistor. Without a defined discharge path, the resulting bias voltage would likely be higher.

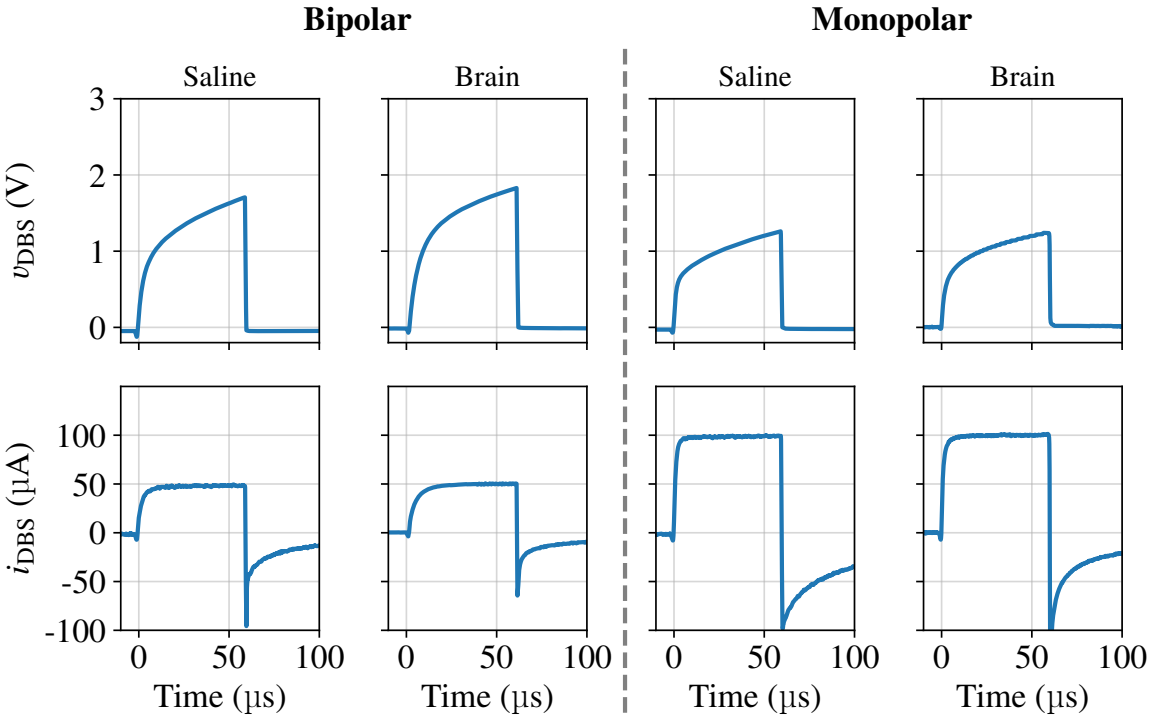

Figure 26: Voltage (v_{DBS}) and current (i_{DBS}) waveforms recorded from STELLA3 using bipolar (left) and monopolar (right) electrode configurations in rat brain and in 0.1 S m^{-1} NaCl solution. Stimulation parameters were adjusted according to the setups used in the 6-OHDA rat and *dt*^{sz} hamster models (50/100 µA, 60 µs, and 130 Hz). Across all stimulation setups, STELLA3 delivers precise constant current pulses with effective passive charge balancing, while maximum stimulation voltages remain below the current source's compliance voltage. These results demonstrate that STELLA3's stimulation unit fulfills the stimulation requirements for both animal models (see Table 2).

5.3.4 Power Consumption during DBS-only Operation

Power consumption during DBS-only operation of STELLA3 was characterized under varying operating and stimulation conditions. Current consumption measurements were obtained using a CX3324A current waveform analyzer (Keysight Technologies, USA) in series with the plus terminal of a 3 V power supply, simulating the nominal battery voltage of a CR-type coin cell. The current was sampled at 2 MSa/s and averaged over a 20 s window. The average power consumption $\overline{P}$ was computed by multiplying the measured average current by the power supply's voltage (3 V).

Power consumption across operating modes Power consumption was first measured across different operating modes of the MSP430 microcontroller at a fixed system voltage of 3.1 V (see Table 6 and Fig. 27B).

Table 6: Power consumption of STELLA3 across MSP430 operating modes (3.1 V system voltage). For modes with DBS enabled, bilateral stimulation was delivered at 50 µA, 60 µs and 130 Hz into 10 kΩ loads.

Mode	DBS Status	CPU Status	Pulse Resolution (µs)	$\overline{P}$ (µW)
LPM4	Off	Off	n/a	13.5
LPM3	On	Off	30.5	22.8
LPM3/0	On	Off	1	32.8
LPM0†	On	Off	1	289
Active	On	On	1/30.5	~ 1250

†LPM0 was not implemented in the final design. Measurement shown for comparison only.

The results show that designing the hardware to enable stimulation pulse generation in LPM3 was a power-efficient design choice, as significantly less power (22.8 µW) is consumed than using LPM0 (289 µW), despite the cost of reduced pulse resolution (30.5 µs vs. 1 µs). To overcome this limitation, a custom hybrid LPM3/0 was implemented. This mode maintains 1 µs resolution while consuming only 32.8 µW, offering a low-power alternative to LPM0.

Additional measurements were conducted using the MSP430's internal clock dividers to evaluate their impact on power consumption. In LPM3, halving the 32.768 kHz clock to 16.384 kHz (corresponding to 61 µs resolution) had no observable effect on power consumption. Similarly, in the hybrid LPM3/0 mode, reducing the DCO frequency to 250 kHz (corresponding to 4 µs resolution), while maintaining the 32.768 kHz clock in LPM3 did not result in any measurable difference in power consumption. These results suggest that in LPM3, the power contribution from PWM generation is already very small due to the low frequency, while in LPM3/0, power consumption is dominated by the overhead from the CPU wake-up transitions. As a result, reducing the clock frequency in either mode provides no benefit in lowering power consumption.

The power-intensive active mode (≈ 1.3 mW) is used solely for BIST procedures, which typically occur infrequently. As a result, its impact on overall battery life remains negligible.

LPM4 shows the lowest power consumption (13.5 µW), making it ideal for long-term storage, which is particularly useful once the battery and STELLA3 are encapsulated.

Power Consumption under varying stimulation conditions Power consumption was further evaluated across the full system voltage range (3.1–3.7 V) under different stimulation conditions for both LPM3 and LPM3/0 at stimulation current amplitudes of 50 µA and 100 µA, using 60 µs pulses at 130 Hz, applied bilaterally into 10 kΩ loads. Fig. 27A shows the power consumption across the full system voltage range, while Table 7 summarizes measurements at the lower and upper voltage boundaries.

Table 7: Power consumption of STELLA3 in LPM3 and LPM3/0 modes at system voltages of 3.1 V and 3.7 V, with stimulation amplitudes of 50 µA and 100 µA. All values correspond to bilateral stimulation using 60 µs pulses at 130 Hz into 10 kΩ loads.

Mode	V_{DD} (V)	$\overline{P}$ @ 2x 50 µA (µW)	$\overline{P}$ @ 2x 100 µA (µW)
LPM3	3.1	22.8	24.9
LPM3	3.7	33.6	36.6
LPM3/0	3.1	33	36
LPM3/0	3.7	50.1	54

As expected, power consumption increases with both higher system voltage and stimulation current in each mode. LPM3/0 mode consistently consumes 10–18 µW more than LPM3 due to the CPU activity required to transition between LPM0 and LPM3.

A higher system voltage increases the overall power draw by increasing the power consumption of the ICs and raising the input power demanded from the boost converter. Therefore, by measuring the current maximum stimulation voltage $\hat{V}_{stim}$ using the BIST method (see Section 5.2.5), the system voltage can be optimally selected to the minimum required value that maintains a constant current through the load, enabling a more power-efficient design.

The increase in power from 50 µA to 100 µA stimulation is relatively small. This is due to the low duty cycles of the stimulation signal (60 µs at 130 Hz, i.e., 0.078%), meaning the average current delivered to the loads remains small compared to the current amplitude value.

5.3.5 Runtime and Implantability

Runtime Based on the measured power consumptions, the expected runtime of STELLA3 when powered by a standard CR coin cell can be estimated. For this purpose, the most representative stimulation setting of 100 µA current amplitude, 60 µs pulse duration and

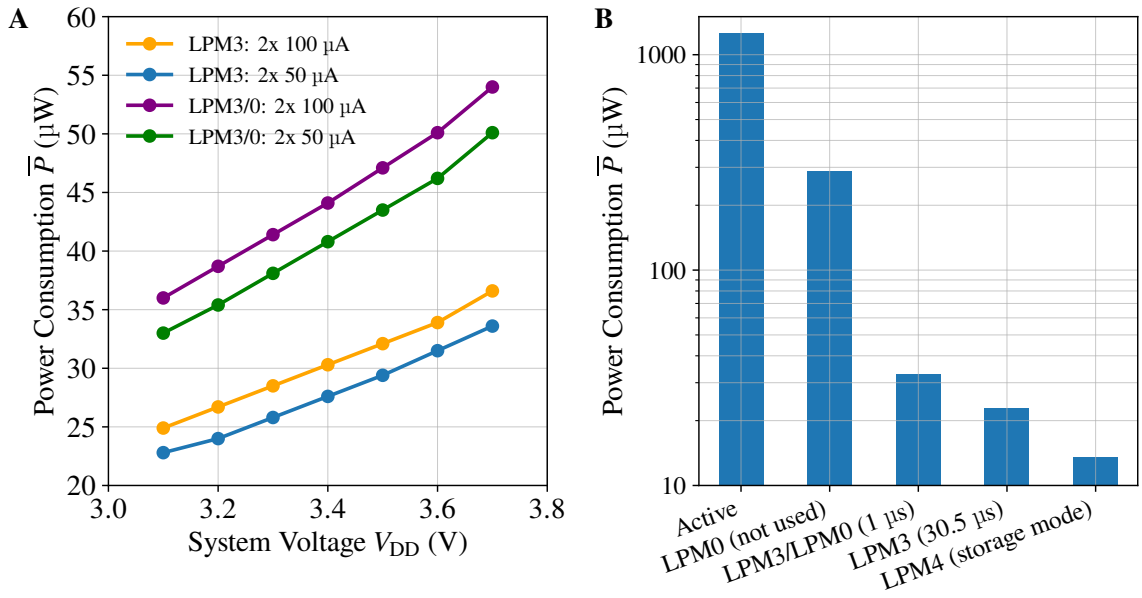

Figure 27: Power consumption of STELLA3 under bilateral stimulation at 50 µA and 100 µA current amplitudes, 60 µs pulse duration and 130 Hz frequency into 10 kΩ loads. (A) Power consumption in LPM3 and LPM3/0 modes across system voltages from 3.1–3.7 V (adapted from [A10]). (B) Power consumption across different MSP430 operating modes at 3.1 V.

130 Hz frequency is used. Under this configuration, the measured power consumption ranges from 24.9 µW in the best case to 36.6 µW in the worst case.

Using these values, the runtime for different available CR coin cell batteries is calculated and summarized in Table 8. The table also considers the volume of the battery, and the height and volume of the STELLA3 PCB + battery stack.

As can be seen, even the smallest available CR battery, the CR1216, provides sufficient energy to power STELLA3 for 137 days in the best case and 84 days in the worst case, clearly exceeding the durations typically required in DBS studies in rodent models for movement disorders, such as PD and dystonia. For reference, the longest stimulation period reported in [114] lasted 30 days, while in the ELAINE project, stimulation durations are defined as 6 weeks (42 days) for rats and 15 days for hamsters. Thus, a CR1216 is already sufficient when only stimulation is applied. By using a CR1225, the runtime can be approximately doubled with only a minor increase in the combined volume of the PCB and battery. Moreover, the use of a CR2032 could theoretically enable runtimes for over three years, which covers the life expectancy of a laboratory rat.

Implantability In its ready-to-implant configuration with a CR1216 coin cell, STELLA3 has a final weight of 2.6 g, a volume of 1.3 cm^3 and a height of 7.5 mm.

Table 8: Battery options and corresponding DBS-only runtime for STELLA3 (Ø13 mm x 3.3 mm).

Battery	**Batt. Vol.** (mm³)	**Total Vol.** (mm³)	**Total Height** (mm)	**Energy** (mWh)	**Runtime (Best / Worst)** (days)
CR1216	196	634	4.9	75	137 / 84
CR1225	307	745	5.8	144	265 / 162
CR2032	1005	1443	6.5	720	1328 (3.6 yr) / 812 (2.2 yr)

As a reference for acceptable implant sizes and weights, established telemetry devices from Data Sciences International (DSI, USA), commonly used in preclinical research, provide useful benchmarks (data retrieved from www.datasci.com):

- HD-X02: Suitable for animals ≥ 19 g (e.g., mice, hamsters), implant weight: 2.2 g (11.6 % of body weight), volume: 1.7 cm^3.
- ETA-F10: Suitable for animals ≥ 17 g (e.g., mice, hamsters), implant weight: 1.6 g (9.4 % of body weight), volume: 1.1 cm^3.
- HD-S02: Suitable for animals ≥ 175 g (e.g., rats), implant weight: 4.7 g (2.7 % of body weight), volume: 3.3 cm^3.

In the ELAINE project, both hamsters (38–52 g, [A11]) and adult rats (≈ 300 g, [A10]) are targeted as rodent models for DBS research.

For hamsters, the CR1216-based STELLA3's volume is slightly above the volume of the ETA-F10 but still below that of the HD-X02. The weight is higher than both, but still corresponds to 6.8–5.0 % of hamster body weight. Thus, in terms of both absolute volume and relative weight, STELLA3 is well within the acceptable implantability thresholds for hamsters.

In rats, implantability is even more favorable. Compared to the HD-S02, the CR1216-based STELLA3 is significantly lighter and occupies less than half the volume. At 2.6 g, it represents only 0.87 % of a 300 g rat's body weight.

In addition to weight and volume, implant height is also a relevant factor for subcutaneous implantability. For reference, the ETA-F10 device with a measured height of 5.6 mm is intended for very small rodents such as mice (≥ 17 g). The CR1216-based STELLA3 implant features a total height of 7.5 mm and has been well tolerated in multiple hamsters [A11, A7], suggesting that this height is suitable for use in this species.

Alternative configurations using the CR1225 and CR2032 are estimated in Table 9. While these options are not required for any currently defined experimental durations, they allow

evaluation of implantability in scenarios demanding extended runtime. The CR1225 configuration increases the implant height to 8.4 mm, with a total volume of 1.5 cm^3 and a weight of 3.1 g. While weight, volume and, height remain acceptable for rats, the increased parameters may present anatomical constraints for hamsters. The CR2032 configuration further increases the implant height to 9.1 mm, along with a larger volume of 3.8 cm^3 and a weight of 8.0 g. This configuration is clearly not implantable into hamsters. However, it may still be viable for adult rats, as successful subcutaneous implantation of encapsulated STELLAs with similar height [A10] and diameter [176] has been demonstrated in this species, with maintained animal welfare.

Table 9: Encapsulation dimensions and weights for STELLA3 with different CR coin cells.

Device	Status	Dimensions (mm)	Encap. Vol. (cm^3)	Weight (g)
STELLA3 + CR1216	Measured	Ø15 x 7.5	1.3	2.6
STELLA3 + CR1225	Estimate	Ø15 x 8.4	1.5	3.1
STELLA3 + CR2032	Estimate	Ø23 x 9.1	3.8	8.0

5.3.6 Contributions to Animal Welfare and *In Vivo* Applications

A central objective throughout the development of all STELLA versions has been to align with the 3R principles of animal research. In the context of this work, the focus was primarily placed on refinement. Refinement was achieved by replacing conventional tethered, backpack- or head-mounted systems with highly miniaturized, fully implantable devices to minimize the physical and behavioral burden on the animals. In addition, fully subcutaneous implantation enables group housing, reduces infection risk, and stress associated with external components, while also preventing animals from manipulating the device themselves or their cage mates.

The refinement achieved by STELLA3 has also been recognized in the review study by [54], which lists it among the examples based on the Directive 2010/63/EU [55] on improving animal welfare in research.

The following paragraphs summarize the experimental findings from DBS research in rats and hamsters, demonstrating how the refined STELLA3 design contributes to improved animal welfare.

Animal welfare contributions in DBS research with rats The benefits of the fully implantable STELLA3 system are demonstrated in the study of [A10], in which the welfare of rats implanted with STELLA3 was evaluated against rats using traditional backpack systems.[9] This study was carried out using STELLA3 with the solid epoxy-based encapsulation yielding a size of 2 cm^3 and 4 g.

[9]The *in vivo* study, including the welfare assessment, was carried out by Maria Kober.

Results show that animals with fully implanted STELLA3 exhibited stable weight gain and showed minimal signs of stress from the seventh postoperative day onwards. Behavioral observations, including regular video documentation, confirmed normal social interaction and overall well-being in implanted animals. Furthermore, animals with implants displayed significantly increased locomotor activity in the light-dark box test (approximately twice as much as animals using backpacks) indicating improved physical comfort and mobility. No differences in anxiety-related behavior were detected between the two groups, suggesting that the enhanced activity was not a result of elevated stress. Additionally, wound healing assessments revealed rapid recovery in all implanted animals, with complete healing typically observed within 1-2 weeks post-surgery. Furthermore, all implants functioned without error throughout the entire stimulation time of 42 days.

In contrast, animals carrying an external backpack device failed to gain weight over time and exhibited intermittent stress responses. Device reliability was also significantly reduced, with a median error-free operation time of only 9 days. These impairments highlight that externally mounted devices such as backpacks can place additional strain on the animals and may influence the interpretation of behavioral study outcomes.

Furthermore, the refined PEEK-epoxy-based encapsulation method developed by the author (see Section 5.2.8), yielding an implant size of 1.3 cm^3 and weight of 2.8 g would further strengthen the animal welfare benefits of the fully implantable approach.

Animal welfare contributions in DBS research with hamsters The welfare impact of the fully implantable STELLA3 in the dystonia hamster was evaluated in a study by [A11]. In this study, the CR1216-based STELLA3 implant, encapsulated using the PEEK-epoxy method (see Section 5.2.8), was used to investigate the effects of DBS in dt^{sz} hamsters.[10]

Throughout the 10–17 day stimulation period, animals displayed progressive weight gain comparable to untreated (naive) controls (see Fig. 29), along with normal activity and species-specific behavior. No infections were reported, and wound healing proceeded without complications. Daily functionality checks confirmed that the implants remained operational with one exception. One implant reported a fault after 14 days due to a broken electrode cable. This issue was accurately identified by STELLA3's BIST feature and was later confirmed after explantation.

Overall, the absence of adverse effects suggests that the implant was well tolerated by the hamsters. Furthermore, the detected broken cable highlights the importance of continuous system monitoring, which is made possible by the BIST mechanism.

[10]The *in vivo* study, including the welfare assessment, was carried out by Anika Lüttig.

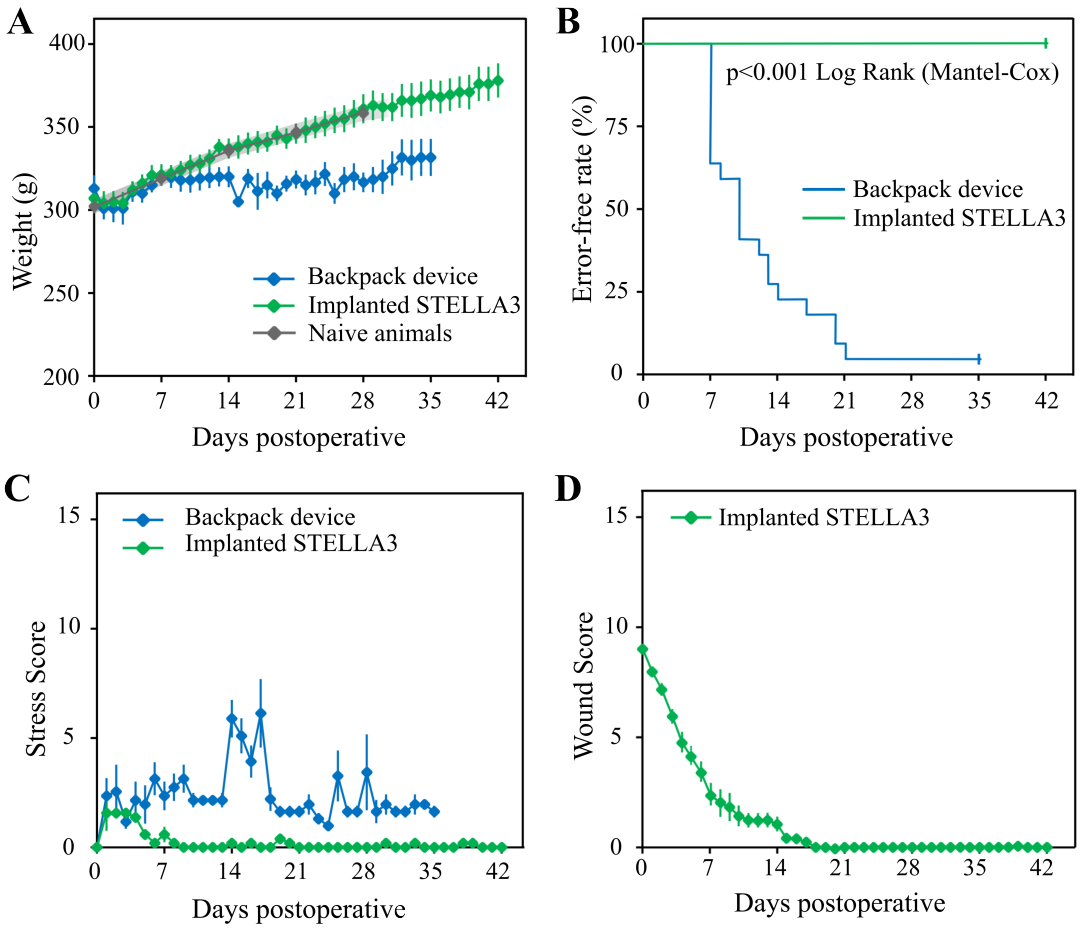

Figure 28: Postoperative outcomes in rats with implanted STELLA3 devices compared to those carrying external backpack devices. Shown are (A) body weight, (B) error-free rate, (C) stress scores, and (D) wound healing over 42 days after surgery. The results demonstrate that fully implantable STELLA3 devices contribute to improved animal welfare compared to external backpack devices. Adapted from [A10]; original plots by Maria Kober.

In summary, the findings clearly demonstrate that fully implantable STELLA3 systems improve animal welfare and data quality in preclinical DBS studies. In rats and hamsters, the compact, lightweight implants were well tolerated, minimizing stress and enabling normal weight gain, natural behavior, and rapid wound healing. Compared to external backpack systems, the STELLA3 implant reduced strain on the animals and increased the experimental reliability in behavioral studies. The fully implantable approach also facilitates group housing, an important animal welfare consideration [66]. Video material provided in the supplementary materials of the publication [A10] further illustrates that the implants are well tolerated and enable undisturbed social interaction in freely moving rats. Overall, the STELLA3 implant enables welfare-compliant chronic stimulation studies and thus represents a major technological contribution to the refinement aspect of the 3R principles.

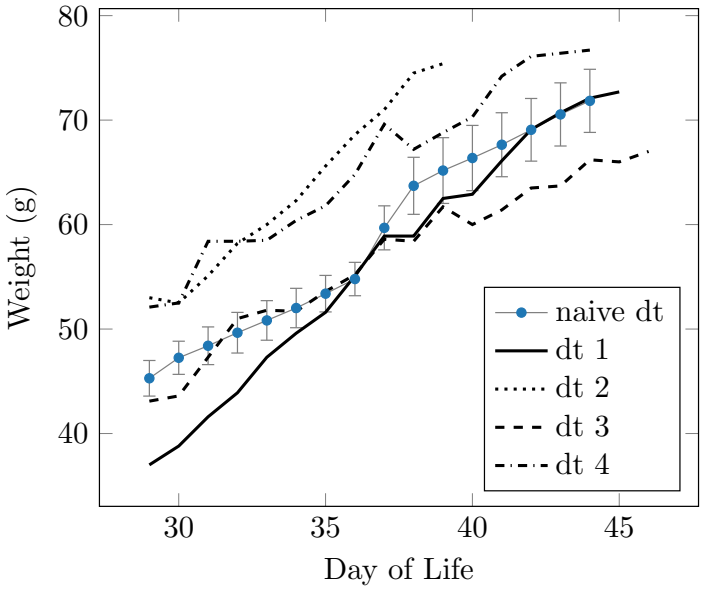

Figure 29: Body weight after implantation of STELLA3 devices in four hamsters at an age of 29 days (dt1-dt4 after subtraction of the weight of the stimulator) in comparison with the weight gain in seven mutant hamsters without surgery (naiv, mean + S.E.M.). The results demonstrate that the use of a compact, lightweight, fully implanted stimulator allows continuous weight gain comparable to that of naive controls, indicating high tolerability and overall animal well-being. From [A11].

Summary of *in vivo* experiments STELLA3 has been successfully employed in various *in vivo* studies, enabling valuable DBS findings while maintaining alignment with animal welfare principles. All DBS studies involving the STELLA3 system were conducted as a subcutaneous implantable device. An overview of these studies, together with those conducted using predecessor systems, is provided below.

- **Neurochemical investigations of DBS:**
  - In a Parkinson's disease (PD) rat model [A15, A16, A17, A10]
  - In a dystonia hamster model [A1, A7][120, 97]
- **Technical research applications:**
  - Implementation of visible light communication (VLC) for implantable devices [A6]
- **Earlier studies using predecessor systems:**
  - In a Parkinson's disease (PD) rat model [176]
  - Behavioral analysis in a dystonia hamster model [A9]

– Neurochemical studies in the same model [A2][145, 146]

5.4 Interim Conclusion of STELLA3

STELLA3 represents a significant advancement in the field of implantable DBS devices for preclinical research in rodents. By deliberately opting for an architecture designed exclusively from off-the-shelf components, STELLA3 combines flexibility, affordability, and accessibility. Because all hardware, firmware, and documentation are open source, STELLA3 can be freely reproduced and further developed within the scientific community.

STELLA3 was evaluated *in vitro*, *ex vivo*, and *in vivo* and reliably provided precise constant-current and passively charge-balanced pulses in both monopolar and bipolar configurations. *In vitro* measurements confirmed that the discharge resistor in parallel to the electrode contacts keeps the bias voltage within the safe range of ±100 mV. The maximum compliance voltage of 2.8 V was confirmed to be sufficient to maintain stable current delivery for the targeted stimulation parameters in both the 6-OHDA rat and *dt*^{sz} hamster models throughout long-term *in vivo* studies.

Its miniaturized PCB form factor, together with its compact, waterproof, and biocompatible encapsulation, allows for fully subcutaneous implantation even in small rodents such as hamsters. In its ready-to-implant configuration using a CR1216, STELLA3 weighs only 2.6 g and occupies a volume of 1.3 cm^3, making it comparable to established commercial telemetry systems such as the DSI ETA-F10 (1.6 g, 1.1 cm^3). Unlike many tethered, head- and back-mounted systems, this fully implantable approach enables group housing, promotes natural behavior, reduces infection risk, and lowers the overall experimental burden. This design therefore aligns directly with the refinement aspect of the 3R principles outlined in the Directive 2010/63/EU [55].

The presented built-in self-test (BIST) demonstrates for the first time the detection of open circuits, short circuits, and compliance voltage violations through an off-the-shelf, microcontroller-based DBS device. This feature has been well received by medical staff, as it enables immediate verification and thereby increases confidence that the stimulation parameters are indeed delivered to the brain tissue.

Ultra-low power consumption is a key strength of STELLA3. Using the smallest commercially available CR coin cell, the CR1216, STELLA3 can achieve runtimes exceeding four months. With a larger coin cell, such as the CR2032, years of operation are possible, even covering the lifespan of a laboratory rat, while still keeping the device's volume and weight within the limits of subcutaneous implantability. This performance surpasses both the project's target of 6 weeks of continuous stimulation and the runtimes reported in comparable DBS studies on movement disorder rodent models, which reach up to one month [114].

When placed into the context of existing rodent DBS devices (see Table 1), STELLA3 represents a significant step forward. STELLA3 is the first dual-channel stimulator that combines ultra-low power consumption ($< 100\,\mu W$), charge-balanced current-controlled stimulation, and built-in self-test function within a small form factor validated for chronic subcutaneous implantation in both rats and hamsters. It is also the first DBS device to be successfully implanted subcutaneously in the dt^{sz} hamster model, and the first to provide comprehensive electrode failure monitoring, which is absent or only partially supported in existing designs.

Moreover, STELLA3 achieves the lowest power consumption currently reported for rodent DBS devices under the stimulation conditions evaluated in this work. This efficiency is partly the result of a deliberate design trade-off in which the compliance voltage was optimized to match the electrode geometries and stimulation parameters defined within this project for the 6-OHDA and dt^{sz} hamster models, which lie within the typical parameter ranges reported in rodent DBS literature. For DBS protocols that require higher injected charge or employ smaller electrodes, larger compliance voltages are necessary. For example, although the PI-SNEX-100 electrodes are also intended for use in the BAC-transgenic model, they are driven at twice the current amplitude compared to the dt^{sz} model, increasing the compliance voltage requirement that exceeds what STELLA3 can provide. Therefore, STELLA4 (see Section 5.9) extends the STELLA3 architecture with increased compliance voltage headroom, enabling a wider range of DBS protocols at the cost of higher power consumption.

5.5 Extension of STELLA3 with a 2.4 GHz Radio Module: STELLA3.1

STELLA3 was developed as a pure stimulation platform with only minimal remote communication capabilities. The only available feedback mechanism is an onboard LED, which reports the results of the magnet-triggered BIST via blinking patterns (see Section 5.2.6). However, based on multiple *in vivo* experiments, several limitations of this setup became evident:

- Subcutaneous implantation attenuates the LED through skin and fur. Device rotation within the animal's body further hampers the visual readout.
- Each BIST requires a magnet swipe, disturbing the animal and adding repetitive workload for the staff. Consequently, only one or two checks per day are typically feasible.
- Human-readable blink codes provide only categorical information and cannot provide numerical values, such as battery voltage.

- Automating readout with cage-mounted optical receivers (Visible Light Communication, VLC) is unreliable due to standard housing conditions and rodent activity [A6].

To address these limitations, STELLA3 was extended with a 2.4 GHz RF module, resulting in the STELLA3.1 version. This section is partially based on the publication by [A14].[11] All development components, including PCB layouts and firmware, have been released as open-source under the repository [194].

5.5.1 PCB and Circuit Design

The objective was to design a radio module capable of extending the existing STELLA3 circuit with RF capabilities, while maintaining low volume to enable subcutaneous implantation and ultra-low power consumption for long-term use. To achieve this, a compact and energy-efficient RF module was designed as a piggyback PCB that can be directly mounted on top of STELLA3 [A14].

Circuit design The circuit is built around the CC2500 transceiver chip, operating in the 2.4 GHz industrial, scientific, and medical band (ISM) band. This chip was selected after thorough evaluation of available 2.4 GHz RF transceivers due to its full SPI interface control and very low power consumption in sleep mode of only 1.2 µW. This low standby power introduces minimal overhead when integrated into STELLA3 when not required or at low to moderate duty cycles. In active operation, the CC2500 consumes 13.3 mA in receive (RX) mode at 250 kBaud, 21.2 mA in transmit (TX) mode at 0 dBm. Communication with the transceiver is managed via the SPI bus, with the CC2500 acting as slave and the MSP430 microcontroller on STELLA3 as master.

A 26 MHz crystal oscillator provides the reference frequency for the CC2500's internal synthesizer. The RF signal is routed to a compact multilayer chip antenna (WE-MCA-7488930245), operating in the ISM band. The matching network was implemented based on the reference design provided by TI, tuning the CC2500's output impedance to the antenna's 50 Ω input impedance.

PCB The RF module was implemented as a circular PCB with a diameter of 13 mm, matching STELLA3's footprint for an optimal form factor. The board employs a two-layer design, with all components mounted on the top side to minimize overall height. A 1.5 mm

[11] The author defined the system architecture and designed the circuit schematic of STELLA3.1. The firmware architecture was conceived by the author, while Obaid Ullah Shah, Munawar Ali, and Enkhtuvshin Janchivnyambuu primarily implemented the firmware. Several refinements were integrated into the final firmware by the author. The *in vitro* experiment and other technical characterizations of STELLA3.1 were conceptualized, carried out, and analyzed by the author. The *in vivo* experiment with STELLA3.1 was conducted by Maria Kober. Dirk Timmermann, Mareike Fauser, and Alexander Storch provided the resources for this research.

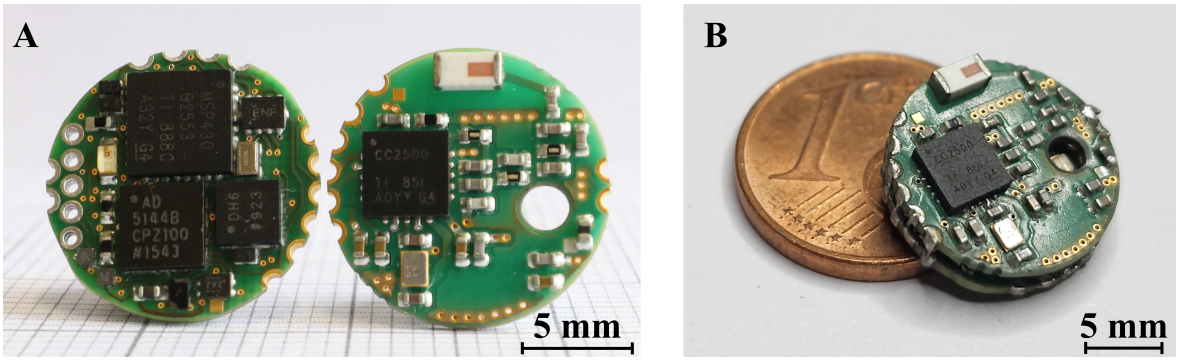

Figure 30: (A)[§] Front views of STELLA3 and its RF module shown side-by-side on millimeter paper. (B) Assembled configuration forming STELLA3.1.

[§] Photo by Felix Uster.

hole allows STELLA3's LED to shine through for visual feedback. As with the main STELLA3 PCB, the SPI bus and power connections are routed to castellated holes along the PCB edge. Short metal wires soldered between the castellated holes of both boards enable a robust mechanical and electrical connection. When stacked, the combined unit measures 13 mm in diameter with a total height of 5.5 mm, and has a weight of 1.0 g. Fig. 30 shows (A) STELLA3 and its RF extension module side-by-side, and (B) the fully assembled configuration, forming the complete STELLA3.1 device.

5.5.2 Firmware Architecture

Designing an energy-efficient RF communication protocol is crucial for size-constrained implantable devices. In DBS rodent research, implant parameters typically require infrequent but immediate updates. For example, stimulation may be disabled once per day, and the animal's reaction must be observed immediately. Additionally, periodic monitoring of the implant status (e.g., results from the BIST) is essential for achieving reproducible results in such studies.

To meet both needs, two lightweight and scenario-specific communication protocols were implemented. A base station, implemented using a Raspberry Pi 3 Model B+, acts as a gateway for accessing and managing the implants. It communicates with the implants wirelessly using two CC2500 radio modules, each connected to a dedicated antenna. This setup allows simultaneous transmission and reception via two parallel RF channels, with CH1 for TX and CH2 for RX. Each implant is uniquely identifiable via an assigned device ID.

The firmware for the Raspberry Pi was written in Python, while the implant-side firmware was implemented in C for the MSP430 microcontroller. The MSP430G2553 provides only 16 kB of flash memory and 512 B of RAM, which constrained the choice of a communication stack. Therefore, no proprietary RF protocol (e.g., SimpliciTI) was used. The size of the C

code is about 10.8 kB, containing RF configuration, scenario-based protocols and STELLA3 code.

Two distinct communication scenarios were implemented:

Scenario 1: Immediate Update of Implant Parameters In this scenario, the user sends configuration parameters to the implant and receives immediate feedback on its current status. These parameters, such as stimulation settings (e.g., current amplitude), metadata (e.g., user name), and operational settings (e.g., TX power), are defined in a configuration file on the Raspberry Pi.

To initiate the process, the user runs a script on the Raspberry Pi that continuously transmits packets on CH1 while simultaneously listening on CH2. At the same time, STELLA3.1 must be activated using a magnet that triggers the Hall sensor. This prompts the MSP430 to activate the CC2500's wake-on-radio (WOR) functionality via SPI, allowing the transceiver to periodically listen for incoming packets, while otherwise remaining in deep sleep [143]. Once a packet is received, WOR is disabled, and the MSP430 immediately applies the configuration updates. Finally, the updated parameters are transmitted back to the Raspberry Pi, which stops transmitting packets and logs the received data into a CSV file.

Scenario 2: Periodic Status Monitoring This scenario allows for periodic monitoring of the implant's status (for example, V_{Bat}, $\hat{V}_{\mathrm{stim}}$, BIST results) at a user-defined communication interval. The desired interval (e.g., once per hour) is specified in the same configuration file on the Raspberry Pi.

To activate this monitoring mode, Scenario 1 must first be executed with the relevant parameter set in the configuration file. Once configured, the user runs a script on the Raspberry Pi that continuously listens on CH2. Meanwhile, the MSP430's internal timer periodically activates the CC2500, which then transmits the implant's status data to the Raspberry Pi. The Raspberry Pi logs each received packet, including a timestamp and the implant's unique ID, to a CSV file. Note that the implant does not expect an acknowledgment of whether its transmitted packets were successfully received. This unidirectional communication strategy was intentionally implemented to minimize both communication overhead and power consumption on the implant side.

5.5.3 Battery Selection for RF Communication

Initially, the operation of STELLA3.1 was tested with a CR1216 coin cell, previously used in STELLA3. However, frequent restarts of STELLA3.1 occurred when the CC2500 entered its WOR mode, producing high-current RX events of 15 ms duration every 5.9 s. Measurements

with an oscilloscope during these cycles revealed that the CR1216 voltage dropped to critical levels, sometimes below the minimum input voltage required by the boost converter (450 mV), causing a collapse of the system voltage and a subsequent restart. For a more detailed analysis, battery voltage and current were recorded for different battery sizes and types using the CX3324A. Representative voltage and current recordings during RX communication are presented for the CR1216 and two SR59 cells in series in Fig. 31A,B. The corresponding minimum battery voltages and peak currents for these configurations, along with additional data for the CR1220 and CR2032, are summarized in a bar chart in Fig. 31C.

The underlying problem is the relatively high internal resistance of coin cells, which is influenced by factors such as cell capacity and chemistry [225, 14]. For low-capacity CR batteries such as the CR1216 (25 mAh, RENATA), this issue is particularly severe. As shown in Fig. 31A, the voltage dropped to as low as 0.74 V, while peak current reached up to 72 mA. It is also evident that the battery voltage requires some milliseconds to recover to its initial value, an important consideration when configuring the timing between consecutive RX events. The situation is further amplified by the boost converter, as lower input voltages require higher input currents, which in turn further reduce the input voltage. This not only increases the power consumption of RF communication but also raises the risk of system restarts when the input voltage falls below the converter's threshold.

Interestingly, using a slightly larger CR1220 (35 mAh, RENATA) cell significantly improved the performance, with a minimum voltage of 2.48 V and peak current of 29 mA. The large CR2032 (260 mAh, RENATA) performed best with a minimum voltage of 2.85 V and 26 mA. These results illustrate the relationship between battery capacity (and thus size) and internal resistance. However, given the 5.5 mm height of STELLA3.1, the use of larger batteries in a stacked PCB-battery configuration is not feasible for implantation in rodents (see Section 5.3.5).

To address this limitation, silver-oxide (SR) cells were evaluated. High-drain (HD) variants of these cells offer significantly lower internal resistance, making them suitable for RF applications. With a nominal voltage of 1.55 V, two SR59 cells (32 mAh, Ø7.9 mm × 2.6 mm, RENATA) were connected in series to achieve 3.1 V, thereby preventing a higher input current required by the boost converter at lower battery voltages. As shown in Fig. 31B, the series-connected SR59 cells performed almost identically to the much larger CR2032, with a minimum voltage of 2.84 V and peak current of 26 mA. Additionally, the voltage recovery time was significantly faster than that of the CR1216 (see Fig. 31B). As the stacked SR59 cells match STELLA3.1's height and feature a small diameter, this configuration allows for a side-by-side PCB-battery design, which defined the drop-shaped housing for STELLA3.1 (see Section 5.5.4 and 5.6.1).

While Li-ion cells are also well known for their low internal resistance (few - few hundred

mΩ [251]), their voltage range (typical 3–4.2 V) is incompatible with the current STELLA3.1 architecture and was therefore not considered here.

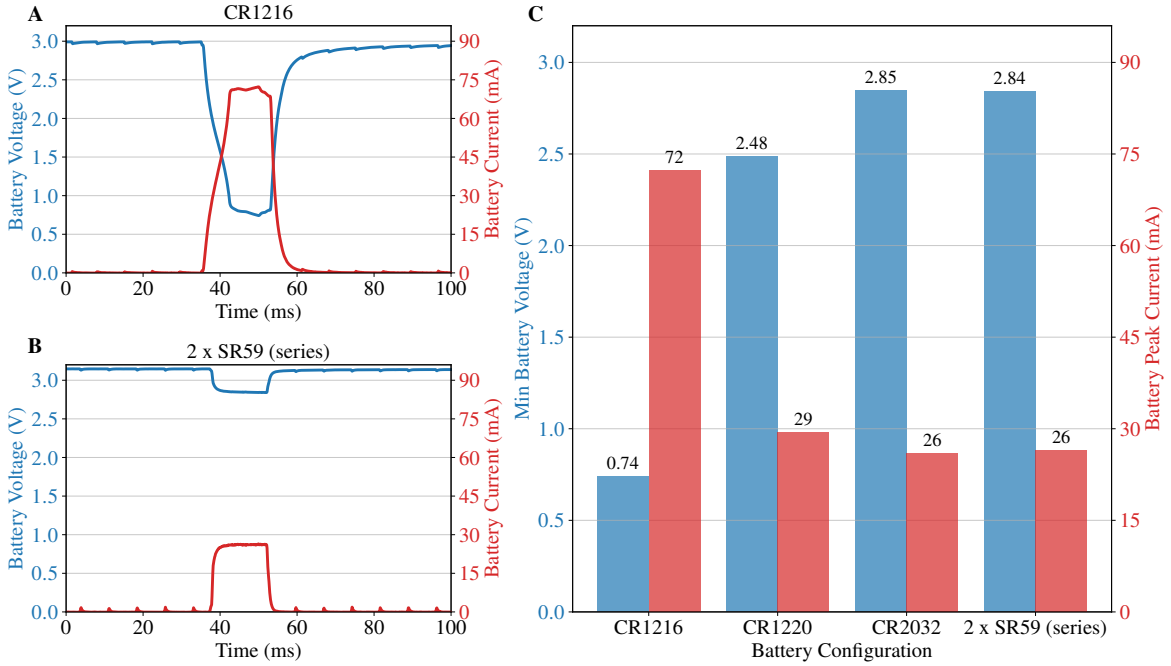

Figure 31: Representative voltage and current recordings during RX events for (A) a single CR1216 and (B) two SR59 cells in series. (C) Minimum battery voltage and peak current for CR1216, CR1220, CR2032, and two SR59 cells in series, shown in a bar chart.

5.5.4 Encapsulation Method: Drop-Shaped Air-Filled Housing

The epoxy potting method described in Section 5.2.8 provides effective waterproofing for long-term implants, but poses two major problems. First, when the battery and stimulator are completely encapsulated in epoxy resin, the stimulator cannot be reused once the battery is depleted, resulting in increased system costs. Second, the epoxy potting drastically affects the RF communication. With epoxy resin ($\epsilon_r \approx 3.5$ at 2.4 GHz [178]) in direct contact with the antenna and matching components, the resonance frequency will be significantly lowered, resulting in highly weak RF performance (see [109, 112] for more details of how non-conductive housings detune the matching network). Compensating for this major shift requires retuning the matching network using an accurate simulation. However, this is often hindered by the lack of permittivity data for the specific epoxy at the relevant frequency, making prior measurement of the material's dielectric properties necessary. Additionally, the dielectric losses of the thick layer of surrounding potted epoxy further lower RF performance.

To address these limitations, an air-filled housing was developed for STELLA3.1. The design consists of two 3D-printed components, a housing body and a press-fit cap.[12] Both were 3D

[12]The air-filled housing method was developed by the author and applied by him in the assembly of multiple

printed from polyethylene terephthalate glycol-modified (PETG), replacing PEEK due to the PETG's reliable printability. As in the final encapsulation step, the PETG is coated with medical silicone, and biocompatibility is therefore ensured.

The housing features a drop-shaped profile that accommodates the battery and stimulator side-by-side, reducing height and thereby minimizing stress on the surrounding tissue (see Fig. 32A). Additional features include side compartments with holes for stimulation leads and an eyelet for surgical fixation. The 3D printed body and cap together weigh 0.9 g. The assembly process shown in Fig. 32B–F uses a single SR48 (1.55 V) cell and represents an early prototype used to validate the waterproofing of the encapsulation in *in vitro* trials. The final design, however, employs a stacked configuration of two SR59 cells in series (3.1 V), as the higher battery voltage was confirmed to provide a stable input voltage during RF events (see Section 5.5.3). Apart from the additional step of electrically connecting the two SR59 cells, the encapsulation workflow is identical to that used for the final SR59-based implants.

For improved reliability, stimulation leads from Open Source Instruments (OSI; Waltham, MA, USA) were selected. The OSI leads feature helical conductors and medical-grade silicone insulation, offering enhanced flexibility and biocompatibility compared to the previously used, more rigid PVC cables (see Fig. 25).

The assembly process involved the following steps (see Fig. 32B-F):

1. Battery leads were spot-welded to the battery terminals, after which the battery was placed into its compartment. The stimulation leads were guided through the body's side openings and both the battery leads and stimulation leads were soldered to the stimulator's castellated holes.

2. The stimulator was positioned in its compartment with the cables arranged in place. The housing was then closed by press-fitting the cap.

3. The assembled unit was coated twice with epoxy resin (Polytec EP 601), during which the device was fully submerged and subsequently cured at room temperature. A third layer of medical-grade silicone (NuSil MED10-6607, USA) was applied using the same procedure.

implants. The PETG 3D housing was conceptualized by the author in collaboration with Felix Uster and the medical team. Felix Uster handled the CAD modeling and 3D printing. Dirk Timmermann provided general guidance on the 3D design and encapsulation method.

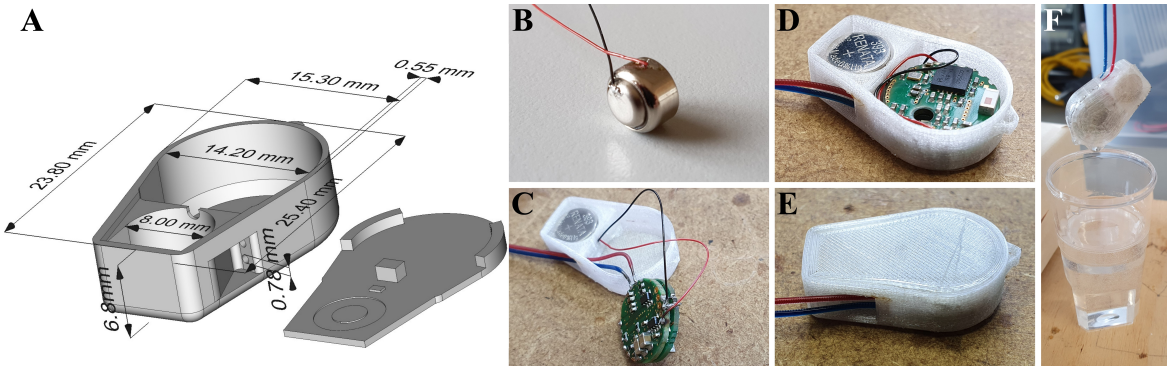

Figure 32: (A)[§] 3D design illustrating the dimensions of the PETG housing body and cap (adapted from [A14]). (B) Battery preparation with spot-welded battery leads. (C) Stimulation leads guided through the body's side openings and soldered together with the battery leads to the castellated holes of the stimulator. (D) Placement of the STELLA3.1 into the housing with arranged leads. (E) Housing closure by press-fitting the cap. (F) Curing after immersion in epoxy resin (silicone coating performed analogously, not shown).

[§] 3D design by Felix Uster.

5.6 Results

5.6.1 Air-Filled Housing: Physical Properties and *In Vitro* Testing

Physical properties Fig. 33A demonstrates the STELLA3.1 implant created using the air-filled encapsulation method, placed next to a 2 euro cent coin for scale. The STELLA3.1 implant is powered by two SR59 cells (Renata) in series and is assembled for unilateral DBS operation. The fully encapsulated unit weighs 3.03 g (excluding electrodes) and measures 23.2 mm × 15.5 mm × 7.1 mm (L×W×H), corresponding to an approximate volume of 2 cm^3. The weight is comparable to that of a 2 euro cent coin, and its maximum width is similar to the diameter of a 1 euro cent coin.

***In vitro* testing** The STELLA3.1 DBS implant (Fig. 33A), together with its OSI leads were fully immersed in a red-colored saline solution at room temperature. STELLA3.1 was configured to transmit status information once per hour (Scenario 2). The Raspberry Pi base station, shown in Fig. 33B, was positioned approximately half a meter away from the *in vitro* setup, and continuously logged incoming data.

The encapsulation failed after 11 weeks, earlier than the estimated battery runtime of 16 weeks. Until failure, communication was reliable, with only infrequent packet losses.

During disassembly, no red tinge was observed in the transparent PETG compartments, but rust coloration was present in the battery compartment. This suggests that humidity, rather than direct fluid entry, had corroded the battery. A mass spectrometry analysis of

the deposit confirmed this interpretation (courtesy of Prof. Dr.-Ing. Fleischer, Institut für Automatisierungstechnik), revealing an elemental composition consistent with steel alloys.

This encapsulation method offers several advantages, including RF compatibility without the need for re-tuning the matching circuit, biocompatibility, cost-effectiveness, and recyclable electronics. However, compared to full epoxy potting, the air-filled design carries the risk of fluid and humidity ingress. For comparison, the STELLA3 implant with epoxy potting remained functional after 21 weeks (see Section 5.2.8). This risk is further increased by the continuous animal movement, which puts strain on the cables and can lead to small gaps forming in the sealed holes. To enhance long-term stability, additional protective measures, such as conformal coatings (e.g., parylene C [83]) applied to the battery and electronics, are recommended to mitigate corrosion.

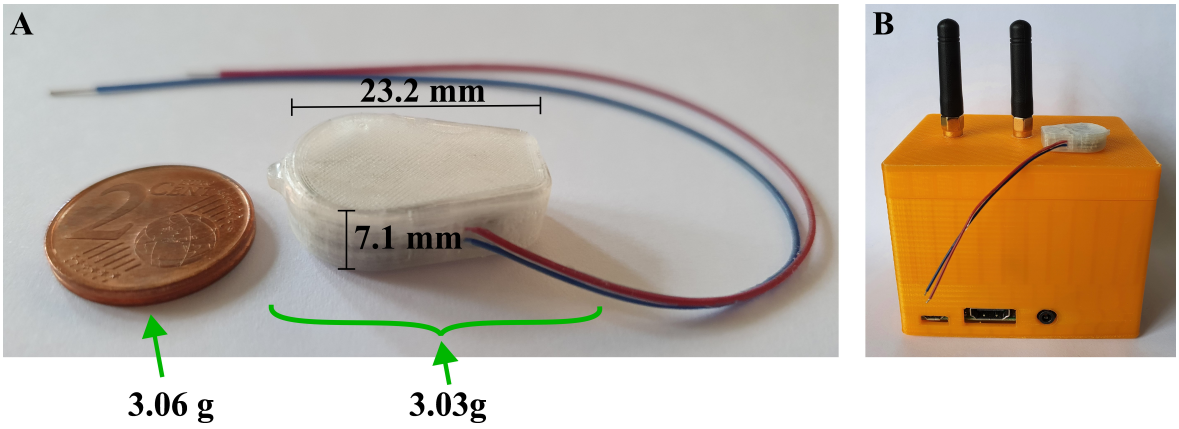

Figure 33: (A) The STELLA3.1 implant encapsulated in the air-filled, drop-shaped housing, shown next to a 2 euro cent coin for scale. OSI cables exit through the side compartments. (B) The base station, consisting of a Raspberry Pi with a dual antenna configuration, shown with the encapsulated STELLA3.1 placed on top (from [A14]).

5.6.2 Power Consumption, Runtime, and Implantability

Power consumption Parameter updates (Scenario 1) are performed only rarely, for example, during the initial phase of a DBS experiment, and therefore contribute negligibly to the battery runtime. The relevant operating mode is the periodic status transmission (Scenario 2), as it enables autonomous monitoring of implant status parameters (e.g., battery voltage, BIST results, $\hat{V}_{\text{stim}}$) during experiments.

Each transmission cycle consists of a computation phase (including BIST) and a short RF transmission. A single cycle, measured with the CX3324A at 3 V, consumed on average about 2.1 mW over 1.8 s. Most of this duration is occupied by the BIST (1.4 s), while the RF transmission itself lasts only 0.7 ms.

Fig. 34 illustrates the estimated average power consumption and runtime for communication intervals ranging from 1 minute to 1 hour. The stacked bars separate the stimulation baseline power (24.9 µW, corresponding to STELLA3 in bilateral stimulation at 100 µA, 60 µs, 130 Hz, V_{DD} = 3.1 V) from the additional power consumption required for computation and RF communication. It is evident that the average power consumption decreases significantly as the communication interval increases, since fewer transmissions per hour reduce the additional power on top of the stimulation baseline. At short intervals (1-2 minutes), the overhead is 34–66 µW. For ≥ 15 min, the overhead drops to only 2–6 µW, making the overhead minor compared to the baseline.

Runtime The dashed black curve shows the corresponding runtime of STELLA3.1 with two SR59 cells in series (3.1 V, 32 mAh). For comparison, the runtime of STELLA3 (stimulation only) is shown, powered by two SR59 cells in series reaching 166 days, and with CR1216 from previous calculations reaching 137 days. At a 1 min interval, the runtime is 45 days, at 2 min 70 days, and for ≥ 15 min intervals it rises to 136–152 days, which is close to the runtime achieved with STELLA3. These results demonstrate that frequent communication drastically reduces battery lifetime, whereas intervals ≥ 15 min deliver runtimes of several months. Since status information, such as BIST results, changes infrequently, transmission intervals of 15 min or even 1 h are sufficient for most experiments. The most dynamic parameter is $\hat{V}_{stim}$, which reflects electrode-tissue interface and solution resistance changes after electrode implantation [87] and therefore benefits from higher temporal resolution.

According to the power consumption measurements, the BIST, rather than RF communication, dominates the power consumption during a transmission cycle. The current linear sweep implementation takes 1.4 s (against 10 kΩ). Replacing it with a binary search would reduce the duration to 61 ms, extending significantly runtimes even at short communication intervals. This optimization is therefore proposed for future implementations.

Implantability and *in vivo* validation Compared to the CR1216-powered STELLA3 (2.6 g, 1.3 cm^3, 7.5 mm height), STELLA3.1 is heavier (+ 0.4 g) and occupies ≈ 54 % more volume (+ 0.7 cm^3), though its maximum height is slightly reduced. The increased weight, volume, and especially length place STELLA3.1 above acceptable implantability thresholds for hamsters. In rats, however, implantability remains favorable. The device corresponds to only 1% of body weight and remains significantly smaller than commercial reference implants such as the HD-S02 (see Section 5.3.5).

In a pilot study [A14], a fully encapsulated STELLA3.1 was implanted into a rat for 8 days with unilateral stimulation (100 µA, 60 µs, 130 Hz). In this study, only Scenario 1 was performed to validate bidirectional communication between the base station and the implant. The implant was activated once per day by a magnet swipe, initiating a bidirectional

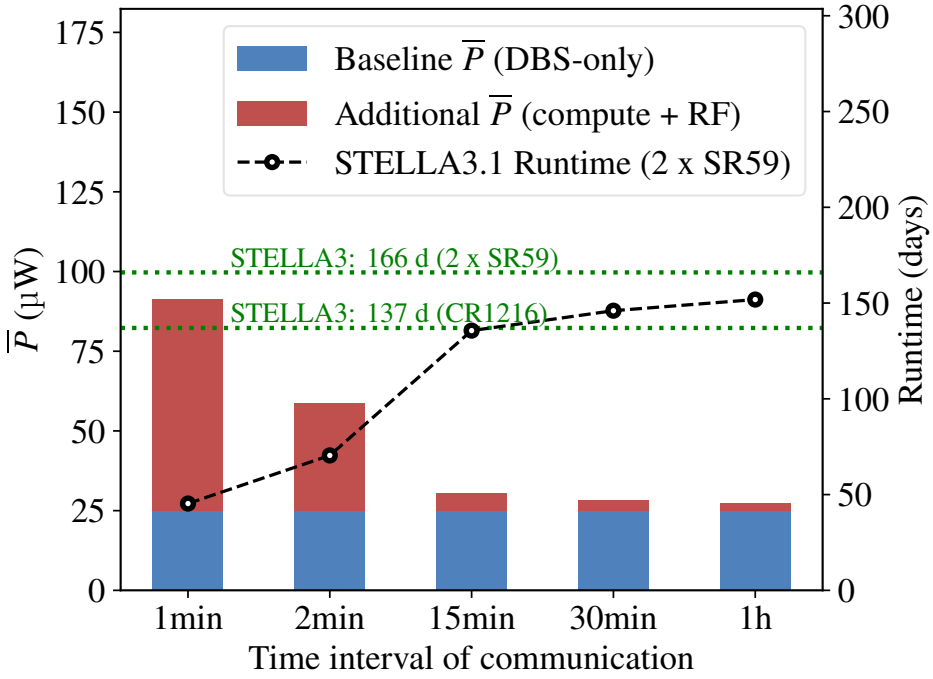

Figure 34: Average power consumption and runtime of STELLA3.1 for communication intervals between 1 and 60 minutes. Stacked bars show baseline (24.9 µW) and additional power consumption, while the dashed black curve indicates the runtime of STELLA3.1 powered by two SR59 cells in series. Adapted from [A14].

communication with the base station for configuration update and status transmission. Stable RF communication was observed over 6 m through implant housing and tissue at −2 dBm TX power. The implant was well tolerated by the rat, and daily status logs confirmed stable operation. The values of $\hat{V}_{\text{stim}}$ ranged from 1.1 V to 1.4 V, reflecting the dynamic biological processes occurring at the electrode after implantation.

5.7 D-Shaped Air-Filled Housing for STELLA3

The main limitation of the PEEK epoxy potting encapsulation was its lack of recyclability. This became particularly problematic during the COVID-19 pandemic, when semiconductor shortages made reproduction more difficult. Results from the STELLA3.1 air-filled encapsulation *in vitro* and *in vivo* experiments demonstrated that air-filled encapsulation was suitable for long-term implantation. Consequently, within the ELAINE project, the focus shifted towards adopting the air-filled encapsulation also for STELLA3.

Since the SR cell side-by-side battery-PCB approach proved too bulky, especially for hamsters, the previous battery-PCB stack approach was reinstated. This enabled a design change,

replacing the drop-shaped housing with a shorter, D-shaped housing.[13]

The basic principle is the same as in the proposed air-filled drop-shaped housing, consisting of a body and a cap (0.6 g in total). However, in the D-shaped design, the electrode leads exit from the front rather than through a side channel. The positioning of the feedthrough holes was optimized to improve cable alignment. Additionally, recesses were integrated around the lead feedthrough to increase the local volume available for silicone filling, thereby improving long-term waterproofness at these critical weak points. The detailed assembly and encapsulation protocol is provided in the Appendix D.

The encapsulation design of the D-shaped STELLA3 implant is shown in Fig. 35A, placed next to the commercial telemetry device ETA-F10 (1.6 g, 18.7 mm × 12.6 mm × 5.6 mm (L×W×H), 1.1 cm^3) for scale. Fig. 35B illustrates the top view, highlighting the footprint, while Fig. 35C shows the side view, emphasizing thickness. The D-shaped STELLA3 implant weighs 2.4 g (including electrodes) and measures 17.4 mm × 14.8 mm × 6.6 mm (L×W×H), corresponding to an approximate volume of 1.3 cm^3. Compared to DSI's ETA-F10, it shows a modest increase in weight (+ 0.8 g) and height (+ 1.0 mm), while maintaining a similar footprint and implant volume. In hamsters, this corresponds to 5–6.8 % of body weight, and in rats < 1 %, which, combined with the small volume, confirms suitable implantability.

Relative to the earlier epoxy-potted STELLA3 design, the D-shaped housing achieves ≈ 7 % weight reduction (2.4 g vs. 2.58 g) and ≈ 12 % reduction in height (6.6 mm vs. 7.5 mm). Compared to the drop-shaped STELLA3.1 design, it is ≈ 21 % lighter (2.4 g vs. 3.03 g) and ≈ 35 % smaller in volume (1.3 cm^3 vs. 2.0 cm^3).

Taken together, these comparisons demonstrate that the D-shaped encapsulation's physical properties outperform both previous encapsulation designs (epoxy-potted and drop-shaped), while achieving values very close to those of the ETA-F10, which is specified for implantation in animals ≥ 19 g.

This encapsulation concept was finally adopted within the ELAINE project for STELLA3. Its compact form and high biocompatibility allowed reliable implantation in both rats and hamsters, reducing post-operative strain and supporting faster recovery. By eliminating the burden associated with existing head- and back-mounted devices, the fully implantable STELLA3 represents a clear refinement in line with animal welfare principles. Both excellent implantability and long-term waterproofness were confirmed across a large number of successful implantations in small rodents.

[13]The final air-filled encapsulation method for STELLA3.0 continues the author's previous drop-shaped housing approach. Felix Uster handled the CAD modeling and 3D printing, while Nils Arbeiter adapted the method to the new housing design and contributed to the assembly of several implants. Denise Franz designed and refined the final protocol (see Appendix D) and tested the implants in several *in vitro* and *in vivo* experiments. Henning Bathel applied the method comprehensively on many implants, from assembly to final encapsulation. Dirk Timmermann provided general guidance on the 3D design and encapsulation method.

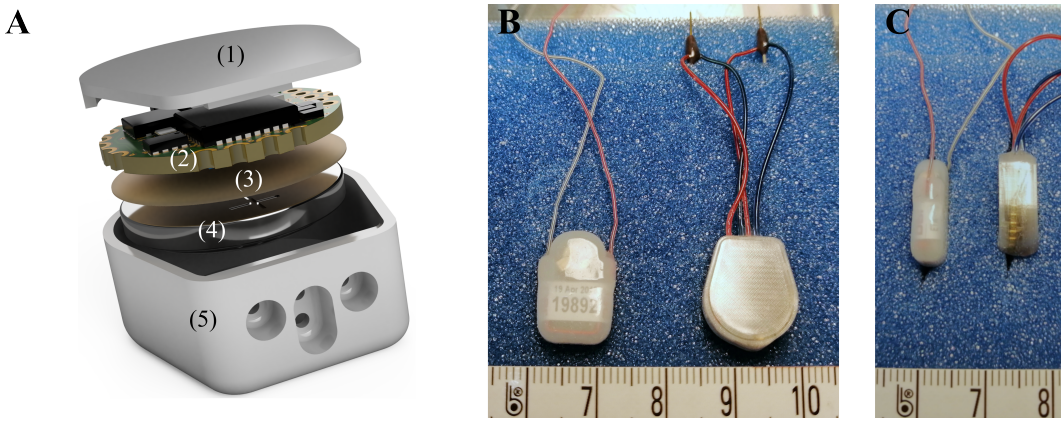

Figure 35: (A) 3D assembly of STELLA3 using the D-shaped housing showing the main components: (1) cap, (2) STELLA3, (3) electrically insulating film, (4) CR1220 coin cell, and (5) main body. (B) and (C) show the encapsulated[§] STELLA3 device (right) compared to the commercial DSI's ETA-F10 (left), in top (B)[*] and side view (C)[*].

[§] Encapsulated by Henning Bathel.
[*] Photographs by Denise Franz.

5.8 Interim Conclusion of STELLA3.1

STELLA3.1 extends the capabilities of STELLA3 by introducing a bidirectional RF communication, elevating the system from a pure stimulation device to a remotely controllable and monitorable DBS platform. In a pilot rat experiment, STELLA3.1 maintained stable RF communication through tissue over a distance of approximately 6 m, enabling remote parameter updates and status reporting (e.g., BIST results) during chronic stimulation. This advancement addresses the limitations of visual LED feedback, which is affected by attenuation, device rotation, and the need for manual activation by a magnet.

An important technical aspect of the design was the selection of high-drain (HD) silver oxide cells capable of driving the current spikes required for RF events. In contrast to smaller CR coin cells such as the CR1216, which collapse under RX events, two SR59 cells connected in series maintained a stable battery voltage. At communication intervals of 15 min or longer, the additional power consumption introduced by RF communication was only a few microwatts above the baseline of STELLA3, resulting in runtimes of 136–152 days, nearly matching STELLA3's runtime with a CR1216.

The epoxy-potting encapsulation method used for STELLA3 proved unsuitable for RF-capable STELLA3.1, as the epoxy's dielectric loading caused significant detuning. To overcome this, an air-filled, 3D-printable PETG housing with a drop-shaped form was developed, allowing side-by-side placement of battery and PCB. This design yielded an RF-compatible housing without the need for impedance re-tuning and enabled electronic recycling. However, it exhibited reduced durability compared to the epoxy-potted implant. *In vitro* results showed

that humidity-related failures occurred after approximately 11 weeks versus 21 weeks for the epoxy-potted version. Although the encapsulated STELLA3.1 shows increased volume (+ 0.7 cm^3) and weight (+ 0.4 g) compared to the epoxy-based CR1216-powered STELLA3, it remains within acceptable implantability limits for rats, albeit exceeding thresholds for hamsters. Based on the advantage of a recyclable air-filled housing, this encapsulation method was adapted and refined for STELLA3, resulting in the compact D-shaped housing, which is exclusively used within the ELAINE project.

STELLA3.1 represents a further advancement within the STELLA family by incorporating bidirectional RF communication into the well-established STELLA3 architecture. In the context of existing rodent DBS devices (see Table 1), STELLA3.1 is the first fully subcutaneous implantable device with bidirectional RF communication validated in rats. At the same time, it retains the ultra-low power, dual-channel, charge-balanced current-controlled stimulation architecture and built-in self-test functionality of STELLA3.

While STELLA3.1 was not the subject of extensive *in vivo* investigation, its development provided an important foundation for the subsequent version of the STELLA family. The lessons learned, particularly in selecting batteries capable of supporting RF communication, RF PCB design, and understanding the impact of encapsulation on RF performance, were incorporated into the design of the next version: STELLA4.

5.9 Realizing a Highly Functional DBS Device: STELLA4

STELLA3 and STELLA3.1 represent significant advancements in the development of fully implantable, low-power DBS systems for preclinical research in small rodents. While the STELLA3 device provides reliable current-controlled and charge-balanced stimulation, STELLA3.1 extends these capabilities with bidirectional wireless communication.

However, clinical DBS research has increasingly shifted toward closed-loop (adaptive) stimulation paradigms, in which physiological biomarkers are monitored and used to dynamically adjust stimulation parameters. Such feedback-based approaches aim to improve therapeutic efficacy and enable individualized stimulation strategies. However, the translation of these concepts into preclinical research remains limited, as existing rodent DBS systems, including STELLA3 and STELLA3.1, lack the capability for biosignal acquisition, on-board processing, and low-power communication required to evaluate adaptive stimulation schemes.

Beyond the absence of appropriate closed-loop functionality, the following technical constraints were identified in the previous versions:

- insufficient compliance voltage for stimulation parameters required by the BAC-transgenic rat model,

- labor-intensive encapsulation procedures,
- high power consumption and limited interoperability of the RF module used in STELLA3.1.

These limitations motivated the next step within the STELLA family: STELLA4. Building on the strengths of its predecessors, STELLA4 introduces several major enhancements:

- **Bluetooth Low Energy (BLE)** for low-power wireless data transmission and device control.
- **On-board biosensing** allows the acquisition of relevant biological signals.
- **On-board computation** supports real-time processing of physiological data, essential for adaptive DBS applications.
- **Enhanced stimulation unit** offers improved functionality and safety.
- **Rechargeability via stimulation leads** allows for convenient recharging of a Li-ion battery without breaking device encapsulation.

Fig. 36 provides a high-level system overview.

This section documents the circuit architecture and validation of STELLA4, focusing specifically on hardware implementation and performance evaluation of power consumption and of the stimulation unit under open-loop conditions. Parts of this section were published in [A13].[14] The validation of BLE communication, biosignal acquisition, and closed-loop DBS operation is planned for future studies and is therefore outside the scope of this work.

5.9.1 System Architecture

The system architecture of STELLA4 is the result of a comprehensive evaluation of multiple design options, including comparisons of specifications, simulations, and hardware prototyping to identify optimal trade-offs between functionality, power consumption, and compact size. The resulting design integrates five major subsystems:

Battery and Power Management

Unlike STELLA3, which relied on non-rechargeable (primary) CR/SR cells, STELLA4 uses a rechargeable Li-ion coin cell (VARTA CoinPower A4X). An innovative recharging method via the stimulation leads eliminates the need for frequent battery replacements. Multiple

[14]The author defined the system architecture, designed the circuit schematic, built and tested the hardware prototypes, and implemented the fundamental MSP430 firmware for DBS application of STELLA4. The overall firmware architecture, including BLE communication, system control, and data acquisition, was developed by Robert Hauser. The *in vitro* experiments and other technical characterizations of STELLA4 were conceptualized, carried out, and analyzed by the author. Christian Haubelt, Dirk Timmermann, Alexander Storch, and Mareike Fauser provided the resources for this work.

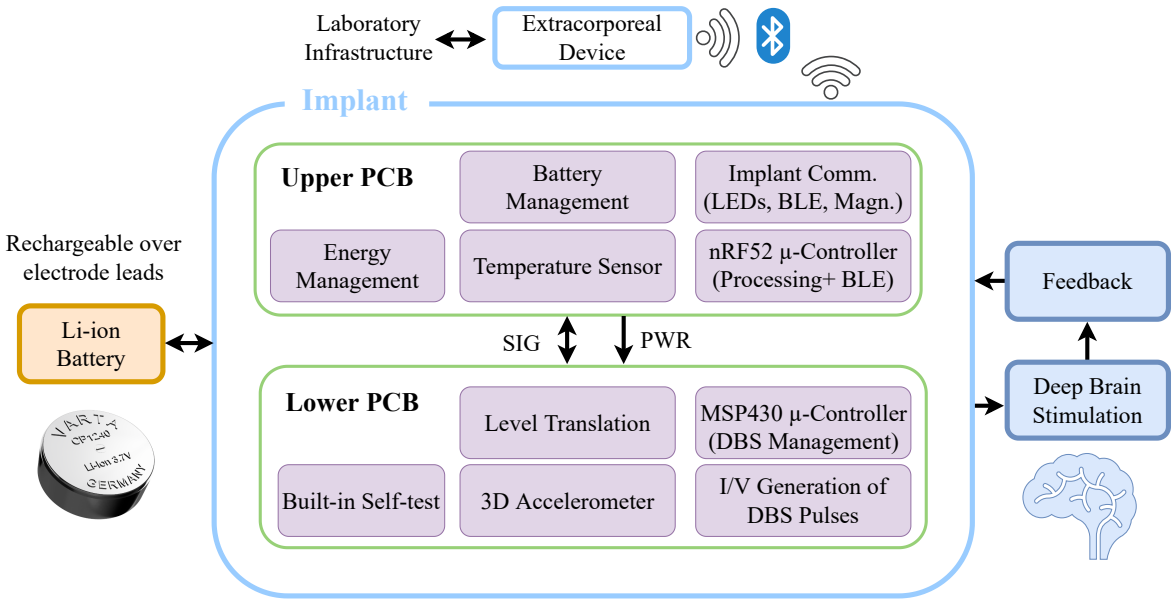

Figure 36: Overview of the STELLA4 system architecture for advanced preclinical DBS research in rodents. Adapted from [A13].

protection mechanisms guard the cell against damage and thermal runaway (see Section 5.9.6 for more details).

A dual-V_{DD} architecture replaces the single-V_{DD} design used in STELLA3, providing separate, stable voltage rails for both digital and analog domains, thus improving the compliance voltage range and energy efficiency under varying load impedances (see Section 5.9.4 for more details).

Control and Computation

The primary control unit is based on the MSP430FR2355 ultra-low power microcontroller [165]. It replaces the earlier MSP430G2553 used in STELLA3, offering an extended feature set (e.g., expanded memory capacity and additional timers). To meet the demands of computationally intensive tasks of real-time closed-loop algorithms, STELLA4 incorporates a second microcontroller: the nRF52833 [174]. This microcontroller is built around a 32-bit ARM Cortex-M4 clocked at 64 MHz and comes with an integrated Bluetooth Low Energy (BLE) radio module, enabling low-power and standardized wireless communication. The system bus comprises the inter-integrated circuit (I^2C) and SPI bus for communication with sensors and actors, which can be tasked either by the MSP430 or the nRF52.

Stimulation

STELLA4 features a multi-modal architecture capable of generating both charge-balanced current-controlled and charge-balanced voltage-controlled DBS pulses, both provided by clinical DBS devices. The MSP430 controls a 2:1 analog switch (TMUX1136) that enables

the selection between the stimulation modes for each channel. The current-controlled mode is generally the preferred configuration, as it maintains a constant current regardless of load impedance changes [108, 101, 132]. Therefore, this mode is particularly optimized for energy efficiency and is the primary focus of this section. In view of current developments in other medical fields, such as traumatology, the voltage-controlled mode also shows promising potential for application in bone regeneration [A4][171, 113]. To support such research directions, STELLA+ incorporates a 10-bit digital-to-analog converter (DAC) implemented with the IC DAC6311 on each channel controlled by the SPI bus, enabling the generation of arbitrary voltage-driven waveforms tailored to the specific research objectives. The stimulation unit of STELLA4 retains the two-channel architecture of its predecessor, with each channel comprising a current source, a blocking capacitor (with a parallel discharge resistance), and a switch for passive charge balancing. The MSP430 handles pulse generation via a PWM signal and adjusts the current amplitude via digital potentiometers. Compared to STELLA3, the stimulation unit incorporates several enhancements, including a wider compliance voltage range, an increased current amplitude range with higher accuracy, and independent channel control (see Section 5.9.7 for more details).

Biosensing

To enable physiological monitoring and support closed-loop DBS, STELLA4 integrates two on-board sensors:

- A high-precision digital temperature sensor (TMP119) for monitoring the animal's body temperature, enabling early detection of fever as an indicator for infection [13].
- A low-power 3-axis accelerometer (BMA400) for detecting and quantifying animal movement, which has been identified as a valuable biomarker for distinguishing between healthy and 6-OHDA-lesioned rats [A8]. Therefore, accelerometry represents a promising biomarker for preclinical adaptive stimulation paradigms.

Built-in Self-test for Stimulation Monitoring (BIST)

STELLA4 features an enhanced built-in self-test for stimulation monitoring (BIST) functionality to detect typical faults in stimulation experiments. The system integrates two operational amplifiers (TLV9052S) and a 10-bit DAC (DAC6311), which replaces the 8-bit digital potentiometer used in STELLA3, thereby providing higher resolution for determining $\hat{V}_{\text{stim}}$.

Wireless Interface

STELLA4 replaces the CC2500 RF module used in STELLA3.1 with the integrated Bluetooth Low Energy (BLE) radio module of the nRF52833 microcontroller. This transition significantly reduces power consumption during data streaming and ensures interoperability

through a standardized wireless protocol. To ensure reliable system access even when BLE communication is unavailable, such as during power-saving operation, STELLA4 includes a redundant offline interface. This functionality is implemented using a low-power magnetoresistive sensor (CT8132BV-HLV), which triggers when a magnetic field is applied, replacing the more power-intensive Hall effect sensor. For visual feedback, the device integrates three status LEDs (red, green, and infrared), providing improved readability and more detailed system diagnostics compared to the single red LED in STELLA3. For example, the green LED indicates a fully charged Li-ion battery.

Fig. 39A illustrates how these subsystems interact. The following subsections provide detailed descriptions of the physical layout, evaluation board, power management, communication architecture, charging concept, and stimulation unit enhancements.

5.9.2 Physical Design and Battery Integration

To accommodate the increased functionality of STELLA4 while maintaining a compact form factor, the piggyback solution from STELLA3.1 was refined using a highly miniaturized 34-contact mezzanine connector. This connector enables both signal and power transfer between two stacked PCBs, resulting in a dual-PCB configuration that doubles the available component area without increasing the device footprint (see Fig. 37A). A second 14-contact mezzanine connector was placed on the lower PCB, providing access to both the I^2C and SPI buses. This allows for the connection of additional sensors and actuators via a plug-in expansion board. To attach the stimulation leads, castellated holes at the lower PCB were designed, which allow a stable solder connection.

The VARTA CoinPower series includes Li-ion cells ranging from 9.4–16.1 mm in diameter, with heights of either 4 mm or 5.4 mm. In STELLA3, vertically stacking the battery and PCB increased the implant's overall height, while in STELLA3.1, placing the battery side-by-side significantly extended its length. To address both limitations, STELLA4 incorporates a circular cutout into the PCB layout to enable a more space-efficient encapsulation. Despite the high circuit complexity, a cutout with a diameter of 12.2 mm was successfully realized, enabling integration of Li-ion coin cells up to this diameter, such as the high-capacity CP1254 A4X (74 mAh, 12.1 mm × 5.4 mm) (see Fig. 37B). While the smaller 9.4 mm variants fit perfectly into the cutout, the 12.1 mm cells slightly extend beyond the PCB outline, forming a small lateral extension of the encapsulation.

5.9.3 Evaluation Board

An evaluation board (Fig. 38A) was designed and manufactured that allows for independent testing of the upper and lower PCB during the development phase. The board is equipped with microconnectors for convenient PCB plug-in (Fig. 38B), providing reliable access to all

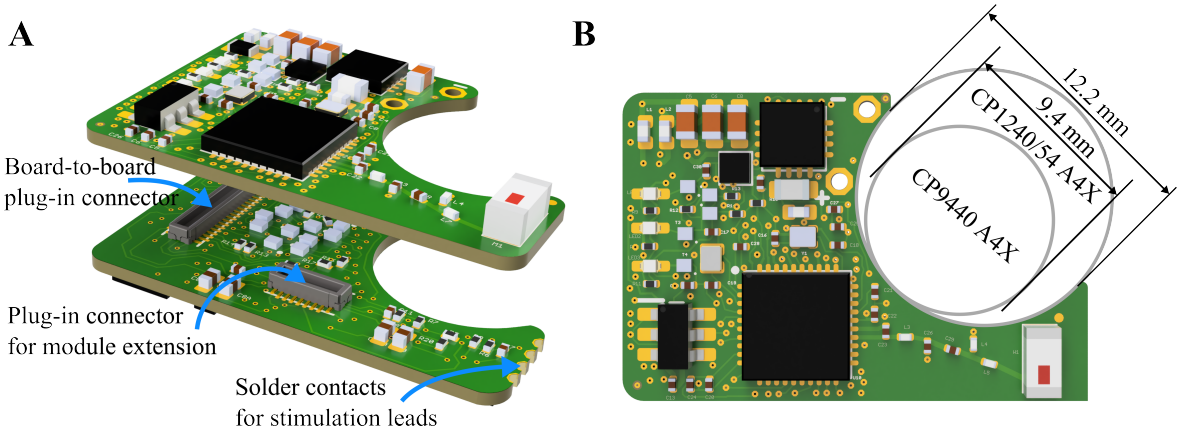

Figure 37: (A) 3D design of the dual-PCB layout, highlighting a mezzanine connector for power and signal transfer between both boards, a second mezzanine connector for future extensions, and castellated holes for stimulation lead attachment (adapted from [A13]). (B) Top view showing compatibility with Li-ion cells up to 12.2 mm in diameter.

critical power rails, signal lines, and the programming interfaces for the MSP430FR2355 and nRF52833 microcontrollers. Furthermore, the board allows access to the I^2C and SPI buses, enabling the evaluation of potential sensors for the DBS device.

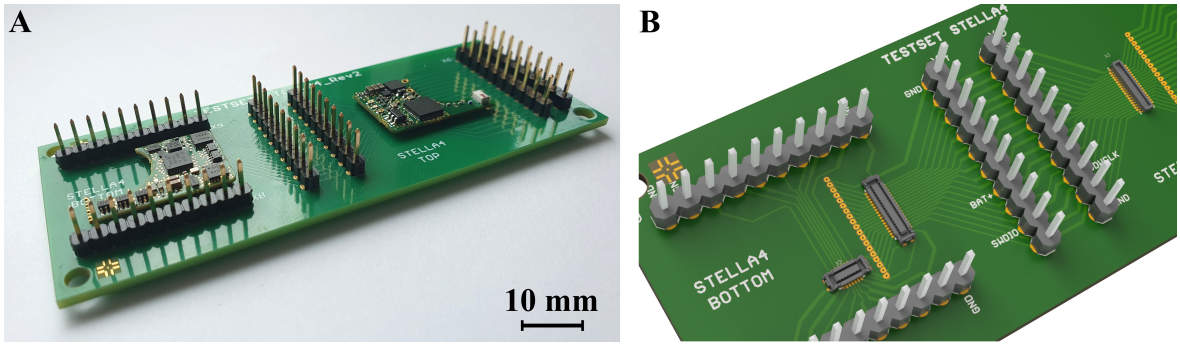

Figure 38: (A) Manufactured evaluation board with upper and lower STELLA4 PCBs connected. (B) 3D model of the evaluation board with unconnected STELLA4 PCBs, highlighting the mezzanine connector interfaces for power and signal access. The evaluation board enables convenient plug-in of the PCBs for system testing, firmware development, and sensor validation.

5.9.4 Power Management

STELLA3 implements a single-V_{DD} approach, where the control and stimulation unit share the same supply voltage generated by a boost converter. While this approach features low circuit complexity, the compliance voltage is limited to 2.8 V only, constrained by the maximum tolerable supply voltage of the microcontroller and sensors.

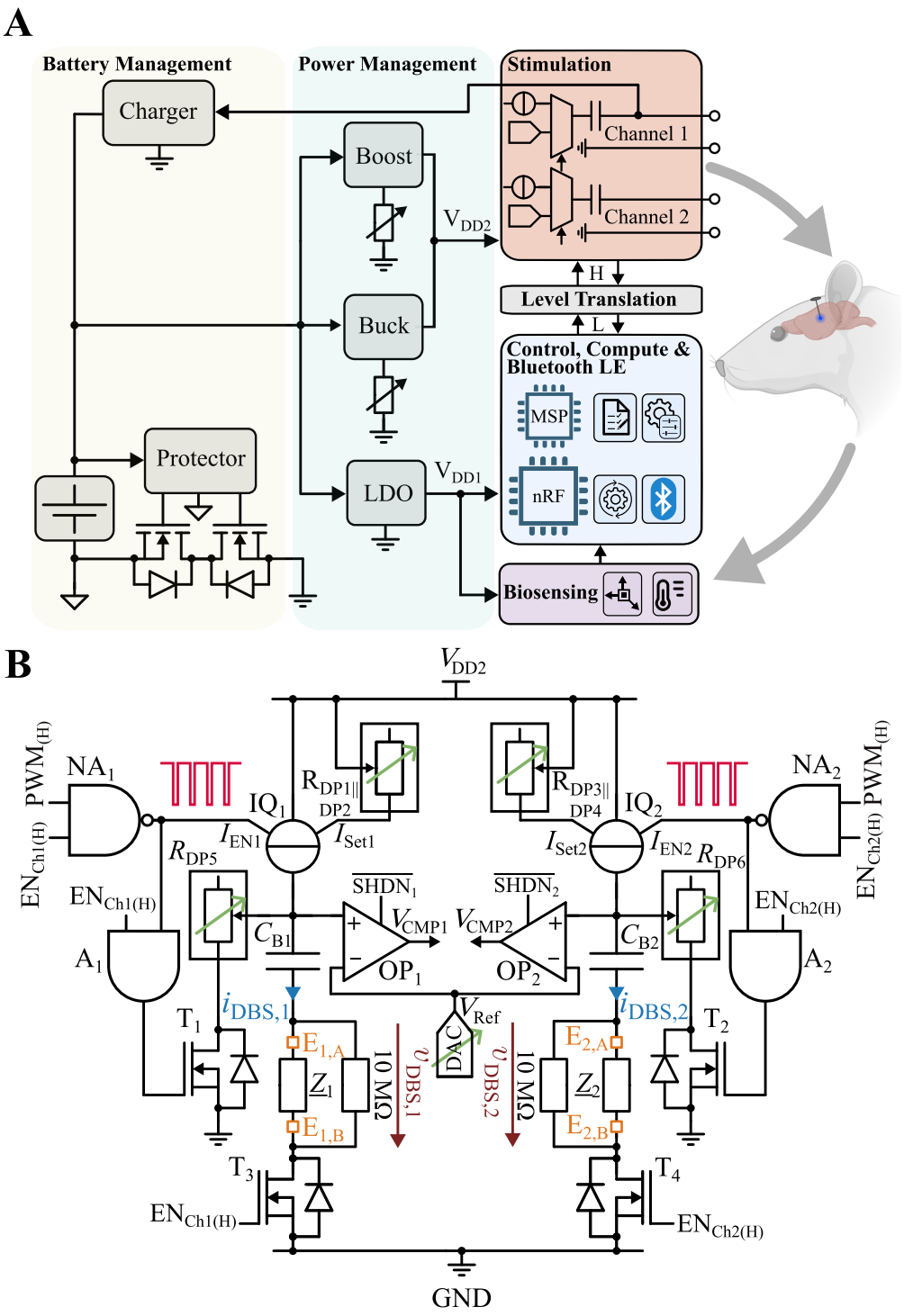

Figure 39: (A) Overview of the complete circuit architecture, including battery management, power management, biosensing, control, level translation, and stimulation blocks. It highlights the closed-loop capability, from biosignal acquisition and on-board computation to the adaptation of stimulation paradigms. (B) Detailed schematic of the symmetrical dual-channel stimulation unit implementing two parallel digital potentiometers for high-resolution current amplitude adjustment, passive charge balancing, independent channel control via enable signals, and crosstalk reduction for interleaved bilateral stimulation. Each channel also includes a built-in self-test mechanism for detecting all three failure conditions (open-circuit, short-circuit, compliance voltage violations) and a 10 MΩ resistor in parallel to reduce the bias voltage induced by the blocking capacitor. Adapted from [A13]. Partly created with BioRender.com.

In STELLA4, a Li-ion battery (VARTA, CoinPower, A4X) operating within a voltage range of 3–4.3 V is used as an energy source. To overcome the compliance voltage limitations of STELLA3, a dual-V_{DD} approach was applied, separating the control and stimulation unit into independent voltage rails. In this configuration, the microcontrollers and peripheral circuitry operate from a fixed 2.8 V rail (V_{DD1}) powered by an LDO (Low-Dropout) regulator (TPS7A0228). This prevents an increase in power consumption of the digital subsystem that would otherwise occur in a single-V_{DD} architecture when the supply voltage is raised to achieve higher compliance voltages. Furthermore, by enabling the nRF's integrated DC/DC converter through dedicated external components, the microcontroller steps the external 2.8 V rail down to an internal core voltage of 1.3 V, thereby improving energy efficiency [174].

Only the stimulation unit's supply voltage is dynamically controlled, enabling higher compliance voltages without increasing the digital subsystem's power consumption. This dynamic control is realized with a flexible buck-boost converter topology. The boost (MAX17227A) and buck (MAX38642A) converters are individual ICs with their outputs tied together. Each converter has an EN pin that is used to enable or disable the outputs. These pins are managed by the MSP430 microcontroller, ensuring that only one converter is active at a time, preventing output conflicts. The output voltage of each converter is controlled by an individual digital potentiometer (AD5142A) in rheostat mode via I^2C. This topology enables the supply voltage for the stimulation unit (V_{DD2}) to be scaled either above or below the battery voltage over a range from 2.5 V to 5.2 V. Combined with the built-in self-test (BIST) that identifies the maximum voltage at the end of the DBS pulse, this method enables energy-efficient adaptation of the supply voltage for the stimulation unit according to the load impedance requirements (compare with Section 5.2.5).

5.9.5 System Communication and Logic-Level Translation

STELLA4 integrates I^2C and SPI buses for digital communication, while both current sources are driven by a single PWM signal generated by the MSP430 microcontroller. Dedicated enable (EN) signals allow the selective power down of specific ICs.

Since the stimulation unit and control subsystems operate at different supply voltages, an efficient level-translation strategy was required to ensure signal integrity across voltage domains. Fig. 40A illustrates the overall communication architecture, showing how sensors and actuators are connected to their respective signal lines and supply rails.

To translate the low-voltage PWM signal (PWM_L) to the higher voltage rail (PWM_H), a translation buffer (74LV1T34) is used (see Fig. 40B). A dedicated IC is critical in this case as it ensures excellent signal integrity across the entire translation range required for the sharp rise and fall time of the rectangular waveform. Although the additional supply current in typical voltage translators increases significantly as the input voltage deviates from the supply

voltage, this approach remains feasible due to very low duty cycles encountered in DBS (e.g., 0.78 % for a pulse duration of 60 µs and a frequency of 130 Hz).

All remaining logic signals (I^2C, SPI, EN), employ basic n-channel MOSFETs with pull-up resistors for level translators (see Fig. 40C). The CSD15380F3 was selected for all MOSFETs due to its small footprint (0.73 mm × 0.64 mm) and excellent switching performance, enabled by very low input and output capacitance (< 10 pF). This discrete approach offers an area and energy efficient solution, well suited to the moderate data rates of on-board STELLA4 communication, with pull-up resistor values chosen as high as possible to ensure minimal current consumption while still meeting the timing requirements of each signal.

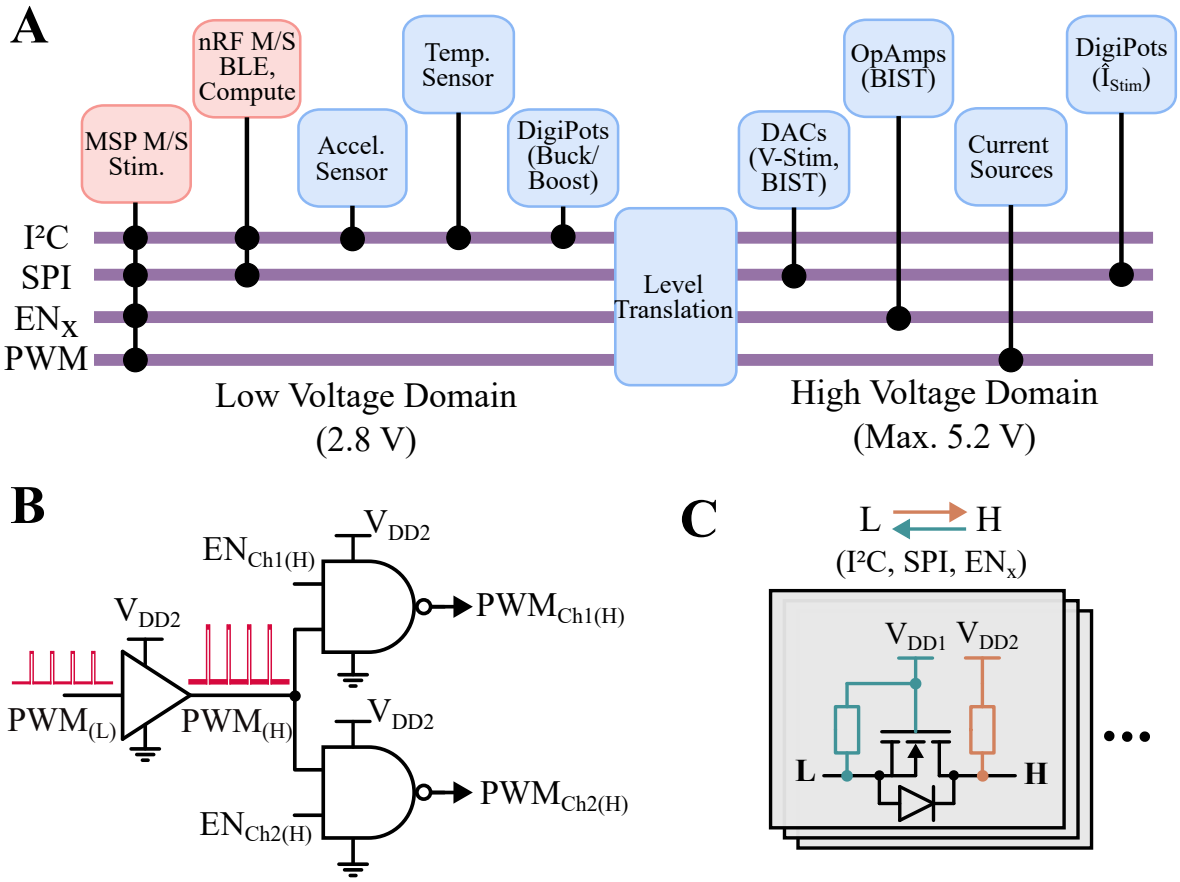

Figure 40: (A) Overall bus architecture illustrating how sensors and actuators interface with their respective communication lines and voltage domain. (B) Translation of the PWM signal into the higher voltage domain V_{DD2} using a translation buffer with subsequent NAND gates for channel control. (C) Logic level translation of I^2C, SPI, and EN signals using n-channel MOSFETs. Adapted from [A13].

5.9.6 Li-ion Battery Charging and Protection

When an electrically active implant is fully encapsulated in epoxy, device reuse becomes impossible after battery depletion, leading to increased system costs and considerable time

required for remanufacturing. Even in air-filled housings, replacing the battery requires a laborious manual process to break and remake the encapsulation.

To address these challenges, STELLA4's circuit is designed to operate on a rechargeable Li-ion battery that eliminates the need for battery replacement. A special feature in this design is that one stimulation channel (Ch_1) functions as both the stimulation output and the battery charging input, allowing convenient recharging directly through the electrode leads for each new experiment. Additionally, this capability allows the encapsulated implant to undergo long-term *in vitro* waterproofing tests and, once verified, be used for subsequent *in vivo* experiments.

According to VARTA's specifications, the Li-ion battery can be recharged approximately 600 times without significant capacity loss. Even if recharged weekly, although this is a very unrealistically frequent scenario, it would still last around 11.5 years.

Charging circuit Battery charging is managed by a dedicated charger IC (BQ25100A), configured to a charge limit of 4.3 V and a charge current of 10 mA. To ensure that the charger IC does not interfere with the stimulation, a bilateral transient voltage suppressor (TVS) diode (SP0201B-ELC-01UTG) with a breakdown voltage of ±9.6 V/1 mA and very low parasitic capacitance 0.15 pF is placed between the stimulation channel and the charger IC input. The low capacitance of the diode is essential, as the high-frequency components of the square wave stimulation signals could otherwise couple into the charging circuit and distort them. In addition, the TVS diode's breakdown voltage remains safely above the maximum stimulation voltage of 4.3 V.

Given the voltage drop across the TVS diode with a charge current of 10 mA, the power source must output approximately 15 V to provide a sufficiently high input voltage for the charger IC. A blocking capacitor in series with the current source (C_B), already present for protecting the brain tissue in a failure event, also acts as high-voltage protection for the current source and the built-in self-test circuitry.

Mechanisms for battery protection Li-ion batteries carry a risk of thermal runaway if operating outside their specified conditions. This is particularly critical when implanted in living organisms. To prevent cell damage and ensure safe operation, the circuit includes protection mechanisms to prevent the cell from falling below its minimum discharging voltage and from exceeding its maximum charging voltage, charging current, and discharge current.

Regarding VARTA's specifications [237], a standard charging of 0.5 C is recommended. The charging IC is therefore set to a charging current of 10 mA, which is appropriate even for the smallest CP9440 A4X cell (29 mAh). Additionally, this low charging current minimizes battery heating, thus reducing thermal stress on the housing.

Additional protection is provided by a dedicated battery protection IC (S-82A1ACA-I6T1U) in combination with two external n-channel MOSFETs. These MOSFETs are controlled by the protection IC and act as a solid-state relay (SSR), disconnecting the battery ground from the system ground if any parameter falls outside the safe range specified by VARTA [237]. If the battery voltage drops below the minimum discharge voltage threshold of 3 V, the IC enters a power-down mode, reducing the battery's discharge current to just 50 nA and thus preventing further cell discharge.

The VARTA CoinPower Series was also selected for its integrated safety feature of three venting holes positioned 120° apart. In the event of a thermal runaway, the battery expands, causing the vents to open and safely release excess pressure. Therefore, an air-filled housing with sufficient expansion space is required. VARTA specifies an additional clearance in the axial direction of up to 1.5 mm [237].

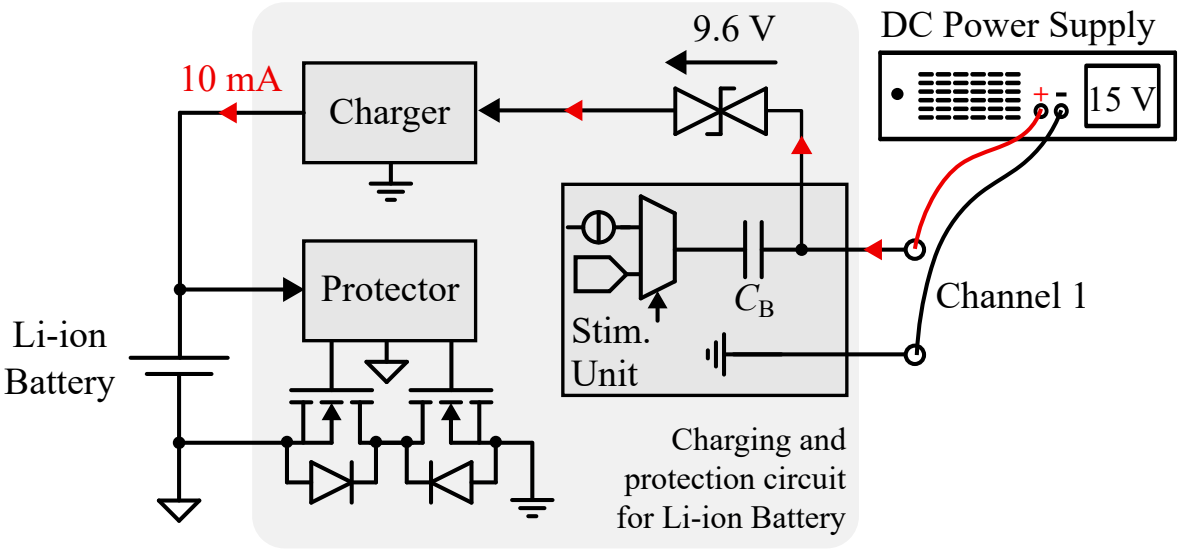

Figure 41: Schematic diagram of the STELLA4 charging and protection concept. The figure shows the circuitry enabling Li-ion battery charging via the stimulation leads, allowing for recharging after full device encapsulation. An integrated battery protection IC safeguards the battery against overdischarge, overcharge, and excessive overcurrent. Adapted from [A13].

5.9.7 Enhancements of the Stimulation Unit

This subsection highlights the specific enhancements made to the stimulation unit of STELLA4 compared to its predecessor, STELLA3. A detailed schematic of the stimulation architecture is shown in Fig. 39B.

Higher accuracy and extended range of current amplitude In STELLA3, the current amplitude was adjusted using a single digital potentiometer connected in parallel with a fixed

30 kΩ resistor. This setup enabled precise adjustment of current amplitudes at 50 µA and 100 µA, tailored to the requirements of the stimulation setup specified in the project (Table 2).

However, adapting the system to different current ranges required fabricating a new PCB with an alternative resistor value. Moreover, this approach only provides high resolution within a limited 60 µA window (for example, 40–100 µA, or 100–160 µA). As a result, it was not possible to perform high-resolution current steps, for instance from 50 µA up to 200 µA. The output current of the pnp BJT current source follows an inverse relationship with the emitter resistance, resulting in a nonlinear behavior that, when using only a single digital potentiometer, causes coarse resolution at higher currents (refer to Fig. 19). Such high-resolution steps are often required in experimental studies where the current amplitude is stepwise increased until side effects occur and then set below that threshold to ensure maximal efficacy while avoiding adverse effects [114, 5, 64, 136].

STELLA4 addresses this limitation by using two digital potentiometers (AD5144, in rheostat mode) connected in parallel. This configuration increases the number of achievable resistance values, as each 8-bit digital potentiometer provides 256 discrete steps. When combined in parallel, these settings yield $256^2 = 65,536$ possible combinations, of which half represent unique resistance pairs when accounting for symmetry.

Fig. 42 illustrates the simulated current amplitudes obtained for various combinations of digital potentiometer end-to-end resistances (10 kΩ, 50 kΩ and 100 kΩ). Single potentiometer configurations are shown for comparison. The results demonstrate that the use of two potentiometers in parallel significantly enhances the resolution and flexibility of the current amplitude adjustment compared to the single potentiometer design. For instance, the 100 kΩ ‖ 100 kΩ configuration yields a minimum current of 26 µA while covering the typical range for movement disorder rodent models (see Fig. F.1) with sub-microampere resolution, and was therefore selected for STELLA4. Other configurations, though not within the scope of this work, achieve for the 10 kΩ ‖ 100 kΩ setup current amplitudes between 39–600 µA with ≈ 2 µA steps, and for the 10 kΩ ‖ 10 kΩ current amplitudes between 145–1000 µA with < 1 µA resolution.

Independent channel control While STELLA3 was limited to the simultaneous activation of both channels, STELLA4 enables independent control of each channel. This is achieved by routing the high-voltage PWM signal (PWM_H) to two NAND gates (NA_1,NA_2), with the other input of each gate connected to a level-shifted EN signal ($EN_{Ch1(H)}$, $EN_{Ch2(H)}$) controlled by the MSP430 (see Fig. 40B). As a result, either channel can be selectively activated or deactivated by its EN signal, reducing current consumption in unilateral operation.

Furthermore, the EN signal can be used to modulate the stimulation in an on-off control scheme, which was validated as an effective control mechanism for adaptive DBS in a recent

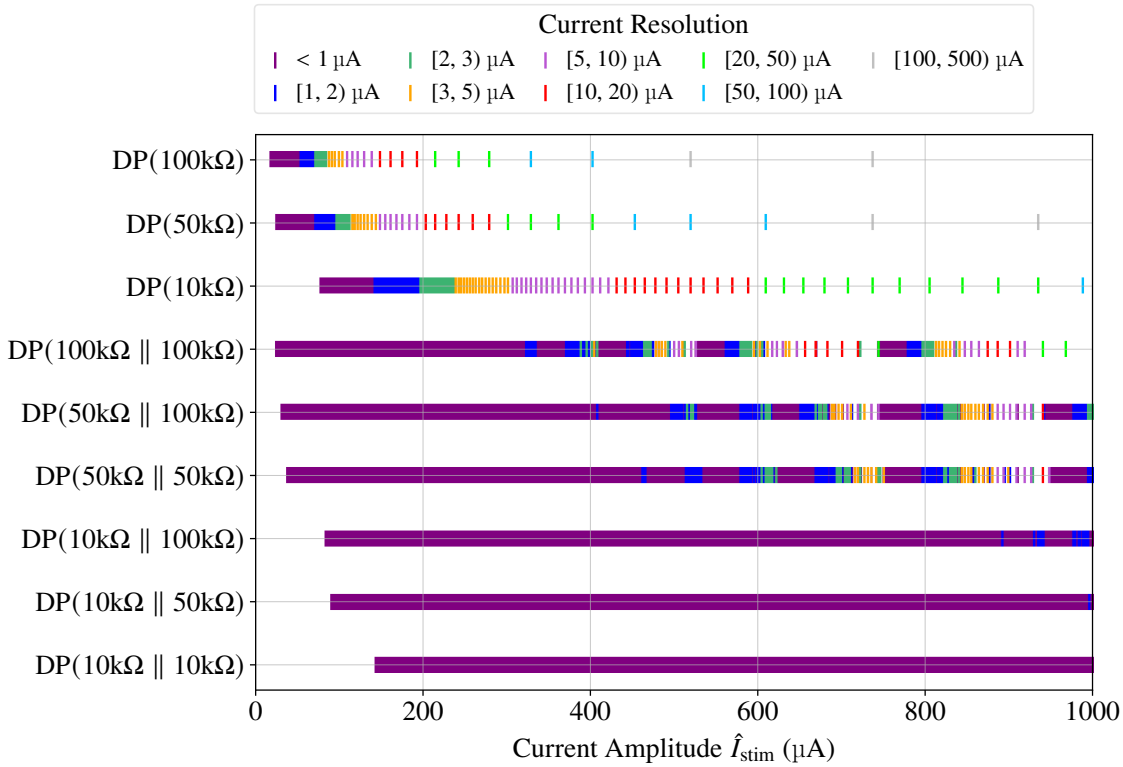

Figure 42: Programmable stimulation current amplitudes of two parallel digital potentiometers with end-to-end resistances of 10 kΩ, 50 kΩ, and 100 kΩ. Each vertical marker represents a discrete current amplitude value. The figure highlights the increased adjustment range and finer resolution obtained with dual potentiometer configurations compared to a single configuration. Note that the shown current amplitudes represent theoretical values, as the actual current delivery is constrained in practice by the compliance voltage of the current source.

study [65]. A potential advantage of this approach is that in the closed-loop scenario, it preserves the underlying stimulation rhythm as the PWM timer has not been interrupted.

Crosstalk reduction in bilaterally implanted but unilaterally stimulation configurations As outlined in Section 7.2, in the case of synchronous DBS of both hemispheres with bipolar electrodes, crosstalk can only be minimized through the use of galvanically isolated stimulation channels.

However, one potential experimental scenario can be optimized: when bilateral bipolar electrodes are implanted, but only one hemisphere is stimulated at a time (i.e., interleaved unilateral stimulation). For this scenario, a dedicated crosstalk reduction circuit was implemented. When the enable signal ($EN_{Ch1(H)}$) is set low, the output of the AND gate (A_1) remains low, ensuring that the n-channel MOSFET T_1, which is responsible for passive charge balancing, remains turned off (regardless of the PWM signal state). This disconnects the

return path of electrode contact E_{1A} from ground. The same enable signal simultaneously controls a second n-channel MOSFET (T_3), which disconnects the return path of electrode contact E_{1B} from ground when low. As a result, both electrode contacts (E_{1A} and E_{1B}) are set to high impedance, which reduces current flowing from the active to the contralateral electrode pair. An identical circuit is implemented for the second channel, enabling interleaved bilateral stimulation with minimized crosstalk interference.

Increased compliance voltage range STELLA3 supported a limited compliance voltage range of 2.2–2.8 V, constrained by its single-V_{DD} power architecture. While this range is sufficient to ensure stable stimulation in the 6-OHDA and *dt*^{sz} hamster setups, STELLA3 is unable to maintain a constant current throughout the stimulation pulse for the BAC-transgenic rat configuration, which requires the bipolar PI-SNEX-100 electrode with a current amplitude of 100 µA (see Table 2 and Fig. 13).

In STELLA4, this limitation was addressed by implementing a dual-V_{DD} architecture, which extended the compliance voltage range to 1.6–4.3 V. This expanded range enables both a wider range for optimal energy efficiency and a higher compliance voltage to accommodate higher load impedances and larger injected charges. Experimental measurements showed that the upper maximum stimulation voltage of the PI-SNEX-100 electrode (90th percentile) is approximately 3.8 V. Thus, a maximum compliance voltage of 4.3 V provides sufficient safety margin to account for biological variations at the electrode-tissue interface.

5.10 Results

Physical properties and encapsulation The overall dimensions of the STELLA4 PCB are 21.9 mm × 14.5 mm × 4 mm, featuring a circular cutout of Ø12.2 mm × 4 mm to accommodate the Li-ion battery. This corresponds to a PCB volume of 803 mm^3 and a PCB weight of 1.15 g.

Encapsulation was performed using a newly developed method based on a 3D-printed reusable silicone mold.[15] In the previous air-filled encapsulation method, the housed stimulation device was submerged in epoxy resin and subsequently cured in air (see Appendix D). In the improved process, the housed device is placed into a custom 3D-printed silicone mold, into which epoxy resin is subsequently cast. This approach ensures a uniform and reproducible encapsulation of multiple implants, significantly reducing fabrication time and material usage [231]. Fig. 43 shows an initially encapsulated STELLA4 implant with a CP9440 A4X battery and external stimulation leads (Open Source Instruments, Waltham, MA, USA).

***In vitro* validation of the stimulation unit** The performance of the stimulation unit of STELLA4 for current-controlled DBS was evaluated under *in vitro* conditions. A PI-SNEX-

[15] This encapsulation method was developed by Henning Bathel.

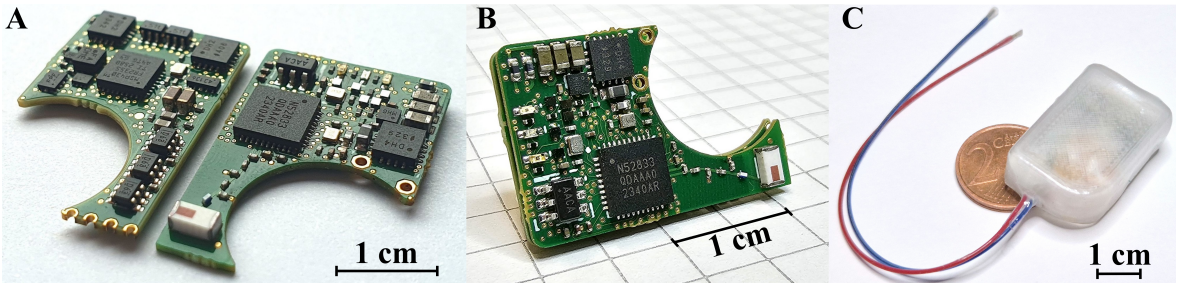

Figure 43: (A) Lower and upper STELLA4 PCBs shown side-by-side. (B) STELLA4 in its stacked configuration, interconnected through the 34-contact mezzanine connector (shown on millimeter paper). (C) STELLA4 encapsulated in an air-filled biocompatible housing[§], shown next to a 2 euro cent coin for size comparison.

[§] Encapsulated by Henning Bathel.

100 microelectrode was connected to one channel of STELLA4 and immersed in a NaCl conductivity standard solution of 0.1 S m^{-1} at controlled 25 °C.

The stimulation parameters were configured via Bluetooth Low Energy (BLE) using a standard smartphone and the *nRF Connect* application (Nordic Semiconductor). Current amplitudes of 50 µA, 100 µA and 150 µA were tested with pulse durations of 60 µs, 90 µs and 120 µs, respectively. Fig. 44A,B illustrate that all stimulation settings were precisely implemented, maintaining a stable constant current output across pulse durations, thus demonstrating the reliable performance of the stimulation unit.

Fig. 44C,D illustrate DBS voltage and current waveforms from a stimulation setup deliberately configured so that the voltage pulse reached the maximum compliance voltage of both STELLA3 and STELLA4. The data confirm maximum compliance voltages of 2.8 V for STELLA3 and 4.3 V for STELLA4, thereby demonstrating that STELLA4 is able to support a wider range of stimulation setups.

Fig. 44F shows the implementation of a randomly timed DBS on–off scheme. The switching pattern was generated by modulating the enable signal ($EN_{Ch1(H)}$) applied to the NAND gate (NA_1) of the first stimulation channel. This signal alternates between 0 V and 4 V, verifying the correct operation of the level translation circuitry (see 5.9.5) These results demonstrate that STELLA4 can reliably control stimulation according to an EN signal, thereby providing a mechanism for closed-loop DBS operation. In future *in vivo* experiments, this enable signal could be automatically driven by the feedback data from the accelerometer, allowing adaptive stimulation in response to the animal's movement.

Power consumption during DBS-only operation Power consumption measurements were performed with the Keysight CX3324A. The current waveform analyzer CX3324A was placed in series with an external power supply and STELLA4. The power supply was set to 3.7 V,

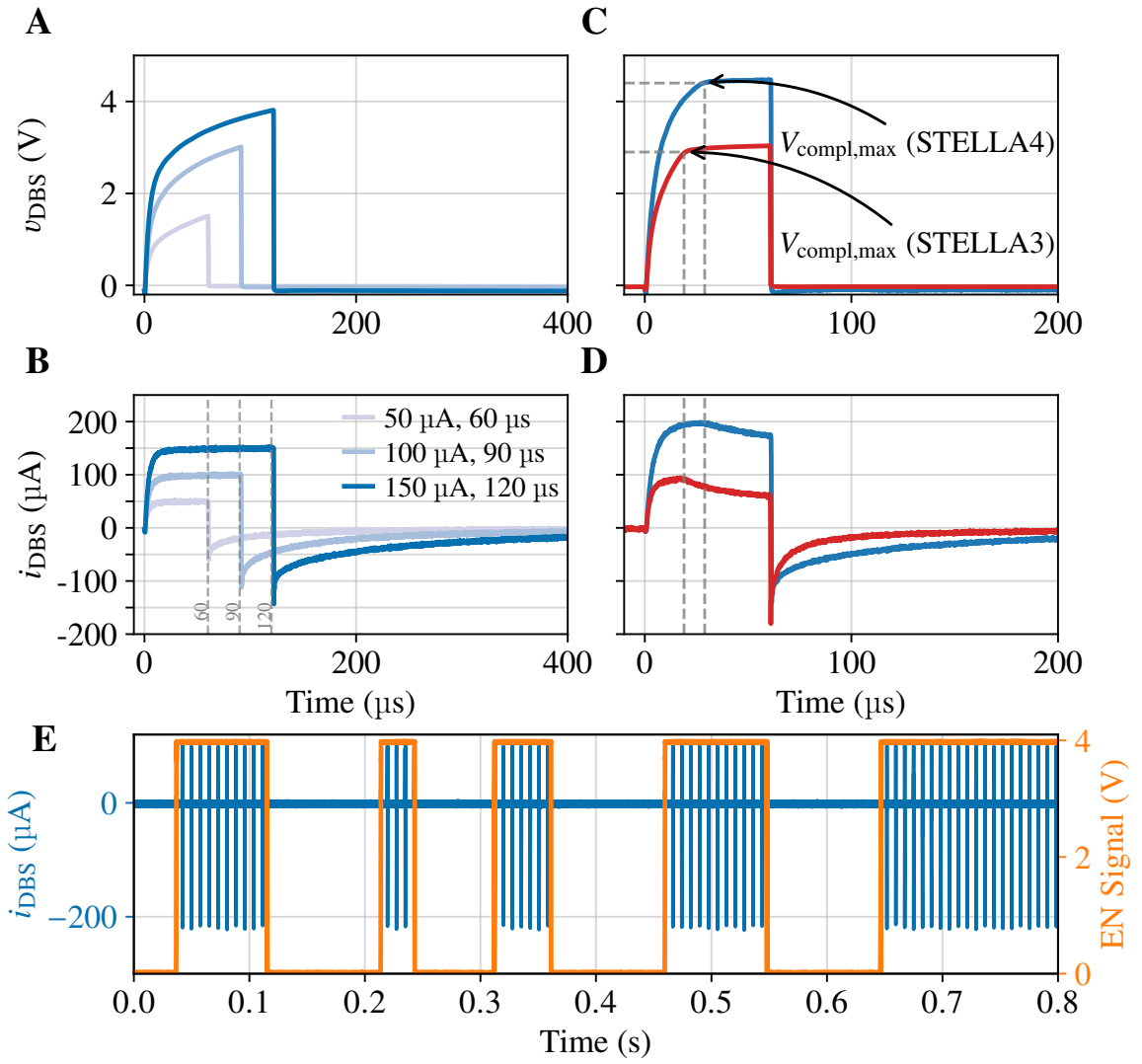

Figure 44: (A) DBS voltage (v_{DBS}) and (B) corresponding current (i_{DBS}) waveforms for different stimulation settings (50 µA/60 µs, 100 µA/90 µs, 150 µA/120 µs), showing constant current pulses with accurate current amplitudes and pulse durations, and effective passive charge balancing. Parameters were wirelessly configured via BLE. (C) Comparison of maximum compliance voltage ($V_{compl,max}$) between STELLA3 and STELLA4, highlighting increased voltage headroom in STELLA4. (D) Corresponding current waveforms, indicating the point where the compliance voltage limitation causes the current to drop. (E) Randomly timed DBS on–off scheme (blue) controlled by the enable (EN) signal (orange). Adapted from [A13].

which is the nominal voltage of the A4X series. The current consumption was then measured over the entire supply voltage range provided by the buck-boost topology, from a minimum of 2.5 V to a maximum of 5.2 V. Furthermore, all measurements were performed in DBS-only mode, using the following stimulation parameters: bilateral stimulation with a load of 10 kΩ, respectively, 100 µA current amplitude, 60 µs pulse duration and 130 Hz frequency.

STELLA4 achieves at its minimum compliance voltage of 1.6 V a power consumption of 32.9 µW and at its maximum compliance voltage of 4.3 V a power consumption of 92.9 µW. The results of the entire compliance voltage range are presented in Fig. 9. The Table 10 lists appropriate battery options and their respective battery runtimes.

Table 10: Battery options and corresponding DBS-only runtime estimates for STELLA4 (21.9 mm × 14.5 mm × 4 mm).

Battery	Dimensions (mm)	Energy (mWh)	Runtime (Best / Worst) (days)
CP9440 A4X	Ø 9.4 x 4.0	107	135 / 48
CP1240 A4X	Ø 12.1 x 4.0	185	234 / 83
CP1254 A4X	Ø 12.1 x 5.4	274	346 / 122

Preliminary *in vivo* Results No DBS studies have been conducted so far with STELLA4. However, an *in vivo* study was carried out to record motor activity in 6-OHDA-lesioned rats (n=24) using STELLA4's accelerometry functionality.[16] The devices were configured to continuously stream accelerometer data via BLE. The results confirm that BLE communication and the accelerometer functioned as intended, with the BLE interface maintaining stable wireless performance despite encapsulation and subcutaneous implantation. While a detailed evaluation of the *in vivo* study lies beyond the scope of this work, the results demonstrate the feasibility of conducting experiments under *in vivo* conditions using STELLA4.

5.11 Interim Conclusion of STELLA4

STELLA4 represents a major step forward compared to its predecessors and the state of the art, offering a highly functional, multimodal and closed-loop DBS platform for preclinical research in rodents. Building upon the architectures of STELLA3 and STELLA3.1, the new system successfully addresses the technical limitations identified in its predecessors by introducing advancements in power and battery management, stimulation unit, and wireless communication.

The redesigned stimulation unit features a parallel digital potentiometer configuration, independent channel control, crosstalk reduction for interleaved bilateral stimulation, and an on–off closed-loop paradigm, providing higher accuracy, flexibility, and energy efficiency. The implementation of a Li-ion battery with recharging capability via the stimulation leads represents a unique innovation, allowing device reuse after encapsulation and thus improving sustainability in research applications. Moreover, the adoption of Bluetooth Low Energy

[16]The *in vivo* experiments were conducted by Mareike Fauser and Meike Statz, while device setup and data collection via BLE was carried out by Robert Hauser.

(BLE) as a standardized communication interface, along with on-board biosensing and computation capabilities with an ARM Cortex-M4, establishes the basis for future closed-loop DBS experiments.

By enabling a maximum compliance voltage of 4.3 V through the dual-V_{DD} architecture, STELLA4 extends the voltage headroom beyond that of STELLA3. This allows stimulation with small, high-impedance electrodes ($\approx$ 100 µm), representing the lower end of reported diameter ranges, while still supporting modal preclinical DBS parameters of 100 µA/60 µs/130 Hz [255]. These conditions also satisfy the stimulation requirements of the BAC-transgenic rat model targeted in the project. The validation in *in vitro* confirmed the reliability of the stimulation unit, demonstrating a precise current-controlled pulse generation and verifying the extended compliance voltage of 4.3 V.

In addition, power consumption measurements showed that STELLA4 maintains an ultra-low power profile for DBS-only operation ($<$ 100 µW) up to the maximum compliance voltage, supporting months of continuous stimulation. By adjusting the compliance voltage between 1.6–4.3 V, optimal energy efficiency can be achieved for the targeted stimulation setup. It should be noted that when comparing the power consumption values between STELLA3 and STELLA4 at a compliance voltage of 2.2 V, STELLA4 consumes roughly only 11 µW more than STELLA3, despite its considerably expanded feature set. This small deviation indicates an effective underlying power-down architecture.

When positioning STELLA4 into the state of the art (see Table 1), STELLA4 uniquely combines dual-channel, charge-balanced, and software-adjustable stimulation with ultra-low power consumption below 100 µW, a built-in self-test (BIST) for stimulation monitoring, bidirectional wireless communication, and closed-loop capability with on-board computation. These features are realized within a compact form factor of less than 1 cm^3, with preliminary *in vivo* experiments demonstrating successful BLE communication and biosignal acquisition of animal movement under subcutaneous implantation in rats.

6 Summary

This dissertation presents the development of a new family of implantable DBS systems designed specifically to overcome the methodological limitations that currently restrict preclinical research in freely moving rodents. The work ranges from defining architectural requirements and characterizing electrode behavior to developing, fabricating, encapsulating, and validating fully functional implants.

A systematic review of 23 existing DBS systems for rodents revealed a significant mismatch between experimental needs and technological capabilities. Many devices rely on externally mounted hardware, offer limited stimulation monitoring, lack closed-loop functionality, or consume excessive power that restricts long-term use. These shortcomings limit experimental flexibility and reproducibility while increasing animal burden. To address this gap, a set of requirements for DBS devices was first established that define the functional and welfare-related design criteria necessary for reliable long-term studies. Particular emphasis was placed on the identification of common failures in the stimulation path, since undetected faults undermine scientific validity.

To enable safe and energy-efficient stimulation, the stimulation load was then characterized through a series of *in vitro* and *ex vivo* experiments using two different microelectrode types. The measurements enabled the derivation of minimum compliance voltage requirements, the identification of electrochemical safety limits, and the development of a simplified analytical model that accurately reproduced stimulation characteristics within the linear regime. The analysis showed that passive charge balancing can be implemented safely without blocking capacitors in these microelectrode setups. When blocking capacitors are used, however, potential risks were identified, which could be mitigated by using a discharge resistor.

Building on these results, a new generation of implantable DBS devices for rodents, constructed entirely from off-the-shelf components, was developed, collectively known as *STELLA*. Through iterative refinement of the design, three distinct generations emerged, whose implementation concepts are presented in this work: STELLA3, STELLA3.1, and STELLA4. Their development was guided by a comprehensive architectural analysis, including simulations and hardware prototyping, to identify optimal trade-offs between functionality, power consumption, and compact size. Across these generations, a dedicated compact, waterproof and biocompatible encapsulation method was developed and tailored to each device's functional needs and physical dimensions. This enabled fully subcutaneous implantation in small rodents and thereby supported reliable and welfare-compliant long-term studies.

STELLA3 introduces a highly miniaturized ($< 1\,\mathrm{cm}^3$), ultra-low power ($24.9\,\mu\mathrm{W}$), dual-channel architecture capable of precise, current-controlled, and charge-balanced stimula-

tion. It integrates a built-in self-test mechanism that is able to detect all three failure cases (open-circuit, short-circuit, compliance voltage violations), significantly improving the interpretability and reliability of stimulation experiments. With runtimes exceeding four months using a single CR1216 battery, STELLA3 is the most energy-efficient DBS device for rodents reported to date under the stimulation setups evaluated in this work. Its lightweight, fully implantable design reduces stress and preserves natural behavior of the animals, thereby making an important technological contribution to the refinement aspect of the 3R principles. Its use has already generated new insights into DBS mechanisms.

STELLA3.1 extends the STELLA3 architecture with bidirectional RF communication, while maintaining a sub-1 cm^3 volume. The energy-efficient communication scheme adds only minimal power overhead, enabling long-term studies with wireless monitoring and parameter adjustment. A dedicated air-filled housing preserves RF performance and results in the first implantable RF-enabled rodent DBS system suitable for chronic studies.

STELLA4 represents the most advanced system of the STELLA family. Within a form factor still below 1 cm^3, it integrates Bluetooth Low Energy (BLE) communication, on-board biosignal acquisition, an enhanced stimulation unit, closed-loop capability, and Li-ion recharging via the stimulation leads. The recharging method allows the encapsulated device to be reused, eliminating the need for repeated labor-intensive encapsulation procedures. A refined power architecture extends the available compliance voltage range while maintaining ultra-low power consumption. The stimulation unit offers greater flexibility and precision, provides independent control of each channel, and supports both current- and voltage-controlled operation, enabling applications beyond neural tissue. These capabilities position STELLA4 as a versatile and multimodal DBS platform that surpasses both its predecessors and the state of the art in rodent DBS technology.

In summary, this dissertation delivers not only a family of novel DBS devices but also a complete methodological framework for designing, encapsulating and validating compact, highly flexible, fully-implantable DBS systems for freely moving rodents. By addressing the major methodological gaps of current rodent DBS research, i.e., insufficient monitoring, inadequate safety and accuracy, limited functional flexibility, lack of closed-loop capability, short runtimes, and excessive animal burden, the STELLA platform enables scientifically robust, ethically responsible and future-oriented preclinical studies. In this sense, STELLA is not merely a stimulator, but a flexible research platform that enables the investigation of novel stimulation strategies and experimental designs.

7 Outlook

7.1 Future Perspectives with STELLA

The introduction of STELLA4 opens up unprecedented research opportunities in the field of preclinical neurostimulation. A central objective of future research is to realize a closed-loop stimulation paradigm that autonomously adapts stimulation parameters based on physiological feedback. Accelerometry appears to be a promising biomarker, and future studies could focus on coupling accelerometer data with stimulation protocols to explore the relationship between motor behavior and neural modulation. Moreover, the modular design of STELLA4 facilitates the integration of additional sensors, further extending the system's use cases. Beyond the movement disorder models investigated in this work, the high flexibility of STELLA4 may provide valuable insights into other neurological or psychiatric disease models and into stimulation targets beyond the brain.

Future work should also investigate how frequently the maximum stimulation voltage must be measured to maintain a valid constant current while ensuring high energy efficiency. For this purpose, the maximum stimulation voltage should be monitored at short intervals to evaluate how dynamically biological processes at the electrode-tissue interface evolve over time, thereby enabling the determination of the optimal measurement frequency for adaptive power management.

Another important question to be addressed is how to avoid or minimize crosstalk during synchronous bilateral DBS with multipolar electrode contacts. Given its potential relevance for achieving reproducible outcomes, this issue is discussed in more detail in the following section.

7.2 Crosstalk Effects in Bilateral DBS

Throughout the work, all *in vitro* and *ex vivo* stimulation experiments were deliberately performed using a unilateral electrode configuration. The reason is that preliminary tests with a bilateral configuration immersed in a conductive medium revealed deviations in the measured return current relative to the adjusted current amplitudes, indicating electrical coupling between both stimulation channels. Since these effects do not originate from the stimulation device itself but rather from current redistribution within the conductive medium, the unilateral setup was chosen exclusively to validate the stimulation output of STELLA. This section aims to draw attention to the potential relevance of such crosstalk effects for current-controlled bilateral DBS.

To investigate this coupling effect, two bipolar PI-SNEX-100 electrode pairs (each consisting of a closely spaced working electrode and counter electrode) were inserted into the left and

right hemispheres of extracted rat brain tissue. Both stimulation channels were configured to deliver identical current-controlled pulses of 200 µA, 60 µs, and 130 Hz, using the stimulation device described in Section 4.2. The current in each return path to ground was measured using the Keysight CX3324A. Fig. 45B presents the recorded stimulation currents. Ideally, both measured return currents should overlap with the adjusted stimulation amplitude of 200 µA and remain constant during the pulse. However, the measurements reveal that the measured return currents strongly deviate from their expected constant current values. The return current of i_{A1} decreases over the stimulation phase and reaches only about 115 µA at the end of the pulse, while i_{A2} increases and peaks at approximately 280 µA. These deviations confirm the presence of crosstalk, in which part of the injected current branches into the electrode contacts of the contralateral microelectrode rather than exclusively through its intended path. Fig. 45A illustrates the equivalent circuit that highlights conductive coupling between both electrode pairs through the shared solution resistances.

This crosstalk effect has also been discussed in related fields such as retinal, vestibular, and cochlear implants. In retinal implants, several studies have shown that crosstalk impairs spatial resolution due to overlapping electric fields, thereby preventing high-resolution imaging [246, 164, 211]. The study of [232] examined current coupling within retinal electrode arrays and demonstrated that simultaneous bipolar stimulation leads to unwanted current branching into return electrodes. Comparable effects have been reported in cochlear and vestibular prostheses. Channel interaction in cochlear implants has been shown to constrain spectral discrimination [215], while vestibular systems have been explicitly designed to minimize channel interferences [46, 103, 104].

Although simultaneous bilateral DBS has become a widely adopted surgical technique for the treatment of Parkinson's disease [149, 191] and dystonia [240, 123], no systematic investigation of crosstalk effects in bilateral DBS using bipolar electrodes has been published to date. The present findings from the preclinical setting demonstrate that maintaining a strictly constant current through a defined tissue region cannot be guaranteed in a bilateral configuration with bipolar electrodes, suggesting potential implications for clinical DBS. When the injected current is partially diverted from the targeted region, the resulting electric field distribution is altered, potentially affecting both the selectivity and efficacy of stimulation. This issue is particularly critical in preclinical studies, where constant current delivery through a defined tissue region is essential for ensuring reproducibility of experimental results. Moreover, biological changes occurring at the electrode following implantation may further modify current redistribution over time. Therefore, future work should aim to quantify and model such crosstalk effects in bilateral DBS under both preclinical and clinical conditions. Since bilateral DBS is typically applied synchronously, future implementations may need to incorporate galvanic isolation strategies to mitigate these crosstalk effects.

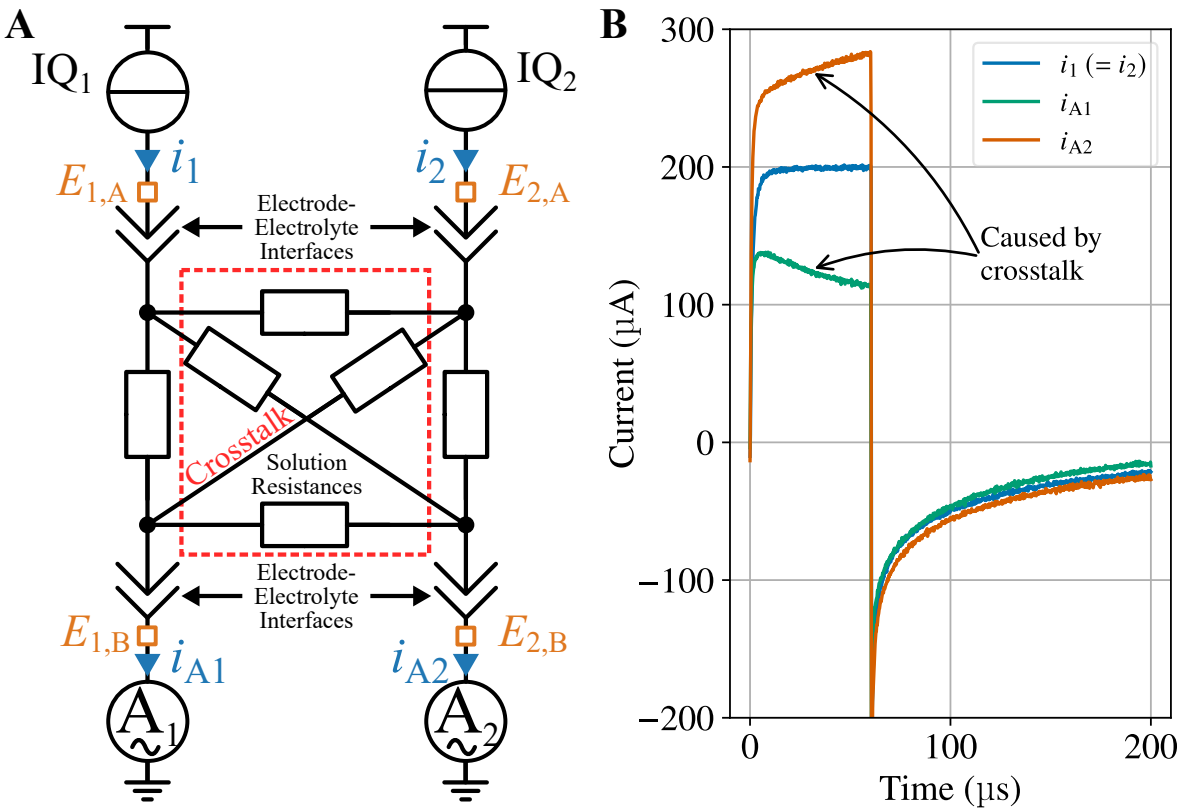

Figure 45: (A) Equivalent circuit representation illustrating the crosstalk pathways between two independently driven stimulation channels (IQ_1 and IQ_2) (adapted from [232]). The shared conductive medium introduces solution resistances that couple both electrode pairs, resulting in unintended current paths between two channels. (B) Experimental results showing measured stimulation currents from both channels during bilateral stimulation in extracted rat brain tissue using two PI-SNEX-100 microelectrodes. Both stimulation channels were adjusted to deliver identical current-controlled pulses of 200 µA, 60 µs, and 130 Hz (only i_1 shown). The strong deviations in the measured current amplitudes (i_{A1}, i_{A2}) relative to the expected source currents (i_1, i_2) indicate current redistribution caused by crosstalk.

References

[1] A. I. Acosta, M. S. Noor, Z. H. T. Kiss, and K. Murari. 'A lightweight discrete biphasic current stimulator for rodent deep brain stimulation'. In: *2015 IEEE Biomedical Circuits and Systems Conference (BioCAS)*. IEEE, 2015, pp. 1–4. DOI: 10.1109/biocas.2015.7348360.

[2] S. D. Adams, K. E. Bennet, S. J. Tye, M. Berk, and A. Z. Kouzani. 'Development of a miniature device for emerging deep brain stimulation paradigms'. In: *PLOS ONE* 14.2 (Feb. 2019). Ed. by N. Pouratian, e0212554. ISSN: 1932-6203. DOI: 10.1371/journal.pone.0212554.

[3] M. Akhtari, N. Salamon, R. Duncan, I. Fried, and G. Mathern. 'Electrical Conductivities of the Freshly Excised Cerebral Cortex in Epilepsy Surgery Patients; Correlation with Pathology, Seizure Duration, and Diffusion Tensor Imaging'. In: *Brain Topography* 18.4 (2006), pp. 281–290. ISSN: 0896-0267. DOI: 10.1007/s10548-006-0006-x.

[4] M. Alpaugh, M. Saint-Pierre, M. Dubois, B. Aubé, D. Arsenault, J. Kriz, A. Cicchetti, and F. Cicchetti. 'A novel wireless brain stimulation device for long-term use in freely moving mice'. In: *Scientific Reports* 9.1 (2019), p. 6444. ISSN: 2045-2322. DOI: 10.1038/s41598-019-42910-7.

[5] N. Apetz, E. Kordys, M. Simon, B. Mang, M. Aswendt, D. Wiedermann, B. Neumaier, A. Drzezga, L. Timmermann, and H. Endepols. 'Effects of subthalamic deep brain stimulation on striatal metabolic connectivity in a rat hemiparkinsonian model'. In: *Disease models & mechanisms* 12.5 (2019), p. dmm039065. ISSN: 1754-8411. DOI: 10.1242/dmm.039065.

[6] O. Aquilina. 'A brief history of cardiac pacing'. In: *Images in paediatric cardiology* 8.2 (2006), p. 17.

[7] S. K. Arfin, M. A. Long, M. S. Fee, and R. Sarpeshkar. 'Wireless Neural Stimulation in Freely Behaving Small Animals'. In: *Journal of Neurophysiology* 102.1 (2009), pp. 598–605. ISSN: 0022-3077. DOI: 10.1152/jn.00017.2009.

[8] N. P. Aryan, H. Kaim, and A. Rothermel. *Stimulation and recording electrodes for neural prostheses*. Vol. 1. SpringerBriefs in Electrical and Computer Engineering Ser. Springer, 2015. 189 pp. ISBN: 9783319100524.

[9] K. Ashkan, P. Rogers, H. Bergman, and I. Ughratdar. 'Insights into the mechanisms of deep brain stimulation'. In: *Nature Reviews Neurology* 13.9 (2017), pp. 548–554. ISSN: 1759-4758. DOI: 10.1038/nrneurol.2017.105.

[10] A. Association. '2015 Alzheimer's disease facts and figures'. In: *Alzheimer's & Dementia* 11.3 (2015), pp. 332–384. ISSN: 1552-5260. DOI: 10.1016/j.jalz.2015.02.003.

[11] K. Badstübner, M. Stubbe, T. Kröger, E. Mix, and J. Gimsa. 'Impedance detection of the electrical resistivity of the wound tissue around deep brain stimulation electrodes permits registration of the encapsulation process in a rat model'. In: *Journal of Electrical Bioimpedance* 8.1 (2017), pp. 11–24. ISSN: 1891-5469. DOI: 10.5617/jeb.4086.

[12] A. Banerjee and S. Nag. 'Energy-Efficient Electrical Stimulation Systems'. In: *Handbook of Neuroengineering*. Springer, 2021, pp. 1–26. DOI: 10.1007/978-981-15-2848-4_104-2.

[13] M. Banet. 'Fever and survival in the rat: the effect of enhancing fever. The effect of enhancing fever'. In: *Pflügers Archiv* 381.1 (1979), pp. 35–38. ISSN: 0031-6768. DOI: 10.1007/bf00582329.

[14] *Battery Internal Resistance*. Technical Bulletin. Version 1.1.0. 2005. URL: https://data.energizer.com/pdfs/batteryir.pdf (visited on 09/03/2025).

[15] C. Baumgartner, P. Hasgall, F. Di Gennaro, E. Neufeld, B. Lloyd, M. C. Gosselin, D. Payne, A. Klingenböck, and N. Kuster. 'IT'IS Database for thermal and electromagnetic parameters of biological tissues, Version 5.0'. In: (2025). DOI: 10.13099/VIP21000-05-0. URL: https://itis.swiss/virtual-population/tissue-properties/database/dielectric-properties.

[16] S. Bhaskara, S. G. KV, S. Datta, S. Gupta, K. Lakshmiramanan, D. M. Das, and H. J. Pandya. 'A Novel Charge Neutral, Programmable, Wireless Brain Stimulation System for Rat Experiments'. In: *2024 8th International Conference on Biomedical Engineering and Applications (ICBEA)*. IEEE, 2024, pp. 124–130. DOI: 10.1109/icbea62825.2024.00031.

[17] N. Blanch-Martínez, S. Arias-Herrera, and A. Martínez-González. 'Behavior of polyether-ether-ketone (PEEK) in prostheses on dental implants. A review'. In: *Journal of Clinical and Experimental Dentistry* 13(5) (2021), e520–e526. ISSN: 1989-5488. DOI: 10.4317/jced.58102.

[18] A. Blömeke, O. Kappelhoff, D. Wasylowski, F. Ringbeck, and D. U. Sauer. 'Open Source Online Electrochemical Impedance Spectroscopy Data Analytics Tool'. In: *Journal of Power Sources* 615 (2024), p. 235049. DOI: 10.2139/ssrn.4829135.

[19] K. N. Bocan, M. H. Mickle, and E. Sejdić. 'Multi-Disciplinary Challenges in Tissue Modeling for Wireless Electromagnetic Powering: A Review'. In: *IEEE Sensors*

Journal 17.20 (2017), pp. 6498–6509. ISSN: 1530-437X. DOI: 10.1109/jsen.2017.2748338.

[20] C. Boehler, S. Carli, L. Fadiga, T. Stieglitz, and M. Asplund. 'Tutorial: guidelines for standardized performance tests for electrodes intended for neural interfaces and bioelectronics'. In: *Nature Protocols* 15.11 (2020), pp. 3557–3578. ISSN: 1754-2189. DOI: 10.1038/s41596-020-0389-2.

[21] A. Boogers, J. Peeters, T. Van Bogaert, B. Asamoah, P. De Vloo, W. Vandenberghe, B. Nuttin, and M. Mc Laughlin. 'Anodic and symmetric biphasic pulses enlarge the therapeutic window in deep brain stimulation for essential tremor'. In: *Brain Stimulation* 15.2 (2022), pp. 286–290. ISSN: 1935-861X. DOI: 10.1016/j.brs.2022.01.012.

[22] B. J. G. van den Boom, A. Elhazaz-Fernandez, P. A. Rasmussen, E. H. van Beest, A. Parthasarathy, D. Denys, and I. Willuhn. 'Unraveling the mechanisms of deep-brain stimulation of the internal capsule in a mouse model'. In: *Nature Communications* 14.1 (2023), p. 5385. ISSN: 2041-1723. DOI: 10.1038/s41467-023-41026-x.

[23] S. B. Borgheai, E. Opri, F. Isbaine, E. R. Cole, R. Jafari Deligani, N. G. Laxpati, B. B. Risk, J. T. Willie, R. E. Gross, N. AuYong, et al. 'Neural pathway activation in the subthalamic region depends on stimulation polarity'. In: *Brain Communications* 7.1 (May 2025), fcaf006. DOI: 10.1101/2024.05.01.24306044.

[24] W. Bouthour, P. Mégevand, J. Donoghue, C. Lüscher, N. Birbaumer, and P. Krack. 'Biomarkers for closed-loop deep brain stimulation in Parkinson disease and beyond'. In: *Nature Reviews Neurology* 15.6 (2019), pp. 343–352. ISSN: 1759-4758. DOI: 10.1038/s41582-019-0166-4.

[25] D. T. Brocker and W. M. Grill. 'Principles of electrical stimulation of neural tissue'. In: *Handbook of clinical neurology* 116 (2013), pp. 3–18. ISSN: 0072-9752. DOI: 10.1016/b978-0-444-53497-2.00001-2.

[26] J. M. Bronstein, M. Tagliati, C. McIntyre, R. Chen, T. Cheung, E. L. Hargreaves, Z. Israel, M. Moffitt, E. B. Montgomery, P. Stypulkowski, J. Shils, T. Denison, J. Vitek, J. Volkman, J. Wertheimer, and M. S. Okun. 'The Rationale Driving the Evolution of Deep Brain Stimulation to Constant-Current Devices'. In: *Neuromodulation: Technology at the Neural Interface* 18.2 (2015), pp. 85–89. ISSN: 1094-7159. DOI: 10.1111/ner.12227.

[27] N. Brum. *spicelib*. https://github.com/nunobrum/spicelib. 2025.

[28] S. B. Brummer, L. S. Robblee, and F. T. Hambrecht. 'Criteria for selecting electrodes for electrical stimulation: theoretical and practical considerations.' In: *Annals of the*

New York Academy of Sciences 405.1 (1983), pp. 159–171. ISSN: 0077-8923. DOI: 10.1111/j.1749-6632.1983.tb31628.x.

[29] N. Brunel and M. C. W. van Rossum. 'Quantitative investigations of electrical nerve excitation treated as polarization. Louis Lapicque 1907 · Translated by:' in: *Biological Cybernetics* 97.5-6 (2007), p. 341. ISSN: 0340-1200. DOI: 10.1007/s00422-007-0189-6.

[30] J. R. Buitenweg, W. L. C. Rutten, W. P. A. Willems, and J. W. van Nieuwkasteele. 'Measurement of sealing resistance of cell-electrode interfaces in neuronal cultures using impedance spectroscopy'. In: *Medical and Biological Engineering and Computing* 36.5 (1998), pp. 630–637. ISSN: 0140-0118. DOI: 10.1007/bf02524436.

[31] A. Burton, S. M. Won, A. K. Sohrabi, T. Stuart, A. Amirhossein, J. U. Kim, Y. Park, A. Gabros, J. A. Rogers, F. Vitale, A. G. Richardson, and P. Gutruf. 'Wireless, battery-free, and fully implantable electrical neurostimulation in freely moving rodents'. In: *Microsystems & Nanoengineering* 7.1 (2021), p. 62. ISSN: 2055-7434. DOI: 10.1038/s41378-021-00294-7.

[32] N. Butz, U. Kalita, and Y. Manoli. 'Active Charge Balancer With Adaptive 3.3 V to 38 V Supply Compliance for Neural Stimulators'. In: *IEEE Transactions on Circuits and Systems I: Regular Papers* 68.10 (2021), pp. 4013–4024. ISSN: 1549-8328. DOI: 10.1109/tcsi.2021.3101550.

[33] H. Cagnan, D. Pedrosa, S. Little, A. Pogosyan, B. Cheeran, T. Aziz, A. Green, J. Fitzgerald, T. Foltynie, P. Limousin, L. Zrinzo, M. Hariz, K. J. Friston, T. Denison, and P. Brown. 'Stimulating at the right time: phase-specific deep brain stimulation'. In: *Brain* 140.1 (Dec. 2017), pp. 132–145. ISSN: 1460-2156. DOI: 10.1093/brain/aww286.

[34] *Calculation of Cell Constants using the Autolab Microcell HC TSC70 and TSC1600*. Tech. rep. Application Note AN-EC-020. Metrohm AG.

[35] A. C. P. Campos, D. S. Kikuchi, A. F. N. Paschoa, M. A. Kuroki, E. T. Fonoff, C. Hamani, R. L. Pagano, and M. S. Hernandes. 'Unraveling the Role of Astrocytes in Subthalamic Nucleus Deep Brain Stimulation in a Parkinson's Disease Rat Model'. In: *Cellular and Molecular Neurobiology* 40.6 (2020), pp. 939–954. ISSN: 0272-4340. DOI: 10.1007/s10571-019-00784-3.

[36] A. P. Carvajales. *The Top Three Ways to Split a Voltage Rail to a Bipolar Supply*. 2016. URL: https://www.ti.com/lit/ta/ssztai6/ssztai6.pdf?ts=1748350974991&ref_url=https%253A%252F%252Fwww.ti.com%252Fdocument-viewer%252Flit%252Fhtml%252FSSZTAI6 (visited on 05/27/2025).

[37] J.-Y. Chang, L.-H. Shi, F. Luo, and D. J. Woodward. 'High frequency stimulation of the subthalamic nucleus improves treadmill locomotion in unilateral 6-hydroxydopamine lesioned rats'. In: *Brain Research* 983.1-2 (2003), pp. 174–184. ISSN: 0006-8993. DOI: 10.1016/s0006-8993(03)03053-1.

[38] P.-H. Chen, Z. Luo, S. Chang, K. Ngo, R. Vatsyayan, J. Lee, T. Porter, D. A. Hall, S. Dayeh, I. Galton, et al. 'A Scalable 256-Channel 12-mA 0.06%-Current-Mismatch 22-V Neurostimulator with Real-Time Current Calibration and Compliance Monitoring'. In: *2025 IEEE Custom Integrated Circuits Conference (CICC)*. IEEE, 2025, pp. 1–3. DOI: 10.1109/cicc63670.2025.10983608.

[39] J. Chen, J. Volkmann, and C. W. Ip. 'A framework for translational therapy development in deep brain stimulation'. In: *npj Parkinson's Disease* 10.1 (2024), p. 216. ISSN: 2373-8057. DOI: 10.1038/s41531-024-00829-5.

[40] Y. Chen, G. Zhu, D. Liu, X. Zhang, Y. Liu, T. Yuan, T. Du, and J. Zhang. 'Subthalamic nucleus deep brain stimulation suppresses neuroinflammation by Fractalkine pathway in Parkinson's disease rat model'. In: *Brain, Behavior, and Immunity* 90 (2020), pp. 16–25. ISSN: 0889-1591. DOI: 10.1016/j.bbi.2020.07.035.

[41] H. Chun, N. Tran, Y. Yang, O. Kavehei, S. Bai, and S. Skafidas. 'A precise charge balancing and compliance voltage monitoring stimulator front-end for 1024-electrodes retinal prosthesis'. In: *2012 Annual International Conference of the IEEE Engineering in Medicine and Biology Society*. IEEE, 2012, pp. 3001–3004. DOI: 10.1109/embc.2012.6346595.

[42] S. F. Cogan. 'Neural Stimulation and Recording Electrodes'. In: *Annual Review of Biomedical Engineering* 10.1 (Aug. 2008), pp. 275–309. ISSN: 1545-4274. DOI: 10.1146/annurev.bioeng.10.061807.160518.

[43] S. F. Cogan, A. A. Guzelian, W. F. Agnew, T. G. H. Yuen, and D. B. McCreery. 'Over-pulsing degrades activated iridium oxide films used for intracortical neural stimulation'. In: *Journal of Neuroscience Methods* 137.2 (2004), pp. 141–150. ISSN: 0165-0270. DOI: 10.1016/j.jneumeth.2004.02.019.

[44] S. F. Cogan, K. A. Ludwig, C. G. Welle, and P. Takmakov. 'Tissue damage thresholds during therapeutic electrical stimulation'. In: *Journal of Neural Engineering* 13.2 (2016), p. 021001. ISSN: 1741-2560. DOI: 10.1088/1741-2560/13/2/021001.

[45] K. S. Cole and R. H. Cole. 'Dispersion and Absorption in Dielectrics I. Alternating Current Characteristics'. In: *The Journal of Chemical Physics* 9.4 (1941), pp. 341–351. ISSN: 0021-9606. DOI: 10.1063/1.1750906.

[46] T. G. Constandinou, J. Georgiou, and C. Toumazou. 'A Partial-Current-Steering Biphasic Stimulation Driver for Vestibular Prostheses'. In: *IEEE Transactions on*

Biomedical Circuits and Systems 2.2 (2008), pp. 106–113. ISSN: 1932-4545. DOI: 10.1109/tbcas.2008.927238.

[47] *Constant phase element - calculating equivalent capacitance*. 2021. URL: https://doc.zahner.de/application_notes/cpe.pdf (visited on 04/17/2025).

[48] J. Couto and W. M. Grill. 'Kilohertz Frequency Deep Brain Stimulation Is Ineffective at Regularizing the Firing of Model Thalamic Neurons'. In: *Frontiers in Computational Neuroscience* 10 (2016), p. 22. ISSN: 1662-5188. DOI: 10.3389/fncom.2016.00022.

[49] A. Cuschieri, N. Borg, and C. Zammit. 'Closed loop deep brain stimulation: A systematic scoping review'. In: *Clinical Neurology and Neurosurgery* 223 (Dec. 2022), p. 107516. ISSN: 0303-8467. DOI: 10.1016/j.clineuro.2022.107516.

[50] Y. Darbaky, C. Forni, M. Amalric, and C. Baunez. 'High frequency stimulation of the subthalamic nucleus has beneficial antiparkinsonian effects on motor functions in rats, but less efficiency in a choice reaction time task'. In: *European Journal of Neuroscience* 18.4 (2003), pp. 951–956. ISSN: 0953-816X. DOI: 10.1046/j.1460-9568.2003.02803.x.

[51] Y. Değirmenci. 'Current DBS programming'. In: *Deep Brain Stimulation* 4 (2024), pp. 29–31. ISSN: 2949-6691. DOI: 10.1016/j.jdbs.2023.12.002.

[52] A. Demosthenous. 'Advances in Microelectronics for Implantable Medical Devices'. In: *Advances in Electronics* 2014.1 (2014), pp. 1–21. ISSN: 2356-6663. DOI: 10.1155/2014/981295.

[53] J. S. Denker. *How to Define Anode and Cathode*. https://www.av8n.com/physics/anode-cathode. Accessed: 2025-10-29. 2004.

[54] A. Díez-Solinska, O. Vegas, and G. Azkona. 'Refinement in the European Union: A Systematic Review'. In: *Animals* 12.23 (2022), p. 3263. ISSN: 2076-2615. DOI: 10.3390/ani12233263.

[55] *Directive 2010/63/EU of the European Parliament and of the Council of 22 September 2010 on the protection of animals used for scientific purposes*. URL: https://eur-lex.europa.eu/legal-content/EN/TXT/PDF/?uri=CELEX:32010L0063 (visited on 06/07/2025).

[56] O. Domansky, R. Sotner, L. Langhammer, J. Jerabek, C. Psychalinos, and G. Tsirimokou. 'Practical Design of RC Approximants of Constant Phase Elements and Their Implementation in Fractional-Order PID Regulators Using CMOS Voltage Differencing Current Conveyors'. In: *Circuits, Systems, and Signal Processing* 38.4 (Oct. 2019), pp. 1520–1546. ISSN: 1531-5878. DOI: 10.1007/s00034-018-0944-z.

[57] M. N. van Dongen and W. A. Serdijn. 'Does a coupling capacitor enhance the charge balance during neural stimulation? An empirical study'. In: *Medical & biological engineering & computing* 54.1 (May 2016), pp. 93–101. ISSN: 1741-0444. DOI: 10.1007/s11517-015-1312-9.

[58] M. A. ElBeialy. *Deep brain stimulation for epilepsy*. Radiopaedia.org, Radiology case (rID: 54345). 2017. DOI: 10.53347/rid-54345. URL: https://radiopaedia.org/cases/deep-brain-stimulation-for-epilepsy-1 (visited on 09/30/2025).

[59] *Electrochemical Impedance Spectroscopy: Part 4 - Equivalent circuit models*. Tech. rep. Application Note AN-EIS-004. Metrohm AG. URL: https://www.metrohm.com/content/metrohm/de_de/applications/application-notes/autolab-applikationen-anautolab/an-eis-004.html (visited on 11/26/2025).

[60] J. R. Eles, A. L. Vazquez, T. D. Y. Kozai, and X. T. Cui. 'In vivo imaging of neuronal calcium during electrode implantation: Spatial and temporal mapping of damage and recovery'. In: *Biomaterials* 174 (2018), pp. 79–94. ISSN: 0142-9612. DOI: 10.1016/j.biomaterials.2018.04.043.

[61] N. Elgrishi, K. J. Rountree, B. D. McCarthy, E. S. Rountree, T. T. Eisenhart, and J. L. Dempsey. 'A Practical Beginner's Guide to Cyclic Voltammetry'. In: *Journal of Chemical Education* 95.2 (Nov. 2017), pp. 197–206. ISSN: 1938-1328. DOI: 10.1021/acs.jchemed.7b00361.

[62] A. S. Elwakil. 'Fractional-Order Circuits and Systems: An Emerging Interdisciplinary Research Area'. In: *IEEE Circuits and Systems Magazine* 10.4 (2010), pp. 40–50. ISSN: 1531-636X. DOI: 10.1109/mcas.2010.938637.

[63] F. Eshaghi, T. Moeinfard, E. Najafiaghdam, and H. Kassiri. 'A Neurostimulator IC With Impedance-Aware Dynamic-Precision One-Shot Charge Balancing'. In: *IEEE Solid-State Circuits Letters* 4 (2021), pp. 202–205. ISSN: 2573-9603. DOI: 10.1109/lssc.2021.3124190.

[64] J. Evers, K. Sridhar, J. Liegey, J. Brady, H. Jahns, and M. Lowery. 'Stimulation-induced changes at the electrode–tissue interface and their influence on deep brain stimulation'. In: *Journal of Neural Engineering* 19.4 (2022), p. 046004. ISSN: 1741-2560. DOI: 10.1088/1741-2552/ac7ad6.

[65] J. Evers, J. Orłowski, H. Jahns, and M. M. Lowery. 'On-Off and Proportional Closed-Loop Adaptive Deep Brain Stimulation Reduces Motor Symptoms in Freely Moving Hemiparkinsonian Rats'. In: *Neuromodulation: Technology at the Neural Interface* 27.3 (2024), pp. 476–488. ISSN: 1094-7159. DOI: 10.1016/j.neurom.2023.03.018.

[66] J. Evers, K. Sridhar, and M. Lowery. 'Feasibility of pair-housing of rats after cranial implant surgery'. In: *Laboratory Animals* 57.1 (Oct. 2023), pp. 69–74. ISSN: 1758-1117. DOI: 10.1177/00236772221122099.

[67] S. G. Ewing, W. J. Lipski, A. A. Grace, and C. Winter. 'An inexpensive, charge-balanced rodent deep brain stimulation device: A step-by-step guide to its procurement and construction'. In: *Journal of Neuroscience Methods* 219.2 (Oct. 2013), pp. 324–330. DOI: 10.1016/j.jneumeth.2013.08.003.

[68] S. G. Ewing, B. Porr, J. Riddell, C. Winter, and A. A. Grace. 'SaBer DBS: A fully programmable, rechargeable, bilateral, charge-balanced preclinical microstimulator for long-term neural stimulation'. In: *Journal of Neuroscience Methods* 213.2 (Mar. 2013), pp. 228–235. DOI: 10.1016/j.jneumeth.2012.12.008.

[69] S. Farjaminejad and A. M. Dingle. 'The role of electrical stimulation in bone regeneration: mechanistic insights and therapeutic advances'. In: *Bioelectronic Medicine* 11.1 (2025), p. 18. ISSN: 2332-8886. DOI: 10.1186/s42234-025-00180-x.

[70] V. Farrow. *Fractional Capacitor SPICE*. https://github.com/Rockscanfly/Fractional_Capacitor_SPICE. 2025.

[71] M. Fauser, M. Ricken, F. Markert, N. Weis, O. Schmitt, J. Gimsa, C. Winter, K. Badstübner-Meeske, and A. Storch. 'Subthalamic nucleus deep brain stimulation induces sustained neurorestoration in the mesolimbic dopaminergic system in a Parkinson's disease model'. In: *Neurobiology of Disease* 156 (2021), p. 105404. ISSN: 0969-9961. DOI: 10.1016/j.nbd.2021.105404.

[72] D. L. Fischer, C. J. Kemp, A. Cole-Strauss, N. K. Polinski, K. L. Paumier, J. W. Lipton, K. Steece-Collier, T. J. Collier, D. J. Buhlinger, and C. E. Sortwell. 'Subthalamic Nucleus Deep Brain Stimulation Employs trkB Signaling for Neuroprotection and Functional Restoration'. In: *The Journal of Neuroscience* 37.28 (2017), pp. 6786–6796. ISSN: 0270-6474. DOI: 10.1523/jneurosci.2060-16.2017.

[73] D. L. Fischer, F. P. Manfredsson, C. J. Kemp, A. Cole-Strauss, J. W. Lipton, M. F. Duffy, N. K. Polinski, K. Steece-Collier, T. J. Collier, S. E. Gombash, D. J. Buhlinger, and C. E. Sortwell. 'Subthalamic Nucleus Deep Brain Stimulation Does Not Modify the Functional Deficits or Axonopathy Induced by Nigrostriatal α-Synuclein Overexpression'. In: *Scientific Reports* 7.1 (2017), p. 16356. ISSN: 2045-2322. DOI: 10.1038/s41598-017-16690-x.

[74] M. Fleischer, H. Endres, M. Sendtner, and J. Volkmann. 'Development of a Fully Implantable Stimulator for Deep Brain Stimulation in Mice'. In: *Frontiers in Neuroscience* 14 (July 2020). ISSN: 1662-453X. DOI: 10.3389/fnins.2020.00726.

[75] F. Fluri, T. Mützel, M. K. Schuhmann, M. Krstić, H. Endres, and J. Volkmann. 'Development of a head-mounted wireless microstimulator for deep brain stimulation in rats'. In: *Journal of Neuroscience Methods* 291 (Nov. 2017), pp. 249–256. ISSN: 0165-0270. DOI: 10.1016/j.jneumeth.2017.08.024.

[76] C. Forni, O. Mainard, C. Melon, D. Goguenheim, L. K.-L. Goff, and P. Salin. 'Portable microstimulator for chronic deep brain stimulation in freely moving rats'. In: *Journal of Neuroscience Methods* 209.1 (July 2012), pp. 50–57. ISSN: 0165-0270. DOI: 10.1016/j.jneumeth.2012.05.027.

[77] W. Franks, I. Schenker, P. Schmutz, and A. Hierlemann. 'Impedance Characterization and Modeling of Electrodes for Biomedical Applications'. In: *IEEE Transactions on Biomedical Engineering* 52.7 (2005), pp. 1295–1302. ISSN: 0018-9294. DOI: 10.1109/tbme.2005.847523.

[78] J. Frey, J. Cagle, K. A. Johnson, J. K. Wong, J. D. Hilliard, C. R. Butson, M. S. Okun, and C. de Hemptinne. 'Past, Present, and Future of Deep Brain Stimulation: Hardware, Software, Imaging, Physiology and Novel Approaches'. In: *Frontiers in Neurology* 13 (2022), p. 825178. ISSN: 1664-2295. DOI: 10.3389/fneur.2022.825178.

[79] H. Fricke and S. Morse. 'The electric resistance and capacity of blood for frequencies between 800 and 41/2 million cycles'. In: *Journal of General Physiology* 9.2 (1925), p. 153. ISSN: 1540-7748. DOI: 10.1085/jgp.9.2.153.

[80] S. Gabriel, R. W. Lau, and C. Gabriel. 'The dielectric properties of biological tissues: III. Parametric models for the dielectric spectrum of tissues'. In: *Physics in Medicine & Biology* 41.11 (1996), pp. 2271–2293. ISSN: 0031-9155. DOI: 10.1088/0031-9155/41/11/003.

[81] Z. Gilbert et al. 'A review of neurophysiological effects and efficiency of waveform parameters in deep brain stimulation'. In: *Clinical Neurophysiology* 152 (2023), pp. 93–111. ISSN: 1388-2457. DOI: 10.1016/j.clinph.2023.04.007.

[82] J. Gimsa, B. Habel, U. Schreiber, U. van Rienen, U. Strauss, and U. Gimsa. 'Choosing electrodes for deep brain stimulation experiments–electrochemical considerations'. In: *Journal of Neuroscience Methods* 142.2 (Mar. 2005), pp. 251–265. ISSN: 0165-0270. DOI: 10.1016/j.jneumeth.2004.09.001.

[83] M. Golda-Cepa, K. Engvall, M. Hakkarainen, and A. Kotarba. 'Recent progress on parylene C polymer for biomedical applications: A review'. In: *Progress in Organic Coatings* 140 (2020), p. 105493. ISSN: 0300-9440. DOI: 10.1016/j.porgcoat.2019.105493.

[84] M. Grossi and B. Riccò. 'Electrical impedance spectroscopy (EIS) for biological analysis and food characterization: a review'. In: *Journal of Sensors and Sensor Systems* 6.2 (2017), pp. 303–325. ISSN: 2194-878X. DOI: 10.5194/jsss-6-303-2017.

[85] A. Grotemeyer, T. Petschner, R. Peach, D. Hoehl, T. Knauer, U. Thomas, H. Endres, R. Blum, M. Sendtner, J. Volkmann, and C. W. Ip. 'Standardized wireless deep brain stimulation system for mice'. In: *npj Parkinson's Disease* 10.1 (Aug. 2024). ISSN: 2373-8057. DOI: 10.1038/s41531-024-00767-2.

[86] D. Gu, K. Andreev, and M. E. Dupre. 'Major Trends in Population Growth Around the World'. In: *China CDC weekly* 3.28 (2021), p. 604. ISSN: 2096-7071. DOI: 10.46234/ccdcw2021.160.

[87] M. Gulino, D. Kim, S. Pané, S. D. Santos, and A. P. Pêgo. 'Tissue Response to Neural Implants: The Use of Model Systems Toward New Design Solutions of Implantable Microelectrodes'. In: *Frontiers in Neuroscience* 13 (2019), p. 689. ISSN: 1662-453X. DOI: 10.3389/fnins.2019.00689.

[88] R. de Haas, R. Struikmans, G. van der Plasse, L. van Kerkhof, J. H. Brakkee, M. J. H. Kas, and H. G. M. Westenberg. 'Wireless implantable micro-stimulation device for high frequency bilateral deep brain stimulation in freely moving mice'. In: *Journal of Neuroscience Methods* 209.1 (2012), pp. 113–119. ISSN: 0165-0270. DOI: 10.1016/j.jneumeth.2012.05.028.

[89] A. Hajizadeh, R. Hafezi, F. Torabi, A. A. Sari, and M. Tajvar. 'Consequences of Population Ageing on Health Systems: A Conceptual Framework for Policy and Practice'. In: *Ethiopian Journal of Health Sciences* 35.1 (2025). ISSN: 2413-7170. DOI: 10.4314/ejhs.v35i1.8.

[90] I. E. Harmsen, G. J. Elias, M. E. Beyn, A. Boutet, A. Pancholi, J. Germann, A. Mansouri, C. S. Lozano, and A. M. Lozano. 'Clinical trials for deep brain stimulation: Current state of affairs'. In: *Brain Stimulation* 13.2 (2020), pp. 378–385. ISSN: 1935-861X. DOI: 10.1016/j.brs.2019.11.008.

[91] D. Harnack, M. Hamann, W. Meissner, R. Morgenstern, A. Kupsch, and A. Richter. 'High-frequency stimulation of the entopeduncular nucleus improves dystonia in dtsz hamsters'. In: *NeuroReport* 15.9 (2004), pp. 1391–1393. ISSN: 0959-4965. DOI: 10.1097/01.wnr.0000130435.75715.64.

[92] D. Harnack, W. Meissner, J. A. Jira, C. Winter, R. Morgenstern, and A. Kupsch. 'Placebo-controlled chronic high-frequency stimulation of the subthalamic nucleus preserves dopaminergic nigral neurons in a rat model of progressive Parkinsonism'.

In: *Experimental Neurology* 210.1 (2008), pp. 257–260. ISSN: 0014-4886. DOI: 10.1016/j.expneurol.2007.10.002.

[93] D. Harnack, W. Meissner, R. Paulat, H. Hilgenfeld, W.-D. Müller, C. Winter, R. Morgenstern, and A. Kupsch. 'Continuous high-frequency stimulation in freely moving rats: Development of an implantable microstimulation system'. In: *Journal of Neuroscience Methods* 167.2 (2008), pp. 278–291. ISSN: 0165-0270. DOI: 10.1016/j.jneumeth.2007.08.019.

[94] C. J. Hartmann, S. Fliegen, S. J. Groiss, L. Wojtecki, and A. Schnitzler. 'An update on best practice of deep brain stimulation in Parkinson's disease'. In: *Therapeutic Advances in Neurological Disorders* 12 (2019), p. 1756286419838096. ISSN: 1756-2864. DOI: 10.1177/1756286419838096.

[95] Z. He, Y. Jiang, H. Xu, H. Jiang, W. Jia, P. Sun, and J. Xie. 'High frequency stimulation of subthalamic nucleus results in behavioral recovery by increasing striatal dopamine release in 6-hydroxydopamine lesioned rat'. In: *Behavioural Brain Research* 263 (2014), pp. 108–114. ISSN: 0166-4328. DOI: 10.1016/j.bbr.2014.01.014.

[96] D. M. Heard and A. J. J. Lennox. 'Electrode Materials in Modern Organic Electrochemistry'. In: *Angewandte Chemie* 59.43 (2020), pp. 18866–18884. ISSN: 0044-8249. DOI: 10.1002/ange.202005745.

[97] M. Heerdegen, D. Franz, V. Neubert, F. Santana-Kragelund, T. Sellmann, C. Werner-Schmolling, J. Starke, K. Spiliotis, F. Richter, A. Richter, and R. Köhling. 'Differential Effects of Short-term and Long-term Deep Brain Stimulation on Striatal Neuronal Excitability in a Dystonia Animal Model'. In: *bioRxiv* (2025), pp. 2025–04. DOI: 10.1101/2025.04.07.647541.

[98] I. D. Hentall. 'A long-lasting wireless stimulator for small mammals'. In: *Frontiers in Neuroengineering* 6 (2013), p. 8. ISSN: 1662-6443. DOI: 10.3389/fneng.2013.00008.

[99] M. S. Heo, H. S. Moon, H. C. Kim, H. W. Park, Y. H. Lim, and S. H. Paek. 'Fully Implantable Deep Brain Stimulation System with Wireless Power Transmission for Long-term Use in Rodent Models of Parkinson's Disease'. In: *Journal of Korean Neurosurgical Society* 57.3 (2015), pp. 152–158. ISSN: 2005-3711. DOI: 10.3340/jkns.2015.57.3.152.

[100] C. Q. Huang, P. M. Carter, and R. K. Shepherd. 'Stimulus Induced pH Changes in Cochlear Implants: An In Vitro and In Vivo Study'. In: *Annals of Biomedical Engineering* 29.9 (2001), pp. 791–802. ISSN: 0090-6964. DOI: 10.1114/1.1397793.

[101] D. Hui, A. A. Murgai, G. Gilmore, S. I. Mohideen, A. G. Parrent, and M. S. Jog. 'Assessing the effect of current steering on the total electrical energy delivered and

ambulation in Parkinson's disease'. In: *Scientific Reports* 10.1 (2020), p. 8256. ISSN: 2045-2322. DOI: 10.1038/s41598-020-64250-7.

[102] A. F. A. Hussein, W. M. Imran, I. Serag, A. Abbas, E. M. Hammad, S. Pastrana-Brandes, S. T. Al-Aish, D. Mahmoud, A. M. Z. Hassan, A. S. Ghattas, M. H. Megali, A. Muthana, A. A. H. Almusawi, and B. Chaurasia. 'Deep brain stimulation (DBS) in movement disorders management: exploring therapeutic efficacy, neurobiological mechanisms, and clinical implications'. In: *Annals of Medicine and Surgery* 87.4 (2025), pp. 2163–2179. ISSN: 2049-0801. DOI: 10.1097/ms9.0000000000003096.

[103] D. Jiang, D. Cirmirakis, and A. Demosthenous. 'A Vestibular Prosthesis With Highly-Isolated Parallel Multichannel Stimulation'. In: *IEEE Transactions on Biomedical Circuits and Systems* 9.1 (2015), pp. 124–137. ISSN: 1932-4545. DOI: 10.1109/tbcas.2014.2323310.

[104] D. Jiang and A. Demosthenous. 'A Multichannel High-Frequency Power-Isolated Neural Stimulator With Crosstalk Reduction'. In: *IEEE Transactions on Biomedical Circuits and Systems* 12.4 (2018), pp. 940–953. ISSN: 1932-4545. DOI: 10.1109/tbcas.2018.2832541.

[105] M. D. Johnson, K. J. Otto, and D. R. Kipke. 'Repeated voltage biasing improves unit recordings by reducing resistive tissue impedances'. In: *IEEE Transactions on Neural Systems and Rehabilitation Engineering* 13.2 (2005), pp. 160–165. ISSN: 1534-4320. DOI: 10.1109/tnsre.2005.847373.

[106] M. D. Johnson, S. Miocinovic, C. C. McIntyre, and J. L. Vitek. 'Mechanisms and Targets of Deep Brain Stimulation in Movement Disorders'. In: *Neurotherapeutics* 5.2 (Apr. 2008), pp. 294–308. ISSN: 1878-7479. DOI: 10.1016/j.nurt.2008.01.010.

[107] K. Kadan-Jamal, F. Wronowski, A. Jin, T. E. Naegele, V. R. Montes, X. Tao, A. Dominguez-Alfaro, C. Lee, and G. G. Malliaras. 'Electrical Stimulation of Cells: Drivers, Technology, and Effects'. In: *Chemical Reviews* 125.15 (2025), pp. 6874–6905. ISSN: 0009-2665. DOI: 10.1021/acs.chemrev.4c00468.

[108] R. M. Kandadai, S. S. Meka, S. Kola, R. Alugolu, and R. Borgohain. 'Constant Current Versus Constant Voltage DBS Stimulators–Changing Trend'. In: *Annals of Indian Academy of Neurology* 26.4 (2023), pp. 368–369. ISSN: 0972-2327. DOI: 10.4103/aian.aian_508_23.

[109] M. A. Khalid, S. Mark, and R. Blakey. *WE-MCA Multilayer Chip Antenna Placement & Matching*. 2018. URL: https://www.we-online.com/catalog/media/o139357v410%20AppNote_ANP057a_WE-MCA%20Multilayer%20Chip%20Antenna%20Placement%20&%20Matching.pdf (visited on 11/23/2025).

[110] M. A. Khan, H. Fares, H. Ghayvat, I. C. Brunner, S. Puthusserypady, B. Razavi, M. Lansberg, A. Poon, and K. J. Meador. 'A systematic review on functional electrical stimulation based rehabilitation systems for upper limb post-stroke recovery'. In: *Frontiers in Neurology* 14 (2023), p. 1272992. ISSN: 1664-2295. DOI: 10.3389/fneur.2023.1272992.

[111] A. D. Kirsch, S. Hassin-Baer, C. Matthies, J. Volkmann, and F. Steigerwald. 'Anodic versus cathodic neurostimulation of the subthalamic nucleus: a randomized-controlled study of acute clinical effects'. In: *Parkinsonism & Related Disorders* 55 (2018), pp. 61–67. ISSN: 1353-8020. DOI: 10.1016/j.parkreldis.2018.05.015.

[112] M. Kiwalkar. *Design and Layout Guidelines for Matching Network and Antenna for WirelessUSB™ LP Family*. 2011. URL: https://www.deviationtx.com/media/kunena/attachments/46/CYRF6936_LayoutandMatching.pdf (visited on 11/23/2025).

[113] A. Klinder, F. Moews, J. Ziebart, Y. Su, C. Gabler, A. Jonitz-Heincke, U. van Rienen, M. Ellenrieder, and R. Bader. 'Effects of electrical stimulation with alternating fields on the osseointegration of titanium implants in the rabbit tibia - a pilot study'. In: *Frontiers in Bioengineering and Biotechnology* 12 (2024), p. 1395715. ISSN: 2296-4185. DOI: 10.3389/fbioe.2024.1395715.

[114] S. Knorr, T. Musacchio, R. Paulat, C. Matthies, H. Endres, N. Wenger, C. Harms, and C. W. Ip. 'Experimental deep brain stimulation in rodent models of movement disorders'. In: *Experimental Neurology* 348 (Feb. 2022), p. 113926. ISSN: 0014-4886. DOI: 10.1016/j.expneurol.2021.113926.

[115] S. Knorr, L. Rauschenberger, U. R. Pasos, M. U. Friedrich, R. L. Peach, K. Grundmann-Hauser, T. Ott, A. O'Leary, A. Reif, P. Tovote, J. Volkmann, and C. W. Ip. 'The evolution of dystonia-like movements in TOR1A rats after transient nerve injury is accompanied by dopaminergic dysregulation and abnormal oscillatory activity of a central motor network'. In: *Neurobiology of Disease* 154 (2021), p. 105337. ISSN: 0969-9961. DOI: 10.1016/j.nbd.2021.105337.

[116] L. Koessler, S. Colnat-Coulbois, T. Cecchin, J. Hofmanis, J. P. Dmochowski, A. M. Norcia, and L. G. Maillard. 'In-vivo measurements of human brain tissue conductivity using focal electrical current injection through intracerebral multicontact electrodes'. In: *Human Brain Mapping* 38.2 (Oct. 2017), pp. 974–986. ISSN: 1065-9471. DOI: 10.1002/hbm.23431.

[117] F. Kölbl, G. N'Kaoua, F. Naudet, F. Berthier, E. Faggiani, S. Renaud, A. Benazzouz, and N. Lewis. 'An Embedded Deep Brain Stimulator for Biphasic Chronic Experiments in Freely Moving Rodents'. In: *IEEE Transactions on Biomedical Circuits*

and Systems 10.1 (2016), pp. 72–84. ISSN: 1932-4545. DOI: 10.1109/tbcas.2014.2368788.

[118] T. Kotnik, D. Miklavčič, and L. M. Mir. 'Cell membrane electropermeabilization by symmetrical bipolar rectangular pulses: Part II. Reduced electrolytic contamination'. In: *Bioelectrochemistry* 54.1 (2001), pp. 91–95. ISSN: 1567-5394. DOI: 10.1016/s1567-5394(01)00115-3.

[119] A. Z. Kouzani, R. P. Kale, P. P. Zarate-Garza, M. Berk, K. Walder, and S. J. Tye. 'Validation of a Portable Low-Power Deep Brain Stimulation Device Through Anxiolytic Effects in a Laboratory Rat Model'. In: *IEEE Transactions on Neural Systems and Rehabilitation Engineering* 25.9 (Sept. 2017), pp. 1365–1374. ISSN: 1534-4320. DOI: 10.1109/tnsre.2016.2628760.

[120] F. S. Kragelund, K. Spiliotis, M. Heerdegen, T. Sellmann, H. Bathel, A. Luettig, A. Richter, J. Starke, R. Köhling, and D. Franz. 'Network-wide effects of pallidal deep brain stimulation normalised abnormal cerebellar cortical activity in the dystonic animal model'. In: *Neurobiology of Disease* 205 (2025), p. 106779. ISSN: 0969-9961. DOI: 10.1016/j.nbd.2024.106779.

[121] A. Kral, F. Aplin, and H. Maier. *Prostheses for the Brain: Introduction to Neuroprosthetics. Introduction to Neuroprosthetics*. Neuronal plasticity and neuroprosthetic devices. London: Academic Press, 2021. 397 pp. ISBN: 0128188936.

[122] J. K. Krauss, N. Lipsman, T. Aziz, A. Boutet, P. Brown, J. W. Chang, B. Davidson, W. M. Grill, M. I. Hariz, A. Horn, M. Schulder, A. Mammis, P. A. Tass, J. Volkmann, and A. M. Lozano. 'Technology of deep brain stimulation: current status and future directions'. In: *Nature Reviews Neurology* 17.2 (Nov. 2020), pp. 75–87. ISSN: 1759-4766. DOI: 10.1038/s41582-020-00426-z.

[123] J. K. Krauss, J. Yianni, T. J. Loher, and T. Z. Aziz. 'Deep Brain Stimulation for Dystonia'. In: *Journal of Clinical Neurophysiology* 21.1 (2004), pp. 18–30. ISSN: 0736-0258. DOI: 10.1097/00004691-200401000-00004.

[124] V. Krishna and A. Fasano. 'Neuromodulation: Update on current practice and future developments'. In: *Neurotherapeutics* 21.3 (2024), e00371. ISSN: 1878-7479. DOI: 10.1016/j.neurot.2024.e00371.

[125] W. S. Kruijt, H. J. Bergveld, and P. H. L. Notten. 'Electronic Network Modeling of Rechargeable Batteries: I. The Nickel and Cadmium Electrodes'. In: *Journal of The Electrochemical Society* 145.11 (1998), p. 3764. ISSN: 0013-4651. DOI: 10.1149/1.1838871.

[126] C. Lamy and P. Millet. 'A critical review on the definitions used to calculate the energy efficiency coefficients of water electrolysis cells working under near ambient

temperature conditions'. In: *Journal of Power Sources* 447 (2020), p. 227350. ISSN: 0378-7753. DOI: 10.1016/j.jpowsour.2019.227350.

[127] A. Lasia. 'The Origin of the Constant Phase Element'. In: *The Journal of Physical Chemistry Letters* 13.2 (2022), pp. 580–589. ISSN: 1948-7185. DOI: 10.1021/acs.jpclett.1c03782.

[128] A. C. Lazanas and M. I. Prodromidis. 'Electrochemical Impedance Spectroscopy–A Tutorial'. In: *ACS Measurement Science Au* 3.3 (2023), pp. 162–193. ISSN: 2694-250X. DOI: 10.1021/acsmeasuresciau.2c00070.

[129] A. Leblois, R. Reese, D. Labarre, M. Hamann, A. Richter, T. Boraud, and W. G. Meissner. 'Deep brain stimulation changes basal ganglia output nuclei firing pattern in the dystonic hamster'. In: *Neurobiology of Disease* 38.2 (2010), pp. 288–298. ISSN: 0969-9961. DOI: 10.1016/j.nbd.2010.01.020.

[130] K. J. Lee, I. Shim, J. H. Sung, J. T. Hong, I. sup Kim, and C. B. Cho. 'Striatal Glutamate and GABA after High Frequency Subthalamic Stimulation in Parkinsonian Rat'. In: *Journal of Korean Neurosurgical Society* 60.2 (2017), pp. 138–145. ISSN: 2005-3711. DOI: 10.3340/jkns.2016.0202.020.

[131] S. F. Lempka, B. Howell, K. Gunalan, A. G. Machado, and C. C. McIntyre. 'Characterization of the stimulus waveforms generated by implantable pulse generators for deep brain stimulation'. In: *Clinical Neurophysiology* 129.4 (2018), pp. 731–742. ISSN: 1388-2457. DOI: 10.1016/j.clinph.2018.01.015.

[132] S. F. Lempka, M. D. Johnson, S. Miocinovic, J. L. Vitek, and C. C. McIntyre. 'Current-controlled deep brain stimulation reduces in vivo voltage fluctuations observed during voltage-controlled stimulation'. In: *Clinical Neurophysiology* 121.12 (2010), pp. 2128–2133. ISSN: 1388-2457. DOI: 10.1016/j.clinph.2010.04.026.

[133] S. F. Lempka, M. D. Johnson, M. A. Moffitt, K. J. Otto, D. R. Kipke, and C. C. McIntyre. 'Theoretical analysis of intracortical microelectrode recordings'. In: *Journal of Neural Engineering* 8.4 (2011), p. 045006. ISSN: 1741-2560. DOI: 10.1088/1741-2560/8/4/045006.

[134] S. F. Lempka, S. Miocinovic, M. D. Johnson, J. L. Vitek, and C. C. McIntyre. 'In vivo impedance spectroscopy of deep brain stimulation electrodes'. In: *Journal of Neural Engineering* 6.4 (2009), p. 046001. ISSN: 1741-2560. DOI: 10.1088/1741-2560/6/4/046001.

[135] J. Li, X. Liu, W. Mao, T. Chen, and H. Yu. 'Advances in Neural Recording and Stimulation Integrated Circuits'. In: *Frontiers in Neuroscience* 15 (2021), p. 663204. ISSN: 1662-453X. DOI: 10.3389/fnins.2021.663204.

[136] Q. Li, Y. Ke, D. C. W. Chan, Z.-M. Qian, K. K. L. Yung, H. Ko, G. W. Arbuthnott, and W.-H. Yung. 'Therapeutic Deep Brain Stimulation in Parkinsonian Rats Directly Influences Motor Cortex'. In: *Neuron* 76.5 (2012), pp. 1030–1041. ISSN: 0896-6273. DOI: 10.1016/j.neuron.2012.09.032.

[137] H. Liu, C. Wang, F. Zhang, and H. Jia. 'An implantable device for neuropsychiatric rehabilitation by chronic deep brain stimulation in freely moving rats'. In: *NeuroReport* 28.3 (Feb. 2017), pp. 128–133. ISSN: 0959-4965. DOI: 10.1097/wnr.0000000000000727.

[138] X. Liu, A. Demosthenous, and N. Donaldson. 'Five valuable functions of blocking capacitors in stimulators'. In: *Proceedings of the 13th annual international conference of the FES society (IFESS08), Freiburg*. 2008, pp. 322–324.

[139] X. Liu, J. Li, W. Mao, Z. Chen, Z. Chen, P. Wan, and H. Yu. 'A Charge Balanced Neural Stimulator Silicon Chip for Human-Machine Interface'. In: *Frontiers in Electronics* 2 (2021), p. 773812. ISSN: 2673-5857. DOI: 10.3389/felec.2021.773812.

[140] J. A. López-Villanueva and S. Rodríguez Bolívar. 'Constant Phase Element in the Time Domain: The Problem of Initialization'. In: *Energies* 15.3 (Jan. 2022), p. 792. ISSN: 1996-1073. DOI: 10.3390/en15030792.

[141] W. Löscher, J. E. Fisher Jr, D. Schmidt, G. Fredow, D. Hönack, and W. Iturrian. 'The sz mutant hamster: a genetic model of epilepsy or of paroxysmal dystonia?' In: *Movement Disorders* 4.3 (1989), pp. 219–232. ISSN: 0885-3185. DOI: 10.1002/mds.870040304.

[142] R. Loss. *Constant Current Sources*. 2025. URL: http://www.loosweb.de/constant_current_sources/doc/en/index.html (visited on 05/26/2025).

[143] *Low-Cost Low-Power 2.4 GHz RF Transceiver datasheet (Rev. C)*. URL: https://www.ti.com/product/CC2500 (visited on 09/01/2025).

[144] A. M. Lozano, N. Lipsman, H. Bergman, P. Brown, S. Chabardes, J. W. Chang, K. Matthews, C. C. McIntyre, T. E. Schlaepfer, M. Schulder, Y. Temel, J. Volkmann, and J. K. Krauss. 'Deep brain stimulation: current challenges and future directions'. In: *Nature Reviews Neurology* 15.3 (2019), pp. 148–160. ISSN: 1759-4758. DOI: 10.1038/s41582-018-0128-2.

[145] A. Lüttig, S. Perl, D. Franz, M. Kotyra, M. Morawski, R. Köhling, and A. Richter. 'Expression of the extracellular matrix component brevican prior and after deep brain stimulation in the dtsz hamster model of dystonia'. In: *Brain Research Bulletin* 230 (2025), p. 111486. ISSN: 0361-9230. DOI: 10.1016/j.brainresbull.2025.111486.

[146] A. Lüttig, S. Perl, M. Zetsche, F. Richter, D. Franz, M. Heerdegen, R. Köhling, and A. Richter. 'Short-term stimulations of the entopeduncular nucleus induce cerebellar changes of c-Fos expression in an animal model of paroxysmal dystonia'. In: *Brain Research* 1823 (2024), p. 148672. ISSN: 0006-8993. DOI: 10.1016/j.brainres.2023.148672.

[147] S. Maesawa, Y. Kaneoke, Y. Kajita, N. Usui, N. Misawa, A. Nakayama, and J. Yoshida. 'Long-term stimulation of the subthalamic nucleus in hemiparkinsonian rats: neuroprotection of dopaminergic neurons'. In: *Journal of Neurosurgery* 100.4 (2004), pp. 679–687. ISSN: 0022-3085. DOI: 10.3171/jns.2004.100.4.0679.

[148] E. Maghsoudloo, M. Rezaei, M. Sawan, and B. Gosselin. 'A new charge balancing scheme for electrical microstimulators based on modulated anodic stimulation pulse width'. In: *2016 IEEE International Symposium on Circuits and Systems (ISCAS)*. IEEE, 2016, pp. 2443–2446. DOI: 10.1109/iscas.2016.7539086.

[149] N. Malek. 'Deep Brain Stimulation in Parkinson's Disease'. In: *Neurology India* 67.4 (2019), p. 968. ISSN: 0028-3886. DOI: 10.4103/0028-3886.266268.

[150] K.-M. Mangold. *Glossar: Grundbegriffe der Elektrochemie*. DECHEMA, Gesellschaft für Chemische Technik und Biotechnologie e.V., 2008. URL: https://dechema.de/kwi_media/Downloads/ec/Studententext_Grundbegriffe+der+Elektrochemie.pdf (visited on 03/26/2025).

[151] E. T. McAdams and J. Jossinet. 'Tissue impedance: a historical overview'. In: *Physiological Measurement* 16.3A (1995), A1–A13. ISSN: 0967-3334. DOI: 10.1088/0967-3334/16/3a/001.

[152] E. T. McAdams, A. Lackermeier, J. A. McLaughlin, D. Macken, and J. Jossinet. 'The linear and non-linear electrical properties of the electrode-electrolyte interface'. In: *Biosensors and Bioelectronics* 10.1-2 (1995), pp. 67–74. ISSN: 0956-5663. DOI: 10.1016/0956-5663(95)96795-z.

[153] E. T. McAdams and J. Jossinet. 'A physical interpretation of Schwan's limit current of linearity'. In: *Annals of Biomedical Engineering* 20.3 (1992), pp. 307–319. ISSN: 0090-6964. DOI: 10.1007/bf02368533.

[154] Medtronic. *Deep Brain Stimulation Systems - Activa Platform*. en-US. URL: https://www.medtronic.com/en-us/healthcare-professionals/products/neurological/deep-brain-stimulation/electrical-stimulation-systems/activa-rc-neurostimulator.html (visited on 09/24/2025).

[155] Medtronic. *Living with DBS - Recharging*. en-IN. URL: https://www.medtronic.com/in-en/patients/treatments-therapies/deep-brain-stimulation-essential-tremor/living-with-dbs/recharging.html (visited on 09/24/2025).

[156] *Medtronic earns U.S. FDA approval for the world's first Adaptive deep brain stimulation system for people with Parkinson's*. en. URL: https://news.medtronic.com/2025-02-24-Medtronic-earns-U-S-FDA-approval-for-the-worlds-first-Adaptive-deep-brain-stimulation-system-for-people-with-Parkinsons (visited on 09/24/2025).

[157] A. C. Meidahl, G. Tinkhauser, D. M. Herz, H. Cagnan, J. Debarros, and P. Brown. 'Adaptive Deep Brain Stimulation for Movement Disorders: The Long Road to Clinical Therapy'. In: *Movement Disorders* 32.6 (2017), pp. 810–819. ISSN: 0885-3185. DOI: 10.1002/mds.27022.

[158] W. Meissner, G. Paul, T. Reum, R. Reese, R. Sohr, R. Morgenstern, and A. Kupsch. 'The influence of pallidal deep brain stimulation on striatal dopaminergic metabolism in the rat'. In: *Neuroscience Letters* 296.2-3 (2000), pp. 149–152. ISSN: 0304-3940. DOI: 10.1016/s0304-3940(00)01659-1.

[159] C. Melon, C. Chassain, G. Bielicki, J.-P. Renou, L. Kerkerian-Le Goff, P. Salin, and F. Durif. 'Progressive brain metabolic changes under deep brain stimulation of subthalamic nucleus in parkinsonian rats'. In: *Journal of Neurochemistry* 132.6 (2015), pp. 703–712. ISSN: 0022-3042. DOI: 10.1111/jnc.13015.

[160] D. R. Merrill, M. Bikson, and J. G. R. Jefferys. 'Electrical stimulation of excitable tissue: design of efficacious and safe protocols'. In: *Journal of Neuroscience Methods* 141.2 (2005), pp. 171–198. ISSN: 0165-0270. DOI: 10.1016/j.jneumeth.2004.10.020.

[161] L. V. Metman, J. A. Karl, C. E. Gill, J. Volkmann, and A. Merola. 'Deep Brain Stimulation Programming: Fundamentals and Advanced Techniques. Fundamentals and Advanced Techniques'. In: *Deep Brain Stimulation Management*. Ed. by W. J. Marks and J. L. Ostrem. Cambridge University Press, 2022, pp. 58–87. DOI: 10.1017/9781108848992.007.

[162] R. E. Millard and R. K. Shepherd. 'A fully implantable stimulator for use in small laboratory animals'. In: *Journal of Neuroscience Methods* 166.2 (2007), pp. 168–177. ISSN: 0165-0270. DOI: 10.1016/j.jneumeth.2007.07.009.

[163] K. M. Miller, J. R. Patterson, J. Kochmanski, C. J. Kemp, A. C. Stoll, C. U. Onyekpe, A. Cole-Strauss, K. Steece-Collier, J. W. Howe, K. C. Luk, and C. E. Sortwell. 'Striatal Afferent BDNF Is Disrupted by Synucleinopathy and Partially Restored by STN DBS'. In: *The Journal of Neuroscience* 41.9 (2021), pp. 2039–2052. ISSN: 0270-6474. DOI: 10.1523/jneurosci.1952-20.2020.

[164] G. K. Moghadam, R. Wilke, G. J. Suaning, N. H. Lovell, and S. Dokos. 'Quasi-Monopolar Stimulation: A Novel Electrode Design Configuration for Performance

Optimization of a Retinal Neuroprosthesis'. In: *PLoS ONE* 8.8 (2013), e73130. ISSN: 1932-6203. DOI: 10.1371/journal.pone.0073130.

[165] *MSP430FR2553 Mixed-Signal Microcontrollers Datasheet*. Version Rev. D. URL: https://www.ti.com/product/MSP430FR2355 (visited on 11/19/2025).

[166] *MSP430G2553 Mixed-Signal Microcontroller Datasheet*. Version Rev. J. URL: https://www.ti.com/product/MSP430G2553 (visited on 11/19/2025).

[167] M. Murbach, B. Gerwe, N. Dawson-Elli, and L.-k. Tsui. 'impedance.py: A Python package for electrochemical impedance analysis'. In: *Journal of Open Source Software* 5.52 (2020), p. 2349. ISSN: 2475-9066. DOI: 10.21105/joss.02349. URL: https://doi.org/10.21105/joss.02349.

[168] T. Musacchio, M. Rebenstorff, F. Fluri, J. M. Brotchie, J. Volkmann, J. B. Koprich, and C. W. Ip. 'Subthalamic nucleus deep brain stimulation is neuroprotective in the A53T α-synuclein Parkinson's disease rat model'. In: *Annals of Neurology* 81.6 (2017), pp. 825–836. ISSN: 0364-5134. DOI: 10.1002/ana.24947.

[169] M. Nashed. *Deep Brain Stimulation (DBS)*. 2025. URL: https://app.biorender.com/biorender-templates/details/t-64c7105cee9636a6f6ab2988-deep-brain-stimulation-dbs (visited on 09/30/2025).

[170] J. Newman. 'Resistance for Flow of Current to a Disk'. In: *Journal of The Electrochemical Society* 113.5 (1966), pp. 501–502. ISSN: 0013-4651. DOI: 10.1149/1.2424003.

[171] P. J. Nicksic, D. T. Donnelly, N. Verma, A. J. Setiz, A. J. Shoffstall, K. A. Ludwig, A. M. Dingle, and S. O. Poore. 'Electrical Stimulation of Acute Fractures: A Narrative Review of Stimulation Protocols and Device Specifications'. In: *Frontiers in Bioengineering and Biotechnology* 10 (2022), p. 879187. ISSN: 2296-4185. DOI: 10.3389/fbioe.2022.879187.

[172] E. Noorsal, K. Sooksood, H. Xu, R. Hornig, J. Becker, and M. Ortmanns. 'A Neural Stimulator Frontend With High-Voltage Compliance and Programmable Pulse Shape for Epiretinal Implants'. In: *IEEE Journal of Solid-State Circuits* 47.1 (2012), pp. 244–256. ISSN: 0018-9200. DOI: 10.1109/jssc.2011.2164667.

[173] K. Nowak, E. Mix, J. Gimsa, U. Strauss, K. K. Sriperumbudur, R. Benecke, and U. Gimsa. 'Optimizing a Rodent Model of Parkinson's Disease for Exploring the Effects and Mechanisms of Deep Brain Stimulation'. In: *Parkinson's Disease* 2011.1 (2011), p. 414682. ISSN: 2042-0080. DOI: 10.4061/2011/414682.

[174] *nRF52833 Product Specification*. Version v1.7. URL: https://docs.nordicsemi.com/bundle/ps_nrf52833/page/keyfeatures_html5.html (visited on 11/19/2025).

[175] S. Nuber, F. Harmuth, Z. Kohl, A. Adame, M. Trejo, K. Schönig, F. Zimmermann, C. Bauer, N. Casadei, C. Giel, et al. 'A progressive dopaminergic phenotype associated with neurotoxic conversion of α-synuclein in BAC-transgenic rats'. In: *Brain* 136.2 (2013), pp. 412–432. ISSN: 1460-2156. DOI: 10.1093/brain/aws358.

[176] M. Nüssel. 'Weiterentwicklung der Tiefen Hirnstimulation (THS) im Tiermodell: Etablierung und Testung eines vollimplantierbaren Systems am Tiermodell der Ratte'. PhD thesis. Universitätsmedizin Rostock, 2022. DOI: 10.18453/ROSDOK_ID00004496.

[177] K. O'Sullivan, M. Orazem, K. Otto, C. Butson, and J. Baker. 'Electrical rejuvenation of chronically implanted macroelectrodes in nonhuman primates'. In: *Journal of Neural Engineering* 21.3 (2024), p. 036056. ISSN: 1741-2560. DOI: 10.1088/1741-2552/ad5703.

[178] M. O. Olbrich, W. Kiermeier, and E. Biebl. 'Evaluation of Potting Possibilities for RF Circuits up to 24 GHz'. In: (Mar. 2006).

[179] W. Olthuis, W. Streekstra, and P. Bergveld. 'Theoretical and experimental determination of cell constants of planar-interdigitated electrolyte conductivity sensors'. In: *Sensors and Actuators B: Chemical* 24.1-3 (1995), pp. 252–256. ISSN: 0925-4005. DOI: 10.1016/0925-4005(95)85053-8.

[180] W. H. Organization. *Global status report on neurology*. 2025. ISBN: 978-92-4-011613-9.

[181] M. Ortmanns, N. Unger, A. Rocke, M. Gehrke, and H. J. Tietdke. 'A 0.1 mm², digitally programmable nerve stimulation pad cell with high-voltage capability for a retinal implant'. In: *2006 IEEE International Solid State Circuits Conference-Digest of Technical Papers*. IEEE, 2006, pp. 89–98. DOI: 10.1109/isscc.2006.1696037.

[182] M. Ortmanns. 'Charge Balancing in Functional Electrical Stimulators: A Comparative Study'. In: *2007 IEEE International Symposium on Circuits and Systems (ISCAS)*. IEEE, 2007, pp. 573–576. DOI: 10.1109/iscas.2007.378802.

[183] M. Ortmanns, A. Rocke, M. Gehrke, and H.-J. Tiedtke. 'A 232-Channel Epiretinal Stimulator ASIC'. In: *IEEE Journal of Solid-State Circuits* 42.12 (2007), pp. 2946–2959. ISSN: 0018-9200. DOI: 10.1109/jssc.2007.908693.

[184] K. J. Otto, M. D. Johnson, and D. R. Kipke. 'Voltage Pulses Change Neural Interface Properties and Improve Unit Recordings With Chronically Implanted Microelectrodes'. In: *IEEE Transactions on Biomedical Engineering* 53.2 (2006), pp. 333–340. ISSN: 0018-9294. DOI: 10.1109/tbme.2005.862530.

[185] M. Paff, A. Loh, C. Sarica, A. M. Lozano, and A. Fasano. 'Update on Current Technologies for Deep Brain Stimulation in Parkinson's Disease'. In: *Journal of*

Movement Disorders 13.3 (2020), p. 185. ISSN: 2005-940X. DOI: 10.14802/jmd.20052.

[186] M. Parastarfeizabadi and A. Z. Kouzani. 'Advances in closed-loop deep brain stimulation devices'. In: *Journal of NeuroEngineering and Rehabilitation* 14.1 (2017), pp. 1–20. ISSN: 1743-0003. DOI: 10.1186/s12984-017-0295-1.

[187] M. Parastarfeizabadi, A. Z. Kouzani, I. Gibson, and S. J. Tye. 'A miniature closed-loop deep brain stimulation device'. In: *2016 38th Annual International Conference of the IEEE Engineering in Medicine and Biology Society (EMBC)*. IEEE, 2016, pp. 1786–1789. DOI: 10.1109/embc.2016.7591064.

[188] S. Paul. *Grundlagen der Elektrotechnik und Elektronik 1. Gleichstromnetzwerke und ihre Anwendungen*. Ed. by R. Paul. 6. Aufl. 2022. Berlin, Heidelberg: Springer Berlin Heidelberg, 2023. 1475 pp. ISBN: 9783662661888.

[189] S. Paul. *Grundlagen der Elektrotechnik und Elektronik 2. Elektromagnetische Felder und ihre Anwendungen*. Ed. by R. Paul. 2. Aufl. 2019. Berlin, Heidelberg: Springer Berlin Heidelberg, 2019. 1677 pp. ISBN: 9783662582213.

[190] J. P. Payonk, H. Bathel, N. Arbeiter, M. Kober, M. Fauser, A. Storch, U. van Rienen, and J. Zimmermann. 'Improving computational models of deep brain stimulation through experimental calibration'. In: *Journal of Neuroscience Methods* 414 (2025), p. 110320. ISSN: 0165-0270. DOI: 10.1016/j.jneumeth.2024.110320.

[191] F. W. Petraglia III, S. H. Farber, J. L. Han, T. Verla, J. Gallis, Y. Lokhnygina, B. Parente, P. Hickey, D. A. Turner, and S. P. Lad. 'Comparison of Bilateral vs. Staged Unilateral Deep Brain Stimulation (DBS) in Parkinson's Disease in Patients Under 70 Years of Age'. In: *Neuromodulation: Technology at the Neural Interface* 19.1 (2016), pp. 31–37. ISSN: 1094-7159. DOI: 10.1111/ner.12351.

[192] R. C. Pinnell, J. Dempster, and J. Pratt. 'Miniature wireless recording and stimulation system for rodent behavioural testing'. In: *Journal of Neural Engineering* 12.6 (2015), p. 066015. ISSN: 1741-2560. DOI: 10.1088/1741-2560/12/6/066015.

[193] R. C. Pinnell, A. P. de Vasconcelos, J. C. Cassel, and U. G. Hofmann. 'A Miniaturized, Programmable Deep-Brain Stimulator for Group-Housing and Water Maze Use'. In: *Frontiers in Neuroscience* 12 (Apr. 2018). DOI: 10.3389/fnins.2018.00231.

[194] F. Plocksties. *The SofTware dEfined impLantabLe modular plAtform (STELLA) for preclinical deep brain stimulation*. Version 1.0. Sept. 2021. URL: https://github.com/SFB-ELAINE/STELLA/.

[195] M. K. Puglia and P. K. Bowen. 'Cyclic Voltammetry Study of Noble Metals and Their Alloys for Use in Implantable Electrodes'. In: *ACS Omega* 7.38 (2022), pp. 34200–34212. ISSN: 2470-1343. DOI: 10.1021/acsomega.2c03563.

[196] L. Pycroft, J. Stein, and T. Aziz. 'Deep brain stimulation: An overview of history, methods, and future developments'. In: *Brain and Neuroscience Advances* 2 (2018), p. 2398212818816017. ISSN: 2398-2128. DOI: 10.1177/2398212818816017.

[197] F. Ramirez de Noriega, R. Eitan, O. Marmor, A. Lavi, E. Linetzky, H. Bergman, and Z. Israel. 'Constant Current versus Constant Voltage Subthalamic Nucleus Deep Brain Stimulation in Parkinson's Disease'. In: *Stereotactic and Functional Neurosurgery* 93.2 (2015), pp. 114–121. ISSN: 1011-6125. DOI: 10.1159/000368443.

[198] R. Ranjandish and A. Schmid. 'An active charge balancing method based on anodic current variation monitoring'. In: *2017 IEEE Biomedical Circuits and Systems Conference (BioCAS)*. IEEE, 2017, pp. 1–4. DOI: 10.1109/biocas.2017.8325209.

[199] R. Ranjandish and A. Schmid. 'An active charge balancing method based on self-oscillation of the anodic current'. In: *2016 IEEE Biomedical Circuits and Systems Conference (BioCAS)*. IEEE, 2016, pp. 496–499. DOI: 10.1109/biocas.2016.7833840.

[200] R. Ranjandish and O. Shoaei. 'Polarity detection base pulse insertion for active charge balancing in electrical stimulation'. In: *2014 IEEE Conference on Biomedical Engineering and Sciences (IECBES)*. IEEE, 2014, pp. 38–41. DOI: 10.1109/iecbes.2014.7047526.

[201] R. Reese, G. Charron, A. Nadjar, I. Aubert, M.-L. Thiolat, M. Hamann, A. Richter, E. Bezard, and W. G. Meissner. 'High frequency stimulation of the entopeduncular nucleus sets the cortico-basal ganglia network to a new functional state in the dystonic hamster'. In: *Neurobiology of Disease* 35.3 (2009), pp. 399–405. ISSN: 0969-9961. DOI: 10.1016/j.nbd.2009.05.022.

[202] *RHS2116 Digital Electrophysiology Stimulator/Amplifier Chip*. URL: https://intantech.com/files/Intan_RHS2116_datasheet.pdf (visited on 06/12/2025).

[203] P. R. F. Rocha, P. Schlett, U. Kintzel, V. Mailänder, L. K. J. Vandamme, G. Zeck, H. L. Gomes, F. Biscarini, and D. M. de Leeuw. 'Electrochemical noise and impedance of Au electrode/electrolyte interfaces enabling extracellular detection of glioma cell populations'. In: *Scientific Reports* 6.1 (2016), p. 34843. ISSN: 2045-2322. DOI: 10.1038/srep34843.

[204] G. L. E. Rueda, M. Ballini, N. V. Hellepute, and S. Mitra. 'Analysis of passive charge balancing for safe current-mode neural stimulation'. In: *2017 IEEE International Symposium on Circuits and Systems (ISCAS)*. IEEE, 2017, pp. 1–4. DOI: 10.1109/iscas.2017.8050621.

[205] M. C. M. Ruiz, R. P. Guimarães, and M. R. Mortari. 'Parkinson's disease rodent models: Are they suitable for DBS research?' In: *Journal of Neuroscience Methods*

380 (2022), p. 109687. ISSN: 0165-0270. DOI: 10.1016/j.jneumeth.2022.109687.

[206] S. B. Ryu, E. K. Bae, J. Kim, Y. S. Hwang, C. Im, J. W. Chang, H.-C. Shin, and K. H. Kim. 'Neuronal Responses in the Globus Pallidus during Subthalamic Nucleus Electrical Stimulation in Normal and Parkinson's Disease Model Rats'. In: *The Korean Journal of Physiology & Pharmacology* 17.4 (2013), p. 299. ISSN: 1226-4512. DOI: 10.4196/kjpp.2013.17.4.299.

[207] M. Saghafi, S. Chinnathambi, and S. G. Lemay. 'High-frequency phenomena and electrochemical impedance spectroscopy at nanoelectrodes'. In: *Current Opinion in Colloid & Interface Science* 63 (2023), p. 101654. ISSN: 1359-0294. DOI: 10.1016/j.cocis.2022.101654.

[208] S. Sahai, E. T. Effendi, E. C. Mahoney, H. R. Tucker, B. J. Moolick, G. Mamone, S. Mikkilineni, M. Gupta, A. Nicholson, F. Y. Chua, K. Akhtar, Z. Hirschstein, E. S. Molho, J. G. Pilitsis, and D. S. Shin. 'Effects of subthalamic nucleus deep brain stimulation on neuronal spiking activity in the substantia nigra pars compacta in a rat model of Parkinson's disease'. In: *Neuroscience Letters* 739 (2020), p. 135443. ISSN: 0304-3940. DOI: 10.1016/j.neulet.2020.135443.

[209] V. Sankar, E. Patrick, R. Dieme, J. C. Sanchez, A. Prasad, and T. Nishida. 'Electrode impedance analysis of chronic tungsten microwire neural implants: understanding abiotic vs. biotic contributions'. In: *Frontiers in Neuroengineering* 7 (2014), p. 13. ISSN: 1662-6443. DOI: 10.3389/fneng.2014.00013.

[210] R. Sauerheber and B. Heinz. 'Temperature effects on conductivity of seawater and physiologic saline, mechanism and significance'. In: *Chemical Sciences Journal* 6.109 (2015).

[211] E. W. Schmid, W. Fink, and R. Wilke. 'Operational challenges of retinal prostheses'. In: *Medical Engineering & Physics* 36.12 (2014), pp. 1644–1655. ISSN: 1350-4533. DOI: 10.1016/j.medengphy.2014.09.004.

[212] M. Schulz, J. Zschabitz, E. Reese, R. Hadar, C. Winter, and R. Thewes. 'A Rechargeable Battery-Driven, More than 4 Weeks Runtime, Biphasic Bilateral DBS Unit for Rodents'. In: *2019 IEEE 8th International Workshop on Advances in Sensors and Interfaces (IWASI)*. IEEE, 2019, pp. 15–19. DOI: 10.1109/iwasi.2019.8791302.

[213] J. M. Shea, C. M. Feigen, E. N. Eskandar, and N. J. Killian. 'Mechanisms of DBS: from informational lesions to circuit modulation and implications in OCD'. In: *Frontiers in Human Neuroscience* 19 (2025), p. 1492744. ISSN: 1662-5161. DOI: 10.3389/fnhum.2025.1492744.

[214] Y. Shi, Q. Chang, and X. Liu. 'An electrode-impedance-aware neurostimulator IC that achieves low-power consumption and fast charge balance'. In: *Journal of Neuroscience Methods* 404 (2024), p. 110058. ISSN: 0165-0270. DOI: 10.1016/j.jneumeth.2024.110058.

[215] J. Snel-Bongers, J. J. Briaire, F. J. Vanpoucke, and J. H. Frijns. 'Spread of Excitation and Channel Interaction in Single- and Dual-Electrode Cochlear Implant Stimulation'. In: *Ear and hearing* 33.3 (2012), pp. 367–376. ISSN: 0196-0202. DOI: 10.1097/aud.0b013e318234efd5.

[216] D. Soh, T. R. ten Brinke, A. M. Lozano, and A. Fasano. 'Therapeutic Window of Deep Brain Stimulation Using Cathodic Monopolar, Bipolar, Semi-Bipolar, and Anodic Stimulation'. In: *Neuromodulation: Technology at the Neural Interface* 22.4 (2019), pp. 451–455. ISSN: 1094-7159. DOI: 10.1111/ner.12957.

[217] J.-Y. Son and H.-K. Cha. 'An Implantable Neural Stimulator IC With Anodic Current Pulse Modulation Based Active Charge Balancing'. In: *IEEE Access* 8 (2020), pp. 136449–136458. ISSN: 2169-3536. DOI: 10.1109/access.2020.3012028.

[218] K. Sooksood, T. Stieglitz, and M. Ortmanns. 'An Active Approach for Charge Balancing in Functional Electrical Stimulation'. In: *IEEE Transactions on Biomedical Circuits and Systems* 4.3 (2010), pp. 162–170. ISSN: 1932-4545. DOI: 10.1109/tbcas.2010.2040277.

[219] A. L. Spieles-Engemann, M. M. Behbehani, T. J. Collier, S. L. Wohlgenant, K. Steece-Collier, K. Paumier, B. F. Daley, S. Gombash, L. Madhavan, G. T. Mandybur, J. W. Lipton, B. T. Terpstra, and C. E. Sortwell. 'Stimulation of the rat subthalamic nucleus is neuroprotective following significant nigral dopamine neuron loss'. In: *Neurobiology of Disease* 39.1 (2010), pp. 105–115. ISSN: 0969-9961. DOI: 10.1016/j.nbd.2010.03.009.

[220] A. L. Spieles-Engemann, K. Steece-Collier, M. M. Behbehani, T. J. Collier, S. L. Wohlgenant, C. J. Kemp, A. Cole-Strauss, N. D. Levine, S. E. Gombash, V. B. Thompson, J. W. Lipton, and C. E. Sortwell. 'Subthalamic nucleus stimulation increases brain derived neurotrophic factor in the nigrostriatal system and primary motor cortex'. In: *Journal of Parkinson's Disease* 1.1 (2011), pp. 123–136. ISSN: 1877-7171. DOI: 10.3233/jpd-2011-11008.

[221] R. Srinivasan and F. Fasmin. *An Introduction to Electrochemical Impedance Spectroscopy*. CRC Press, Mar. 2021. ISBN: 9781003127932. DOI: 10.1201/9781003127932.

[222] T. Sukhu, M. Kennelly, and R. Kurpad. 'Sacral neuromodulation in overactive bladder: a review and current perspectives'. In: *Research and Reports in Urology* Volume 8 (2016), pp. 193–199. ISSN: 2253-2447. DOI: 10.2147/rru.s89544.

[223] F. Tala, J. Leiber, H. Fisher, N. S. Muppaneni, and B. C. Johnson. 'A Low-Cost, Wireless, Multi-Channel Deep Brain Stimulation System for Rodents'. In: *2021 43rd Annual International Conference of the IEEE Engineering in Medicine & Biology Society (EMBC)*. IEEE, 2021, pp. 7526–7529. DOI: 10.1109/embc46164.2021.9629826.

[224] A. Taschwer, N. Butz, M. Kohler, D. Rossbach, and Y. Manoli. 'A Charge Balanced Neural Stimulator with 3.3 V to 49 V Supply Compliance and Arbitrary Programmable Current Pulse Shapes'. In: *2018 IEEE Biomedical Circuits and Systems Conference (BioCAS)*. IEEE, 2018, pp. 1–4. DOI: 10.1109/biocas.2018.8584755.

[225] *Technical Note of Coin Manganese Dioxide Lithium Battery*. TCN-CR-002-E. URL: https://www.murata.com/-/media/webrenewal/products/batteries/micro/cr/tcn-cr-001-200722.ashx?la=en&cvid=20210526041011000000 (visited on 09/03/2025).

[226] Y. Temel, V. Visser-Vandewalle, B. Aendekerk, B. Rutten, S. Tan, B. Scholtissen, C. Schmitz, A. Blokland, and H. W. M. Steinbusch. 'Acute and separate modulation of motor and cognitive performance in parkinsonian rats by bilateral stimulation of the subthalamic nucleus'. In: *Experimental Neurology* 193.1 (2005), pp. 43–52. ISSN: 0014-4886. DOI: 10.1016/j.expneurol.2004.12.025.

[227] Y. Temel, V. Visser-Vandewalle, S. Kaplan, R. Kozan, M. A. Daemen, A. Blokland, C. Schmitz, and H. W. Steinbusch. 'Protection of nigral cell death by bilateral subthalamic nucleus stimulation'. In: *Brain Research* 1120.1 (2006), pp. 100–105. ISSN: 0006-8993. DOI: 10.1016/j.brainres.2006.08.082.

[228] U. Tietze, C. Schenk, and E. Gamm. *Electronic Circuits. Handbook for Design and Application*. 2nd edition. Berlin, Heidelberg: Springer Berlin Heidelberg, 2008. 1543 pp. ISBN: 9783540786559.

[229] H. Tomiyasu, H. Shikata, K. Takao, N. Asanuma, S. Taruta, and Y.-Y. Park. 'An aqueous electrolyte of the widest potential window and its superior capability for capacitors'. In: *Scientific Reports* 7.1 (2017), p. 45048. ISSN: 2045-2322. DOI: 10.1038/srep45048.

[230] M. Tonge. 'Technological developments in electric-based DBS'. In: *Deep Brain Stimulation* 4 (2024), pp. 36–41. ISSN: 2949-6691. DOI: 10.1016/j.jdbs.2023.12.001.

[231] *Traditio et Innovatio: Magazin der Universität Rostock* 1 (2025). ISSN: 1432-1513. URL: https://www.uni-rostock.de/storages/uni-rostock/UniHome/Presse/Magazine/uni-magazin2025.pdf.

[232] N. Tran, M. Halpern, S. Bai, and E. Skafidas. 'Crosstalk current measurements using multi-electrode arrays in saline'. In: *2012 Annual International Conference of the IEEE Engineering in Medicine and Biology Society*. IEEE, 2012, pp. 3021–3024. DOI: 10.1109/embc.2012.6346600.

[233] U. Ungerstedt. '6-hydroxy-dopamine induced degeneration of central monoamine neurons'. In: *European Journal of Pharmacology* 5.1 (1968), pp. 107–110. ISSN: 0014-2999. DOI: 10.1016/0014-2999(68)90164-7.

[234] United Nations, Department of Economic and Social Affairs, Population Division. *World Population Ageing 2019 Highlights*. ST/ESA/SER.A/430. UN, Dec. 2019. ISBN: 9789210045537. DOI: 10.18356/9df3caed-en.

[235] J. Valsa, P. Dvorak, and M. Friedl. 'Network model of the CPE'. In: *Radioengineering* 20.3 (2011), pp. 619–626.

[236] J. Valsa and J. Vlach. 'RC models of a constant phase element'. In: *International Journal of Circuit Theory and Applications* 41.1 (Oct. 2011), pp. 59–67. ISSN: 1097-007X. DOI: 10.1002/cta.785.

[237] VARTA. *Technical Handbook CoinPower - Rechargable Li-Ion Button Cells Generation A4*. URL: https://www.texim-europe.com/getfile.ashx?id=130672.

[238] R. Vatsyayan, D. Cleary, J. R. Martin, E. Halgren, and S. A. Dayeh. 'Electrochemical safety limits for clinical stimulation investigated using depth and strip electrodes in the pig brain'. In: *Journal of Neural Engineering* 18.4 (2021), p. 046077. ISSN: 1741-2560. DOI: 10.1088/1741-2552/ac038b.

[239] R. Vatsyayan and S. A. Dayeh. 'A universal model of electrochemical safety limits in vivo for electrophysiological stimulation'. In: *Frontiers in Neuroscience* 16 (2022), p. 972252. ISSN: 1662-453X. DOI: 10.3389/fnins.2022.972252.

[240] M. Vidailhet, L. Vercueil, J.-L. Houeto, P. Krystkowiak, A.-L. Benabid, P. Cornu, C. Lagrange, S. T. du Montcel, D. Dormont, S. Grand, S. Blond, O. Detante, B. Pillon, C. Ardouin, Y. Agid, A. Destée, and P. Pollak. 'Bilateral Deep-Brain Stimulation of the Globus Pallidus in Primary Generalized Dystonia'. In: *New England Journal of Medicine* 352.5 (2005), pp. 459–467. ISSN: 0028-4793. DOI: 10.1056/nejmoa042187.

[241] N. P. Visanji, I. Kamali Sarvestani, M. C. Creed, Z. Shams Shoaei, J. N. Nobrega, C. Hamani, and L.-N. Hazrati. 'Deep brain stimulation of the subthalamic nucleus preferentially alters the translational profile of striatopallidal neurons in an animal model of Parkinson's disease'. In: *Frontiers in Cellular Neuroscience* 9 (2015), p. 221. ISSN: 1662-5102. DOI: 10.3389/fncel.2015.00221.

[242] S. Wang, A. Lu, and C.-J. Zhong. 'Hydrogen production from water electrolysis: role of catalysts'. In: *Nano Convergence* 8.1 (2021), p. 4. ISSN: 2196-5404. DOI: 10.1186/s40580-021-00254-x.

[243] S. Wang, Y. Jiang, A. Yang, F. Meng, and J. Zhang. 'The Expanding Burden of Neurodegenerative Diseases: An Unmet Medical and Social Need'. In: *Aging and disease* 16.5 (2024), p. 2937. ISSN: 2152-5250. DOI: 10.14336/ad.2024.1071.

[244] X. F. Wei. 'Analysis and design of electrodes for deep brain stimulation'. PhD thesis. 2009. URL: https://hdl.handle.net/10161/1084.

[245] J. Whitestone, A. Salih, and T. Goswami. 'Investigation of a Deep Brain Stimulator (DBS) System'. In: *Bioengineering* 10.10 (2023), p. 1160. ISSN: 2306-5354. DOI: 10.3390/bioengineering10101160.

[246] R. G. H. Wilke, G. K. Moghadam, N. H. Lovell, G. J. Suaning, and S. Dokos. 'Electric crosstalk impairs spatial resolution of multi-electrode arrays in retinal implants'. In: *Journal of Neural Engineering* 8.4 (2011), p. 046016. ISSN: 1741-2560. DOI: 10.1088/1741-2560/8/4/046016.

[247] J. C. Williams, J. A. Hippensteel, J. Dilgen, W. Shain, and D. R. Kipke. 'Complex impedance spectroscopy for monitoring tissue responses to inserted neural implants'. In: *Journal of Neural Engineering* 4.4 (2007), pp. 410–423. ISSN: 1741-2560. DOI: 10.1088/1741-2560/4/4/007.

[248] M. Wilson, L. Cowie, V. Farrow, M. Cree, and J. Scott. 'Rapid time-domain simulation of fractional capacitors with SPICE'. In: *Journal of Computational Electronics* 23.3 (2024), pp. 667–689. ISSN: 1569-8025. DOI: 10.1007/s10825-024-02160-x.

[249] M. Wilson, M. Elbohouty, L. Voss, and D. Steyn-Ross. 'Electrical impedance of mouse brain cortex in vitro from 4.7 kHz to 2.0 MHz'. In: *Physiological Measurement* 35.2 (2014), p. 267. ISSN: 0967-3334. DOI: 10.1088/0967-3334/35/2/267.

[250] A. Witt and A. Flint. *Chemie fürs Leben: Elektrochemie - 3. Konzeptbaustein: Electron meets energy – Eine Einführung in die quantitativen Beziehungen der Elektrochemie - ein schülerorientiertes Konzept zur schulischen Behandlung des Themas Elektrochemie*. Universität Rostock - Institut für Chemie, 2016. URL: https://www.didaktik.chemie.uni-rostock.de/storages/uni-rostock/Alle_MNF/Chemie_Didaktik/Forschung/Elektrochemie/Elektrochemie3.pdf.

[251] A. Wood and S. Force. *Internal Resistance of a Battery*. https://www.ossila.com/pages/internal-resistance-of-a-battery. Ossila. (Visited on 09/03/2025).

[252] H. A. Yiğit, H. Uluşan, S. Chamanian, and H. Külah. 'Charge Balance Circuit for Constant Current Neural Stimulation with Less than 8 nC Residual Charge'. In:

2019 IEEE International Symposium on Circuits and Systems (ISCAS). IEEE, 2019, pp. 1–5. DOI: 10.1109/iscas.2019.8702790.

[253] M. K. York and E. Moro. 'No differences in neuropsychological outcomes between constant current and voltage current subthalamic deep brain stimulation for Parkinson's disease'. In: *Annals of Translational Medicine* 5.7 (2017), p. 177. ISSN: 2305-5839. DOI: 10.21037/atm.2017.03.43.

[254] J. Zhang and J. D. Z. Chen. 'Systematic review: applications and future of gastric electrical stimulation'. In: *Alimentary Pharmacology & Therapeutics* 24.7 (2006), pp. 991–1002. ISSN: 0269-2813. DOI: 10.1111/j.1365-2036.2006.03087.x.

[255] K. K. Zhang, R. Matin, C. Gorodetsky, G. M. Ibrahim, and F. V. Gouveia. 'Systematic review of rodent studies of deep brain stimulation for the treatment of neurological, developmental and neuropsychiatric disorders'. In: *Translational Psychiatry* 14.1 (2024), p. 186. ISSN: 2158-3188. DOI: 10.1038/s41398-023-02727-5.

[256] S. Zhao, G. Li, C. Tong, W. Chen, P. Wang, J. Dai, X. Fu, Z. Xu, X. Liu, L. Lu, et al. 'Full activation pattern mapping by simultaneous deep brain stimulation and fMRI with graphene fiber electrodes'. In: *Nature Communications* 11.1 (2020), p. 1788. ISSN: 2041-1723. DOI: 10.1038/s41467-020-15570-9.

[257] J. Zimmermann. https://github.com/j-zimmermann/ImpedanceFitter. GitHub repository.

[258] J. Zimmermann, K. Budde, N. Arbeiter, F. Molina, A. Storch, A. M. Uhrmacher, and U. van Rienen. 'Using a Digital Twin of an Electrical Stimulation Device to Monitor and Control the Electrical Stimulation of Cells in vitro'. In: *Frontiers in Bioengineering and Biotechnology* 9 (2021), p. 765516. ISSN: 2296-4185. DOI: 10.3389/fbioe.2021.765516.

List of Peer-Reviewed Publications

[A1] D. Franz, F. S. Kragelund, M. Heerdegen, S. Perl, A. Lüttig, F. V. Plocksties, H. Bathel, A. Richter, and R. Köhling. 'Network-wide modulation of synaptic plasticity and spike patterns in motor circuits after pallidal deep brain stimulation in a dystonia model'. In: *Neurobiology of Disease* 214 (2025), p. 107037. ISSN: 0969-9961. DOI: 10.1016/j.nbd.2025.107037.

[A2] M. Heerdegen, M. Zwar, D. Franz, M. F. Hörnschemeyer, V. Neubert, F. Plocksties, C. Niemann, D. Timmermann, C. Bahls, U. van Rienen, M. Paap, S. Perl, A. Lüttig, A. Richter, and R. Köhling. 'Mechanisms of pallidal deep brain stimulation: Alteration of cortico-striatal synaptic communication in a dystonia animal model'. In: *Neurobiology of Disease* 154 (2021), p. 105341. ISSN: 0969-9961. DOI: 10.1016/j.nbd.2021.105341.

[A3] J. Heller, C. Niemann, F. Plocksties, C. Haubelt, and D. Timmermann. 'Towards virtual prototyping of electrically active implants using SystemC-AMS'. In: *MBMV 2020-Methods and Description Languages for Modelling and Verification of Circuits and Systems; GMM/ITG/GI-Workshop*. VDE. 2020, pp. 1–8. ISBN: 9783800752218.

[A4] P. W. Kämmerer, N. Engel, R. Bader, V. Engel, B. Frerich, D. Heimes, J. Kröger, L. Lembcke, F. Plocksties, H. Raben, U. van Rienen, A. Springer, D. Timmermann, J. Zimmermann, and M. Dau. 'Safety and preliminary efficacy of an electrically stimulated implant for mandibular bone regeneration: a pilot study in a large animal model'. In: *Clinical Oral Investigations* 29.5 (Apr. 2025), p. 226. ISSN: 1436-3771. DOI: 10.1007/s00784-025-06303-7.

[A5] P. W. Kämmerer, V. Engel, F. Plocksties, A. Jonitz-Heincke, D. Timmermann, N. Engel, B. Frerich, R. Bader, D. G. E. Thiem, A. Skorska, R. David, B. Al-Nawas, and M. Dau. 'Continuous Electrical Stimulation Affects Initial Growth and Proliferation of Adipose-Derived Stem Cells'. In: *Biomedicines* 8.11 (Nov. 2020), p. 482. ISSN: 2227-9059. DOI: 10.3390/biomedicines8110482.

[A6] M. Koschay, H. Richter, M. Statz, M. Kober, J. Puschmann, F. Plocksties, A. Storch, V. Kühn, and D. Timmermann. 'Case-Study on Visible Light Communication for Implant Monitoring'. In: *2022 IEEE Biomedical Circuits and Systems Conference (BioCAS)*. IEEE, 2022, pp. 275–279. DOI: 10.1109/biocas54905.2022.9948625.

[A7] M. Kotyra, S. Perl, A. Lüttig, D. Franz, H. Bathel, J. Marx, F. Plocksties, D. Timmermann, U. van Rienen, S. A. Fietz, R. Köhling, and A. Richter. 'Effects of longer-term pallidal stimulation on the severity of dystonia in a phenotypic animal model'.

In: *Experimental Neurology* 396 (Feb. 2025), p. 115548. ISSN: 0014-4886. DOI: 10.1016/j.expneurol.2025.115548.

[A8] J. Otto, M. Statz, H. Weber, M. Koschay, M. Kober, F. Plocksties, D. Timmermann, C. Haubelt, A. Storch, M. Fauser, F. Grützmacher, and S. Spors. 'Accelerometry is a valid method to distinguish between healthy and 6-OHDA-lesioned parkinsonian rats'. In: *Scientific Reports* 15.1 (Aug. 2025), p. 31883. ISSN: 2045-2322. DOI: 10.1038/s41598-025-17278-6.

[A9] M. Paap, S. Perl, A. Lüttig, F. Plocksties, C. Niemann, D. Timmermann, C. Bahls, U. van Rienen, D. Franz, M. Zwar, M. Rohde, R. Köhling, and A. Richter. 'Deep brain stimulation by optimized stimulators in a phenotypic model of dystonia: Effects of different frequencies'. In: *Neurobiology of Disease* 147 (Jan. 2021), p. 105163. ISSN: 0969-9961. DOI: 10.1016/j.nbd.2020.105163.

[A10] F. Plocksties, M. Kober, C. Niemann, J. Heller, M. Fauser, M. Nüssel, F. Uster, D. Franz, M. Zwar, A. Lüttig, J. Kröger, J. Harloff, A. Schulz, A. Richter, R. Köhling, D. Timmermann, and A. Storch. 'The software defined implantable modular platform (STELLA) for preclinical deep brain stimulation research in rodents'. In: *Journal of Neural Engineering* 18.5 (Sept. 2021), p. 056032. ISSN: 1741-2552. DOI: 10.1088/1741-2552/ac23e1.

[A11] F. Plocksties, A. Lüttig, C. Niemann, F. Uster, D. Franz, M. Kober, M. Koschay, S. Perl, A. Richter, R. Köhling, A. Storch, and D. Timmermann. 'Strategies on Deep Brain Stimulation Devices for Effective Behavioral Studies in Rodents'. In: *2022 IEEE-EMBS Conference on Biomedical Engineering and Sciences (IECBES)*. IEEE, Dec. 2022, pp. 376–381. DOI: 10.1109/iecbes54088.2022.10079260.

[A12] F. Plocksties, C. Niemann, R. Bader, F. Möws, H. Seitz, P. W. Kämmerer, M. Dau, V. Kamp, J. Heller, and D. Timmermann. 'Requirements and Design of an Implant for Electrical Stimulation for Bone Regeneration in Animals'. In: *2020 IEEE 2nd Global Conference on Life Sciences and Technologies (LifeTech)*. IEEE, Mar. 2020, pp. 157–160. DOI: 10.1109/lifetech48969.2020.1570619159.

[A13] F. Plocksties, C. Niemann, M. Fauser, A. Storch, D. Timmermann, and C. Haubelt. 'STELLA+: Expanding the Research Potential for Long-Term Deep Brain Stimulation Studies in Freely-Moving Rodents'. In: *Proceedings of the 18th International Joint Conference on Biomedical Engineering Systems and Technologies - BIODEVICES*. INSTICC. SciTePress, 2025, pp. 74–87. ISBN: 978-989-758-731-3. DOI: 10.5220/0013305200003911.

[A14] F. Plocksties, O. U. Shah, F. Uster, M. Ali, M. Koschay, M. Kober, A. Storch, and D. Timmermann. 'Energy-Efficient modular RF interface for fully implantable electrical

devices in small rodents'. In: *2021 IEEE Biomedical Circuits and Systems Conference (BioCAS)*. IEEE, Oct. 2021, pp. 1–6. DOI: 10.1109/biocas49922.2021.9645022.

[A15] M. Statz, M. Kober, F. Schleuter, H. Bathel, F. Plocksties, D. Timmermann, U. van Rienen, M. Fauser, and A. Storch. 'Effects of deep brain stimulation in the subthalamic nucleus (STN-DBS) on cellular plasticity in catecholaminergic systems in a hemiparkinsonian rat model'. In: *Brain Stimulation* 16.1 (Jan. 2023), pp. 313–314. ISSN: 1935-861X. DOI: 10.1016/j.brs.2023.01.577.

[A16] M. Statz, F. Schleuter, H. Weber, M. Kober, F. Plocksties, D. Timmermann, A. Storch, and M. Fauser. 'Subthalamic nucleus deep brain stimulation does not alter growth factor expression in a rat model of stable dopaminergic deficiency'. In: *Neuroscience Letters* 814 (Sept. 2023), p. 137459. ISSN: 0304-3940. DOI: 10.1016/j.neulet.2023.137459.

[A17] M. Statz, H. Weber, F. Weis, M. Kober, H. Bathel, F. Plocksties, U. van Rienen, D. Timmermann, A. Storch, and M. Fauser. 'Subthalamic nucleus deep brain stimulation induces functional deficits in norepinephrinergic neurotransmission in a Parkinson's disease model'. In: *Brain Research* 1841 (Oct. 2024), p. 149128. ISSN: 0006-8993. DOI: 10.1016/j.brainres.2024.149128.

[A18] F. Uster, F. Plocksties, and D. Timmermann. 'Decentral load control for data centers'. In: *2020 International Conferences on Internet of Things (iThings) and IEEE Green Computing and Communications (GreenCom) and IEEE Cyber, Physical and Social Computing (CPSCom) and IEEE Smart Data (SmartData) and IEEE Congress on Cybermatics (Cybermatics)*. IEEE, 2020, pp. 350–359. DOI: 10.1109/ithings-greencom-cpscom-smartdata-cybermatics50389.2020.00070.

[A19] F. Uster, F. Plocksties, and D. Timmermann. 'Room Lighting for Grid Stabilization'. In: *2021 5th International Conference on Smart Grid and Smart Cities (ICSGSC)*. IEEE, June 2021, pp. 39–44. DOI: 10.1109/icsgsc52434.2021.9490433.

A State of the Art in Detail (Part I)

Table A.1: Comparison of key features in existing rodent DBS devices designed with off-the-shelf components. Adapted from [A13]

DBS Device	PCB volume category	Device control				Data output technology		Provided device/ physiological data							Device mounting			Stimulation properties						Extra features	
		Radio frequency (RF)	Reed switch/Magnetic sensor	Physical switch/potentiometer	Optical	Radio frequency (RF)	Optical	High-accuracy temperature	3-axis acceleration	Local field potentials (LFP)	Stimulation monitoring (BIST)	Battery status	Stimulation on/off	Stimulation protocol	Head	Back	Implant	Dual-channel	Current-controlled	Voltage-controlled	Charge-balanced	SW-adjustable stim. parameters	Closed-loop DBS capabilities	Auto-set compliance voltage	On-board battery recharge
Battery-powered																									
STELLA4 [A13]	L	●	●	-	-	●	●	●	●	-	●	●	●	●	-	-	●	●	●	●	●	●	●	●	●
STELLA3/3.1 [A10] /[A14]	VL/L	-	●	-	-	-	●*	-	-	-	●	●	●	-	-	-	●	●	●	-	●	●	-	●	-
Bhaskara2024[16]	VH	●	-	●	-	●	-	-	-	-	-	-	-	-	-	●	-	-	●	-	●	◐	-	-	-
Grotemeyer2024[85]	VL	-	●	-	-	-	●	-	-	-	●§	-	●	-	-	-	◐♣	-	●	-	●	●	-	-	-
Tala2021[223]	VH	●	-	-	-	●	-	-	-	-	●	-	●	-	-	●	-	●	●	-	●	●	-	-	-
Fleischer2020[74]	VL	-	●	-	-	-	●	-	-	-	●§	-	●	-	-	-	●	-	●	-	●	●	-	-	-
Adams2019[2]	H	-	●	-	-	-	●	-	-	-	-	●	●	-	-	●	-	-	●	-	●	●	-	-	-
Alpaugh2019[4]	M*	-	-	-	-	-	●	-	-	-	-	●	-	-	-	-	●	-	●	-	●	◐	-	-	-
Schulz2019[212]	L	-	-	●♯	-	-	●	-	-	-	-	●	-	-	-	●	-	●	●	-	●	◐♯	-	-	●
Pinnell2018[193]	L	-	●	●♯	-	-	●	-	-	-	-	-	●	-	●	-	-	●	●	-	●	◐♯	-	-	-
Fluri2017[75]	M	-	-	●	-	-	●	-	-	-	●§	-	●	-	●	-	-	-	●	-	●	●	-	-	-
Liu2017[137]	M	●	-	-	-	●	-	-	-	-	●§	●	●	-	●	-	-	-	◐♮	-	-	●	-	-	-
Kouzani2017[119]	L	-	●	●	-	-	●	-	-	-	-	-	-	-	-	●	-	-	●	-	●	◐	-	-	-
Parastarfeizabadi2016[187]	VL	-	-	-	-	-	●	-	-	◐	-	-	-	-	●	-	-	-	●	-	●	◐	●	-	-
Kölbl2016[117]	L	-	-	-	-	-	-	-	-	-	-	-	-	-	●	-	-	◐△	●	-	●	●	-	-	-
Pinnell2015[192]	H	●	-	●	-	●	-	-	-	●	-	-	-	-	●	-	-	●	●	-	-	●	●	-	-
Acosta2015[1]	VL	-	-	-	-	-	-	-	-	-	-	●	-	-	-	●	-	-	●	-	●	●	-	-	-
Hentall2013[98]	L	-	●	-	-	-	●*	-	-	-	-	-	-	●	●	-	-	-	◐♮	-	●	●	-	-	-
Ewing2013[67]	H	-	●	-	-	-	●	-	-	-	-	●	-	-	-	-	●	●	●	-	●	●	-	-	-
de Haas2012[88]	L	-	●	-	-	-	●	-	-	-	-	●	●	-	-	-	●	-	◐♮	-	●	◐	-	-	-
Forni2012[76]	L	-	-	-	-	-	-	-	-	-	-	-	-	-	●	-	-	-	●	-	-	◐	-	-	-
Harnack2008[93]	M	-	●	-	-	●	-	-	-	-	-	-	●	●	-	-	●	-	●	-	●	◐	-	-	-
Battery-free (Wireless power transfer)																									
Burton2021[31]	VL	●	-	-	-	-	●	-	-	-	-	-	●	-	-	-	●	-	-	●	●	●	-	-	-
Heo2015[99]	M	●	-	-	●	-	●	-	-	-	-	-	●	-	-	●	-	-	-	●	●	◐	-	-	-
Millard2007[162]	L	●	-	-	-	-	●	-	-	-	-	-	●	-	-	-	●	-	●	-	●	◐	-	-	-

● = Feature is implemented;
◐ = Feature is partially implemented;
- = Feature is not implemented;
♮ = Inadequate current source design (see 3.3);
△ = Inadequate dual-channel design (see 3.3);
♯ = Manual current adjustment via potentiometer;
§ = No method/circuit description provided;
♣ = Partial subcutaneous implant only;
* = Estimated from photographic scale;

VL: Very Low (Volume < 500 mm^3)
L: Low (500 mm^3 ≤ Volume < 1000 mm^3)
M: Medium (1000 mm^3 ≤ Volume < 2000 mm^3)
H: High (2000 mm^3 ≤ Volume < 5000 mm^3)
VH: Very High (Volume ≥ 5000 mm^3)

B State of the Art in Detail (Part II)

Table B.1: Comparison of compliance voltage, charge balancing mode, battery runtime (DBS-only) and physical properties in existing rodent DBS devices designed with off-the-shelf components. Adapted from [A10].

DBS Device	Compliance Voltage (V)	Charge Balancing	Battery Runtime (DBS On)	Battery Configuration	Battery Weight (g)	Total Weight (g)	Battery Vol. (mm^3)	PCB Size (mm)	PCB Vol. (mm^3)	PCB+Battery Vol. (mm^3)
Battery-powered										
STELLA4 [A13]	1.6–4.2	Passive	124 days♯	CP9440 A4X	0.8	2	280	21.9x14.5x4 (Ø12.2x4 cutout)	803	1083
			318 days♯	CP1254 A4X	1.8	3	620			1423
STELLA3.1 [A10]	2.2–2.8	Passive	136 days (4 comm./h)♯	2xSR59	2x0.5	2/3□	2x127	Ø13x5.5	730	984
STELLA3 [A10]	2.2–2.8	Passive	137 days♯	CR1216	0.6	1.2/2.6□	200	Ø13x3.3	425	625
			3.6 years♯	CR2032	2.8	3.4/7.6□	1000			1425
Bhaskara2024[16]	5^{DC}/–	Active	n/a	n/a	10	19.9	n/a	43x38x5*	8170	n/a
Grotemeyer2024[85]	$3.1^{batt.}$/$1.9^{corr.}$	Passive	52 days	2xV364	2x0.3	2	2x70	(10x9+17x9)x2*	486	626
Tala2021[223]	5	Active	40 h w/ RF	400 mAh Zn:Air	n/a	15	n/a	43x24x15	15480	n/a
Fleischer2020[74]	$3.1^{batt.}$/$1.9^{corr.}$	Passive	30 days	2xSR916	2x0.5	2.3	2x117	10x10x2*	200	434
Adams2019[2]	10	Active	9 h	CR2032	3	5	1000	30x25x3*	2250	3250
Alpaugh2019[4]	2.1	Active	30 days	2xSR48	2x1.1	4.7	2x260	n/a	n/a	n/a
Schulz2019[212]	7	Active	31 days	Li-ion (401430)	5	10	1792	36x20x1	720	2512
Pinnell2018[193]	12	Act.+Pas.	30 h	CR1225	0.9	2.8□	300	Ø12.5x5	613	913
Fluri2017[75]	$3.1^{batt.}$/$1.9^{corr.}$	Passive	30 days	2xV364	2x0.3	2.5	2x70	n/a	1477	1617
Liu2017[137]	3♮	n/a	3 months w/ rests	CR2032	3	6	1000	Ø20x4	1256	2256
Kouzani2017[119]	$3^{batt.}$/$2.1^{corr.}$	Passive	22 days	CR2032	3	4.75	1000	15x18x3*	810	1810
Parastarfeizabadi2016[187]	$3^{batt.}$/$2.2^{corr.}$	Passive	10 h w/ closed-loop	CR1025	0.7	1.4	196	11.4x3*	306	502
Kölbl2016[117]	17	Active	6 days	3xp675	3x1.8	13.8□	3x550	26x12x3*	936	2586
Pinnell2015[192]	18	n/a	50 h w/o, 8 h w/ cl. loop	CR1/3N	2.3	8.5	1141	28x17x7	3332	4473
Acosta2015[1]	11.5	Active	14 days	4xZn:Air	4x0.32	2.3	352	8x7x2*	112	464
Hentall2013[98]	34♮	Passive	42 days w/ rests	2xSR41	2x0.6	2□	2x160	n/a	688	1008
Ewing2013[67]	20^{DC}/$19.1^{corr.}$	Passive	10 days	ICP521630PM	5.4	11.5□	3052	31.5x17x5.7	2228	5280
de Haas2012[88]	4.65♮	Active	10 h	3xSR416	3x0.13	2.1□	3x30	25x8x3*	600	690
Forni2012[76]	$6^{batt.}$/–	n/a	7 days	2xCR1220	2x0.8	6.5	2x250	28x9x3*	756	1256
Harnack2008[93]	18^{DC}/–	Active	28 days	2xSR48	2x1.1	13□	2x260	35x17.1x3*	1796	2316
Battery-free (Wireless power transfer)										
Burton2021[31]	V-Ctl.	Passive	Dep. on WPT eff.	-	-	0.046	-	n/a	20	-
Heo2015[99]	V-Ctl.	Active	Dep. on ext. batt.	-	-	-	-	-	-	-
Millard2007[162]	5	Active	Dep. on WPT eff.	-	-	2.5	-	14x12x6□	1008□	-

* = Estimated from photographic scale;

♯ = Estimated at V_{DD} = 3.1 V (STELLA3/STELLA3.1) and V_{DD2} = 3.1 V (STELLA4), corresponding to a compliance voltage of 2.2 V; setting: 100 µA, 60 µs and 130 Hz (bilateral);

♮ = Inadequate current source design (see 3.3); □ = With housing;

C Overview of STELLA Specifications

Feature	STELLA3/ STELLA3.1	STELLA4
Architecture		
PCB Specifications		
Configuration	Single PCB / Dual PCB (soldered)	Dual PCB (plug-in)
Dimensions	Ø 13 mm x 3.3/5 mm (H)	21.9 x 14.5 x 4 mm (LxWxH) (Ø 12.2 mm cutout)
PCB Volume	425 mm^3 / 730 mm^3	803 mm^3 (cutout subtracted)
PCB Weight	0.65 g / 0.96 g	1.14 g
Module Extension via	Soldering (castellated holes)	Plug-in (mezzanine connector)
Battery Type	≤ 3.1 V (e.g. SR, CR)	VARTA CoinPower A4X Li-ion
Rechargeability	×	✓ (via electrode cables)
V_{DD} Domains	Single-V_{DD}	Dual-V_{DD}/Level Translation
Performance		
Processing	16-bit RISC (up to 16 MHz)	16-bit RISC (up to 24 MHz) + 32-bit ARM Cortex-M4 (64 MHz)
Compliance Voltage Range	2.2–2.8 V	1.6–4.3 V
Power Consumption (DBS-on)	≈ 25 µW (V_{Compl} = 2.2 V)	≈ 36 µW (V_{Compl} = 2.2 V)
Communication		
LEDs	Single LED (red)	Three LEDs (red/green/IR)
Magnetic Sensor	Hall Sensor	TMR Sensor (lower I_Q)
Radio Frequency	2.4 GHz (Custom)	2.4 GHz (Bluetooth Low Energy)
Sensors		
Temperature Sensing	×	✓ (high-accuracy temp. sensor)
Motion Sensing	×	✓ (3-axis accelerometer)
Stimulation		
Stimulation Mode	Current-controlled	Current-controlled (voltage opt.)
SW-adj. Stim. Param.	✓	✓
Frequency Resolution	30.5 µs	30.5 µs
Pulse Duration Resolution	30.5/1 µs	30.5 µs
High-res Current Range	30–100 µA	30–500 µA
Channel No.	Dual	Dual
Independent Channel Control	×	✓
Closed-loop Stimulation	×	✓ (motion as feedback signal, on-board computation, offline evaluation)
Safety & Reproducibility		
Blocking Capacitor	✓	✓ (reduced offset voltage)
Charge Balancing Method	Passive	Passive (more area/energy-efficient)
Stim. Monitoring (BIST)	✓	✓ (higher accuracy)

Table C.1: Overview of STELLA3/STELLA3.1/STELLA4 features.

D Air-Filled Encapsulation Protocol for STELLA3

1. **Battery Preparation**
   a) Connect the positive (+) and negative (-) terminals of the battery with leads of approx. 3 cm length using spot welding.
   b) Spray all sides of the battery with a protective varnish (Plastik 70, Kontakt Chemie).
   c) Allow the varnish to dry for approx. 30 minutes.
2. **Assembly of Electrodes and Battery**
   a) Guide the electrode leads through the openings of the housing body.
   b) Solder the electrode leads according to the pin assignment.
   c) Solder the battery leads according to the pin assignment.
   d) Place the battery first, followed by the PCB into the housing, ensuring an electrical insulating film between them. The LED must face toward the cap.
   e) Test the device with a magnet to verify the blinking pattern (4x4).
   f) Power off STELLA3.
   g) Close the housing body with the cap.
3. **Encapsulation Process**
   a) Seal the electrode lead entry points in the housing with NuSil MED10-6607 (NuSil, USA).
   b) Seal the gap between the cap and housing with a thin line of NuSil MED-1511.
   c) Place the unit in a drying oven at 42 °C until the silicone is cured ($\approx$ 4 h).
   d) Verify the electrode seals. If defects are observed, repeat steps (a)–(c). Small holes can be filled with NuSil MED-1511.
   e) Mix epoxy resin EP 601 (Polytec, Germany) Part A and Part B in a 100:35 ratio (e.g., 5 g Part A + 1.75 g Part B, sufficient for 2–3 encapsulations).
   f) Remove air bubbles using a vacuum system.
   g) Coat the capsule fully with epoxy resin (either by submerging it or using a pipette) and remove excess epoxy with a brush.
   h) Suspend the capsule and cure in an oven at 42 °C for $\geq$ 8 h. Remove drips within first 30 minutes.
   i) After curing, repeat (g)–(h) for a second epoxy layer.
   j) Store the leftover epoxy in a closed container in the refrigerator.
   k) Once cured, apply a final layer of NuSil MED10-6607 (either by submerging it or using a pipette, remove excess silicone).
   l) Suspend and cure at 42 °C for $\geq$ 8 h. Remove drips within the first 30 minutes.
   m) Test the device with a magnet to verify the blinking pattern (4x4).
   n) Power off STELLA3.
   o) The STELLA3 implant is now fully encapsulated and ready for use.

E Setup for Recording Stimulation Current and Voltage

Signal acquisition was performed using the Keysight CX3324A, referred to by the company as *Device Current Waveform Analyzer*. This instrument allows the simultaneous recording and storage of current and voltage signals. All stimulation pulses were recorded in an *upright* orientation, and no signal inversion was applied during data processing. A detailed explanation of this convention is provided in Section 2.2.1. For all measurements, cathodic stimulation was applied, with the counter electrode connected to the stimulation output and the working (core) electrode connected to ground.

Current measurement Current measurements were carried out using the CX1102A current probe connected in series to ground with the probe's internal shunt resistor of 50 Ω.

Voltage measurement Voltage was recorded on a separate channel of the CX3324A using the CX1151A passive probe interface adapter connected to a standard oscilloscope probe. To prevent the measurement setup from loading the stimulation circuit by the relatively low input resistance of standard oscilloscopes (typically 1 MΩ, or 10 MΩ when using 10x probes), the voltage measurement was buffered using an operational amplifier (OPA2810, common-mode input impedance 12 GΩ ‖ 2.5 pF) configured as unity gain buffer powered from a dual supply. Buffering was particularly important for accurately measuring the bias voltage, which would otherwise be reduced due to loading effects.

The resulting recording setup is illustrated in Fig. E.1. Here, v_{DBS} denotes the voltage drop across the electrode contacts, while i_{DBS} represents the corresponding DBS current flowing through the load impedance $\underline{Z}$. Because the adjusted current amplitudes did not exceed 200 µA, the resulting voltage drop across the shunt resistor was considered negligible ($\leq$ 10 mV).

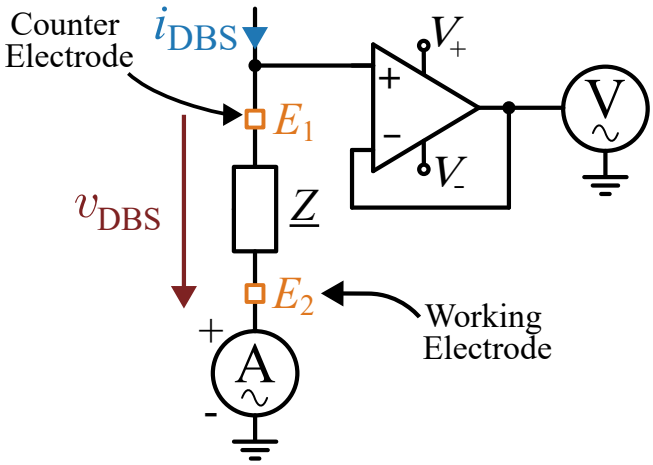

Figure E.1: Schematic of the recording setup for DBS voltage and current measurements.

F DBS Parameters Used in Rodent PD/Dystonia Studies

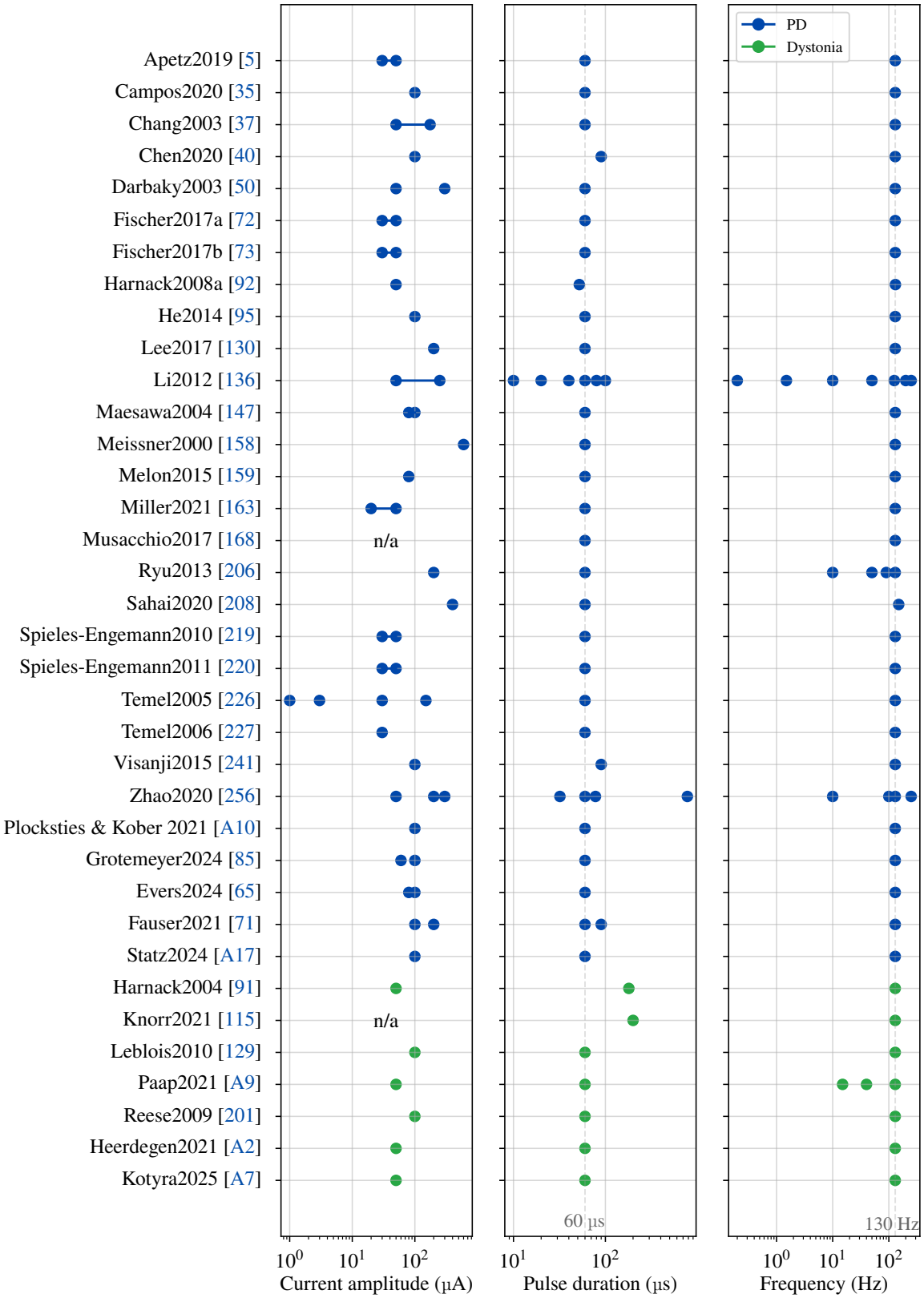

Figure F.1: Visualization of adjusted stimulation parameters (current amplitude, pulse duration, and frequency) in DBS studies using rodent models of Parkinson's disease (PD) and dystonia, adapted from the table in [115] and revised with updated references.

Selbstständigkeitserklärung

Hiermit erkläre ich, dass ich die von mir vorgelegte Arbeit mit dem Titel

Design and Implementation of a Flexible Research Platform for the Study of Deep Brain Stimulation

selbstständig und ohne unerlaubte fremde Hilfe angefertigt, keine anderen als die angegebenen Quellen und Hilfsmittel verwendet und die den verwendeten Quellen und Hilfsmitteln wörtlich oder inhaltlich entnommenen Stellen als solche kenntlich gemacht habe.

Rostock, den 28.11.2025

_____

Franz Veit Plocksties